Title
Molecular Mechanisms of Mechanosensitivity in Focal Adhesions

Author
Shams, Hengameh

Publication Date
2016

Peer reviewed|Thesis/dissertation

Molecular Mechanisms of Mechanosensitivity in Focal Adhesions

By
Hengameh Shams

A dissertation submitted in partial satisfaction of the
requirements for the degree of
Doctor of Philosophy
in

Applied Science and Technology

in the Graduate Division of the

University of California Berkeley

with Designated Emphasis on

Nanoscale Science and Engineering

Committee in charge:
Mohammad R. K. Mofrad, Chair
Professor Shaofan Li
Professor Seung-Wuk Lee
Professor Van P. Carey

Spring 2016

Molecular Mechanisms of Mechanosensitivity in Focal Adhesions

Abstract

Molecular Mechanisms of Mechanosensitivity in Focal Adhesions

By
Hengameh Shams

A dissertation submitted in partial satisfaction of the
requirements for the degree of
Doctor of Philosophy
in

Applied Science and Technology
with Designated Emphasis on
Nanoscale Science and Engineering

Mohammad R. K. Mofrad, Chair

Physical environment guides tissue regeneration and morphology in both health and disease. In the past three decades, several experiments illustrated that mechanical cues are captured and transduced to biochemical signals in the cellular level (mechanotransduction) mediated by cell adhesion. Cells adhere to their microenvironment through large protein assemblies known as focal adhesions that directly couple intra- and extra-cellular matrices and play a critical role in many vital cell functions including proliferation, differentiation and cell fate. It is inherently difficult to investigate the molecular basis of focal adhesion formation and growth using current experimental methodologies due to the fine time- and length-scales of protein-protein interactions. Here, I used molecular dynamics simulations to investigate the underlying molecular mechanisms of focal adhesion formation and maturation with atomic resolution.

Integrins are key focal adhesion receptors that reside on the cell membrane and mediate bi-directional signaling between cell cytoskeleton and ECM. Focal adhesions are a mixture of integrin-associated protein complexes known as integrin modules that forms the basic adhesion units. Integrin module formation is initiated by talin binding to the integrin tail, which is shown to be sufficient for integrin activation. A few other focal adhesion proteins can also directly engage with integrin's cytoplasmic tail and link it to the actin cytoskeleton. It is not yet clear how simultaneous (cooperative) versus sequential (competitive) binding of focal adhesion proteins to integrin with respect to talin result in different functionalities of integrin modules. In the first part of this study, competitive versus cooperative integrin binding between two important focal adhesion proteins –filamin and α-actinin– with talin were studied. The purpose of this aim was to gain insight on integrin module formation that eventually determines its functional properties.

Maturation of focal adhesions follows an increase in local forces. A well-established hypothesis on force transmission across focal adhesion complexes is the presence of mechanosensitive elements that change their conformations in response to force. In the second part of this study, we investigated and argued force-induced conformational changes of two important focal adhesion proteins –vinculin and α-actinin– in order to shed light on their role in transmission of forces across focal adhesions leading to adhesion maturation and growth.

In conclusion, this study unravels the structural basis of mechanosensitivity of key focal adhesions. Furthermore, important molecular interactions that give rise to mechanosensitivite characteristics of focal adhesions were studies. Important impacts of the current study include but are not limited to the following: 1) our results was used to complement previous experimental studies and also construct new hypotheses for future experiments; 2) Understanding regulatory mechanisms of focal adhesions is critical for developing novel therapeutics for many diseases involving cell adhesion including cancer as it enhances target recognition and the accuracy of drug delivery systems. 3) In addition, performing extensive simulations on protein complexes will contribute to improving the accuracy of various aspects of computational methods including empirical force fields that is indicative of our understanding of fundamental physical and chemical principles governing protein-protein interactions. 4) And most importantly, this work provides a fundamental insight into the relation between structure and function of mechanosensitive proteins in focal adhesions.

In dedication to my parents Nahid Alaei and Yahya Shams for their patience, support and understanding and most importantly their unconditional love.
And to the love of my life, Mehrzad Tartibi.

Table of contents

List of Figures and Tables

Figures:

Chapter 1

Chapter 2

Chapter 3

Section 3.1

Section 3.2

Section 3.3

Chapter 4

Section 4.1

Tables:

Acknowledgements

I wish to express my most sincere gratitude to my research advisor and dissertation chair Professor Mohammad Mofrad, who has mentored me throughout this work. He has the attitude of a father and the substance of a genius. He conveyed a spirit of confidence and adventure necessary for training an independent researcher since day one. It has been a true honor to be his graduate student.

My special thanks goes to Professor Shaofan Li, my qualification exam chair, for his continuous encouragements and advice at every step of my graduate study and the present dissertation. I would also like to deeply thank my dissertation committee members Professors Seung-Wuk Lee and Van P. Carey for their valuable feedbacks and great support.

Current and previous Mofrad lab members, Javad Golji, Mehrdad Mehrbod, Mohammad Azimi, Ruhollah Mousavi Baygi, Kiavash Garakani, and my dear friends Hanif Mahboobi Zeinab Jahed, Mohadesseh Peyro, Zainab Haydari and Mohammad Soheilypour have all contributed significantly to this work and have always been a source of great advice and collaboration.

I gratefully acknowledge my funding sources at University of California Berkeley. I was honored to be Chancellor's Fellow for the first two years of my graduate study and received the prestigious UC Dissertation Fellowship in my last year.

I thankfully acknowledge two of the most incredible Professors I had at UC Berkeley Ron Gronsky and Kimmen Sjolander who taught me how to learn and transfer my knowledge to others. Also, I would like to thank Linda Von Hoene for her unique workshops in regards to teaching and learning.

I am very grateful to the AS&T head graduate advisor Professor Daryl Chrzan for his guidance and advice throughout my graduate study. I also thank the former and current graduate student advisors of the AS&T program, Patricia Berumen and Ariana Castro for their hard work and exceptional care for students. Additionally, I heartily thank Laurie Roach and Jeret Lemontt for all their help in the dissertation submission process.

I would like to thank my lovely Vida Alaei (aunt) and Ahmad Javdani (uncle) who have always been there for me and my cousins Shabnam, Shervin and Shiva Javdani for all their help and attention when I first came to Berkeley. My time at Berkeley would not have been so wonderful without my friends, Ameneh Ahadi, Zeinab Jahed and Golnaz Baharnouri.

And finally I would like to give my foremost appreciation to my amazing parents and most precious gifts in life, Yahya Shams and Nahid Alaei who have always supported me in all my pursuits. I owe them everything and their happiness is my most important priority and motivation in life.

I greatly thank my soulmate Mehrzad Tartibi whose love has given me strength in this venture and my second parents Mohammad Tartibi and Talieh Yousefiani for their unconditional love.

CHAPTER 1: The 'stressful' life of adhesion molecules: A review on the mechanisms and approaches for characterizing mechanosensitivity in adhesomes

Cells need to constantly communicate with their microenvironment for their survival and thus have developed complicated sensory machinery for various external signals throughout the evolution. Cells associate with their microenvironment through large protein complexes known as focal adhesions that are specifically trained to transmit mechanical signals to and from the extracellular matrix (ECM). Focal adhesions (FA) are highly engaged with the actin cytoskeleton and are responsible for controlling cell shape and motility(Galbraith et al. 2002), which are essential for many important cellular functions such as migration, proliferation, differentiation and growth(Mofrad 2009). Focal adhesions are part of a powerful intracellular machinery orchestrating mechanotransduction pathways, i.e. underlying transducing environmental signals to biochemical cascades(Galbraith et al. 2002; Burridge et al. 1988). However, mechanisms through which FA formation and maturation are regulated have not yet been fully understood. Integrins are central focal adhesion receptors residing on the cell membrane and conducting bi-directional signaling(Giancotti 1997). More than 150 proteins are involved in signal transduction through integrins (Harburger & Calderwood 2009) but only a few are capable of directly linking integrin to the actin cytoskeleton, which make them particularly interesting. In this cCapter, we will review important focal adhesion players and their function. Furthermore, several state-of-the-art methodologies for detecting and exploring molecular mechanisms through which focal adhesion players perform their function will be reviewed.

What is mechanosensitivity?

Mechanosensitivity refers to the ability of sensing and responding to mechanical forces and is tightly associated to various biological functions. Mechanosensitivity occurs in various scales ranging from molecules to organs and thus should be characterized accordingly. The main focus of the present dissertation is on the molecular mechanisms of mechanosensitivity in focal adhesions. However, since cell-level approaches can give valuable insight into finer scales, we included a brief overview of the principles and techniques in this Chapter. Mechanosensation is the very first event prior to activating downstream mechanotransduction pathways and thus understanding its regulatory mechanisms is essential. Mechanosensitivity most likely regulates inner cellular events as well as more global cellular response to its microenvironment as forces on the ECM are much higher than what is required for cell translocation *per se*. Functional distinctions can be introduced between force transmission versus transduction capability of proteins based on whether a certain protein acts as a passive linker or undergoes force-induced conformational changes, respectively.

Where do forces come from?

Forces are sensed in the cellular level and further down in the molecular level, but they may be generated in higher scales or from a continuous flow. For instance, endothelial cells (EC) lining the vessel wall are constantly exposed to pulsatile blood flow. Smooth muscle cells (SMCs) are situated underneath the EC monolayer and are responsible for the generation of contractions and for regulating the diameter of the blood vessel. The outermost layer of the blood vessel is populated by fibroblasts, which are responsible for modulating the extracellular matrix (ECM) of this heterogeneous tissue. The various cell populations are separated by unique layers of deposited ECM proteins of diverse and variable composition. Note that cells in this example

experience various mechanical microenvironments, e.g., endothelial cells experience shear stress from blood flow and the rigidity of the underlying elastin-dominated ECM and cell-cell contacts. The SMCs and the fibroblasts are situated in the interstitium of the blood vessel and, therefore, the shear stress that they experience is only that of the interstitial flow, which is much lower than that of the blood flow exposed on ECMs. All these forces are ultimately captured and transduced in the molecular level.

Focal adhesions: Different layers and their associated proteins

Focal adhesions are large protein complexes that extend from the cell membrane to tens of nanometers away where they are connected to the actin cytoskeleton. Their components are selected from a large pool of various molecules including kinases, phosphatases and structural/adaptor proteins. Focal adhesions are one of the most crucial mechanosensitive subcellular organisms and the force transmission across them is mediated by a series of physical interactions between their constitutive proteins. The composition of early adhesions are significantly changed upon increasing the local stress level and eventually each focal adhesion plaque applies traction forces ranging from 1-10 kPa over an area of one micrometer square distributed throughout many proteins (Kuo et al. 2011). However, it is not yet clear how focal adhesion players dynamically change in response to mechanical cues and induce conformational changes in one another (Plotnikov et al. 2012; Balaban et al. 2001; Iwamoto & Calderwood 2015). In order to address this, a comprehensive understanding of the role of each focal adhesion protein, its recruitment time and interplay with other signaling agents is required. For instance, certain types of molecules are found for the whole lifetime of an adhesion site, while others may be recruited upon higher tension. However, it should be noted that even though some types of proteins are seen for a long time, the individual molecules dynamically exchange with new ones within that time frame. This is a well-known characteristic of a system in thermodynamic equilibrium: Although macroscopic properties seem to stay constant, the microstate of the system constantly changes. Specifically, the life-time of focal adhesions is in the order to minutes but, according to the fluorescence recovery after photobleaching (FRAP) experiments, the time scale for the kinetics of diffusion (or flow) of most focal adhesion proteins such as FAK, talin, zyxin, α-actinin and vinculin is less than 30 seconds suggesting that proteins are replaced rapidly(von Wichert et al. 2003; Lele et al. 2008).

Cell migration requires high traction forces generated on the ECM causing relative cell movement to its microenvironment. Focal adhesions generate friction necessary for walking against the substrate and prevent slippage. This notion has been suggested under the molecular clutch hypothesis in which adhesions act as clutches between the rearward actin retrograde flow (Figure 1-1) and the extracellular matrix (ECM). The actin retrograde flow is responsible for producing and applying forces from the cytoplasm to the ECM(Pollard & Cooper 2009), which is higher in the lamelliopodia than lamella due to the myosin contraction that captures and slows down the retrograde flow. It has been shown that cells adjust the strength of their adhesions based on the stiffness of the substrate just like us choosing the appropriate shoes for the ground we need to walk on. Interestingly, the flow of different focal adhesion molecules is correlated with the layer in which they reside in. For instance, α-actinin flow was very similar and strongly coupled both in terms of speed and direction with the actin flow showing direct interaction among them (Kanchanawong et al. 2010). As the localization of molecules move further away from actin, the molecular flow showed less coupling with the retrograde flow. While vinculin and talin flows showed less coupling with the actin flow as they are localized further away from

the actin regulatory later. Integrin flow had the lowest coupling with the actin flow due to their direct binding with the ECM molecules. This also showed that the clutch hypothesis does not suggest a rigid behavior as the two ends of the engaged clutch undergo different flow rates(Case & Waterman 2015). The kinetic energy of the flow is partially dissipated due to slip bonds between proteins and partially stored as potential energy of the focal complexes attached to integrins, which are arrested by the ECM proteins and become immobilized in the lipid membrane. If nascent adhesions are not engaged with actin retrograde flow, they will undergo quick turnovers (~ 1 minutes)(Choi et al. 2008). Myosin II contractility is required for further maturation of focal adhesions, resulting in growth along the direction of the actin retrograde flow(Gardel et al. 2008; Choi et al. 2008; Oakes et al. 2012).

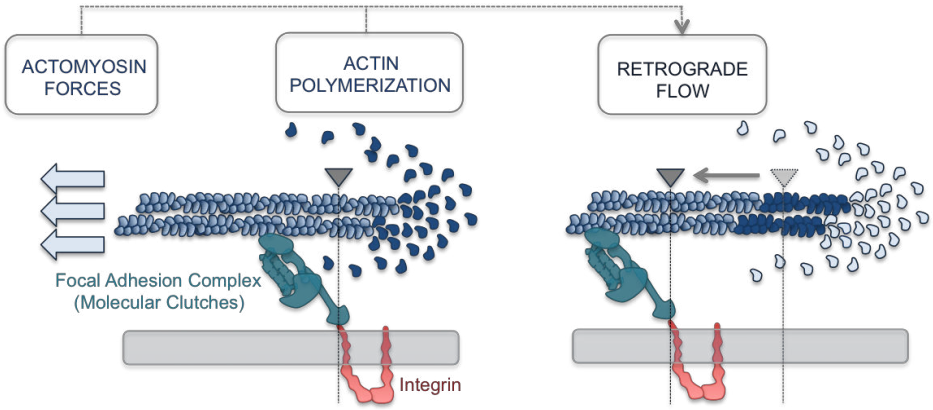

Figure 1-1. Actin retrograde flow. Actin polymerizes at the cell edge and actomyosin forces are applied to the end of actin fibers in the distal regions. The combination of these effects results in a rearward flow of actin relative to the cell edge. As focal adhesion complexes (molecular clutches) link integrin receptors to the actin cytoskeleton, the rearward actin flow is slowed down and transmitted to the extracellular matrix in the form of traction forces.

Focal adhesions consist of different layers, which are unique both in terms of composition and function (Figure 1-2). The integrin signaling layer is the closest to the plasma membrane and consists of many integrin regulatory proteins including FAK and talin head. Most of these proteins become engaged with the integrin cytoplasmic tail in the thickness of about 20 ns (Figure 1-2). Mechanical signals are further transmitted to the force transduction layer, which is an intermediate part between integrin signaling and the cytoskeleton, and contains mechanosensitive proteins such as vinculin and talin's rod domain. The next layer starting above 50 ns from the ECM is the actin regulatory layer where both actin and its binding proteins such as α-actinin and VASP reside. The mechanism of interactions within each FA layer is unique to that layer in terms of the capability of proteins to either transmit mechanical signals to their binding partners or transduce the signals by alternating their own binding affinity for other proteins. Also, focal adhesion players may act as either passive force transmitters or active mechanotransducers in different stages of focal adhesion formation and growth. Therefore, we review some of the important players in each FA layer and the current understanding about their mechanosensitive behavior. The localization of these molecules to each layer of focal adhesions depends on the stage of focal adhesion formation. Myosin II machinery is triggered by the mechanical signals transmitted from the substrate and pulls on the actin filaments that constantly polymerize against the cell membrane. These forces are further transmitted to the substrate through focal adhesion complexes mediated by a network of physical interaction between focal

adhesion proteins. In this work, we investigated how physical interactions between the following key focal adhesion proteins acting as mechanosensors regulates force transmission from the ECM to the actin cytoskeleton.

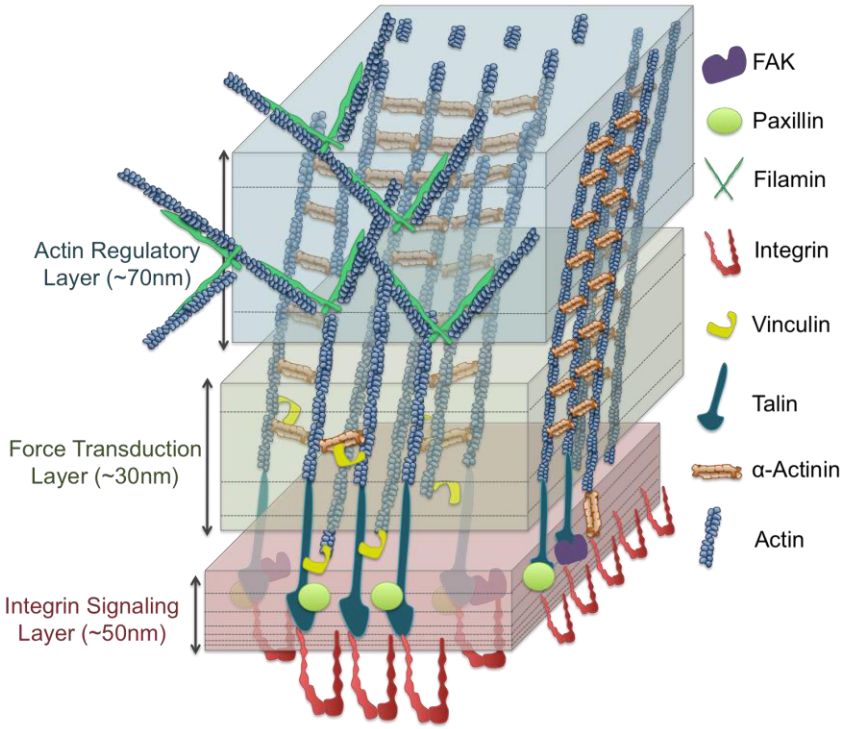

Figure 1-2. Different layers of focal adhesions. This semi-three-dimensional view of focal adhesion layers shows localization of key focal adhesion players and their cross-talk. Integrin receptors (*red*) are resided in the lipid membrane and are activated via talin (*dark cyan*) binding in the integrin signaling layer. Other important signaling molecules such as FAK (*purple*) and paxillin (*light green*) also function in this layer. The front side of focal adhesion (closer to the cell edge) is connected to mesh-like actin structures in lamellipodia as shown by dendric actins connected by filamins (*green*). Each focal adhesion layer has a unique composition of proteins that regulate force transmission within each layer. Stress fibers consisting of organized actin bundles are linked to the distal regions of focal adhesion. The force transduction layer is rich in vinculin (*yellow*) and talin head, which play important roles in force transmission. Actin and actin binding proteins such as α-actinin (*orange*) are localized in the actin regulatory layer.

Integrin: The integrators

Integrin molecules are formed via dimerization of various α- and β- subunits resulting in 24 functional heterodimers(Harburger & Calderwood 2009). Each subunit consists of a large extracellular domain (ectodomain), a transmembrane followed by a cytoplasmic domain transmitting forces bi-directionally between the inner and outer cellular environments. In the inactive conformation, the transmembrane domains of two integrin subunits are in close contact along with their extracellular domains being packed together and bent towards the membrane(Campbell & Humphries 2011), which show low affinities for the ECM ligands. Thereby, major conformational changes are required for an effective binding to the ECM that can be initiated from both intra- and extra-cellular environments (Figure 1-3).

Integrin activation is key to focal adhesion formation and is triggered from both intra- and extra-cellular interactions (Harburger & Calderwood 2009; Coutinho et al. 2007; Truong et

al. 2015). Downstream of integrin activation is the breakage of the transmembrane interactions between integrin subunits that ultimately result in full separation of the transmembrane helices (Coutinho et al. 2007; Kim et al. 2003; Mehrbod et al. 2013). This is followed by a global change in the extracellular domain of the integrin heterodimer switching it from a bent to a straight conformation for an effective engagement with the extracellular ligands. Thereby, integrins are classified as mechanotransducers as their affinity for the ECM ligands is mechanically regulated. Talin binding to the integrin tail is arguably both necessary and sufficient for integrin activation, however, it is not yet clear how such binding on the cytoplasmic side is sensed in the extracellular domain. Furthermore, other molecules such as kindlin, α-actinin and filamin may either compete or cooperate with talin for integrin activation and thus may also contribute to regulating integrin signaling. It should be noted that integrins are clustered together in order to engage more actin filaments to focal adhesion sites leading to adhesion maturation(Ridley et al. 2003; Schwartz 2010; Tadokoro et al. 2011).

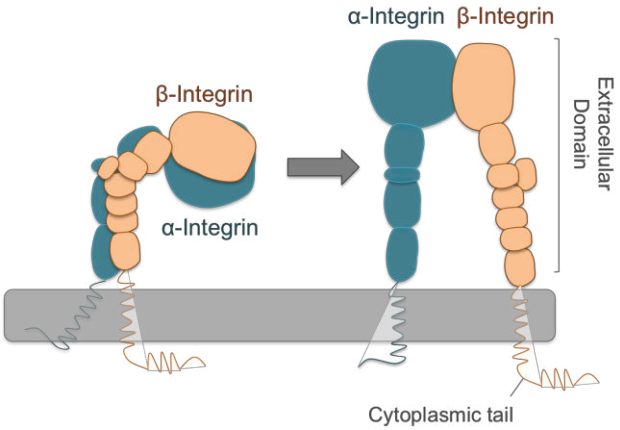

Figure 1-3. Integrin dimers consisting of α- and β-subunits. Extracellular domains are in the bent conformation in the inactive state and activated and the extracellular domains become straight.

Talin: The glowing dragon of the carnival

Talin's role in integrin activation has been extensively studied (Wegener et al. 2007; Critchley & Gingras 2008) Integrins regulate their ligand binding affinity by undergoing conformational changes in their extracellular domain(Kim et al. 2003). It has been shown that talin affects integrin activation by engaging to the β-subunit(Wegener et al. 2007). Talin first binds to the membrane-distal (MD) region of β-integrin that keeps the inactive state of integrin monomers intact. Talin binding is followed by and leads to breakage of a salt bridge between the subunits and their separation(Wegener et al. 2007).

Talin binding to the β-integrin tail results in disrupting key interactions between the transmembrane domains of integrin subunits named inner- and outer-membrane clasps (Wegener et al. 2007; Tadokoro et al. 2003; Lee et al. 2007). Talin has a rod-shape structure with a head domain, also known as the FERM domain, consisting of F0 to F3 lobes, which contains binding sites for integrin, paxillin and FAK. The FERM domain is followed by the rod and dimerization domains at the C-terminal end of the molecule, which are both mechanosensitive. The rod domain of talin is highly mechanosensitive and contains multiple vinculin binding sites, which become exposed upon exerting 2-5 pN of forces and engage with the actin cytoskeleton through vinculin (Lee et al. 2007; Golji & Mofrad 2013; Golji et al. 2011; Lee et al. 2008). The C-

terminal end of the talin molecules also directly associate with actin but around 30 nm farther from the plasma (Golji & Mofrad 2014). Vinculin binding prevent talin deactivation(Yao, Goult, et al. 2014; del Rio et al. 2009) (Figure 1-4).

α-Actinin: The linker master

α-Actinins crosslink both parallel and anti-parallel actin filaments to form polar and bipolar actin bundles, respectively(Djinović-Carugo et al. 1999; Blanchard et al. 1989; Otey & Carpen 2004). Previous studies have shown that α-actinins are found at anchoring junctions between the cytoskeleton and the membrane in smooth muscle cells and at

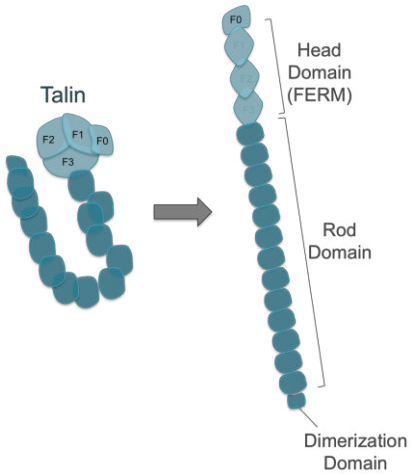

Figure 1-4. Talin is a mechanosensitive protein. Talin's head domain also known as the FERM domain binds to integrin while its rod domain contains several vinculin binding sites, which are not exposed in the absence of mechanical tension. Two talin molecules dimerize through their C-terminal.

focal adhesion sites in non-muscle cells(Zhang & Gunst 2006). α-Actinins may serve as mechanosensors and undergo conformational changes upon stress application through which their affinity for other focal adhesion molecules may change and start a series of biochemical events leading to signal transduction.

α-Actinin is an anti-parallel homodimer as confirmed and its full-length structure was resolved by Liu et al. in 2004 (Liu et al. 2004). Each α-actinin monomer has an actin-binding domain (ABD) at its N-terminus that is composed of two calponin homology (CH) domains(Shams et al. 2016) (Figure 1-5). The rod domain is connected to the ABD domain via a flexible neck region and consists of four spectrin repeats (R1-R4) interacting strongly with the neighboring monomer (affinity~10 pM)(Kahana & Gratzer 1991; Golji et al. 2009). Integrin binds between R1 and R2 spectrin repeats while vinculin binding site (αVBS) is inhibited in R4(Shams et al. 2012). Importantly, there is an intrinsic 90^{o} left-hand twist in the rod domain that puts ABDs of the two ends in different orientations relative to each other (please see Chapter 5 section 1 for more details).

The C-terminal end of each α-actinin monomer contains a calmodulin-like domain (CaM) with two EF-hand motifs, which are next to the ABD domain of the other monomer .(Figure 1-5) The CaM domain is involved in regulating the α-actinin function in a cell-dependent manner: In the non-muscle α-actinin (isoforms 1,4), the actin binding affinity is controlled by the interaction between the Ca^{2+} ions and the EF-hand motifs, (Burridge & Feramisco 1981) while muscle α-actinin (isoforms 2,3) are regulated by phosphatidylinositol 4,5-bisphosphate (PIP2) and have

lost the capability of engaging with the Ca^{2+} ions throughout the evolution(Fukami et al. 1994; Burridge & Feramisco 1981; Fraley et al. 2003).

Vinculin: Stretch and fetch

Vinculin is a globular protein consisting of a head domains (Vh) and a tail domain (Vt) (Ziegler et al. 2006). It binds to important focal adhesion molecules such as α-actinin and talin at its head domain (D1) while actin binding occurs at the tail domain (Vt) as shown Figure 1-6. Vinculin activation is a critical process that has been studied through experimental (Izard et al. 2004; Bakolitsa et al. 2004; Bois et al. 2006; Huang et al. 2011; Chen et al. 2006) and computational (Golji & Mofrad 2010; Golji et al. 2011) investigations. These studies suggested that the vinculin activation mechanism involves both talin and actin and probably enhances vinculin binding to both of these binding partners (Golji et al. 2011). It has been suggested that vinculin reinforces the linkage between α-actinin and the actin

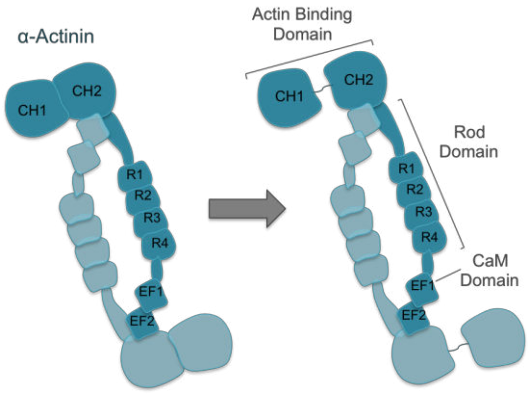

Figure 1-5. The structure of α-actinin. This protein is an anti-parallel homodimer and its structure is composed of an actin binding domain, rod domain and CaM domain. The actin binding domain exits in either open or closed conformation. In the closed conformation CH domains are in contact, while in the open conformation CH domains are separated.

cytoskeleton(Kelly et al. 2006). Also, it has been proposed that α-actinin association with vinculin head induces vinculin activation (Bois et al. 2006) but the mechanism is still illusive.

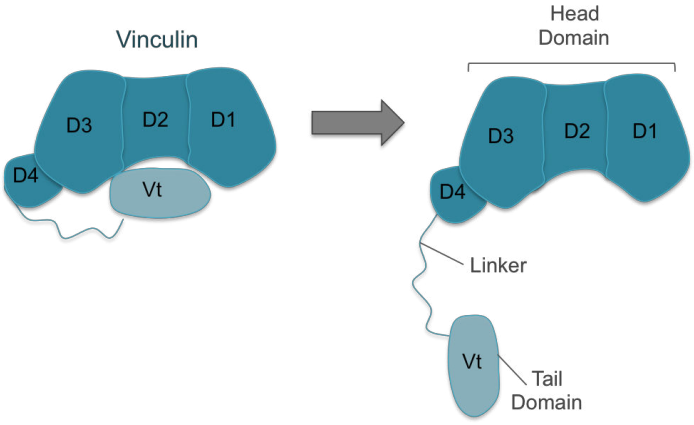

Figure 1-6. The structure of vinculin. The vinculin molecule has a head domain consisting of D1 to D4 lobes, which is connected to the tail domain through a prolin-rich linker region. In the inactive conformation, head and tail

domains are in contact and the actin binding site on the vinculin tail is inhibited. Upon force application, the tail domain comes off and becomes exposed.

Filamin: Famous for networking

The cytosolic protein filamin plays a key role in regulating cellular structure, adhesion and motility by crosslinking actin filaments into the three-dimensional orthogonal networks of the cytoskeleton. In addition, filamin plays a crucial regulatory role in cell shape and motility by interacting with over 90 diverse proteins including channels, transmembrane receptors, and transcription factors(Sampson et al. 2003; Feng & Walsh 2004; Popowicz et al. 2006). One such binding partner is the transmembrane αβ heterodimer integrin, which is a versatile signal transducer. Integrins transmit mechanical forces bi-directionally while linking extracellular matrix proteins to the focal adhesion machinery.

Filamin influences cellular adhesion via a variety of pathways. While filamin is indirectly required for vimentin-mediated integrin recycling to the cell membrane, thereby increasing integrin expression on the cell surface and promoting cell adhesion and spreading(Kim, Nakamura, Lee, Hong, et al. 2010; Kim, Nakamura, Lee, Shifrin, et al. 2010), the direct interaction of filamin with integrin is mediated through multiple integrin binding sites on various domains of filamin, facilitating integrin clustering(Ithychanda et al. 2009). These versatile functions of filamin can also be important determinants of "inside-out" integrin-mediated signaling that plays a critical role in both cell adhesion and motility.

Filamin is a V-shaped homodimer with 24 Ig-like repeated domains, two hinge regions, one dimerization domain, and one actin binding domain on each monomer (Figure 1-7). The actin binding domain (ABD), composed of two calponin homology domains, is situated at the N-terminal, followed by 15 repeated Ig-like domains in a linear structure, a hinge domain, and Ig-like repeats (16 to 23), which are arranged compactly in a paired structure. Repeat 23 is succeeded by a second hinge region and the last Ig-like domain, IgFLN24, which functions as the dimerization domain at the C-terminal of each monomer(Pudas et al. 2005; Kesner et al. 2010). The filamin family contains three human isoforms, the most abundant of which is filamin A (FLNa), ubiquitously found in all cell types. In all filamin isoforms, immunoglobulin-like repeat 21 (IgFLNa21) binds most strongly to integrin and is typically considered the main integrin binding site(Kiema et al. 2006). However, sequence homology comparisons and NMR studies suggest that IgFLNa21 is part of a subgroup of filamin repeats that all bind integrin and similar ligands (e.g. GP1bα and migfilin)(Ithychanda et al. 2009). This subgroup of filamin repeats include IgFLN domains 4, 9, 12, 17, 19, 21, and 23(Ithychanda et al. 2009). In IgFLNa21, the ligand binding site is the CD face composed of two β strands, which is auto-inhibited by the first β strand of IgFLNa20(Kiema et al. 2006; Lad et al. 2007) (please see Chapter 3 Section 1 for details).

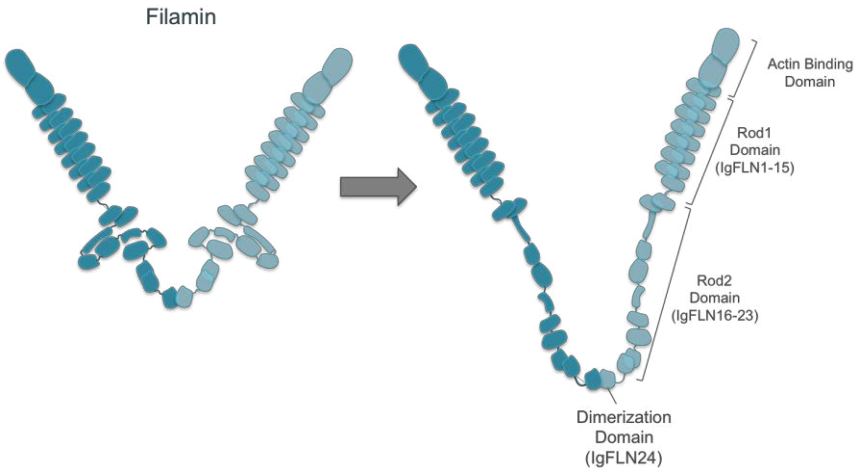

Figure 1-7. The structure of α-actinin of filamin. The filamin molecule is a V-shaped molecule consisting of two same monomers. Each filamin monomer is One of the main integrin binding sites (orange) is inhibited in IgFLthe rod2 domain, which becomes exposed via mechanical tension.

PIP2: Good things come in small packages

Phospholipid phosphatidylinositol 4,5-bisphosphate (PIP2) is important in transmitting signals from the plasma membrane to the actin cytoskeleton as well as activation of enzymes, membrane trafficking. Many focal adhesion proteins such as talin, vinculin and α-actinin are known to bind PIP2, which may regulate their role in integrin-mediated signal transduction. The non-uniform distribution of PIP2 molecules in the lipid membrane implies that proteins may be recruited to those regions more effectively. It has been shown that PIP2 orchestrates the flow of focal adhesion proteins inside the cytoplasm, i.e. regulates their passive diffusion of focal adhesion proteins. Furthermore, the primary role of PIP2 is to anchor proteins to the lipid membrane but it has recently been established that it also often serves as a second messenger itself(Sjöblom et al. 2008).

The ECM

The ECM experiences various states of stress and strain that can result in significant changes in cell morphology. Cells adapt to their microenvironment by producing or removing ECM constituents in order to reach a new equilibrium state. If stresses are either too high or too low in the ECM and the cell cannot promote an equilibrium via remodeling the ECM, it will undergo apoptosis. Degradation and generation of the ECM molecules may occur via both positive or negative feedback mechanisms that ultimately lead to either cell fate or successful cell adhesion, respectively (Humphrey et al. 2014).

Experimental tools for detecting cellular and molecular responses to mechanical stress

Cell-Level approaches

Different cells in the body are subject to different types of mechanical stress such as shear, tension and periodic forces(Bukoreshtliev et al. 2013; Buschmann et al. 2010), which determines the ultimate cell morphology. Various methods have been developed for exploring and quantifying cellular response to different stress regimes. For instance, endothelial cells (EC)

experience high shear stress in arteries, which is reduced in veins. EC response to uniaxial stress can be studied via culturing them on stretchable PDMS substrates and finite element methods are used to model the stress distribution. In the continuum approaches, an average Young's modulus should be assigned to cells, which represents the constitutive relationship between applied stress and cell deformation (strain). However, cells are highly heterogeneous and thus by treating them as continuum materials, much information is lost about their dynamics. Furthermore, shear stress can be applied to adherent cells using microfluidic approaches. The amount of shear stress applied on the cells is dependent upon the position of cells relative to the center of the microfluidic device as well as the viscosity of the fluid. By tagging proteins in cell-level approaches, their stress-dependent distribution can be monitored over time.

Pillar arrays can be made to varying dimensions, thereby allowing the determination of substrate rigidity and force measurements. Pillar displacement is measured in live cells and is used to determine cellular forces applied to the substrate. Traction force microscopy uses embedded fluorescent beads (often of two colors) and finite element analysis to measure substrate deformations by the cell.

Focal adhesion proteins are constantly subject to mechanical forces that may be both spatially and temporally variable. Therefore, conformational changes of proteins may be highly dependent upon the local mechanical environment. Thereby, cell-level techniques can provide valuable information about force-dependent recruitment of focal adhesion proteins. However, molecular-based approaches are required to study detailed mechanisms of mechanosensitivity in focal adhesion proteins.

Atomic Force Microscopy

The atomic force microscopy (AFM) is used across both cellular and molecular scales in order to characterize either cellular properties such as Young's modulus or force-induced conformational changes of proteins. However, the AFM cantilever properties such as stiffness, moment of intertia and material properties will be adjusted for each use(Bukoreshtliev et al. 2013). The experimental procedure for proteins involves attaching them to a substrate and pull on them from the other end using the tip of atomic microscope. As forces are applied unfolding kinetics can be monitored individual domains of proteins they increase until forces are transmitted to the next domain

Fluoresence recovery after photobleaching (FRAP)

There are several experimental methods for studying important molecular events each having their owns advantages and drawbacks. Fluorescence recovery after photobleacing (FRAP) is used to study diffusion and binding kinetics between proteins and protein trafficking(Day et al. 2012). In this method a GFP tag is fused into the structure of protein of interest. The fluorescence is bleached and the diffusion of proteins is tracked into the dark area. The dynamics of fluorescence recovery reveals mobility of the tagged protein and can be used to estimate the association and dissociation constants to its potential binding partners.

A newly developed method for investigating force-dependent recruitment of proteins is called micropatterned coverslips. Ciobanasu et al. functionalized the patterns with talin molecule and acromyosin network was formed on top of the coverslip(Ciobanasu et al. 2014). The actomyosin forces stretched the rod domain of talin that activated it for vinculin binding. Vinculin molecules were tagged with fluorescence tags diffusing in the solution. Vinculins were

recruited to talin in the equilibrium state and stay attached. Part of the sample was bleached using FRAP and the recovery time was measured in order to find vinculin's dissociation rate.

Fluoresence resonance energy transfer (FRET)

Fluoresence resonance energy transfer (FRET) is a method classically used for studying protein-protein binding. Recent advances in this technique resulted in development of an implementable FRET-based sensor into the protein structure that can track and quantify tension and conformational changes across a single structure. As the tension sensor is integrated into the protein, several control constructs are designed to evaluate functionality of both protein and fluorephores in the final construct. The tension sensors are calibrated using single-molecule force spectroscopy in order to find a force-emission reference graph. Protein expression levels and localizations are checked by western blotting and fluorescence microscopy, respectively. The tension sensors work based upon energy transfer between two fluorophores. A donor in an excited state approximate to an acceptor can transfer energy through dipole-dipole coupling. The energy transfer is inversely proportional to the sixth power of the distance. Changes in the FRET efficiencies indicate sensitivity to distance between two fluorophores. The measured tension within the vinculin and integrin molecule measure were found to be 2.5pN and 1-40pN, respectively.

Optical traps

Micrometer diameter beads made from dielectric materialss are centered using laser beams and as the bead is moved from the center, the diffraction pattern of the laser will cause pulling forces to put the bead back to the equilibrium position. This methodology is used to measure intramolecular forces or estimate association and dissociation constants (Iskratsch et al. 2014).

Computational methodologies for detecting molecular mechanosensitivity

Experimental methods have limitation in providing sufficient resolution for studying molecular events and thus it is difficult to understand mechanisms. Computational simulations have been developed to fill this gap by modeling molecular interaction as precisely as possible.

Molecular Modeling

In molecular dynamics (MD) simulations, the structural data of proteins is taken as the input and the time evolution of proteins is modeled via integrating Newtonian equations of motions (see Chapter 2 for more details). MD simulations can be used to model protein-protein interactions, conformational switching and even protein folding. Results are then validated against experimental data either directly or indirectly depending on the nature and size of the system under study. It is also possible to model the effect of biochemical changes such as mutations and phosphorylation in proteins on their function. Moreover, mechanical forces can be applied to protein in MD simulations and thus it is possible to study their mechanosensitivity. Various free energy calculation methods have been developed for finding binding affinities. However, it should be noted that molecular modeling has various limitations:

1) The system size can easily go up to millions of atoms after including water molecules and thus the computational cost of simulating such large systems can be extremely high. In some cases it is possible to use coarse-grained molecular dynamics in order to reduce the computational cost given that the required force field parameters are available.

2) If the resolution of the initial structural data is low, simulation results will not be reliable. The reason is that the initial position and velocity of each atom affects its final state unless the system is equilibrated for an infinite type such that an equilibrium state is reached.

3) The physiological conditions may involve the presence of many proteins and other molecules that may influence the dynamics of the system under study. However, due to both size and parameter limitations it is not possible to include all important factors. Therefore, one needs to carefully choose and model the system of interest in order to avoid factors that can significantly reduce the accuracy of the output trajectories. Furthermore, simulations need to be repeated a few times in order to obtain statistically significant results.

Normal mode analysis

Proteins are biological polymers and can be treated as complex mechanical objects especially when they are folded into a 3D structure. Normal mode analysis (NMA) is a technique in which natural modes of proteins can be calculated using a simple bead and spring approach. Aside from rigid body motions, namely translational and rotational modes, the lowest frequency modes are usually the most likely to occur. Normal mode analysis is usually employed to gain insight into the mechanical coupling of different domains of proteins and mechanisms by which internal mechanical forces are propagated and induce conformational changes on other parts. NMA analysis along with molecular dynamics simulations can give valuable insights into mechananosensitive properties of proteins.

Conclusions

Mechanosensing is mediated by force-induced changes either in protein conformations or in the kinetics of assembly and disassembly of protein complexes. A conformational change in a protein is a biased thermodynamic procedure consisting of many small steps that are driven by thermal motions of the system. These tiny thermal giggles are directed toward to a more global change as a certain stimuli, such as the presence of another binding partner or mechanical forces, perturb the local environment. External stimuli may also change the free energy profile of the system and thus affect the probability of reaching a previously inaccessible state or even define a new structural state.

A central question in focal adhesion assembly is the mechanism of force-induced recruitment of proteins to the adhesion sites. Cellular processes are dominantly diffusion-driven implying that molecules freely wonder inside the cell until they are captured by other binding partners. One hypothesis is that forces locally activate molecules, which promotes further binding with other molecules. For instance, the rod domain of talin has several vinculin binding sites that are inhibited under low-tension condition. As the acto-myosin forces are applied on the talin molecule, the rod domain is extended and vinculin binding sites are exposed for association. Another possibility is that proteins form complexes prior to engaging/entering the rest of focal adhesion body and diffuse as a complex. In other words, no external force may be required for moderating complex formation but as the complex itself can act as a mechanosensitive entity. For instance, paxilin and FAK co-localize near the plasma membrane and most likely diffuse as a complex. Also, curve fitting on FRAP results for FA proteins showed that the dynamics of molecular travelling as complexes to adhesion sites are different from individual proteins(Case & Waterman 2015).

According to the clutch hypothesis, focal adhesions (FAs) mediate transient indirect interactions between the retrograde-moving actin cytoskeleton and ECM-bound integrins (Figure

1-1). However, it is not yet clear how forces transmitted across FAs impact and allow individual FA proteins to act as mechanosensors. The main focus of this work is to understand the mechanisms by which the binding between two proteins regulates force transmission across focal adhesions.

Furthermore, proteins' response to tension can decide their localization and function at focal adhesions. For instance, the interaction between two proteins is reinforced upon force application (catch bond), while other interaction can easily become weakened (slip-bond). Interestingly, the overall structure of a focal adhesion acts as catch bond. Furthermore, binding can preserve a certain conformation of a protein. Interestingly, the overall mechanical properties of focal adhesion are dependent on the rigidity sensing allowing for controlling force transmission to the substrate. FA maturation requires tension to be applied across FAs, either from intracellular myosin contractility or extracellular pulling. Mature FAs remain attached to actin stress fibers throughout their lifetime, and their maintenance requires association with contractile F-actin bundles**.** During maturation, FAs undergo a compositional change as they grow and elongate in the direction of retrograde flow.

Therefore, it would be useful to gain a profound understanding of domain-based mechanosensitivity in order to find correlations between the type of forces experienced by proteins and their constituent domains. This would allow for characterizing newly discovered mechanosensitive proteins developing modular approaches for exploring mechanical responsiveness of proteins. Moreover, it may give new insights into engineering novel proteins that can be used for both designing molecular gauges for measuring intramolecular forces and rescuing phenotypes resulted from defective mechanical response. Furthermore, a comprehensive understanding of domain-dependent mechanosensitivity may account for potential redundancies in function.

The forces generated in the actin cytoskeleton are transmitted across transmembrane receptors to other cells through a series of mechanosensitive subcellular structures so called cell-cell adhesions. These cell-cell contacts act analogous to focal adhesions in terms of transmitting forces to the extracellular environment in diverse cellular processes(Case & Waterman 2015). Specifically, similar structural patterns have been observed in cell-cell adhesive junctions. α-Catenin directly binds to cadherins in cell-cell adhesion, which is analogous to the binding between talin and integrin in cell-substrate adhesion(Yao, Qiu, et al. 2014). Furthermore, vinculin is recruited to talin rod in a force-dependent manner, a similar patterns have been observed in vinculin binding α-Catenin. Specifically, the helical bundle region of α-Catenin exists in a conformation that inhibits vinculin head binding. . As the cytoskeletal forces necessary for unwrapping these domains are applied to the α-catenin molecule, the likelihood of vinculin binding increases (Figure 1-8). It was shown that forces larger than 430PN can result in full unfolding of these regions and thus also prevented vinculin binding(Yao, Qiu, et al. 2014).

There are also similarities between proteins in FAs and those in linkages between cytoskeleton and nucleoskeleton (LINC complexes). The four spectrin repeats of the α-actinin monomer undergo stretching forces transmitted from its actin binding domain at the N-terminal domain of this molecule. The nesprin-2G molecule contains 56 spectrin repeats linking the peri-nuclear space to actin bundles extended over the nucleus (TAN lines) and is responsible for transmitting forces to the nucleus as shown in Figure 1-9. Although nesprins are much longer than α-actinin, they most likely share common features in terms of mechanical response.

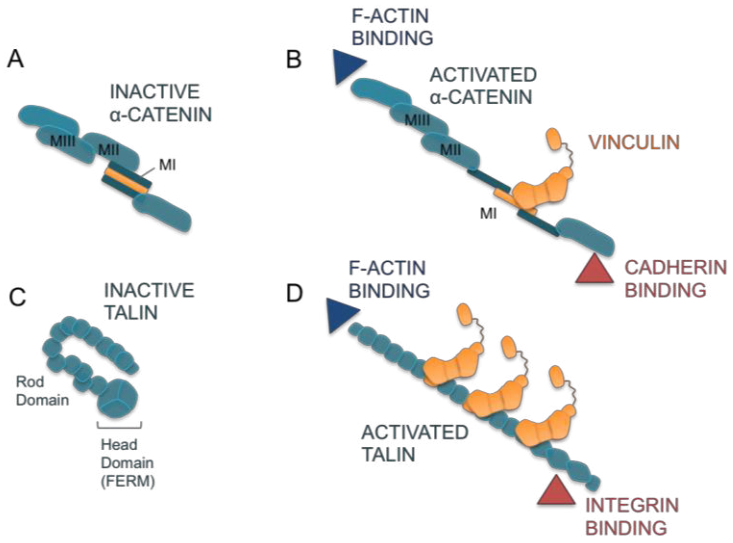

Figure 1-8. Similar mechanical response of α-catenin in cell-cell adhesion and talin in focal adhesions. Both α-catenin and talin bind to the actin cytoskeleton on one side and to membrane receptors on the other side. A) The vinculin binding site of α-catenin is inhibited in domain MI. B) As forces are applied to the molecules, it stretches and the binding site becomes exposed. C) Talin has several vinculin binding sites along its rod domain, which are inhibited in the absence of mechanical forces. D) Tension increases talin's affinity for vinculin binding.

A need for an integrated approach

Describing the mechanical behavior of proteins is complicated as it depends on many factors including to binding other partners, dynamic nature, various transitional states and force-dependency of equilibrium states(Lv et al. 2014). For instance, it is not yet clear how some protein-protein interactions such as $\alpha_5\beta_1$ acts as catch bond and becomes much stronger under force, while others such as talin show slip-bond behavior(Kong et al. 2009; Jiang et al. 2003). Furthermore, the wide range of tension at Fas along with composition dependency of FA mechanosensitivity suggest diverse mechanisms by which individual molecules respond to tension. Moreover, force response of an individual protein may not generally be unique and may vary upon the mechanical environment, e.g. one or more 'mechanically activated' structures may exist, thereby, proteins would be able to adapt to their environment. Furthermore, it is still unclear how forces are propagated within a single protein structure. For instance, binding on one side can result in allosteric changes in distal parts of the structure. Therefore, highly structure-based approaches are needed to understand and characterize mechanosensitivity of proteins.

The design and engineering of nanoscale devices for biomedical applications require a more thorough understanding of principles governing physical phenomena at this scale. Due to their extraordinary mechanical, chemical, optical and thermal properties, carbon nanotube (CNT)-based devices have attracted major attention in a variety of applications ranging from scaffolds for neural tissue growth to gene delivery(Yang et al. 2007; Bianco, Kostarelos, et al. 2005; Singh et al. 2005; Harrison & Atala 2007; Pantarotto, Singh, et al. 2004). More recently, studies have shown that CNT insertion in various cell types is possible, making them a promising tool for intracellular transport.(Kostarelos et al. 2007; Pantarotto, Briand, et al. 2004; Shi Kam et al. 2004; Kam et al. 2006; Heller et al. 2005) Due to their biocompatibility(Smart et al. 2006) and unique ability to translocate through the plasma membrane without harming cell viability,(Kostarelos et al. 2007) CNTs have been used for the intracellular delivery of various

biological cargos such as proteins, peptides DNA, and nucleic acids(Lacerda et al. 2007a; Kam et al. 2006; Kam & Dai 2005; Shi Kam et al. 2004; Heller et al. 2005; Cherukuri et al. 2004; Lu et al. 2004; Bianco, Hoebeke, et al. 2005; Pantarotto, Briand, et al. 2004; Lacerda et al. 2007b). In this work, we examined the interaction between single-wall carbon nanotubes and the actin cytoskeleton.

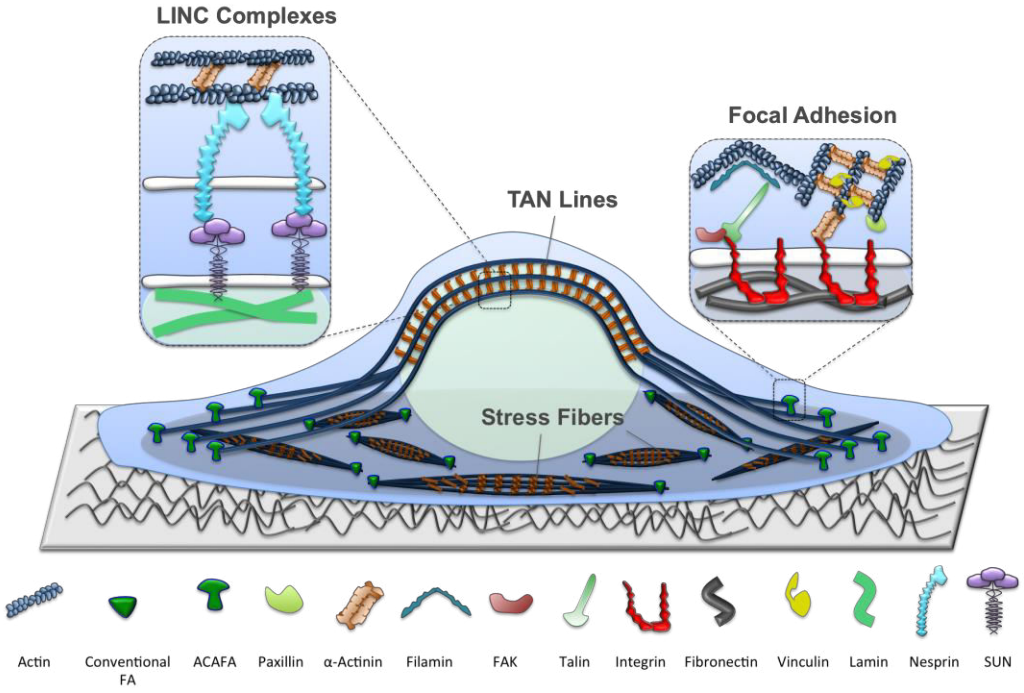

Figure 1-9. Force transmission to and from the actin cytoskeleton. Cytoskeletal structures transmit forces to both the extracellular matrix and inside the nucleus via their connection to focal adhesions and LINC complexes, respectively. LINC complexes are physical linkages between the cytoskeleton and nucleoskeleton and consist of SUN and nesprin proteins. Stress fibers resided on the basal cell level are linked only to focal adhesions, while actin bundles on top of the nucleus, also known as TAN lines, are connected to focal adhesions on one side and to LINC complexes on the other side.

The design and engineering of nanoscale devices for biomedical applications require a more thorough understanding of principles governing physical phenomena at this scale. Due to their extraordinary mechanical, chemical, optical and thermal properties, carbon nanotube (CNT)-based devices have attracted major attention in a variety of applications ranging from scaffolds for neural tissue growth to gene delivery(Yang et al. 2007; Bianco, Kostarelos, et al. 2005; Singh et al. 2005; Harrison & Atala 2007; Pantarotto, Singh, et al. 2004). More recently, studies have shown that CNT insertion in various cell types is possible, making them a promising tool for intracellular transport.(Kostarelos et al. 2007; Pantarotto, Briand, et al. 2004; Shi Kam et al. 2004; Kam et al. 2006; Heller et al. 2005) Due to their biocompatibility(Smart et al. 2006) and unique ability to translocate through the plasma membrane without harming cell viability,(Kostarelos et al. 2007) CNTs have been used for the intracellular delivery of various biological cargos such as proteins, peptides DNA, and nucleic acids(Lacerda et al. 2007a; Kam et al. 2006; Kam & Dai 2005; Shi Kam et al. 2004; Heller et al. 2005; Cherukuri et al. 2004; Lu et al. 2004; Bianco, Hoebeke, et al. 2005; Pantarotto, Briand, et al. 2004; Lacerda et al. 2007b).

In this work, we examined the interaction between single-wall carbon nanotubes and the actin cytoskeleton.

Ongoing model organism studies combined with mathematical modeling and novel cellular biophysical and imaging approaches promise further answers. Structural biology and molecular dynamics simulations studies will be needed to characterize intermediate activation conformations to verify the proposed role of strain in the activation process. Tension sensors provide information about the level of forces. The ultimate purpose is to define activation mechanisms of mechanosensors. Spatial organization in focal adhesion is important to understand direction and amount of forces acting on the molecules and also binding partners(Case et al. 2015).

Finding the relation between structure and function of proteins has long been a critical question in molecular biology. Focal adhesions are known to be mechanosensitive molecular complexes consisting of various proteins that together orchestrate force transmission from the extracellular matrix to the actin cytoskeleton. The structural and functional features of these proteins are unique since they individually have to sense and respond to mechanical forces by changing their conformation. The central objective of this dissertation is to understand structural basis of mechanosensitivity in key focal adhesion proteins. Specifically the diagram shown in Figure 1-10 illustrates

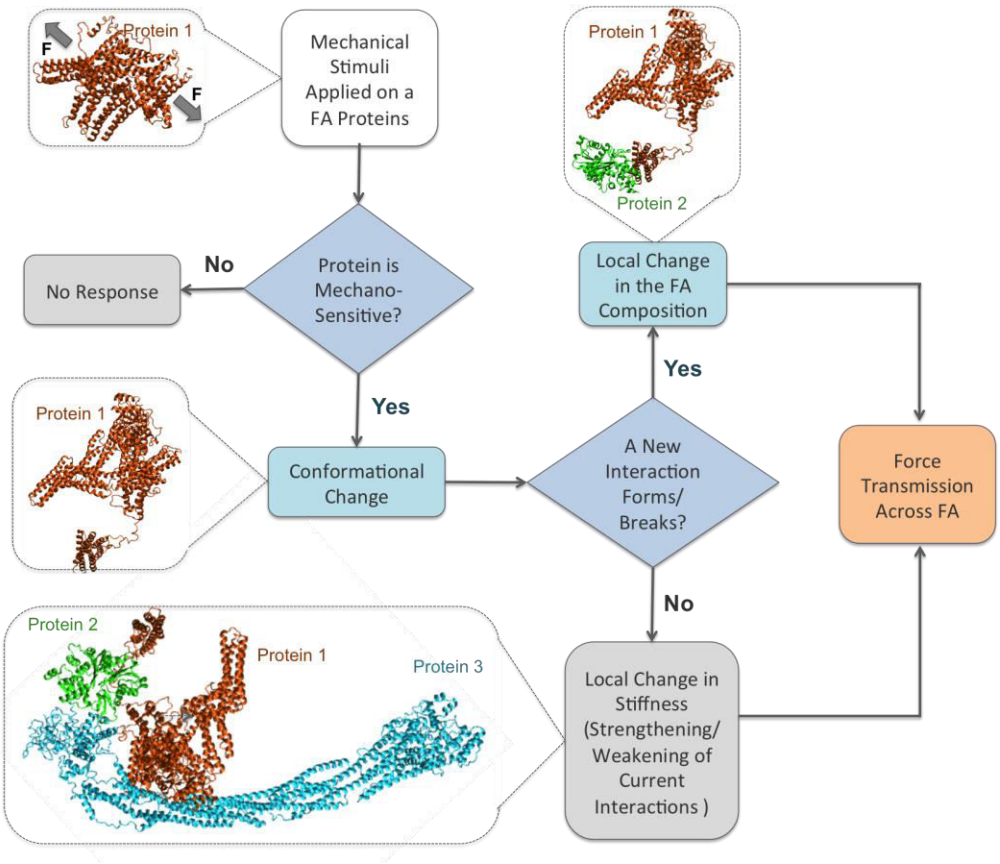

Figure 1-10. The mechanism of force transmission across focal adhesions. Boxes with dashed borders are visual examples of the step to which they are connected. As mechanical forces are applied to mechanosensitive proteins, they respond by changing their conformation and as a result either a new interaction forms/breaks or the strength of current interactions may be modified. If a new interaction is formed or disrupted, the local composition of focal

adhesions will change. If the local composition remains intact, mechanical forces will modify interfaces of the protein complex resulting in changes in the local stiffness of FAs.

Chapter 2 is dedicated to the methodology used in the present dissertation. Specifically, this Chapter covers fundamental principles behind molecular modeling as well as pre- and post-processing techniques used in this study. The following Chapters are dedicated to the mechanisms of force transmission within different focal adhesion layers (Figure 1-2). Specifically, Chapter 3 covers the integrin signaling layer and important regulatory interactions of cytoplasmic proteins with the integrin tail. Chapter 4 focuses on the force transduction layer and highly mechanosensitive proteins such as vinculin. And finally Chapter 5 is devoted to the actin regulatory layer in which the role of an important actin binding protein, α-actinin, in the formation of actin bundles was studied. This Chapter also covers the effect of carbon nanotubes on the shape of cytoskeletal structures.

CHAPTER 2: Methodology

Principles of Molecular Dynamics

The time evolution of N interacting particles can be modeled using molecular dynamics simulations. The equation of motion of the i-th particle is then:

$$m_i \frac{\partial^2 r_i}{\partial t^2} = F_i$$

Where r_i and F_i are coordinates and the net force acting on this particle. The force is the negative of the derivative of the potential function defining the interactions among particles and usually consists of both bonded and non-bonded interactions, which are discussed later in this Chapter.

$$F_i = -\frac{\partial V}{\partial r_i}$$

These equations are integrated and both coordinate and velocity of each particle are updated in each time step, which can be recorded throughout the simulation. The frequency of writing to output files will determine the time resolution of trajectories but since biological systems consists of thousands to millions of atoms, writing too frequently will result in unreasonably big data files, while low-frequency writing will cause a low resolution output. Thereby, there is an optimum frequency of writing, which directly depends on the system under study.

It should be noted that molecular dynamics is a general N-body simulation method that has been used for various systems. However, this work is focused on simulating proteins and thus descriptions are geared towards this purpose and may not be generalizable to other types of systems.

Preprocessing the system

Protein systems should be prepared prior to performing molecular dynamics. The first step is to obtain or construct the initial structure of proteins. Many protein structures have already been resolved using experimental techniques such as x-ray crystallography and NMR, and have been archived in the Protein Data Bank (PDB). However, the resolved structure are not necessarily in their native state and thus may not be ready for simulations due to the following reasons: 1) the resolution of some the structural determination methods are low and thus the position of some atoms are not accurately determined. 2) Experimental procedures and conditions such as ion concentration may affect the native position of atoms. 3) In some cases, proteins are resolved as complexes and in order to model their binding with each other or with other partners, the unbound structures need to be acquired. 4) Some parts of the structure might be missing and thus had to be separately modeled and so on.

Minimization and Equilibration

In order to fix or reduce the impact of the abovementioned structural flaws mainly 1 to 3, molecules need to be minimized and equilibrated first. There are several algorithms for minimizing the initial structure of proteins, which all aim to remove bad contacts between atoms and guide the system to reach its closest local free energy minimum [ref]. However, minimization is usually not sufficient for reaching a stable equilibrium and thus primary molecular dynamics simulations are suggested to shake the system to its nearest equilibrium state. The condition of the equilibration simulations may vary upon the source of instability. For instance, maintaining constant volume (NVT) may result in faster equilibration in some cases,

while main simulations may run with constant pressure (NPT). It has been observed that heating and annealing simulations are efficient ways for reaching the equilibrium state.

Protein Structure Prediction

Point 4 needs to be handled differently. Disordered regions of proteins are hard to crystalize and are usually missing from the reported structure. However, those regions may play key roles in the protein function and thus cannot be neglected in some cases. One example is the active sites of enzymes that usually lack a secondary structure and stick out of the molecule in the form of loops or turn. Moreover, even secondary structures within an important domain of the protein may be absent in the released structure. Thereby, prediction methods are highly useful in addressing such shortcomings and are widely used to gain a better insight about the relation between the structure and function of proteins. These methods rely on the similarity between the sequences of the protein of interest and available structures in the PDB bank. The rule of thumb is that if sequence similarity is higher than 50%, the reliability of the predicted structure is in an acceptable range(Baker & Sali 2001). Two of the most commonly used tools available for performing protein structure prediction are PHYRE2 and SWISSMODEL(Kelley et al. 2015; Guex & Peitsch 1997; Biasini et al. 2014).

Docking

Protein-protein binding is widely studied by molecular dynamics simulations but it encompasses its own challenges. For instance, the crystal structure of the complex of interest may not be available and/or binding sites may not have been determined by experimental methods. The interface between the two proteins should be predicted in order to model their binding. Docking algorithms have been developed to match protein surfaces and rank their probability. They can incorporate both geometrical compatibility and interaction energy of the two proteins. Docking solutions may be validated via experimental studies and/or modeling. If the docked complex is equilibrated for long and remain stable, it will most likely be reliable. Two of the servers used in my work are PatchDock/FireDock and Hex(Schneidman-Duhovny et al. 2005; Ritchie 2008).

Solvation and Ionization

Proteins are in aqueous solution in physiological conditions and thus any effort in modeling their behavior should incorporate the role of water molecules. The most accurate manner of adding the water effect is including explicit water molecules in the system as they can form hydrogen bonds with each other and protein and thus can account for hydrophobic interactions as well. However, random addition of water molecules could result in undesired artifacts such as putting them in hydrophobic regions of proteins or lipid membranes and thus care must be taken as the system is solvated by automated algorithms.

Residues contain partial charges and a protein molecule may not be neutral as a whole. This can cause problems and make the system unstable during MD simulation due to the periodic boundary conditions that is usually applied. Therefore, counter ions are added to the system in order to neutralize the excessive charges. Also, depending on the physiological condition of the protein environment, a certain ion concentration should be applied.

Force Field

Force fields are made of two separate parts:

1. A series of equations known as the potential function used for calculating the potential energy and its derivative, which gives the force
2. A set of parameters that should be implemented in the potential function

It should be noted that these equations and parameters should be consistent.
The potential function is divided into two parts: bonded and nonbonded terms and constraints.
NonBonded interactions: Are calculated between pairs of atoms i and j as follows:

$$V(r_1, \dots, r_N) = \sum_{i<j} V_{ij}(r_{ij})$$

$$F_i = -\sum_j \frac{dV_{ij}(r_{ij})}{dr_{ij}} \frac{r_{ij}}{r_{ij}} = -F_j$$

These are calculated based on the list of neighboring atoms. This list is based on the closest atoms that do not have any bonded interactions that are within a certain radius. This list is updated every and in a very few timesteps.
Lennard-Jonemos:

$$V_{LJ}(r_{ij}) = \frac{C_{ij}^{(12)}}{r_{ij}^{12}} - \frac{C_{ij}^{(6)}}{r_{ij}^{6}}$$

$$F_i(r_{ij}) = \left(\frac{12C_{ij}^{(12)}}{r_{ij}^{13}} - \frac{6C_{ij}^{(6)}}{r_{ij}^{7}}\right)\frac{r_{ij}}{r_{ij}}$$

Parameters $C_{ij}^{(12)}$ or $C_{ij}^{(6)}$ depend on the type of atoms.
Coloumb interactions:
The Ewald sum is over N particles with their periodic images:

$$V = \frac{f}{2}\sum_{n_x}\sum_{n_y}\sum_{n_z*}\sum_{i}^{N}\sum_{j}^{N}\frac{q_i q_j}{r_{ij,n}}$$

$n = (n_x, n_y, n_z)$ are box indices. The $(n_x, n_y, n_z) = 0$ when i=j.
$r_{ij,n}$ is the real distance between charges. This sum slows converges and be broken into two terms with faster convergence and a constant.

$$V = V_{dir} + V_{rec} + V_0 \qquad (17.2)$$

$$V_{dir} = \frac{f}{2}\sum_{i,j}^{N}\sum_{n_x}\sum_{n_y}\sum_{n_z*}\frac{q_i q_j \operatorname{erfc}(\beta r_{ij,n})}{r_{ij,n}} \qquad (18.2)$$

The erfc is the error function.

$$V_{rec} = \frac{f}{2\pi}\sum_{i,j}^{N} q_i q_j \sum_{m_x}\sum_{m_y}\sum_{m_z^*}\frac{\exp[-(-\pi m/\beta)^2 + 2\pi i m \,.\, (r_i - r_j)]}{m^2}$$

$$V_0 = \frac{-f\beta}{\sqrt{\pi}}\sum_{i}^{N} {q_i}^2$$

Where m is the wave vector and β is a parameter that determines the relative weights of the reciprocal and direct. The cutoff distance is chosen as

The computational cost of the reciprocal space grows with N^2 or N^(3/2) and it is not possible to use them for large systems. Particle mesh Ewald was developed to increase the efficiency of summation in the reciprocal space and instread of summing over the wave vectors, charges are placed on a mesh. Fast Fourier Transform is taken on this 3D space and energy in the reciprocal spaced is calculated as a sum over the mesh in the frequency space. The sum with the particle mesh Ewald scales with Nlog(N) and works better for large systems

Bonded interactions: This includes bonds, angles and dihedrals. The list of bonded interactions are not updates.

Bonds: This terms is normally a harmonic potential between two atoms with a stiff spring constant, which models a covalent bond.

$$V_b(r_{ij}) = \frac{1}{4} K_{ij}^b (r_{ij} - b_{ij})^2$$

And forces are obtained as (Figure 2-1),

$$F_i(r_{ij}) = K_{ij}^b (r_{ij}^2 - b_{ij}^2) r_{ij}$$

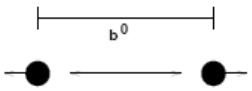

Figure 2-1. A bond is made between two atoms.

Angle potential (Figure 2-2),

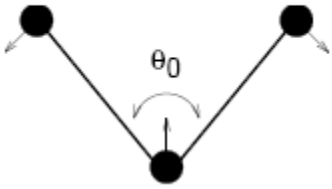

Figure 2-2. An angle is made by three atoms.

$$V_a(\theta_{ijk}) = K_{ij}^b (\theta_{ijk} - \theta_{ijk}^0)^2$$

Dihedral: Angle φ is defined between planes made by atoms (i,j,k) and (j,k,l). Angle zero occurs when i and l are on the same side.

Since this potential is not periodic, it is better if ξ_0 is far from *.180*

$$V_{id}(\xi_{ijkl}) = K_\xi (\xi_{ijkl} - \xi_0)^2$$

These dihedrals are used to keep groups such as aromatic rings in place or preventing the molecule from falling on its mirror image (Figure 2-3). Improper dihedrals are shown in Figure 2-4.

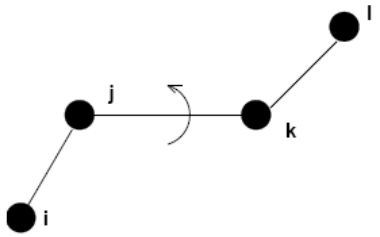

Figure 2-3. A dihedral angle is made by four atoms.

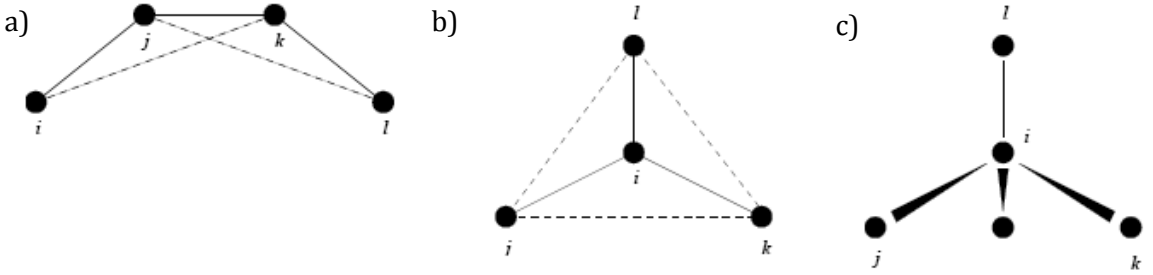

Figure 2-4. The improper dihedral angles. The improper dihedral angle is made as shown in the figure between (i,j,k) and (j,k,l) that results in a) out-of-plane bending or b) exchanging two rings c) or going out of the structure

$$V_d(\varphi_{ijkl}) = K_\varphi(1 + \cos(n\varphi - \varphi_s))$$

Urey-Bradley term:

$$V_a(\theta_{ijk}) = K_u(u - u_o)^2$$

This term controls the bending angle of 1,3 nonbonded interactions. u is the distance betweem 1,3 atoms that is harmonically contrained

Constraints: These potentials are used to control the system movement and are used to limit large changes but these terms are not part of the force field. The position of one or a group of atoms can be fixed or harmonically restrained in space:

$$V_{pr}(r_i) = \frac{1}{2}K_{pr}|r_i - R_i|^2$$

R_i is the equilibrium position. This is very useful during equilibration. Atoms could be contrained to move in a plane or a line. Constraints are applied to a constant list of atoms.

.

Umbrella Sampling

The phase space of proteins is complex due to the high number of degree of freedom. Proteins cover their phase space in a sufficient amount of time some regions are hardly accessible due to high potential barriers and thus are rarely sampled unless either the time goes to infinity or some external factor forces them to reach those regions. Lack of sampling is a serious issue in molecular dynamics simulations as the time is much less than the ergodic limit. The free

energy profile is obtained along one degree of freedom, also called the reaction coordinate, via the probability distribution function $P(x)$ as follows:

$$A(x) \approx KT\ln[P(x)]$$

Where K and T are Boltzman constant and temperature, respectively. Various free energy calculation methods have been developed out of which umbrella sampling is one of the most commonly used. In this method an external harmonic potential $V_i(x)$ is applied along the reaction coordinate in order to restrain it to a certain equilibrium value and the rest of the system is freely sampled. The equilibrium value is shifted along the reaction coordinate until the whole reaction coordinate is covered from states A to B. The energy function of the i-th position of the bias potential (i-th window):

$$E_i = E_0 + V_i(x)$$

$$V_i(x) = \frac{1}{2}K\left(x - x_{0,i}\right)^2$$

Resulting in a set of histograms. The probability distribution function with the application of the biased potential is $p_{b,i}(x)$ which is related to unbiased potential with

$$P_{b.i}(x) = A_i P(x) e^{-V_i(x)/K_B T}$$

Where A_i is the normalization constant and can also be represented as $e^{-K_i/K_B T}$
Therefore, K_i can be found as

$$e^{-K_i/K_B T} = \int P(x) e^{-V_i(x)/K_B T} dx$$

In order to obtain the unbiased distribution function, the biased potential should be removed for which the Weighted Histogram Analysis Method (WHAM) is used. Rearranging the above equation gives and thus the unbiased potential is

$$P_{b,i}(x) = P(x) e^{-[V_i(x) - K_i]/K_B T}$$

$$P(x) = \sum_i^N n_i P_{b,i}(x) \left[\sum_j^N n_j \exp\left(\frac{-V_i(x) - K_i}{K_B T}\right)\right]^{-1}$$

Where n_j is the data in the i-th window and N is the number of windows.
The above two equations are simultaneously solved, usually the algorithm starts with a set of guessed and obtained P will be put back in the equation until the answer if obtained with a desired accuracy.

There are a few points to consider for getting a reliable potential of mean force. First, the resulted histograms must sufficiently overlap with their peaks entered at the equilibrium position. The resulted potential of mean force should be smooth otherwise the spring constant and the number of windows should be adjusted.
It should be noted that the following Chapters contain their own standalone materials and methods with all the details necessary for reproducing specific models used in these Chapter.

CHAPTER 3: Regulatory mechanisms of integrin signaling through cytoplasmic interactions (Integrin signaling layer)

Section 3.1 Mechanisms of integrin and filamin binding and their interplay with talin during early focal adhesion formation[1]

At the focal adhesion site, filamin competes with talin, the central integrin activator, for an overlapping binding site on integrin, with potential negative modulation of integrin activation (Calderwood et al. 2001; Kiema et al. 2006). Talin binds the membrane distal segment of integrin's β_3 cytoplasmic tail at ^{739}WDTANNPLYDEA^{750}, which provides the site of the initial interaction between talin and integrin(García-Alvarez et al. 2003). The activation of integrin by talin is mediated by a subsequent interaction at the more membrane proximal (MP) region of the integrin tail which may unclasp the constituent subunits of integrin (Vinogradova et al. 2002; Wegener et al. 2007). However, disruption of talin's first interaction with the membrane distal portion can inhibit integrin activation as well as a disrupted second interaction with the membrane proximal (MP) portion of integrin(Wegener et al. 2007). The competition of filamin against talin's first interaction with integrin at its membrane distal end could be a protective mechanism for regulating adhesion in response to mechanical forces. However, the mechanism of filamin and talin competition is not yet clear.

The crystal structure of IgFLNa21 bound to β_7 integrin, and the observations in several experimental studies suggest that auto-inhibition of IgFLNa21 by IgFLNa20 can be regulated via several pathways including alternative splicing of filamin, phosphorylation of both integrin and filamin, and also mechanical forces applied to filamin (Kiema et al. 2006; Lad et al. 2007; Chen et al. 2009). IgFLNa20-21 exhibits a precisely tuned mechanosensitivity to gradual increases in force. The auto-inhibitory IgFLNa20 is first separated from the cryptic binding site on IgFLNa21 at 2-5 pN forces, and then IgFLNa20 and IgFLNa21 unravel when exposed to larger mechanical forces (Figure 3.1-1)(Chen et al. 2013; Rognoni et al. 2012). The removal of auto-inhibition via relatively small forces is sufficient to elicit a substantial (as much as 17-folds) increase in its affinity for binding of mechanosensitive transmembrane ligands including glycoprotein Ib (GPIb)(Rognoni et al. 2012). This interesting property enables filamin to fulfill its role as a sensitive mechanotransducer positioned on the force-transmitting webs of actin and at the highly interactive focal adhesion. Filamin also binds several other members of the integrin family including β_{1A}, β_{1D}, β_2, and β_3 integrins(Stossel et al. 2001).

In this study, we used molecular modeling to examine the interaction and binding of IgFLNa21 to $\alpha_{IIb}\beta_3$ integrin, highlighting possible mechanisms of early dynamics including various protein-protein interactions and the sequence in which they occur. In addition, we predicted the potential effect of the IgFLNa20 auto-inhibitory strand on integrin binding by comparing the interactions between integrin and filamin in the presence and absence of the auto-inhibitory strand. Moreover, we postulate a plausible role for integrin in releasing filamin from its auto-inhibitory configuration. Finally, we study the effect of talin on the filamin-integrin interaction and explore possible scenarios of the interplay among these molecules.

Recent studies have extensively explored the mechanism of inside-out activation of integrin by talin using molecular dynamics (MD) to model the conformational changes and

[1] The content of this Chapter has been published in Integrative Biology in 2015, Volume 7, Issue 10, Pages 1285-1296 (Truong et al. 2015).

interactions, which lead to full activation of integrin(Provasi et al. 2014; Kalli et al. 2011). Here we focus on the localization of talin and filamin to adhesion sites and their interactions prior to previously described mechanisms of integrin activation once the ligands have already been bound. Our results suggest that the order of binding events at the integrin β_3 tail is a key factor in regulating integrin activation.

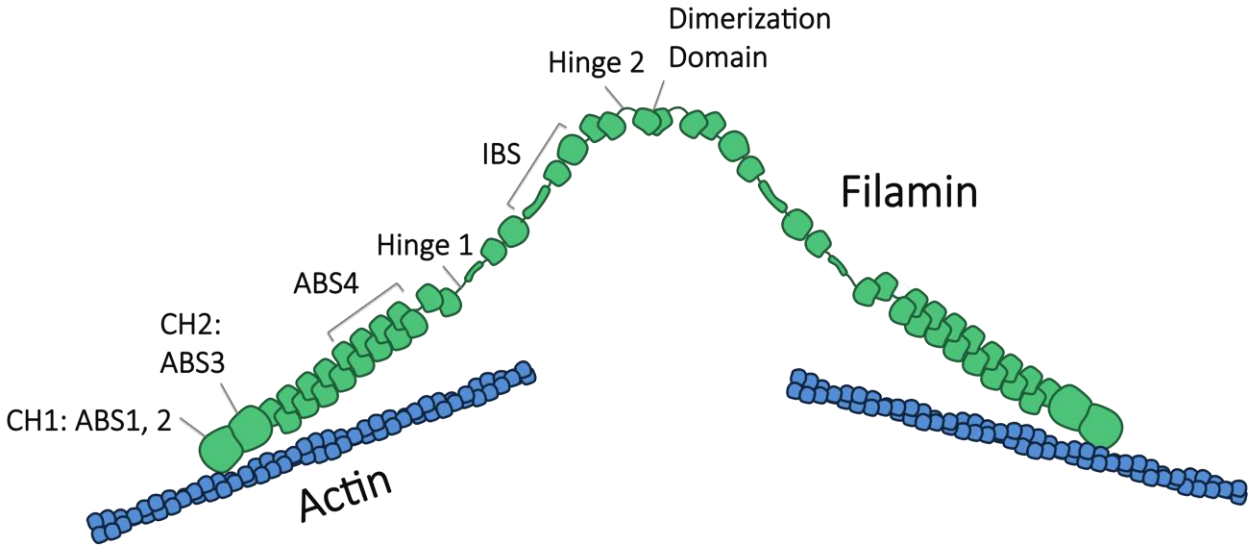

Figure 3.1-1. Schematics of filamin interaction with actin filaments. Each filamin monomer consists of 24 Ig repeats and two hinge regions between repeats 16-17 and 23-24. The actin binding domain (ABD) is located at the N-terminal end, while the main integrin binding sites (IBS) are on repeats 19 and 21 that are auto-inhibited by repeat 20. Filamin monomers dimerize through their last Ig repeat.

Materials and Methods

The interaction of filamin with integrin and talin was investigated using molecular dynamics models developed in the software package NAMD (Phillips et al. 2005) with CHARMM27 force field(MacKerell, et al. 1998). The structures used here include the transmembrane and cytoplasmic domains of $\alpha_{IIb}\beta_3$ integrin (PDB ID: 2K9J), IgFLNa21 (PDB ID: 2BRQ), IgFLNa19-21 (PDB ID: 2J3S) and talin from the talin-integrin complex (PDB ID: 3G9W) All simulations contained a POPC lipid membrane generated by the membrane builder plug-in from the Visual Molecular Dynamics (VMD) package. Proteins were placed at a minimum of 10Å apart to avoid steric contacts and solvated using TIP3P explicit water model and the ion concentration was set to 0.15M NaCl. Simulations were linearly heated to 310 K and the temperature was held constant for equilibration as a closed system. An NPT ensemble utilizing Langevin dynamics was applied to hold the pressure at 1 atm. Electrostatic force calculations were made using the particle mesh Ewald (PME) method. The time step was 2 fs, and the cutoff distance for non-bonded interactions was 1.2 nm. Visualizations were performed using VMD (Humphrey et al. 1996).

Molecular Dynamics of IgFLNa21 CD face and Activated Filamin Binding

To model the dynamics of IgFLNa21 binding to β_3 integrin, one IgFLNa21 molecule was isolated from a crystal structure (PDB ID: 2BRQ) containing two IgFLNa21s bound to two different β_7 integrins. This IgFLNa21 was placed near the β_3 tail of an $\alpha_{IIb}\beta_3$ integrin whose extracellular domains were excised and that was embedded in a POPC lipid membrane.

Seven trials of this model were equilibrated for 20 ns. Successful trials were used to analyze important electrostatic and hydrophobic interactions leading to binding between integrin and filamin. For the purpose of defining specific hydrophobic interactions within the hydrophobic region of FLNa21, the residues on either side of the inserting Ile^{757} on each strand of the CD face were chosen to represent the hydrophobic pocket.

The interaction between these three residues proved to be the stable core of the hydrophobic insertion, although other hydrophobic residues that make up the CD face surrounding them likely lend strength to the hold on Ile^{757}. These neighboring residues include Ala^{2272}, Ile^{2273}, and Ile^{2283}.

The activated structure of filamin(Chen et al. 2009), containing repeats 19 to 21, was used to study its interaction with integrin. The initial distance of the activated filamin from integrin was similar to that in the simulation of only repeat 21 binding to integrin. The simulations resulted in strong bound conformation of activated filamin and integrin, which was in turn used in simulations done in the presence of talin (see 'Filamin and talin competition in integrin binding' in **Materials and Methods**).

The final bound structure resulting from the end of the successful trial was used for ten more simulations. Each of these simulations involved reheating to 310 K in order to randomize velocities and then an equilibration step for 10 ns. From the last 10 ns, average energies of interaction were calculated for the final bound structure of IgFLNa21 with β_3 integrin.

The IgFLNa20 Auto-inhibitory Strand

Two models were created by placing the crystal structure of IgFLNa19-21 (PDB ID: 2J3S) 10Å away from two different sides of the backbone of the β_3 integrin tail. The cut $\alpha_{IIb}\beta_3$ integrin was placed in a POPC lipid membrane. Five trials of each model were heated linearly to 310 K to randomize molecular velocities and then equilibrated for 13 ns each. Average energies of interaction were calculated from the last 8 ns of all ten trials, and from all trials from each model alone. The first 5 ns were left out in order to account for a period of minimization and equilibration.

Filamin and Talin Competition in Integrin Binding

In this phase of the study, talin was also included in simulations and positioned in various distances from filamin and integrin. Since the crystal structure of talin is not entirely available, only the F2 and F3 domains that contain the integrin binding site were used in our simulations(Anthis et al. 2009) (PBD ID: 3G9W). The regions of integrin and filamin used in this part were similar to the previous parts of this study.

Three simulation sets with five trials were performed for 5 ns in order to examine the role of talin in filamin-integrin interaction. In the first set, both talin and filamin were positioned at distances larger than the cut-off range for non-bonded interactions relative to integrin (the closest atoms were farther away than 15 Å). In the second set, talin was positioned in the vicinity of the filamin-integrin complex found from the previous simulations (see 'Molecular Dynamics of IgFLNa21 CD face and Activated Filamin Binding' in **Materials and Methods**). In the third set, the available structure of talin was put in complex with integrin, while filamin was positioned away from its binding site on integrin(Anthis et al. 2009). All simulations were minimized and equilibrated prior to the production run. The condition for temperature, pressure and ion concentration was the same as the previous simulations. Although the simulation box changed for each system according to the system size, all satisfied the minimum image convention by

setting the minimum distance between the salute and the simulation cell wall to be greater than 22 Å.

Upon completion of all simulations, the following pairwise energies were calculated and averaged among 5 trials: 1) Between integrin subunits; 2) β-Integrin and filamin, 3) β-Integrin and talin; 4) α-Integrin and filamin; 5) α-Integrin and talin; And also 6) mutual interaction between filamin and talin. Also, all important residues participating in the above interactions were analyzed and discussed. Visualizations were performed using VMD. For reviewing general principles of molecular dynamics, please see Chapter 2 of the present dissertation.

Results

Integrin signaling is regulated via various interactions at integrin's cytoplasmic tail in a mechanosensitive manner. Talin is a key player in integrin activation and its interplay with other focal adhesion molecules controls further downstream events (Petrich et al. 2007; Ye, Lagarrigue, et al. 2014). It has previously been proposed that filamin binding to the β integrin tail prevents adhesion formation via blocking talin association to integrin (Kiema et al. 2006), however the molecular mechanism of such competition is not yet clear. Furthermore, the auto-inhibited state of filamin shows a low affinity for integrin binding and needs to become activated either through mechanical or chemical cues prior to effective engagement with integrin (Lad et al. 2007; Chen et al. 2009). In this study, we explored the molecular mechanisms of integrin binding to filamin in both auto-inhibited and activated states. Using all-atom molecular dynamics (MD) models, we investigated the competition between talin and filamin at the β_3 integrin tail during early stages of adhesion formation.

It should be note that while the energy of salt bridges are usually overestimated in standard MD force fields(Debiec et al. 2014), some MD force fields including CHARMM22 and CHARMM27 are able to provide sufficient accuracy compared to experimental studies(Piana et al. 2011). Furthermore, here we are mostly interested in comparing either different configurations of protein complexes or different states of a single molecule, e.g. inhibited versus activated filamin, and thus relative energies signify more than the absolute values. Also, since molecular dynamics simulations are stochastic in nature and average values are more meaningful, all reported energies are computed averages from multiple trials of MD simulations.

The Activated conformation of Filamin Binding to Integrin

Analysis of the molecular dynamics trajectories of β_3 integrin and uninhibited IgFLNa21 binding revealed an early hydrophobic anchorage as Ile^{757} on β_3 integrin inserted itself into the exposed hydrophobic pocket on the surface of FLNa21 formed by Leu^{2271} and Phe^{2285}, which appeared to be critical for stable binding between the molecules (Figure 3.1-2A). This result matched a previously reported insertion of Ile^{782} on β_7 integrin into the same FLNa21 hydrophobic pocket(Kiema et al. 2006). This interaction stabilized the orientation that permitted the two surfaces to have the most favorable contact by bringing together the cores of each binding region. Other simulations in which integrin and filamin failed to bind did not establish this hydrophobic contact and consequently separated even when a strong electrostatic contact was initially created. We believe that this stability is generated by the key positioning of Ile^{757} not only between the C and D strands of the CD face, but also between its proximal and distal attachments. Its function as a fastener for the appropriate binding arrangement is consequently necessary for the stability required to secure a tight bind in the likely event that integrin and filamin do not optimally position themselves before they interact. The hydrophobic insertion of an Ile into the CD strands of IgFLNa21 is also conserved in β_7 integrin and in IgFLNa20(Lad et al. 2007). We have shown that it is also conserved in β_3 integrin and appears to be an important component of ligand binding to the CD face of IgFLNa21.

This hydrophobic contact happened within the first nanosecond, allowing strong electrostatic interactions to happen more stably shortly thereafter. Specifically, the securing of the two binding faces together, resulting from the previously mentioned hydrophobic contact, brought Arg^{760} within the vicinity of Asp^{2287}, forming a strong salt bridge at the membrane distal (MD) end of integrin's β tail (Figure 3.1-2B). Afterward, a second salt bridge formed closer to the membrane proximal (MP) end of β integrin when Lys^{748} and Glu^{2276} bind, which secured the

two proteins together at both ends of filamin's CD face (Figure 3.1-2B). Prior to the formation of this second salt bridge, a transient electrostatic interaction occurred between Glu^{749} and Lys^{2280} from 2 ns to 6 ns, which helped to bring the C-terminal end of FLNa21 strand C towards β_3 integrin. These two salt bridges that formed at the membrane proximal end competed with one another since IgFNA21 must change its orientation in order to bind either Lys^{748} or Glu^{749}. Although both residues did bind within the course of our 30 ns total simulations, the salt bridge between Glu^{749} and Lys^{2280} was of a more transient nature. On the other hand, Lys^{748} and Glu^{2276} almost always interacted after the aforementioned salt bridge dissociates, but their interaction was unstable and shifted between high and low energy states. We concluded that the binding between integrin and filamin is likely to be stronger and more stable at the membrane distal end of the integrin tail while it is weaker and less stable at the membrane proximal end. The average simulated energies for the four specific interactions mentioned above were calculated from the ten trials and reported in Table 1.

Table 3.1-1. Important interactions between integrin and filamin.

Interaction	Average Interaction Energy (kcal/mol)*
Hydrophobic pocket - Ile^{757} : Leu^{2271} and Phe^{2285}	-6.6 ±1.1
Salt Bridge - Arg^{760} : Asp^{2287}	-81 ±10
Salt Bridge - Lys^{748} : Glu^{2276}	-59 ±31
Salt Bridge - Glu^{749} : Lys^{2280}	-5.5 ± 6.2

*The average interaction energies for specific residues important in the binding between integrin and filamin were calculated across ten extended trials of a successful bind in molecular dynamics simulations. This demonstrates that the strongest stable interaction is the salt bridge between Arg^{760} and Asp^{2287}. The hydrophobic pocket insertion is weak because it is composed of Van der Waals forces, but it remains very stable. The salt bridge between Lys^{748} and Glu^{2276} is very unstable, appearing to switch between a low and a high energy state in all simulations, averaging in the end to a strength of -59 kcal/mol. The transient salt bridge that formed between Glu^{749} and Lys^{2280} within 2 ns and that disappeared by 5 ns, was indeed transient as its average interaction energy was negligible for an electrostatic interaction.

As illustrated in Figure 3.1-2C, the average interaction energy between β_3 integrin and FLNa taken among 10 trials, became more stable after 8 ns when salt bridges were formed. Although the electrostatic interactions contributed more to the total interaction energy and were quantitatively stronger, they were relatively transient compared to the first hydrophobic interaction that lasted during the entire length of the simulations. In other trials where electrostatic interactions formed without the hydrophobic pocket interaction, the overall energy tended to dissipate over time as molecules did not display high surface contacts.

The α_{IIb} subunit of integrin did not show any direct interaction with filamin in our model, and the interface between α_{IIb} integrin and β_3 integrin remained stable throughout the progression of filamin binding to β_3 integrin as assessed by stable interaction energies at the inner membrane clasp (IMC). Since the inactive conformation of integrin was used in our

simulations, we confirmed that integrin activation was not required for filamin binding(Kiema et al. 2006).

In the next step, we predicted the major interactions and their relative contributions to filamin and integrin binding. Our simulations suggested that three progressive interactions are important for IgFLNa21 binding to the cytoplasmic tail of β integrin: 1) First, a hydrophobic insertion of Ile^{757} at the center of the CD face of filamin; 2) second, a strong salt bridge at the membrane distal end of integrin between Arg^{760} and Asp^{2287}; 3) finally, a weaker salt bridge at the more membrane proximal end of integrin between Lys^{748} and Glu^{2276} . Our results also confirmed that filamin binding neither activated integrin nor required integrin activation at any stage as was previously shown(Kiema et al. 2006). This was verified by the stability of integrin's IMC interaction throughout the entire simulation. To our knowledge, these important interactions required for the successful binding between filamin and integrin have not been previously reported.

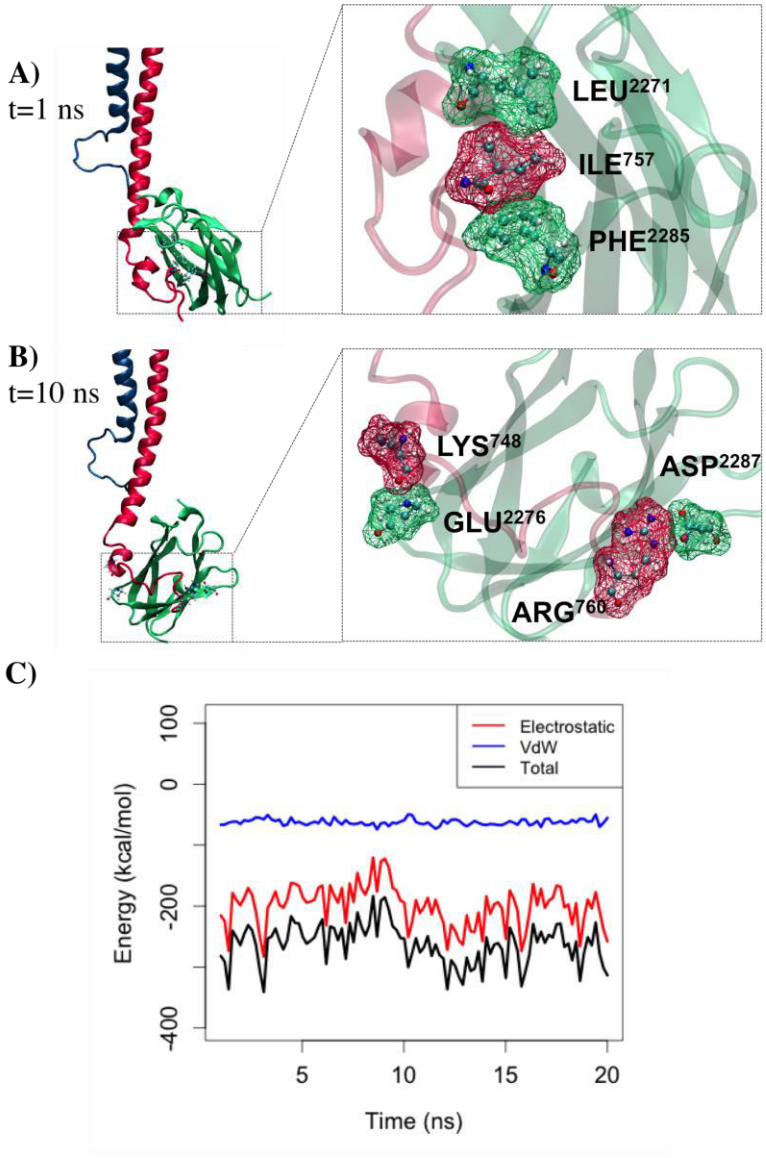

Figure 3.1-2. Interactions between uninhibited filamin and β_3 integrin. A) The model depicts FLNa21 CD strands (*green*) and β_3 integrin (*red*) backbones in ribbon representation. At 1 ns, the two proteins began to interact when Ile^{757} on β_3 integrin inserted into the hydrophobic pocket formed by Leu^{2271} and Phe^{2285}. This hydrophobic interaction stabilized the binding between integrin and filamin by promoting high surface contacts. B) Arg^{760} formed a strong, persistent salt bridge with Asp^{2287} that accounted for most of the strength of binding between integrin and filamin around 2 ns and lasted until the end of simulation (snapshot shown here). Another salt bridge formed between Lys^{748} and Glu^{2276} closer to the MP end of β_3. C) The interaction energy between β_3 integrin and uninhibited IgFLNa21 was averaged across ten trials of reheating and equilibration for 10 ns. The average energy of the electrostatic interactions accounted for most of the strength of binding.

The Auto-inhibitory Strand of Filamin Binding to Integrin

Filamin is known to regulate its binding to integrin at IgFLNa21 via a self inhibitory interaction between the first strand of IgFLNa20 with the CD face of IgFLNa21, which is the binding site for the β tail of integrin(Lad et al. 2007). The interaction between the auto-inhibited state of IgFLNa19-21 and integrin was explored in two different orientations of filamin with respect to the integrin tail. In the first model (Model 1), the inhibited IgFLNa21 CD face was placed in proximity to the filamin-binding site on integrin as determined by the presence of Ile^{757} (Figure 3.1-4A), while in the second model (Model 2), it faced residues on the opposite surface of the integrin tail (Figure 3.1-4B). These two orientations were modeled to assess the affinity of filamin in its auto-inhibited state to integrin while positioned with and without resemblance to its orientation when bound to integrin in its active state. The results showed that of the overall ten trials with β_3 integrin in the presence of auto-inhibited filamin, five exhibited a fairly stable binding between filamin and integrin. Four of the five successful trials were derived from Model 2 and interactions were consistently stronger in Model 2 compared to Model 1 (Figure 3.1-4).

In reference to the strength of the interactions we observed in these models, Model 2 exhibited stronger and more stable interactions between filamin and integrin. In this model, the integrin β tail interacted at average energies reaching -103 kcal/mol at the auto-inhibitory strand and reaching -67 kcal/mol at the inhibited IgFLNa21 CD face (Table 3.1-1). The average energy of interaction between integrin and filamin in trials that exhibited binding at these regions was -54 ±18 kcal/mol at the CD face and -57±29 kcal/mol at the auto-inhibitory strand. In addition, twice as many trials exhibited binding of integrin with the auto-inhibitory strand versus with the CD face beneath it. As such, interactions between integrin and auto-inhibited filamin seem to be achievable even at the covered CD face, but could occur with greater strength and likelihood with the auto-inhibitory strand itself.

Model 1 demonstrated infrequent interaction between integrin and filamin in its auto-inhibited state. Only one trial demonstrated any interaction, which occurred most strongly between Glu^{749} on integrin and Arg^{2139} on the auto-inhibitory strand. Of note, the configuration of both molecules during this interaction resembled the orientation of binding between uninhibited filamin and integrin. That is, the more membrane proximal portion of integrin bound the turn connecting the C and D strands of IgFLNa21. Occasionally, there were also interactions between Arg^{760} and Glu^{749} (Figure 3.1-3).

In contrast, Model 2 exhibited consistent interactions between integrin and filamin in its auto-inhibited state. Two consistently stable interactions were observed: (1) Lys^{748} on integrin engaged with inhibited filamin at two residues on both components of filamin, that is Glu^{2282} on the CD face and Glu^{2142} on the auto-inhibitory strand; (2) Glu^{749} on integrin interacted weakly

Table 3.1-2 The average energy of interaction across each trial of Model 1 and Model 2

Trial Number	Average Interaction Energy Between Integrin and CD Face of FLNa21 (kcal/mol)	
	Model 1	Model 2
1	-9	7
2	1	-4
3	-15	-67
4	-8	0.14
5	0	-42
	Average Interaction Energy Between Integrin and Autoinhibitory FLNa20 (kcal/mol)	
	Model 1	Model 2
1	-7	-40
2	-20	-33
3	-64	-42
4	-5	-11
5	1	-103

with a highly basic region on the auto-inhibitory strand consisting of three arginine residues, $Arg^{2146\text{-}2148}$. These interactions are depicted in Figure 3.1-3. Interactions of Model 1 and 2 are summarized in Table 3.1-2.

From our MD simulations, we predicted that filamin in its auto-inhibited state may interact with integrin in a stable manner at a position distinct from its conformation during binding in an active state. The responsible residues on integrin were the same ones responsible for the weaker salt bridges formed when integrin bound to filamin in its active state. However, they appeared to bind the auto-inhibitory strand itself, and to a lesser degree the covered CD face of filamin.

A Competition between Filamin and Talin

The competition between talin and filamin for the same binding site on integrin was proposed to be one of the most important regulatory mechanisms for integrin activation(Kiema et al. 2006), however, the details of their interplay are not yet fully understood. Previous studies showed that increased filamin binding to integrin in Chinese hamster ovary cells inhibited migration(Calderwood et al. 2001). On the contrary, the presence of talin is essential for forming nascent adhesions and is found localized to protruding regions of lamellipodium indicative of its major role in cellular motility as well as adhesion (Zaidel-Bar et al. 2003; Lawson et al. 2012). Outcomes concerning integrin functionality including cell migration and adhesion appear then to

be regulated by filamin binding(Calderwood et al. 2001; Liu et al. 2015), which is complicated by competition with activating ligands such as talin (Kiema et al. 2006).

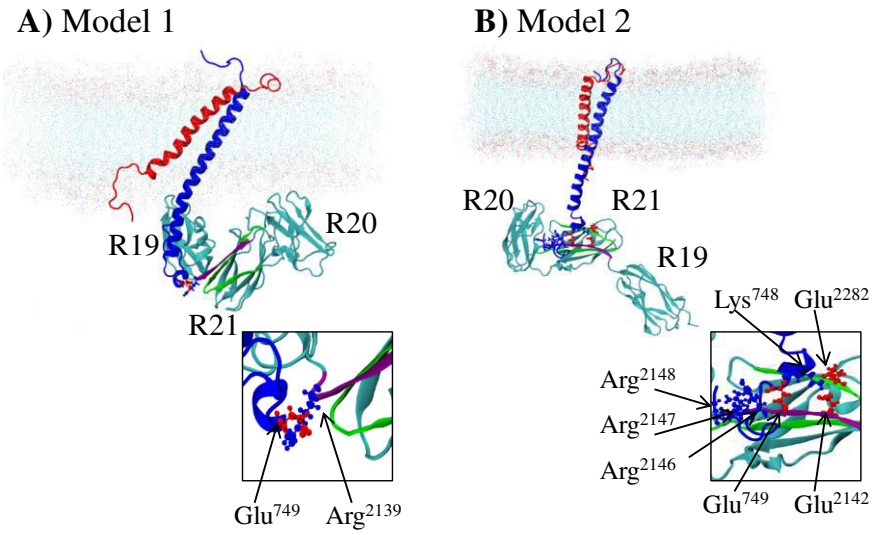

Figure 3.1-3. Two possible models for the interaction between filamin and integrin. A) Model 1 reveals one stable interaction from one of five trials. This interaction is between the integrin β_3 cytoplasmic tail and the auto-inhibitory strand at Glu^{749} and Arg^{2139}, respectively. B) Model 2 reveals two interactions, and integrin interacts more strongly at the auto-inhibitory strand than at the IgFLNa21 CD face in all four of five trials that demonstrated binding. The stronger interaction is between Lys^{748} and Glu^{2142} on the auto-inhibitory strand or Glu^{2282} on the IgFLNa21 CD face. There is also a weak interaction between Glu^{749} and a basic region consisting of $Arg^{2146-2148}$. Acidic residues are shown in red, basic residues in blue. The auto-inhibitory strand is depicted in purple and the IgFLNa21 CD face in green.

In this study, we hypothesized that the order of binding events among at the integrin tail prior to integrin activation is most likely a key factor in promoting subsequent signaling pathways. Specifically, the objective of this study was to understand the early dynamics of the competition between filamin and talin interactions with the integrin tail, which ultimately localizes them to the adhesion sites. We examined three possible scenarios: 1) In the first scenario, filamin and talin were placed at equal distances from their binding site on the integrin tail such that none was favored; 2) In the second scenario, talin was placed closer to integrin (also referred to as the talin-bound simulations) and lastly 3) filamin was moved closer to integrin, while talin was positioned farther away (also referred to as the filamin-bound simulations).

In the first scenario, we investigated the relative likelihood of filamin and talin binding to integrin in a fair competition. Although the simulation time (5 ns) was not sufficient for the formation of stable interactions, it provided an important insight on the early dynamics of the system. The integrin tail either swung closer to filamin or stayed at the same position in all five trials. Therefore, integrin could engage at least weakly with filamin but not with talin, especially towards the end of simulations.

In order to investigate the interplay between talin and filamin in the second scenario, the native structure of the talin F2 and F3 domains in complex with the β-integrin tail was obtained from the protein data bank (PDB ID: 3G9W)(Anthis et al. 2009). The F2 and F3 domains of talin were oriented correctly, based on the crystal structure of the complex, with respect to their

binding site on integrin but slightly moved away within the cut-off distance of the non-bonded interactions to allow surface adjustments at the integrin-talin interface. On the other hand, filamin was placed farther away such that it had a lower chance to interact with its binding site on integrin.

All interaction energies observed during the process of integrin activation is signified by a reduction in the interaction between α and β subunits at the cytoplasmic side, and thus talin, as a primary activator of integrin, was expected to weaken the strength of integrin dimerization. The pairwise interaction energy of integrin subunits showed a 50 kcal/mol decrease upon talin binding (Figure 3.1-5A). The interaction energy between talin and β-integrin, which was averaged over five trials, indicated an oscillatory behavior ranging between 0 and -200kcal/mol suggesting that the presence of filamin reduced the stability of talin-integrin interactions (Figure 3.1-5B). Talin was bound towards the C-terminal end of β-integrin tail mainly through electrostatic interactions. Also, filamin binding to integrin overlapped with the partial dissociation of integrin subunits in the last 1 ns (Figure 3.1-5C).

Further analyses of the simulation trajectories of the second scenario showed an interesting prediction of the force transmission dynamics from the point of contact between talin and integrin to the interface between integrin subunits (Figure 3.1-6A). Specifically, an interaction between TRP988 on α-integrin and ILE719 on β-integrin was replaced by an

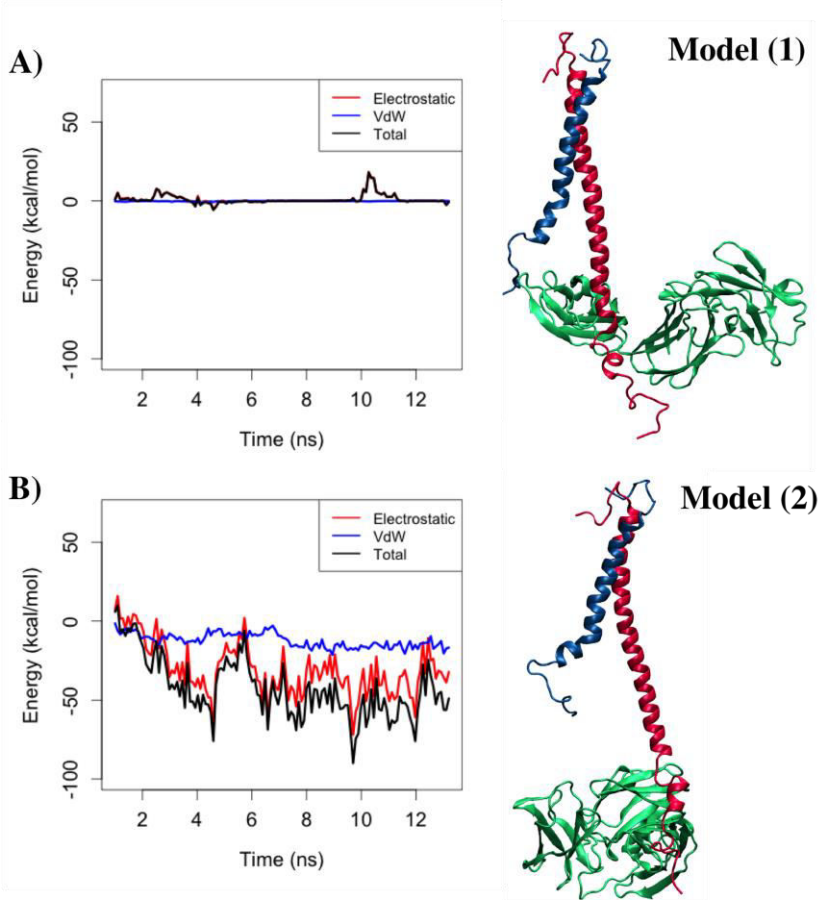

Figure 3.1-4. Stabilities of the filamin-integrin complex in Models 1 and 2. Two models were created to simulate a randomized encounter between inhibited filamin containing IgFLNa20-21 and β_3 integrin. A) The first orientation placed the inhibited FLNa21 CD face on the side of integrin that is favorable for binding when uninhibited. It faced

the residues on integrin that typically interact with the filamin CD face. As expected, the energy of interaction was negligible indicating that inhibited filamin did not have a tendency to bind to the standard filamin binding site on β_3 integrin. B) The second orientation placed the inhibited FLNa21 CD face opposite to the side of integrin that is favorable for uninhibited binding. It faced different residues from those that typically interact with the filamin CD face resulting in an energy showed a relatively strong association between inhibited filamin and β_3 integrin.

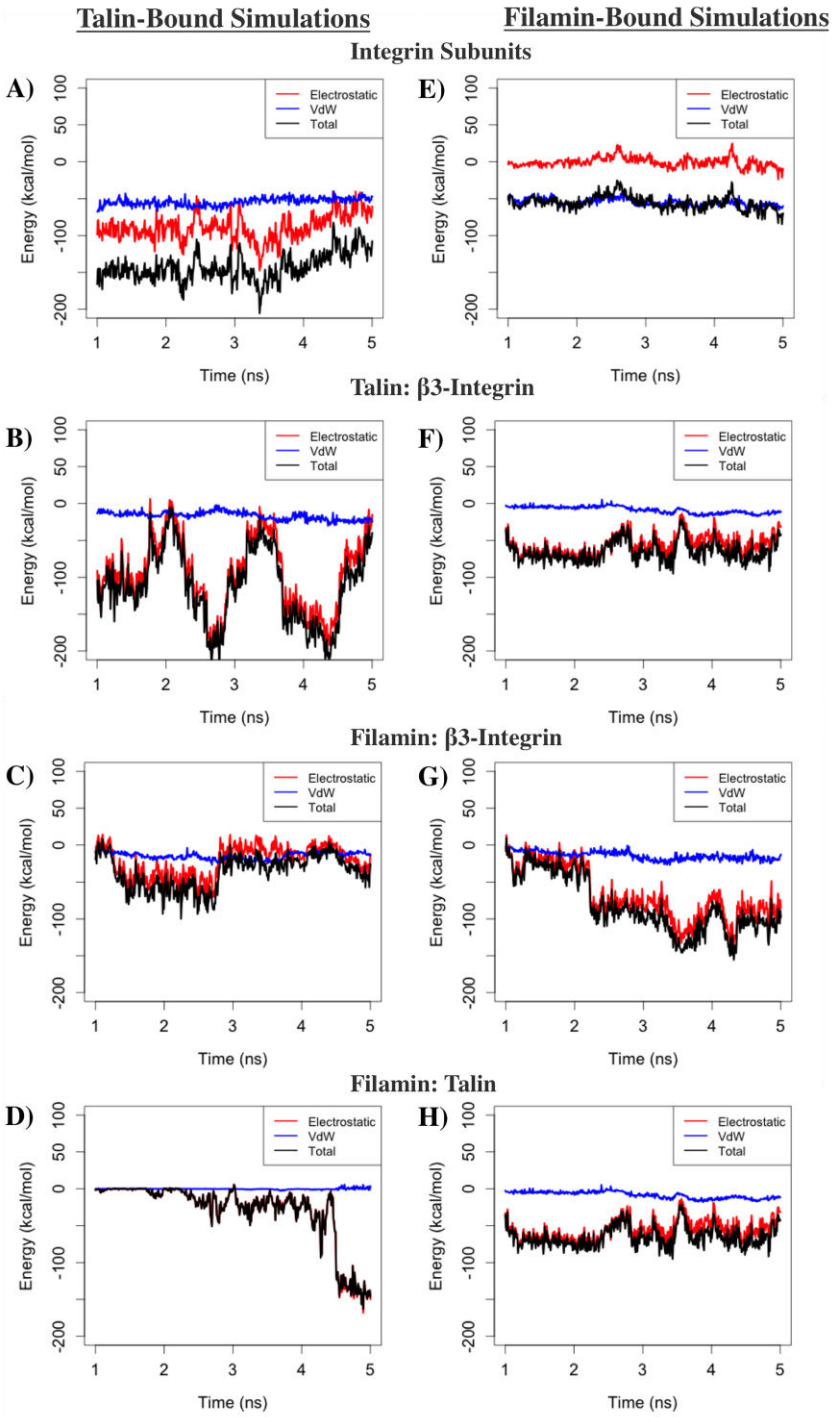

Figure 3.1-5. **Average energies of all pairwise interactions.** A comparison between talin-bound and filamin-bound simulations: Electrostatic (*red)*, van der Waals (*blue*) and total energies (*black*) are shown. Talin-bound simulations: A) The total interaction energy of integrin subunits shows a 50 kcal/mol increase starting around 3.2 ns. B) Talin

interaction with β_3-integrin demonstrated an oscillatory behavior. C) Filamin weakly interacted with β_3-integrin in the first half of simulations but dissociated in the second half. D) The interaction energy between talin and filain becomes stronger towards the end of simulations. Filamin-bound simulations: E) The interaction energy of integrin subunits was constant but got approximately 110 kcal/mol weaker compared to talin-bound simulations. F) Talin interaction with β_3-integrin was much weaker than in the talin-bound simulations was first bound to integrin, while G) filamin-integrin interaction was about five times stronger than talin-bound simulations. H) Unlike the talin-bound simulations, filamin and talin got engaged since the beginning of simulations.

interaction between TRP988 and TRP715 after around 3 ns, which occurred in response to talin association with the β 3-integrin tail. The transmembrane helix of β 3-integrin is connected to a smaller helix (residues 743–750) on the cytoplasmic side via a loop region . Initially, the small cytoplasmic α-helix was not fully aligned with its binding site on the F3 domain of talin as GLU^{375} on the F3 domain was associated with LYS^{738} on the β-integrin tail. After 2 ns, LYS^{738} was released from GLU^{375} and associated with GLU^{378}, which contributed to the alignment between the small α-helix of integrin and F3 domain of talin leading to formation of new electrostatic interactions (Figure 3.1-6B-E). Interestingly, filamin engaged with both integrin and talin simultaneously (Figure 3.1-5C-D) through one of its residues (VAL^{255}), which formed an interaction with PRO^{366} on talin after 3 ns. Since filamin bound to the lower segment of integrin tail closer to the C-terminal, we observed that it affected the alignment between the small α-helix on β-integrin and the β-sheet face of the F3 domain of talin (Figure 3.1-6).

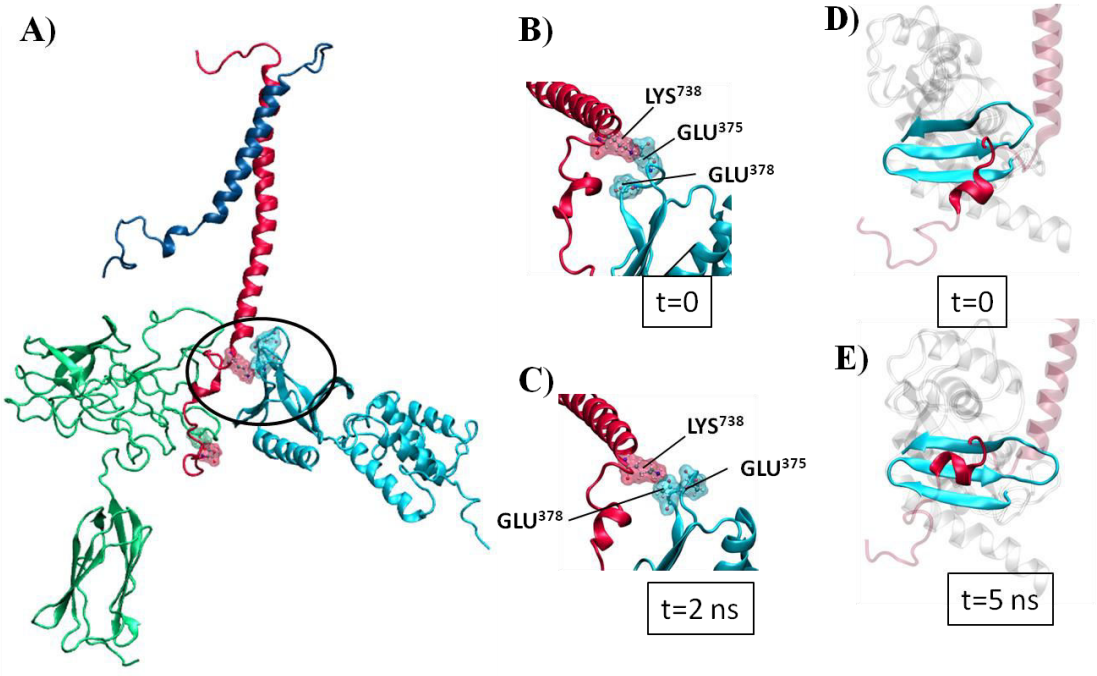

Figure 3.1-6. **The competition between filamin and talin for the same binding site on integrin in the talin-bound simulations.** A) Talin bound to the more proximal region of the integrin tail, while filamin associated with the distal portion of β_3-integrin (the binding residues are circled). B) The dynamics of talin-integrin binding showed that Lys^{738} acted as an anchor that held talin in place by switching from interacting with GLU375 C) to GLU378 at 2 ns in order for the small α-helix of the cytoplasmic side of β_3-integrin to align with its binding site on the F3 domain of talin (D, E).

In the third scenario, filamin was positioned at a closer proximity of β-integrin removed talin such that interactions were more likely to occur between integrin and filamin. Although

talin could engage with integrin in this scenario, the interaction between integrin subunits remained intact (Figure 3.1-5E). However, the overall interaction energy between integrin subunits was significantly decreased (~110 kcal/mol) compared to that in the talin-bound simulations (second scenario shown in Figure 3.1-5A). In order to understand such energy difference, the final configuration of the integrin dimer in the filamin-bound system was aligned with that in the talin-bound system.

Interestingly, a notable decrease in the angle between integrin subunits, which was initially set at 25° (Ye, Snider, et al. 2014) in the filamin-bound system, was observed. This angle change resulted in reducing several interactions at the N-terminal end of the transmembrane part of the integrin dimer as well as a segment of ectodomain including ASP^{692} and VAL^{696} of α-integrin with ALA^{956} and ILE^{964} of β-integrin, respectively (Figure 3.1-7). On the other hand, some interactions in both transmembrane and cytoplasmic regions were notably stabilized due to the parallelization of the transmembrane domains of integrin subunits. Therefore, the reduction in the interaction energy is not indicative of integrin activation.

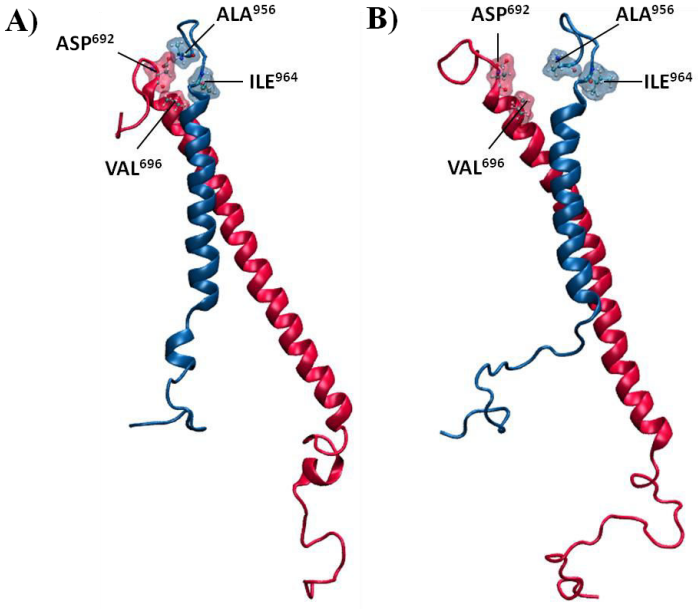

Figure 3.1-7 – Difference in the alignment of integrin monomers between talin-bound and filamin-bound simulations. Integrin subunits form a 25° angle with each other inside the lipid membrane that accounts for the formation of several stable interactions between integrin subunits including ASP^{692} and VAL^{696} of β_3-integrin with ALA^{956} and ILE^{964} of α-integrin **A)** This angle was maintained in the talin-bound simulations, while **B)** it was notably reduced in the filamin-bound simulations.

After equilibrating the filamin-bound system, both talin and filamin formed simultaneous interactions with integrin as shown in Figures 4F and 4G. Within the first 2 ns, talin maintained a weak but stable interaction with β-integrin, while the energy of filamin-integrin interaction continuously decreased. The filamin–integrin energy was stabilized after 2 ns, while the talin–integrin was decreased. A relatively stable interaction between filamin and talin was also observed. (Figure 3.1-5H).

In the third scenario, filamin associated with the lower end of the integrin tail, while talin engaged with the same small α-helix in the middle region of the integrin cytoplasmic tail as observed in the talin-bound simulations but with a lower energy. Initially, GLY^{760} on β-integrin

interacted with SER^{100} and ILE^{240} on the CD face of filamin, however after 3.8 ns an interaction with talin forced the integrin tail to detach and move towards the lipid membrane eventually interacting with PHE^{242} on the CD face of filamin (Figure 3.1-8).

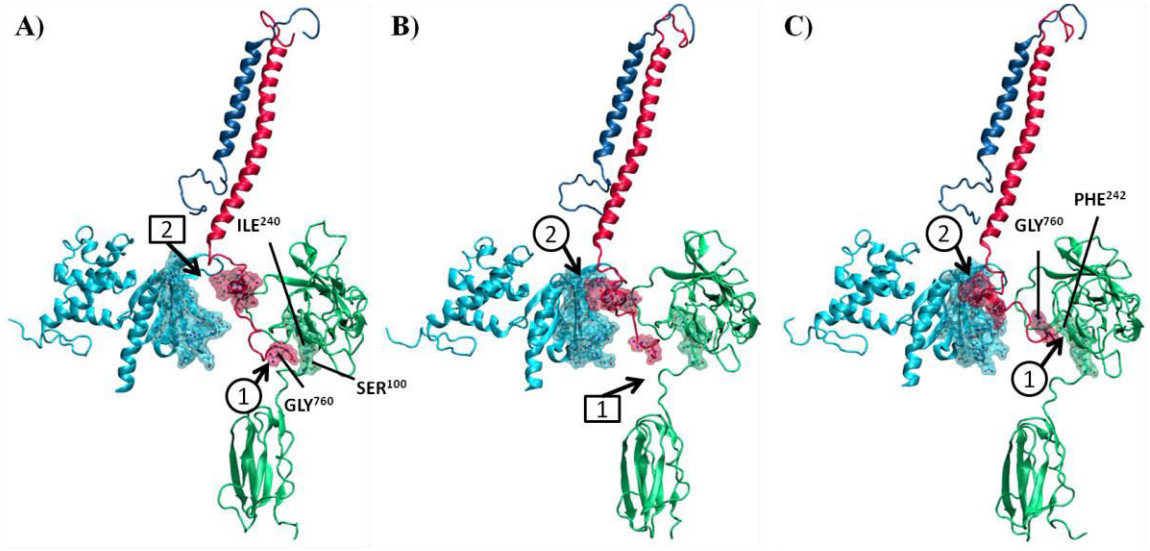

Figure 3.1-8. The competition between filamin and talin for the same binding site on integrin in the filamin-bound simulations. The dynamics of filamin-bound simulations: A) In the beginning of simulations, GLY^{760} of β-integrin is associated with both SER^{100} and ILE^{240} of the distal portion of the CD face with respect to the lipid membrane (site 1). However, the small α-helix of β-integrin tail is not yet engaged with talin (site 2). B) As β-integrin binds talin, GLY^{760} is separated and pushed closer to the membrane and C) associates with PHE^{242} located on the proximal region of the filamin CD face. Circles and squares indicate association and dissociation, respectively.

Generally, our simulations showed that talin bound closer to the inner membrane clasp (IMC) on the integrin tail, while filamin associated with the membrane distal region of the β-integrin and thus did not affect the IMC interaction. Furthermore, the interaction between filamin and talin depended on the order of their bindings to the integrin tail.

Discussion

Filamin plays an important structural and mechanotransducing role in the cell, allowing for versatility in cellular shape and motility. The structure of filamin allows for its own regulation of integrin binding by an auto-inhibitory strand on IgFLNa20. At focal adhesions, talin activates integrin while filamin plays an opposite role as it competes with talin for integrin binding.

Filamin's interactions with other proteins in the cell could provide a deeper understanding of diseases linked to filamin mutations. For instance, defects in FLNa that result in the disease periventricular nodular heterotopia have led to cases of individuals who present with platelet dysfunctions including thrombocytopenia and hemorrhage with abnormal platelet morphology. This represents a specific situation in which a reduction in FLNa's interactions with transmembrane receptors such as $\alpha_{IIb}\beta_3$ integrin have led to abnormal platelets and impaired interactions between platelets and vessel walls(Nurden et al. 2011). By unraveling the mechanism by which integrin and FLNa bind to perform their functions, it may be possible to

elucidate the underlying pathophysiology and design novel means for treatment of such disorders. Here we used $\alpha_{IIb}\beta_3$ integrin from platelets in all our simulations.

Prior studies have described binding between filamin and integrin either at equilibrated states in which stable interactions had already been formed with filamin or with given various external parameters such as force applied to filamin(Pentikäinen & Ylänne 2009; Rognoni et al. 2012). In order to elucidate the role of earlier transient interactions, which set the stage for binding filamin, we have developed molecular dynamics models to simulate important initial interactions including the role of filamin's auto-inhibitory strand and its dynamics in relation to talin.

Our results showed that the auto-inhibitory strand on IgFLNa20 engages strongly with IgFLNa21 with average interaction energy of -282 ±46 kcal/mol preventing it from efficient binding with the β_3 integrin tail. Beside the mechanism of alternative splicing, removal of this interaction requires mechanical force to be transmitted through the cytoskeleton with or without residue phosphorylation, indicating that the CD face of IgFLNa21 is tightly concealed in filamin's native conformation. In cases where there is insufficient force to expose the CD face of IgFLNa21, it becomes necessary to examine the effect of the auto-inhibitory strand on the interaction between filamin and integrin.

In simulations where IgFLNa21 was inhibited by IgFLNa20, the auto-inhibitory strand did not completely impede interactions between integrin and filamin. Integrin also continued to weakly interact with inhibited filamin, but more with the auto-inhibitory strand than with the partially exposed residues of the IgFLNa21 CD face. As a result, inhibited filamin may be held within the vicinity of a nearby focal adhesion in a weak but stable manner ready to become activated and reinforce adhesions.

It is interesting to note that inhibited filamin interacted with integrin more consistently in an orientation opposite to the actual filamin binding site (Model 2). This signified the increased likelihood that after filamin is released from its auto-inhibition, the filamin binding site will be available on the integrin tail. In order to bind an integrin that has been weakly interacting with in its auto-inhibited state, the uninhibited filamin must either wrap itself around integrin or detach and reorient itself. The potential implications of this relocating process are unknown.

Lad et al. posited that binding between β_7 integrin and filamin is strong enough to overcome the auto-inhibitory interaction with IgFLNa20 and that binding between integrin and filamin is stronger than the auto-inhibition(Lad et al. 2007). We did not see evidence of greater binding between β_3 integrin and IgFLNa21 than between IgFLNa20 and IgFLNa21 as the average interaction energy between uninhibited FLNa21 and β_3 integrin was -170 kcal/mol, compared to -282 kcal/mol between FLNa20 and FLNa21. This difference may be attributed to the use of β_3 integrin in our simulations rather than β_7 integrin. In our studies, auto-inhibited filamin exhibited increased interaction energies with integrin within the range of at least one extra electrostatic interaction. Stochastic fluctuations which allowed higher interaction energies at times during our simulations may allow integrin and IgFLNa20 to compete more evenly for IgFLNa21 binding.

In addition, the interaction between integrin and the auto-inhibitory strand itself may be an important first step in removing auto-inhibition altogether and toward uninhibited filamin and integrin binding. There was some evidence for this in the binding preference of auto-inhibited filamin to residues on integrin that orient it to the conformation of uninhibited binding in our simulations. Specifically, one stable interaction between Glu^{749} and Arg^{2139} bound the membrane

proximal portion of the integrin β_3 cytoplasmic tail to the region by the turn between the C and D strands of IgFLNa21.

Consequently, we propose a step-wise mechanism for filamin activation through integrin binding: (i) A reduction in the strength of IgFLNa20-IgFLNa21 interaction upon integrin binding to the auto-inhibitory strand; (ii) Complete dissociation of the auto-inhibitory strand in response to cytoskeletal forces; (iii) Association of integrin with the exposed CD face, which prevents it from possible deactivation (Figure 3.1-9). In other words, integrin binding to the IgFLNa20 inhibitory strand may act as a transient interaction that imposes forces on the inhibitory strand and reduces the strength of association between IgFLNa20 and IgFLNa21. We hypothesize that this interaction will then be coupled with the forces coming from the cytoskeleton, giving rise to filamin activation and reinforcement of integrin binding. In our simulations, we did not involve cytoskeletal forces due to the complexity of incorporating the dynamics of such forces in the process of a binding event. Instead, we used both the activated and inhibited segments of filamin in two independent simulations. Hence, we did not observe full activation of filamin due to the lack of cytoskeletal forces but an energy analysis predicted that integrin interaction indeed lowers the energy barrier needed to expose the CD face of IgFLNa21.

Chen, Kolahi et al. proposed that filamin binding to integrin was highly modifiable through a phosphorylation mechanism(Chen et al. 2009). Here, the idea of filamin's role as a "tunable mechanosensor"[2] was extended to also include interactions with IgFLNa20. Stable interactions between integrin and the IgFLNa20 auto-inhibitory strand suggested that filamin had some affinity for integrin constitutively, whether or not it senses a force through the cytoskeleton. This fits into a mechanoprotective role for filamin binding to integrin to regulate adhesion under mechanical stress conditions. Under stress, filamin will uncover its cryptic binding sites easily. However, under no-stress conditions in which steered molecular dynamics are not applied, filamin was predicted to still bind integrin even while auto-inhibited by IgFLNa20.

Interactions between integrin and the auto-inhibitory strand may play other roles as well. Kiema et al. 2006 hypothesized that, in the event of a dysfunctional IgFLNa21, the presence of other filamin repeats which could bind integrin (i.e. IgFLNa19) may be able to partially compensate for its loss of function. Our findings suggest it is possible that integrin's affinity for the auto-inhibitory strand (IgFLNa20) may also partially provide a compensatory mechanism for a defective IgFLNa21. Future studies of filamin's role as an integrin binding partner might explore the effects of auto-inhibitory strand binding in the context of phosphorylation or mechanical force applied to filamin.

Several studies suggested that the interplay among talin and filamin is crucial for regulating integrin activation in migrating cells(Kiema et al. 2006). As nascent adhesions start to form, talin molecules are recruited, while filamin concentration increases during the maturation stage. Although, talin is the main integrin activator, it may not be required for further cell spreading. Different types of integrin show distinct regulatory mechanisms in their interactions with filamin and talin(Calderwood et al. 2001). Here we report important predictions inferred from MD simulations on the order of talin and filamin binding to integrin $\alpha_{IIb}\beta_3$ and its effect on regulating the dynamics of integrin activation. It should be noted that integrin activation can primarily characterized by weakening of the linkage between integrin subunits (Wegener et al. 2007).

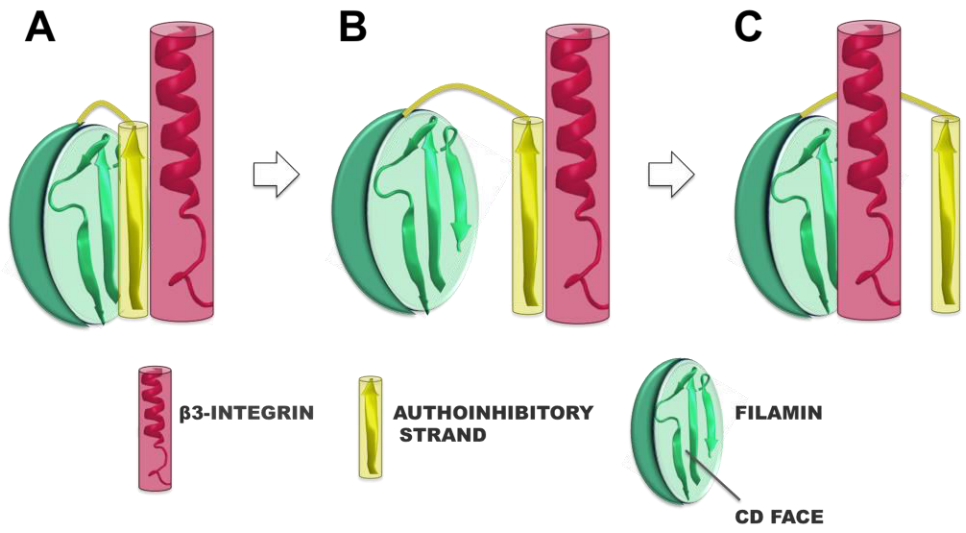

Figure 3.1-9 The mechanism of filamin activation through integrin binding. A) Relatively weak interaction between filamin and the auto-inhibitory strand may reduce the strength of inhibitory interactions and also serves as an anchorage point. B) As actin forces applied on the rod domain of filamin, are transmitted to the complex of auto-inhibitory strand and integrin, it may result in dissociating the auto-inhibitory strand from IgFLNA21 and leaving the CD face exposed to water. C). Also, since the auto-inhibitory strand binds to the opposite side of the integrin tail relative to the filamin binding site, integrin can subsequently dissociate from the auto-inhibitory strand and engage with the activated filamin on its actual binding site and prevent further deactivation of the molecule.

We compared two different cases in terms of the relative positions of talin and filamin with respect to integrin: (1) In the first case, talin was positioned relatively closer to the β-integrin tail compared to filamin while, (2) in the second case, filamin was put closer to integrin. Comparing the interface between the integrin monomers in both cases revealed that major talin association to integrin prior to filamin resulted in destabilizing the interface (Figure 3.1-5A). However, as shown in Figure 3.1-5C, talin interaction with integrin was highly fluctuating due to the presence of filamin indicating that filamin interfered with the dynamics of talin-integrin binding. Furthermore, the interaction between filamin and talin increased towards the end of talin-bound simulations that resulted in destabilization of the talin-integrin complex indicating the competition between talin and filamin. On the contrary, in the filamin-bound simulations, the interaction between filamin and talin was formed early on and lasted all throughout the simulations. This suggests that the interaction between filamin and talin may be dependent on the order of their binding to the integrin tail. Furthermore, talin binding is necessary and most likely sufficient for integrin activation, and consecutive filamin binding may not affect the process of integrin activation only if talin is already bound to integrin.

In the filamin-bound simulations, the interface between integrin subunits was stable but energetically lowered compared to the talin-bound simulations (Figure 3.1-5E). That was due to an angle change between integrin subunits resulting in the disruption of several interactions mainly within the transmembrane region of integrin subunits. This angle change may act as a lock for further signal transmission across the transmembrane region, and hence the increase in the energy of the integrin dimer in the filamin-bound simulations did not indicate activation but may in fact show functional stabilization of the inactivate conformation of integrin. Even though talin associated with integrin in the filamin-bound simulations, it did not cause any changes at the interface between integrin subunits. Moreover, here we observed that neither active nor

inactive filamin changed the strength of integrin dimerization. Therefore, we predict that filamin may act as an inhibitor of integrin activation if it first binds to integrin regardless of presence or absence of talin.

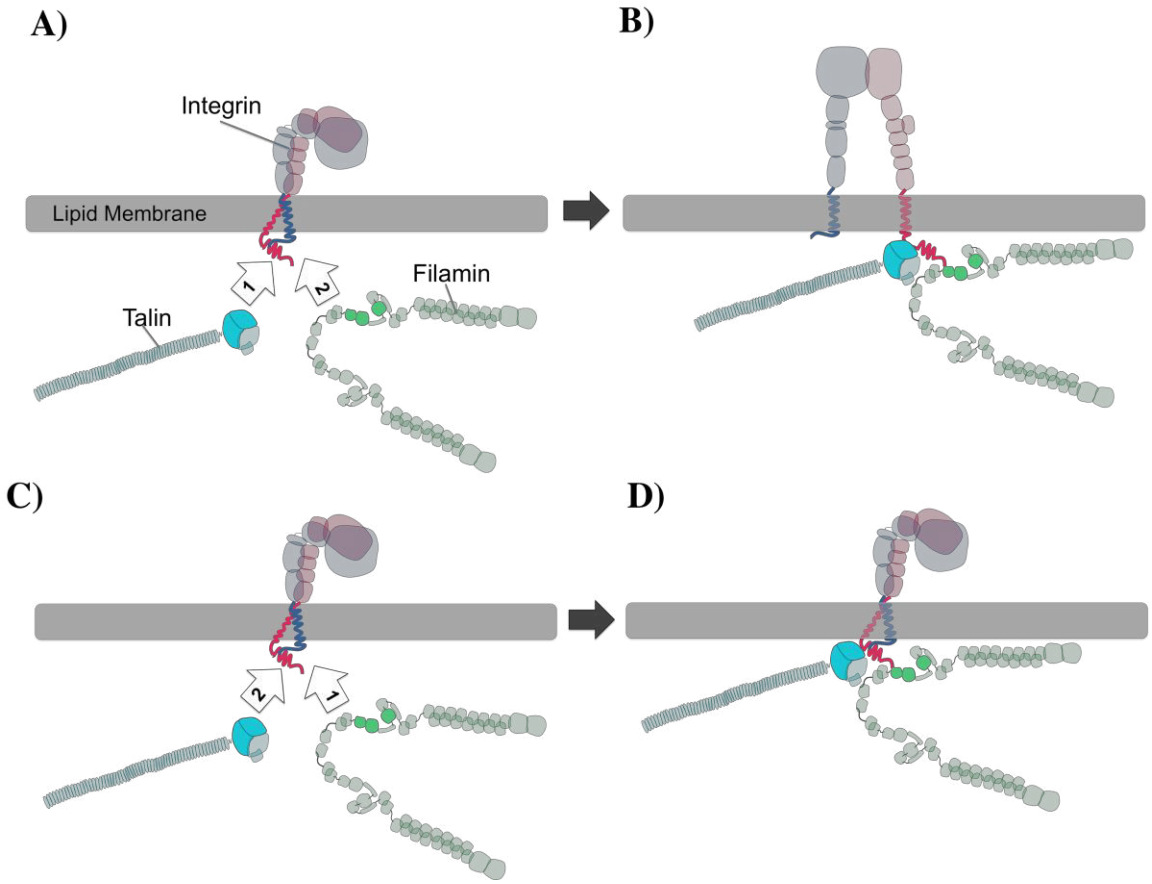

Figure 3.1-10. Summary of the talin-filamin interplay durin integrin activation. A-B) In simulations where talin was associated with the inactive conformation of integrin prior to filamin, the interactions between integrin subunits were weakened. C-D) However, as the sequence of binding events was reversed and filamin was engaged with integrin before talin, the inhibited conformation of integrin was remained intact. The transparent regions of molecules were not included in our model.

In the filamin-bound simulations, the interface between integrin subunits was stable but in order to explore a fair competition between filamin and talin, a set of simulations was designed in which filamin and talin were positioned at the same distance from their binding site on integrin giving both equal chances to engage with integrin. Our results suggested that integrin tail floated towards filamin and even slightly interacted, while there was no notable interaction formed with talin. It should be noted although the simulations (5 ns) was not long enough for the formation of a stable protein complex, it provided a valuable insight on the early dynamics of the competition between talin and filamin. All reported results were averaged across five trials in order to improve the statistical significance.

Several systems are known to exist with relationships comparable to that of filamin and talin in regards to competition for integrin binding, and there is much variance between the mechanisms and consequences of these systems. Kindlin and talin, for example, have been found to have sequence homology with each other and both bind to integrin β tails, however kindlin

and talin are cooperative in effect and are partners in the activation of integrin(Ye, Lagarrigue, et al. 2014). In another example, RIAM and vinculin have also been found to be mutually exclusive by structure in their binding to talin, but unlike filamin versus talin competition for integrin, binding of RIAM versus vinculin appears to occur under more distinguishing circumstances with vinculin binding only unfolded talin domains and RIAM only binding folded talin domains(Calderwood et al. 2013; Goult et al. 2013).

In summary, we proposed a mechanism for filamin activation through integrin binding to the auto-inhibitory strand associated with IgFLA21. Also, we predicted that filamin interference with talin-induced integrin activation depends on the sequence of binding events (Figure 3.1-10). Moreover, our results suggested that the mutual interactions between filamin and talin regulate their competition for integrin binding. Our simulations complement some previous experimental studies and will hopefully inspire future experimental investigations including testing new mutations involved in the proposed mechanisms.

Section 3.2 Cytoplasmic regulation of the integrin-mediated signal transmission through alternating response modes of the integrin transmembrane domain

Mechanical signaling between cells and their environment is critical for a variety of complex and vital cellular functions including mechanotransduction, migration, differentiation and growth (Minton 2014; Katta et al. 2015; Vogel 2006). More than 150 signaling and scaffolding molecules are involved in orchestrating both short- and long-term mechanical events that regulate cell adhesion and spreading for which the time-scale ranges from a few nanoseconds to days (Jahed et al. 2014; Galbraith et al. 2002). The order in these molecular players are recruited to the adhesion sites depends upon the type and intensity of the environmental stimuli. Early adhesions consisting of a very few molecules grow in size and become more mature as forces from the substrate increase and are farther transmitted towards the cytoplasm (Carisey et al. 2013; Gardel et al. 2008; Galbraith et al. 2002). These mature focal adhesions are strongly attached to the cytoskeleton moderating and translating the actin retrograde flow into traction forces exerted on the substrate (Gardel et al. 2008).

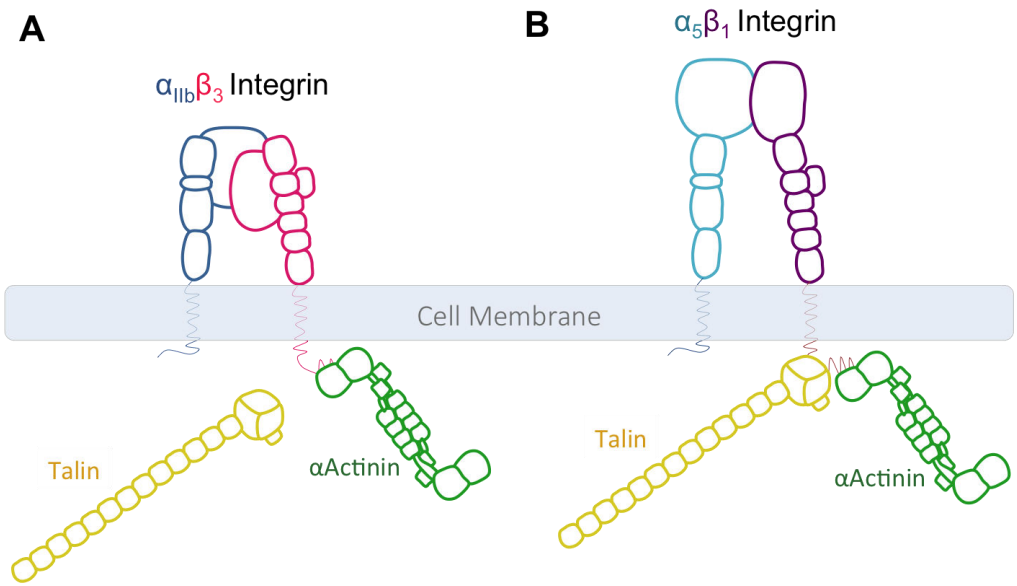

Figure 3.2-1. Distinct roles of α-actinin in regulating β_3- and β_1-integrins subunits. A) α-actinin competes with talin for the β_3-integrin tail. As it binds β_3-integrin, talin can no longer activate integrins. B) However, α-actinin binding does not inhibit β_1-integrin activation through talin association. The cooperative regulatory mechanism of β_1-integrin is completely different from supposedly competitive role of α-actinin in activating β_3-integrin.

Although talin is the key player in initiating integrin activation, it is not the only molecule capable of engaging with the integrin tail. Other proteins such as filamin and α-actinin can also associate with integrin and directly couple it with the actin cytoskeleton (Calderwood et al. 2001; Chen et al. 2009; Kiema et al. 2006; Kim et al. 2010; Calderwood et al. 2013; Ye, Snider, et al. 2014; Haydari & Mofrad n.d.; Moser et al. 2009; Truong et al. 2015). However, the effect of these molecules on the integrin activation process is strongly dependent upon their interplay with talin (Ye, Lagarrigue, et al. 2014). More specifically, they interfere with integrin activation through either competing or cooperating with talin. α-Actinin is one of the most prominent players in focal adhesion maturation (Roca-Cusachs et al. 2013; Zaidel-Bar et al. 2003; Galbraith et al. 2002), which involves force transmission between the cytoskeleton and adhesion sites, as it

both cross-links actin filaments (Hampton et al. 2007; Hotulainen & Lappalainen 2006; Ciobanasu et al. 2014; Shams et al. 2016) and engages them with focal adhesions (Shams et al. 2012; Tadokoro et al. 2011; Edlund et al. 2001).

The effect of α-actinin binding on talin's interaction with two different types of integrin heterdimers, namely $\alpha_{IIb}\beta_3$ and $\alpha_5\beta_1$, has been recently studied (Roca-Cusachs et al. 2013). The β3 integrin is necessary for nascent adhesion formation, while the β1 integrin is involved in more mature adhesions. The localization time of α-actinin and talin was monitored at both integrin tails to capture the order of binding events. Their results indicated that α-actinin would compete with talin for the β_3-integrin tail, while it most likely enhances talin binding to the β_1-integrin. This difference indicates that α-actinin would inhibit talin binding to early adhesions but may enhance binding in mature adhesions.

Such distinctions in dynamics and composition of integrin adhesions may play an important role in specificity of the singling properties of integrins and their associated proteins (Ye, Lagarrigue, et al. 2014). Nevertheless, the molecular mechanisms by which α-actinin and talin interact and communicates with each other at the integrin tail has remained illusive. The objective of the present study is to shed light on the key steps and sequence of binding events that regulate integrin activation through cytoplasmic interactions at the integrin tail.

Materials and Method

All molecular models were pre-processed in Visual Molecular Dynamics (VMD) (W Humphrey et al. 1996) and simulations were performed with NAMD (Phillips et al. 2005) using the CHARMM27 force field (MacKerell, et al. 1998) The system configuration of main simulations consisted of the full-length α-actinin (PDB ID: 1SJJ), F0 to F3 domains of talin (PDB ID: 3IVF) and only the transmembrane and cytoplasmic parts of either αIIbβ3 or α5β1 integrins, while α-actinin was excluded in the control simulations. The high-resolution crystal structure of $\alpha_{IIb}\beta_3$ integrin is available in the PDB bank (PDB ID: 2KNC) but the α5β1 integrin crystal structure is not available, thus the $\alpha_{IIb}\beta_3$ was submitted to the PHYRE2 server as the template for homology modeling. The output model was quite reliable with the confidence level of 99.9% reported by PHYRE2. In the initial configuration of all binding simulations, the integrin binding site on talin and α-actinin were positioned at equal distances from the integrin cytoplasmic tail allowing a few water layers being formed between the molecules such that no interaction was assumed or formed in the beginning of the simulations.

A triclinic box was generated in order to account for the elongated structure of α-actinin and, also to ensure that molecules do not interact with their periodic image. The box size was finally set to 41.2x18.2x15.8 nm^3. The TIP3P water model was used fo solvating the system and water molecules were deleted from the hydrophobic part of the lipid membrane (Jorgensen et al. 1983). The excessive charge of the system was neutralized using KCl ions and the overall ion concentration was set to 150 mM reproducing the physiological conditions. The final number of reached 1,918,344 and 1,918,175 for αIIbβ3 and α5β1 simulations, respectively.

The SHAKE algorithm was applied to constraint bond lengths and geometry. The temperature was maintained at 310 and the pressure was kept at 1 bar using Langevin methods. Periodic boundary condition was applied in all three directions for and simulations ran with a time-step of 2 fs. The Particle Mesh Ewald (PME) method was used to model the electrostatic interactions efficiently in periodic cells. The van der Waals (VDW) interactions were calculated using a switching parameter for smoothly truncating the VDW potential at the cutoff distance. The initial configurations of simulations cells were minimized for 100,000 steps in order to relax

the structures and remove all bad contacts. Then, minimized structures were equilibrated for 1 ns in the NPT ensemble and some variables such as energy, pressure and the root mean square deviation (RMSD) were monitored throughout the simulations. The fully equilibrated structures were then used in production runs that lasted for 60 using the NPT ensemble with the same parameters as the equilibrations simulations. The VMD software was used for all visualizations (W. Humphrey et al. 1996) and the Bio3D package in R was employed for post-processing the results (Grant et al. 2006). Normal mode analysis was done using the NOMAD-Ref server (Lindahl et al. 2006). For reviewing general principles of molecular dynamics, please see Chapter 2 of the present dissertation.

Results

Integrin activation is directly dependent upon talin binding at its cytoplasmic tail. Although, it has been shown that talin binding is both necessary and sufficient for inducing integrin activation(Tadokoro et al. 2003), other cytoplasmic proteins can also play an important regulatory role in this process. It was previously shown that α-actinin binding to β_3-integrin tail inhibited talin association impairing integrin activation. On the contrary, co-localization of both talin and α-actinin at the β_1-integrin tail suggested a cooperative role for α-actinin in activating $\alpha_5\beta_1$ integrin. However, it has not been clear how the molecular mechanism of the integrin binding was different between these two cases. We used molecular modeling with sufficient spatial and temporal resolutions and investigated the regulatory role of α-actinin on both talin-induced activation of $\alpha_{IIb}\beta_3$ and $\alpha_5\beta_1$ integrins.

In order to test our hypothesis, we designed two separate simulation setups with their corresponding control experiments: Talin and α-actinin were placed at equal distances from the **1)** β_3-integrin or **2)** β_1-integrin tail for which the transmembrane domain (TMD) of integrins were embedded in the lipid membrane. In the control simulation, the α-actinin molecule was excluded from the system. All simulations ran for 30ns and were repeated three times in order to produce statistically significant results.

The competition between talin and α-actinin at the $\alpha_{IIb}\beta_3$-integrin

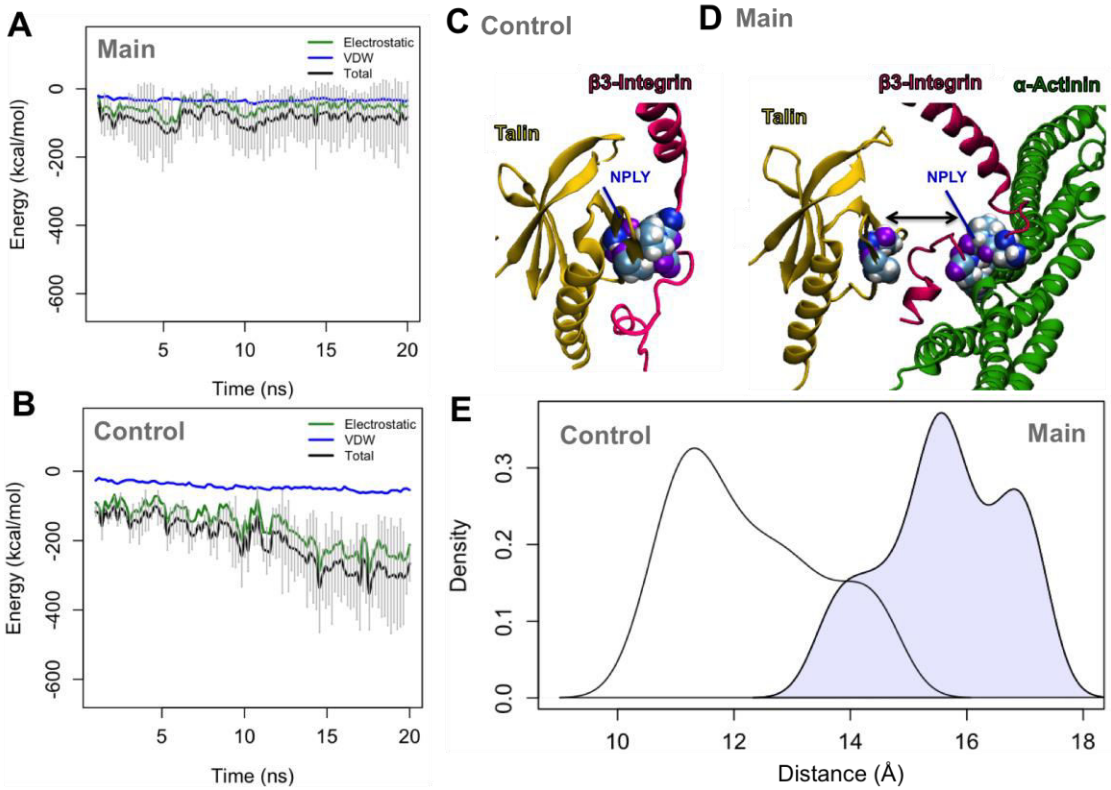

Figure 3.2-2. The molecular mechanism of the competition between α-actinin and talin in regulating $\alpha_{IIb}\beta_3$ integrin. A) The interaction energy between talin and β_3-integrin tail in the presence of α-actinin averaged over three trials was insignificant. B) This interaction energy in the absence of α-actinin in the control simulation was dropped down to -300 kcal/mol after 15 ns. C) Talin (yellow) bound to the NPLY motif of β_3-integrin (mauve) in the control simulation after 30 ns. D) α-actinin (green) pulled the NPLY motif away from talin and towards its integrin

binding site between R1 and R2. E) The density plot of the distance between the NPLY motif and talin in the control (white) simulation peaked at 11 Å, while in the main simulation (blue) the peak occurred at 16 Å.

Talin engaged with the NPLY motif on the β_3-integrin cytoplasmic tail after 15 ns of simulation in the control simulations (Figure 3.2-2A). This is in agreement with previous studies that showed the F3 subdomain in talin binds to the first NPxY motif in integrin tails (Calderwood at al. 2002; 2003). On the contrary, the presence of α-actinin resulted in significantly lower interaction of talin with the β_3-integrin (Figure 3.2-2B) as the NPLY motif was attracted to the integrin binding site between R1 and R2 repeats in the α-actinin rod domain (Figure 3.2-2C). Moreover, our results showed that α-actinin directly associated with integrin with a notably higher strength compared to talin. This suggests that α-actinin competes with talin for the same binding site on the integrin tail and most likely inhibits talin engagement.

The density plot of the average distance between talin and integrin tail illustrates the effect of α-actinin is positioning the integrin tail relative to talin (Figure 3.2-2D). The peak value of the talin-integrin distance in the control simulation was located at 11 Å, while the peak was shifted to 16 Å in the main simulation showing that the β_3-integrin tail was considerably moved away from talin in favor of α-actinin binding. This behavior was observed consistently among all three trial.

The effect of α-actinin on the binding between talin and $\alpha_5\beta_1$-integrin

The initial configuration of the simulation performed with $\alpha_5\beta_1$ was very similar to that of the simulations with $\alpha_{IIb}\beta_3$ in terms of the relative position molecules, however the effect of α-actinin on the binding between talin and β_1 turned out to be completely the opposite. The interaction between talin and β_1-integrin formed in both control and main simulations. In the first 15 ns of the main simulation, the interaction energy between talin and β_1-integrin linearly decreased, while this energy remained stable in the control simulation (Figure 3.2-3A, B). However, talin-integrin interaction was slightly weakened in the second 15 ns of the main simulations and the average energy was comparable to that in the control simulation (Figure 3.2-3A, B). This demonstrated that the α-actinin molecule had a positive impact on the initial talin binding most likely by aligning it favorably to the β_1-integrin tail. As talin formed a stable interaction with β_1, α-actinin binding remained intact. Thereby, talin and α-actinin molecules could simultaneously interact with opposite faces of the β_1-integrin tail.

The complex of talin, α-actinin and β_1-integrin showed a packed set of residues in their binding regions (Figure 3.2-3C). In order to qualitatively indicate the packing, the zero interaction zone was marked in blue. However, in the control simulation, talin and β_1-integrin loosely interacted and the space in which no interaction occurred, also referred to as the zero interaction zone, was larger (Figure 3.2-3D). It should be noted that the zero interaction zone is not necessarily an empty space but it rather represents a region with no interaction between the molecules.

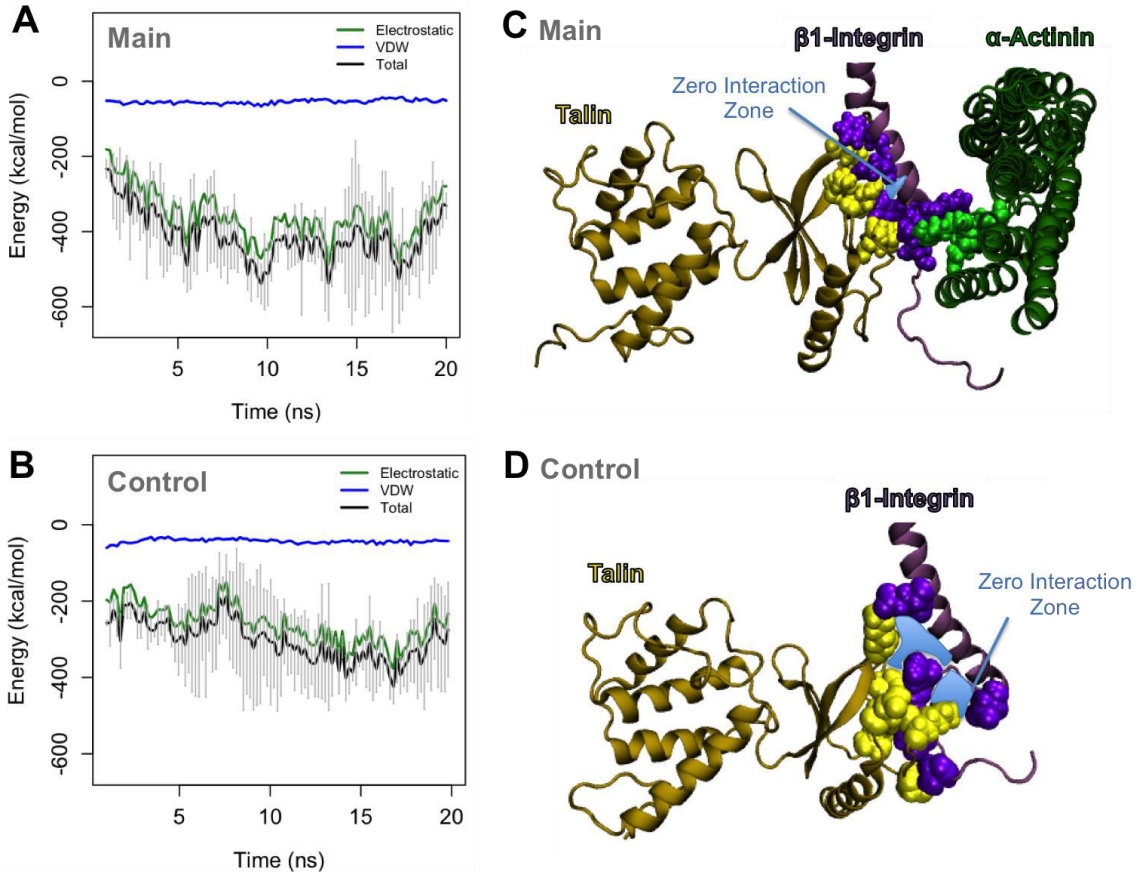

Figure 3.2-3. Cooperative role of α-actinin in talin-induced activation of the $\alpha_5\beta_1$ integrin. A) The average interaction energy of talin and β_1-integrin in the presence of α-actinin dropped below -400 kcal/mol in the first 15 ns, however, it stabilized to 400 kcal/mol throughout the following 15 ns. B) In the control simulations where α-actinin was excluded from the system, the initial drop in the integrin-talin interaction was not observed and the final energy was lowered to about -250 kcal/mol compared to the main simulations. C) α-actinin (green) and talin (khaki) simultaneously interacted with the β_1-integrin tail resulting in a very packed conformation of residues at the binding site. The zero interaction zone (blue) is defined as a space with no significant interaction between the molecules, which was reduced in the main simulation. D) In the control simulations, the zero interaction zone was much larger implying that the presence of α-actinin results in a closer packing of residues and thus a more solid interaction between the two molecules.

The effect of cytoplasmic interactions on activating integrins $\alpha_{IIb}\beta_3$ and $\alpha_5\beta_1$

The first step towards integrin activation, so called the 'pre-activated state', is the dissociation between the TMD of the integrin subunits. Therefore, the interaction energy of the subunits for both $\alpha_{IIb}\beta_3$ and $\alpha_5\beta_1$ in both main and control simulations were monitored. The presence of α-actinin along with talin at the β_3-integrin tail resulted in lower fluctuations of the interaction energy (light pink) compared to the control simulation where α-actinin was eliminated, however, the average interaction energy was not significantly changed. In case of $\alpha_5\beta_1$ integrin, the presence of α-actinin markedly decreased the strength of α_5-β_1 interaction in the main simulation compared against the control simulation. However, the level of fluctuations of the main simulation (shown by the dark cyan box plot) was reduced compared to the control simulation (light cyan), thus α-actinin stabilized the $\alpha_5\beta_1$ dimer.

In order to find the correlation between high fluctuations of interaction energy and actual physical movement of residues along integrins, we calculated the root mean square fluctuations (RMSF) of β-integrin subunit in all simulations (Figure 3.2-4). The RMSFs of the cytoplasmic domain of both β_1 and β_3-subunits were higher in the control compared to the main simulation (Figure 3.2-5A) illustrating that α-actinin binding constrained motion of that region. Also, the RMSF of the cytoplasmic region was generally higher than the TMD domain, which was surrounded by the lipid molecules in our simulation (Figure 3.2-5).

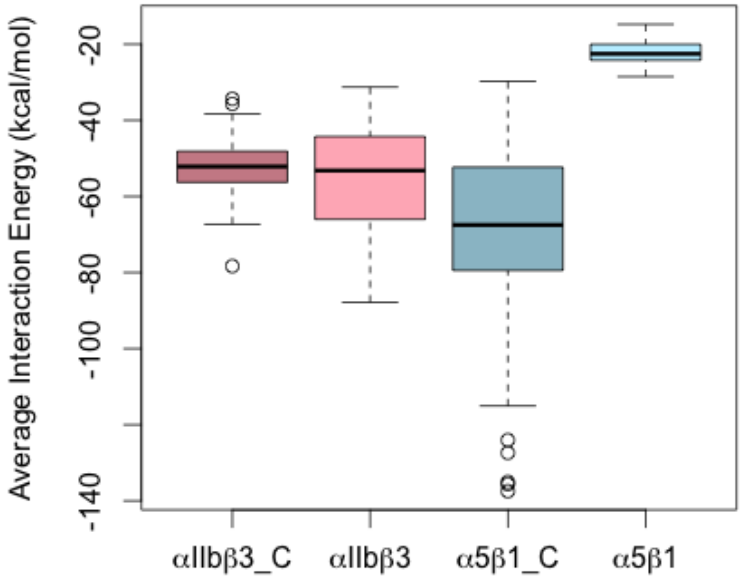

Figure 3.2-4. Average interaction energies between integrin subunits. Boxplots give information about both average (represented by the black horizantal lines in the middle of boxes) and fluctuations of the interaction energy between integrin subunits. The binding energy between the α_{IIb} and β_3 integrin subunits in the control simulation (labeled as $\alpha_{IIb}\beta_3$_C) was significantly decreased upon talin association, while this interaction was maintained in the presence of both talin and α-actinin (labeled: $\alpha_{IIb}\beta_3$). On the contrary, there was a slight increase in the average interaction energy of $\alpha_5\beta_1$ in the presence (labeled: $\alpha_5\beta_1$) and absence of α-actinin ($\alpha_5\beta_1$_C). Also, α-actinin binding limited high fluctuations of the binding energy.

Furthermore, the RMSF of β_3-TMD in the control simulation was smooth indicating a coupled motion of residues along this domain (Figure 3.2-5A). However, there was a sudden change in the RMSF of residues near A711 in the main simulation that may imply decoupling of motion around that point (Figure 3.2-5A). Unlike β_3-integrin, the RMSF of β_1-integrin was mostly jagged and the curve of the main simulation closely followed the control curve on the extracellular and transmembrane side of integrin, while the main curve appears smoother towards the cytoplasmic side (Figure 3.2-5B). Furthermore, the fluctuations of the cytoplasmic side of both integrins were reduced upon α-actinin binding (Figure 3.2-5). The different between the RMSF of β_1 and β_3 integrins suggested that signal transmission along integrin is also type-specific.

The binding between Talin and α-actinin

An interesting engagement between talin and α-actinin was observed only at the β_3-integrin cytoplasmic domain (Figure 3.2-6A). Three key interactions were responsible for the significant drop in the interaction energy of talin and α-actinin that was consistent among all trials: Two salt

bridges were formed between E464 of α-actinin and basic residues, R360 and K361 on the talin head; Also, a polar-polar interaction was observed between GLN460 of α-actinin and E375 on talin. All residues on α-actinin were located between R1 and R2, which was within the reported integrin binding site. In the simulations with $\alpha_5\beta_1$, all residues involved in α-actinin-talin interaction were all engaged with the β_1-integrin, thus talin and α-actinin were dissociated in this case (Figure 3.2-6B). To our knowledge, this binding site has not been previously reported and it may suggest a mechanism by which α-actinin reorient talin and prevents its effective interaction exclusively with β_3-subunit since it did not occur with β_1.

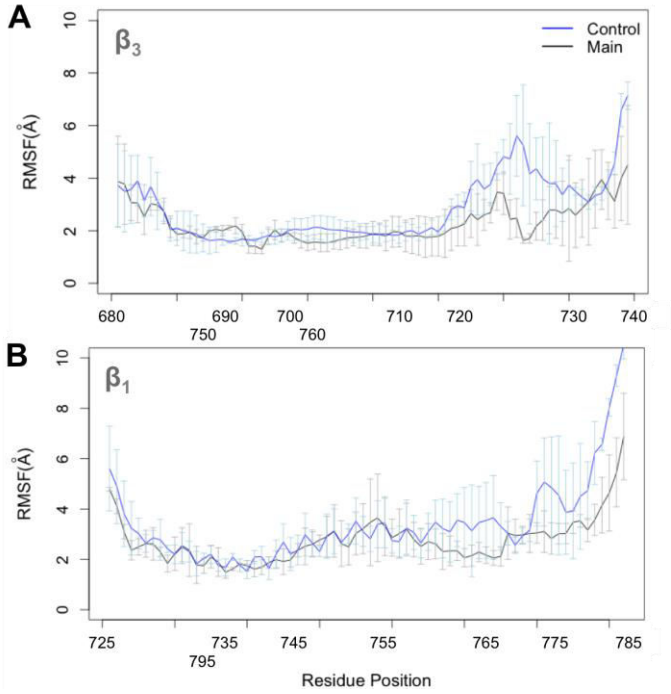

Figure 3.2-5. The RMSF fluctuations of A) β_3 versus B) β_1 integrin. The black plots show the control simulation. The difference between the two may indicate distinct signal transduction. See which residue reside in the middle of the low fluctuation region.

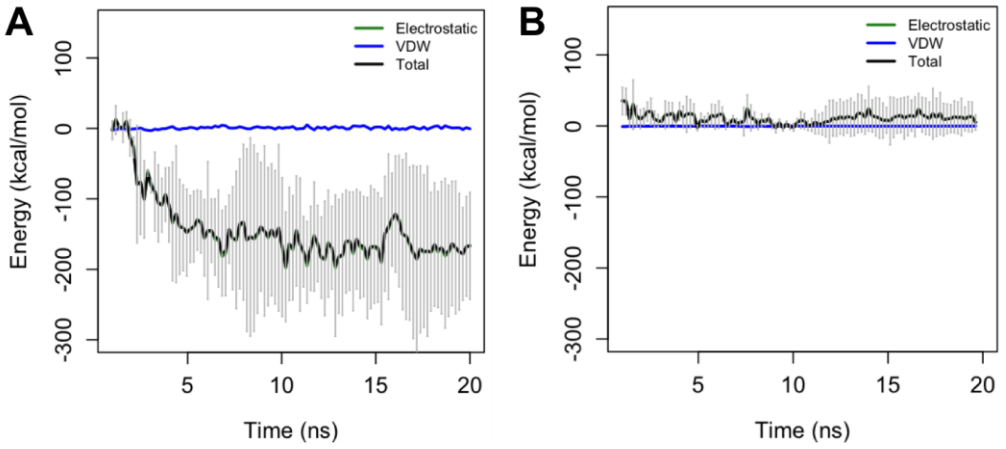

Figure 3.2-6. The binding between talin and α-actinin is most likely a regulatory mechanism in integrin activation. A) The interaction between α-actinin and talin was significantly strengthened at the β_3 integrin tail compared to that interaction at β_1-subunit (B).

Normal Mode Analysis of the integrin TMD

The continuum approximation of the TMD backbone structure of integrin is a simple mechanical beam, thus its first natural mode is expected to be simple in-plane bending. The normal mode analysis (NMA) on the integrin TMD in fact confirmed that the first non-rigid motion of this domain is bending as shown by the dashed arrows in Figure 3.2-7A. However, the motion of the N-TMD and C-TMD were decoupled as the kink was formed in the structure (Figure 3.2-7B). Furthermore, the root mean square fluctuations (RMSF) of the C-α atom of all residues along the TMD domain showed completely distinct motions for the straight versus the kinked structure. The fluctuations of residues are smoothly coupled for the straight TMD but it notably reduced at residue 711, which acts as a nodal point. Moreover, the N-TMD that is on the extracellular side of the protein moves in-phase with the C-TMD region most likely transferring energy to the extracellular domains. On the contrary, the RMSF of the bend structure is rough and showed a strong decoupling between the N-TMD and C-TMD near residue A711. Furthermore, the extracellular region is almost stationary behaving as a semi-nodal point.

Discussion

Dynamic bidirectional signaling through integrins is required for regulating cell adhesion in both physiological and pathological conditions. A physical coupling between the cytoplasm and the extracellular matrix is essential for integrin-mediated signal transmission across the lipid membrane. Cells form nascent adhesions with weak or no engagement between integrin receptors and the actin cytoskeleton. However, as forces are increased at these sites, activated integrins are clustered along the cell edge and strongly engage with cytoskeletal filaments resulting in adhesion maturation. Therefore, the first major step in adhesion formation is integrin activation that can be triggered by both inside-out and outside-in processes.

Talin associates with the cytoplasmic tail of β-integrins and increases their affinity for the extracellular ligands by inducing conformational changes in both transmembrane and extracellular domains of integrin heterodimers. Although it has been shown that talin is both necessary and sufficient for integrin activation, other proteins such as filamin, α-actinin, kindlin and FAK can associate with the integrin tail and interfere with the activation process (Calderwood et al. 2013; Tadokoro et al. 2003; Truong et al. 2015). The order in which these proteins bind to integrin and their potential interactions with talin can play an important regulatory role in activating integrins, which is still illusive.

β_1-Integrin is important in adhesion maturation and thus is not particularly active in adhesion complexes, while β_3-integrin is fully engaged with the ECM since early adhesions are formed (Lau et al. 2009; Roca-Cusachs et al. 2013; Kim et al. 2010; Kelly & Taylor 2005). α-Actinin is an interesting molecule as it plays a rather contradictory role in regulating $\alpha_{IIb}\beta_3$ versus $\alpha_5\beta_1$ integrins and thus comparing its interactions at both integrin tails may reveal fundamental molecular distinctions. Sheetz et al. showed that α-actinin competes with talin for associating with β_3-integrin, while it promotes β_1-integrin activation and thus most likely cooperates with talin in the latter case. However, it is not yet clear how cooperative versus competitive mechanisms work in the molecular scale. In this study, we investigated talin-mediated signal transmission from cytoplasmic to the TMD domains of these two types of integrins in the presence and absence of the α-actinin molecule.

Our control $\alpha_{IIb}\beta_3$ simulations consistently showed that talin bound to the NPLY motif of the β_3-integrin tail after diffusing through a couple of water layers, which was in agreement with the previous studies and confirmed the reliability of our molecular models. However, these interactions were markedly weakened upon including α-actinin in the simulations as it completely retracted talin from the β_3-integrin tail and inhibited their binding. As a result α-actinin was exclusively bound and maintaining the inhibited conformation of β_3-integrin. It should be noted that this conclusion is an extrapolation of our simulations as the $\alpha_{IIb}\beta_3$ integrin activation typically initiates within the microsecond timescale (Provasi et al. 2014).

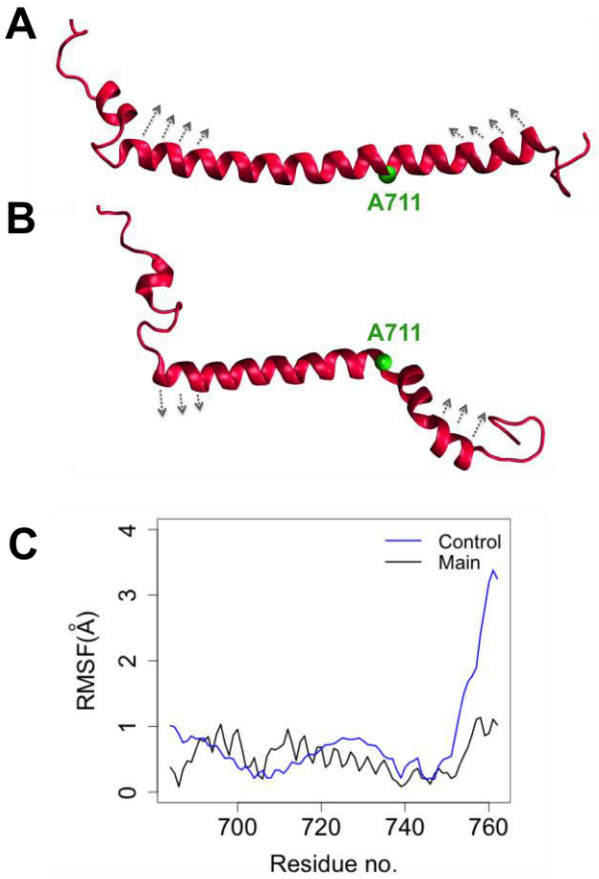

Figure 3.2-7. **The TMD conformation is changed upon α-actinin binding.** A) The final configuration of the talin-bound structure of the TMD is straight. The NMA of this structure showed an in-phase motion of the N- and C-terminal regions of the TMD. Dashed arrows show the direction of motion in the first simple bending mode of the structure. B) On the contrary, the α-actinin-bound structure [shows: a better word?] kink in the middle, which decouples the motion of the N-TMD and C-TMD. C) The RMSF calculations of the structure during NMA revealed that the β-integrin in the control simulations (the structure shown in Figure A) is different from that in the main simulations (the structure shown in B) from three aspects: 1) The motion of the cytoplasmic region of the integrin in the main simulation is restricted by α-actinin binding; 2) the residue fluctuations are smoothly translated in the control simulation, while the jagged motion of residues throughout the structure and a clear decoupling of motion happening at reside 711 was obvious. 3) the extracellular region of β_3-integrin shows almost zero fluctuations for the bent conformation of TMD, while this region shows notable fluctuations for the straight TMD conformation.

Interestingly, talin binding to β_1-integrin was notably enhanced by including α-actinin in the simulations (Figure 3.2-3) as was shown by Roca-Cusachs et al. (Roca-Cusachs et al. 2013). Specifically, our simulations predicted that α-actinin stabilizes talin's initial engagement with the

integrin tail and forms a complex with talin and β_1-integrin, which was also in agreement with the observation made by Roca-Cusachs et al. (Roca-Cusachs et al. 2013). Furthermore, the simultaneous interaction of α-actinin and talin lowers the binding energy between the $\alpha_5\beta_1$ integrin subunits showing a clear cooperative role for α-actinin. In order to understand the underlying binding mechanisms among integrin, talin and α-actinin, we explored the molecular interactions on the cytoplasmic side and their potential effects on the distal regions of the involved proteins.

Furthermore, we observed a very stable interaction between talin and α-actinin at the β_3-integrin tail, which is most probably an important factor in regulating the β_3-integrin activation as these molecules compete for the same binding site on the integrin tail. To our knowledge, this interaction has never been reported in the previous literature and could serve as a new target for future experimental studies on integrin signaling.

Moreover, our results showed a clear difference between the conformation of the β_3-integrins TMD in the presence and absence of α-actinin. In the control simulation, the β_3-integrin has a straight α-helical conformation, while a kink was formed in the simulations with α-actinin. Previous literature showed that the continuity of the integrin TMD is key to integrin activation (Ye, Snider, et al. 2014). The β_3-integrin makes a 25° angle with the α_{IIb}-subunit, thus integrin monomers cross each other inside the lipid membrane. The location of the kink observed in our simulations is near the crossing point of integrin subunits and occurred at the position of residue A711 on β_3-integrin. Interestingly, it was shown that the A711P mutation results in a flexible kink that breaks the continuity of β_3-TMD decoupling the tilting motion of the integrin heterodimer and thus blocking integrin activation. Therefore, our results suggest that α-actinin interactions can induce changes in the β_3-TMD conformation similar to the A711P mutation that would inhibit integrin activation and signaling.

The question is how does α-actinin-induced conformational changes of the TMD domain prevent $\alpha_{IIb}\beta_3$ signaling? Normal mode analysis on both bent and straight conformations of β_3-integrin showed that the mechanical modes of the TMD domain are significantly altered upon α-actinin binding. Specifically, the first simple bending mode of the straight β_3-TMD domain was disrupted at the A711 such that the N-TMD and C-TMD motions went out-of-phase. Furthermore, it was shown that talin binding increases the tilting angle of β_3-integrin in the lipid membrane disrupting the inner membrane clasp. However, the kink at A711 maintains the inner membrane clasp.

The root mean square fluctuations (RMSF) of residues in the first bending mode showed that energy is transferred between the N-TMD and C-TMD similar to a cosine wave such that the last residue residing on the extracellular side of TMD experienced the highest motion. This change resulted in near-nodal behavior of the N-TMD most likely decoupling the motions of TMD from the extracellular domain of β_3. On the contrary, the kinked structure experiences a near-node vibration and most of the energy instead of being smoothly transferred across the TMD domain would rather be dispersed via local fluctuations of TMD residues. Lastly, increased local motions of the β_3-TMD atoms of the bent conformation suggest an inefficient transfer of mechanical energy across the membrane after α-actinin association.

Previous studies have discussed the effect of other cytoplasmic interactions at the integrin tail. For instance, it has been observed that filamin binding at the β-integrin tail competes with talin for the same binding site and leads to impaired integrin activation. On the contrary, kindlin binding promotes adhesion formations and results in adhesion strengthening. Major approaches for examining the effect of these proteins are mostly limited to fluorescence imaging and knock-

out experiments, which can only provide macroscopic information about their significance in integrin activation.

In conclusion, our results showed that α-actinin binding induces integrin-specific conformational changes in the TMD domain, which can significantly modify mechanical signal transmission across integrin molecules (Figure 3.2-8). Furthermore, we proposed a mechanism for regulating integrin activation through conformational changes of the TMD domain via cytoplasmic interactions. These molecular models provide valuable insights into the mechanisms by which cytoplasmic proteins regulate mechanical signal transmission across integrins that in turn cause macroscopic changes in cell adhesion and spreading.

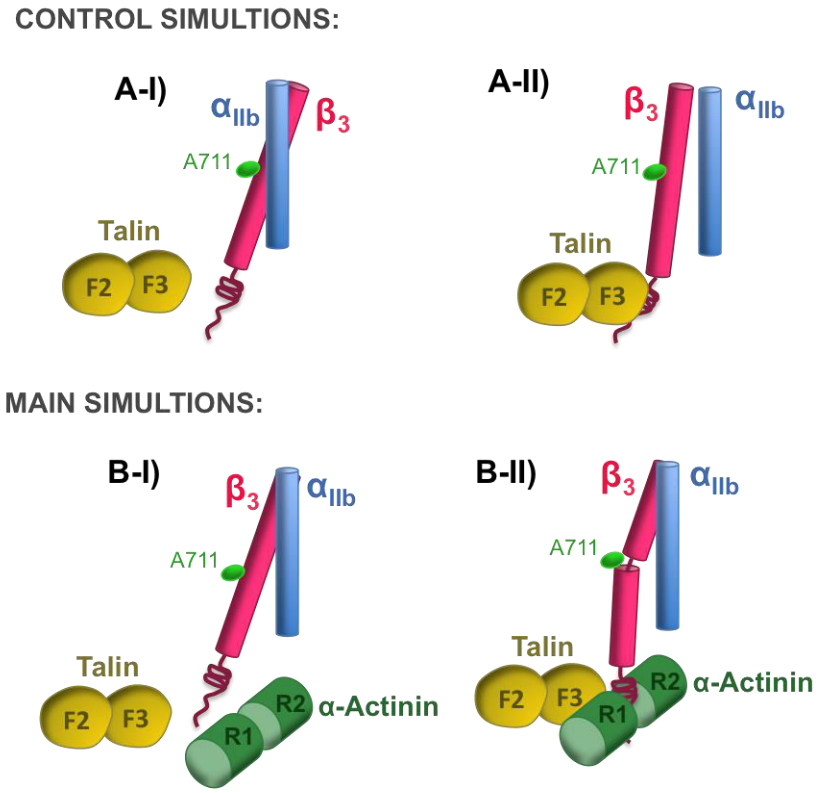

Figure 3.2-8. Cytoplasmic interactions regulate integrin-mediated signal transmission via changing the TMD conformation. A-I) In the inactive conformation of integrin, the TMD domains of integrin subunits directly interact. A-II) As talin associates with the cytoplasmic tail of β_3-integrin, it breaks the interaction between integrin subunits changing the relative positions of α_{IIb} and β_3 integrin subunits but it does not alternate the TMD conformation. In our control simulation, the F3 domain of talin was placed near the integrin β_3 tail forming a notable interaction in 30 ns of simulation. B-I) In the main simulations, the whole structure α-actinin was included in the system (full-length is not shown for clarity). α-Actinin engaged with integrin tail preventing talin binding and resulted in a kink in the TMD of β_3-subunit. It also formed a direct interaction with talin. The whole α -actinin is not shown for clarity but was present in our simulations.

Section 3.3 α-Actinin's interaction with PIP2 increases its association with the lipid membrane

Actin cross-linkers play a critical role in regulating cytoskeletal dynamic arrangements in order to control cell shape and motility (Hotulainen & Lappalainen 2006; Ridley et al. 2003). Stress fibers consist of actin bundles cross-linked via α-actinin molecules (Shams et al. 2016) and are connected to the extracellular matrix (ECM) through focal adhesion (FA) complexes. α-Actinin is also able to form a direct link between actin and integrin receptors. Therefore, regulation of α-actinin's function is vital for cellular response to mechanical cues. α-Actinin is an anti-parallel dimer having a rod-shape structure. Each monomer has one actin-binding domain at N-terminus, followed by four spectrin repeats (R1-R4) and a camodulin homology domain (CaM). The integrin binding site of α-actinin is located between R1 and R2 spectrin repeats (Otey et al. 1993). The rod domain of α-actinin has a coiled-coil conformation, which is stabilized by strong electrostatic interaction between the two monomers being in an anti-parallel arrangement of monomers. Several mechanisms exist for regulating α-actinin in FA one of which is through PIP2 binding (Figure 3.3-1)

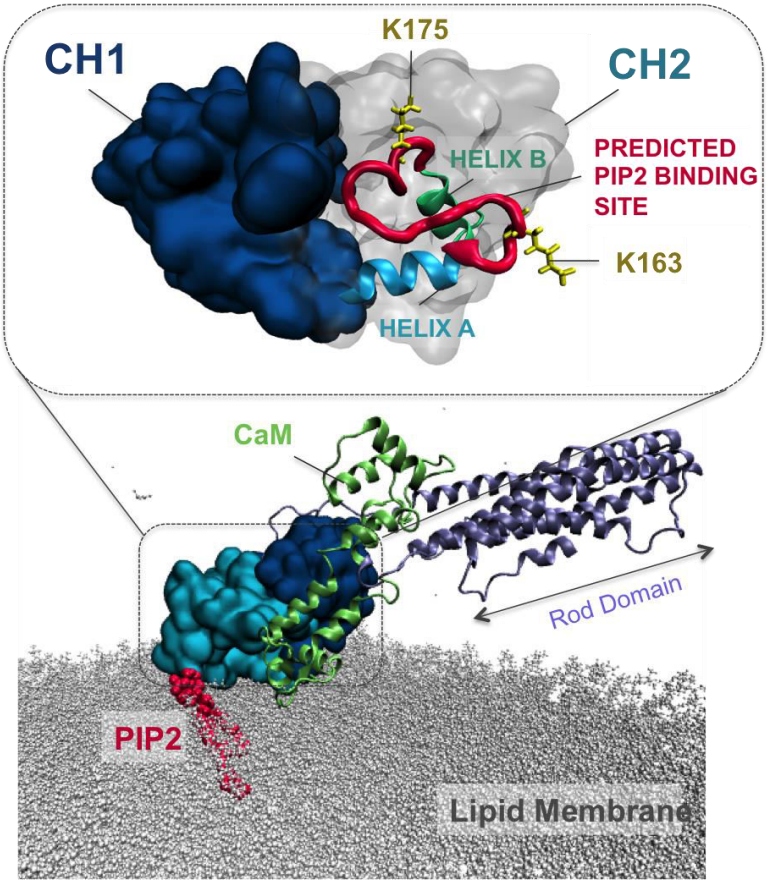

Figure 3.3-1. **The PIP2 binding site on α-actinin molecule was placed close to PIP2 embedded in the lipid membrane.** The α-actinin molecule was positioned near PIP2 (red) embedded in the lipid membrane (gray). Only CH1 (dark blue), CH2 (cyan) CaM (lime) and one fourth of the α-actinin rod domain (ice blue) were included in the simulation cell. The predicted PIP2 binding site is mapped between helices A (blue) and B (green) of the CH2 domain (red). A couple of positively charged residues namely K163 and K175 (yellow) are potentially important sites for PIP2 binding.

Phosphatidylinositol 4,5-bisphosphate (PIP2) is a phospholipid involved in regulating several transmembrane and signaling proteins (Sakisaka et al. 1997). Specifically, PIP2 is essential for focal adhesion turnover through direct interaction with many important adhesion proteins such an vinculin, talin and α-actinin (Fukami et al. 1994; Sakisaka et al. 1997). The actin-binding domain of α-actinin can take either a closed or an open conformation (Galkin et al. 2010). In the closed conformation, two CH domains are in contact and thus part of the actin-binding site is inhibited, while in the open conformation CH domains are separated and actin-binding sites are more exposed (Shams et al. 2016). The PIP2 binding site is within the CH2 domain right after the third actin-binding site. However, the mechanism of this regulation is still elusive. The objective of the present study is to shed light on the molecular mechanism of PIP2 interaction with α-actinin.

Materials and Methods

The full-length model of α-actinin (PDB ID: 1SJJ) was truncated at ¼ of its rod domain such that the final structure included the CH domains in the closed conformation connected to the R1 spectrin repeat of one monomer along with the CaM domain and R4 of the other monomer (Liu et al. 2004). The predicted PIP2 binding site between helices A and B of the CH2 domain contained two positively charged residues, namely K163 and K175. Given the higher likelihood of interactions of PIP2 with these lysine residues, we examined both their individual and combined interactions with the PIP2 molecules. Specifically, we constructed three sets of simulations as follows: 1) Residue K163 positioned next to a single PIP2 molecule embedded in the lipid membrane; 2) Residue K175 oriented towards a single PIP2 in the membrane; and 3) Two PIP2 molecules each positioned next to one of the lysine. In all simulations, the initial distance between PIP2 and its binding residue was about 10Å. Although no constraints were applied to the rod domain of α-actinin, it neither folded nor the position changed throughout the simulations. Both structure of PIP2 and its associated parameters adapted in the CHARMM27 force field were obtained from Professors Ramone Latorre and Daniel Aguayo from the Center for Bioinformatics & Molecular Simulation at Talca University in Chile.

The lipid membrane was modeled using the Membrane Builder plugin in the Visual Molecular Dynamics (VMD) Package (Humphrey et al. 1996). The systems dimensions were specified as 2.2x2.2x1.3 nm^3 and the total number of atoms reached around 600,000. The system was solvated using the TIP3P explicit water model. The extra charge of the system was neutralized via adding counter ions and the final ion concentration of the system was set to 15mM of KCl mimicking physiological conditions in the cytoplasm.

All simulations were performed using NAMD molecular dynamics programs and CHARMM27 force field (Phillips et al. 2005; MacKerell et al. 2001). Periodic boundary conditions were applied in all three directions. Temperature and pressure were maintained at physiological values of 310 K and 1 atm, respectively (Nosé 1984). The time-step of 2 fs was used. All structures were minimized for 50,000 steps and then further equilibrated for 1ns prior to the production runs, which was then performed for 20ns. Three trials were performed for each simulation in order to obtain statistically reliable results. Postprocessing the simulations was done using both VMD and the Bio3D package in R (Grant et al. 2006). For reviewing general principles of molecular dynamics, please see Chapter 2 of the present dissertation.

Results

The PIP2 molecule plays an important regulatory role in adhesion sites. Many focal adhesion proteins have a PIP2 binding site, which either anchors them to the lipid membrane or induce conformational changes that in turn regulates their binding with another partner. The negatively charged phosphate group can form strong electrostatic interactions with positive charges on the protein surface and thus PIP2 binding site is usually an exposed region of the protein. α-Actinin binds PIP2 through a loop region between helices A and B of the CH2 domain (red region in Figure 3.3-1). Two positively charged residues, namely K163 and K175, exist in this region that were independently examined for PIP2 binding. Furthermore, we tested their simultaneous interaction with two PIP2 molecules in order to understand their ability collective effect of multiple PIP2s on anchoring α-actinin to the lipid membrane. In order to avoid confusion, each set of simulations was given a name that is shown in parentheses front of the subtitle.

The interaction between K163 and PIP2 (K163 simulations)

The CH2 domain of α-actinin was positioned near the lipid membrane such that the residue K163 of CH2 was facing the PIP2 molecule in the initial configuration of the system. This orientation was also the optimal way of exposing the PIP2 predicted binding site on α-actinin to PIP2 without causing any steric clash between the protein and the lipid membrane. A strong electrostatic bond was made between K163 and PIP2, which remained stable for the first 10ns of the simulations (Figure 3.3-2A). However, K163 got partially dissociated as R846 of the CaM domain got weakly engaged with PIP2 (Figure 3.3-2A-B). Although the interaction energy of R846 with PIP2 was not significant (Figure 3.3-2B), it was sufficient for destabilizing K163-PIP2 interaction indicated by the large error bars as it was competing for the negative charge of the phosphate group. The total interaction energy showed that K163 and R846 were the only main interactions of PIP2 with α-actinin (Figure 3.3-2C).

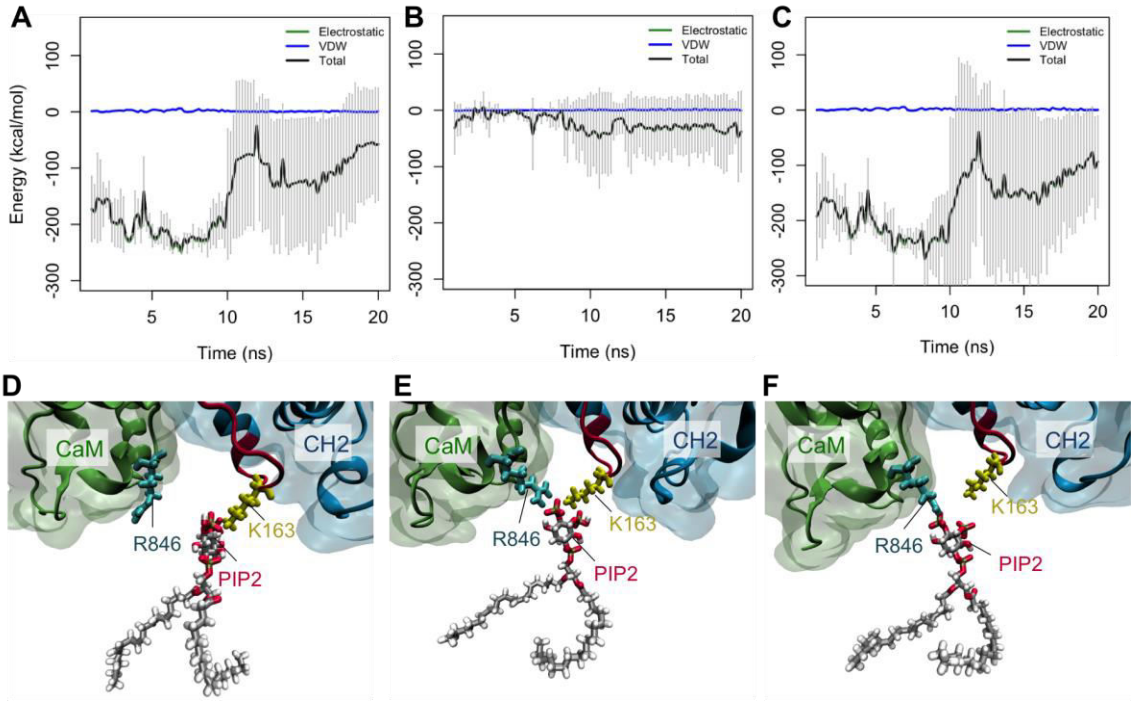

Figure 3.3-2. **K163 within the predicted PIP2 binding region was placed near the PIP2 molecule.** A) The interaction energy between K163 and PIP2 was purely electrostatic and became unstable in the second half of the simulation. B) A slight interaction was formed between PIP2 and R846 of the CaM domain. C) The total interaction energy shows that only K163 and R846 were involved in PIP2 binding. D) In approximately the first half of all simulations PIP2 was only engaged with K163, while after around 8 ns, R846 also interacted with PIP2 (E). F) Towards the end of the simulation, K163 interaction was destabilized. Lipids are not shown for clarity.

Three main configurations were observed for PIP2 interacting with CH2 as the competition between R846 and K163 for PIP2 was established (Figure 3.3-2D-F). The PIP2 molecule was either engaged with K163 or R846 but also found to be associated with both of these residues in some instances. PIP2, which caused partial dissociation of the PIP2 negative charges from the polar heads of lipid molecules in order to maximize its contact with α-actinin (Figure 3.3-5A).

The interaction between K175 and PIP2 (K175 simulations)

Residue K175 was another candidate for PIP2 binding tested in our simulations. It should be noted that the position of this lysine was closer to the structural region of CH2 compared to K163 but since the α-actinin molecule could not be rotated relative to its position in the K163 simulations due to the steric clash of some residues, it was just translated to place K175 close to PIP2. Unlike the K163 simulations where PIP2 was only engaged with K163 in the beginning, PIP2 interacted with a couple of other positively charged residues, namely R198 and R199 that were within the loop region between the third and fourth helices of CH2 (Figure 3.3-3A-B). The locations of these residues were structurally close to K175 and thus competed with it for PIP2 binding. Thereby, the stability of K175-PIP2 interaction was decreased upon strengthening the R198/199 binding with PIP2. The total energy of the system in this set of simulations was clearly higher than that in the K163 simulations (Figure 3.3-3C).

Two of the most commonly observed configurations of the system in the K175 simulations were PIP2 bound to either just R198/R199 or to both K175 and R198/199 (Figure 3.3-3D-E). The higher concentration of positive charges at R198/R199 pulled PIP2 away from K175 and was engaged with most of the simulation time. The PIP2-lipid interaction was more stable compared that in the K163 simulations (Figure 3.3-5B). This most likely indicated a lower net normal force on PIP2 compared to the K163 simulations due to the close positioning of residue K175 and R198/R199 to the membrane.

The interaction of two PIP2s with both K163 and K175 simultaneously (Two PIP2 simulations)

We examined simultaneous interaction of a couple of PIP2 molecules with both K163 and K175 in order to investigate any collective or allosteric effects of PIP2 binding to α-actinin. The total interaction energy of K163 and K175 with both PIP2 molecules were unstable and diminished towards the end of the simulations (Figure 3.3-4A). Since R198/R199 were spatially approximate to K175, they formed strong interactions with K175-bound PIP2 from the very beginning of the simulations and became even more stable as the bond between K175 and PIP2 was weakened (Figure 3.3-4B). R198/R199 contributed to most of the overall interaction energy between α-actinin and PIP2 holding strongly to one of the PIP2 molecules (Figure 3.3-4C).

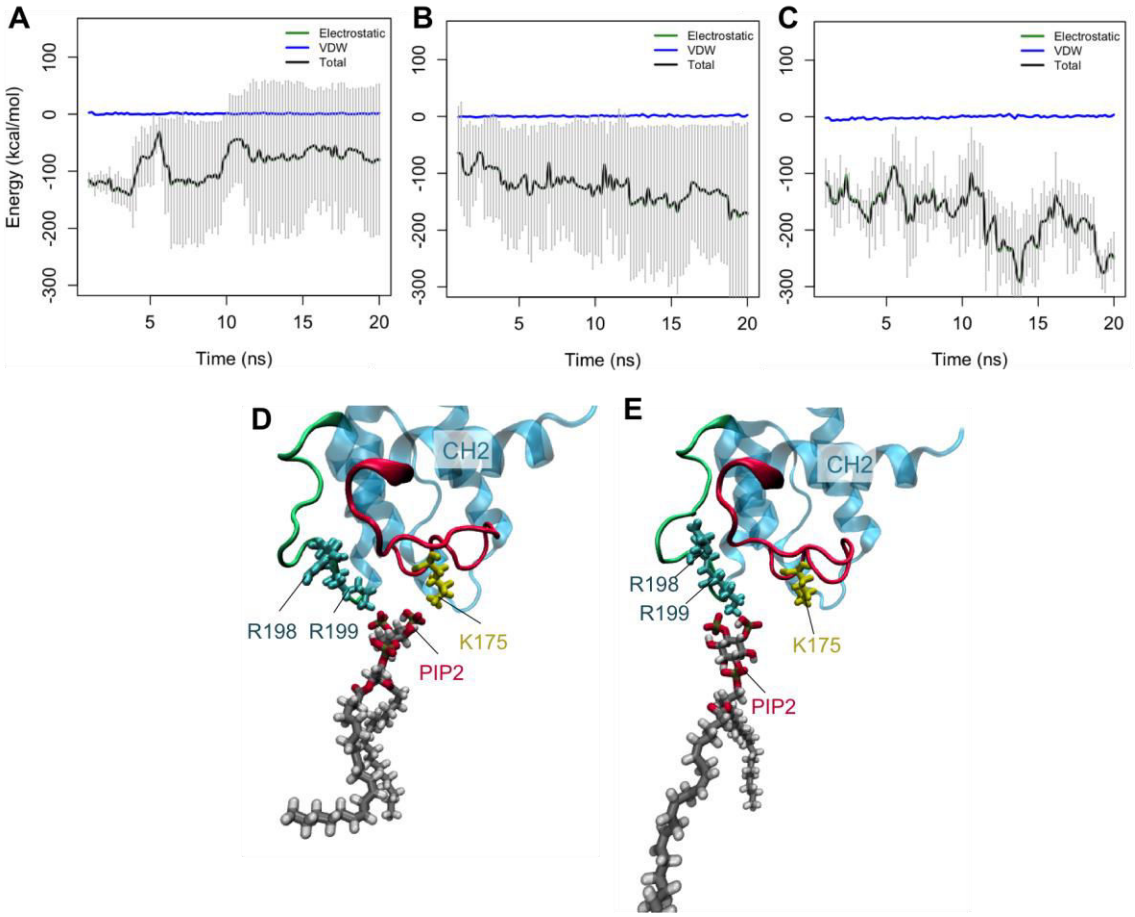

Figure 3.3-3. K175 within the predicted PIP2 binding region was positioned approximate to the PIP2 molecule. A) The interaction between K175 and PIP2 also became more unstable after 10 ns. The overall strength of K175 interaction with PIP2 was lower than K163 (Figure 3.3-1A). B) Residues R198 and R199 located in the loop region next to the PIP2 predicted binding site were involved in binding since the beginning of the simulations. C) The total interaction energy between PIP2 and α-actinin was stable throughout these sets of simulations. Lipids are not shown for clarity.

The initial orientation of the α-actinin molecule was kept similar to the single PIP2 binding simulations while two PIP2 molecules were placed close to their corresponding binding residues within the lipid membrane (Figure 3.3-4D). R198/R199 rapidly got involved in competing with K175, while K163 was still bound to PIP2 without any interference from the CaM domain (Figure 3.3-4E). Finally, K163 dissociated from PIP2 allowing it to float away in the lipid membrane whereas R198/R199 were strongly engaged with one of the PIP2 molecules (Figure 3.3-4F). The interaction between PIP2 and the lipid membrane was similar to that in the K175 simulations.

The intramolecular interactions of α-actinin

It has been proposed that the interaction between CaM and neck is important for actin binding and PIP2 regulates this interaction. In addition to the previously mentioned simulations, we also ran a control simulation where PIP2 was removed from the lipid membrane for the comparison purposes. The CaM and neck interaction was clearly unstable and weaker in the presence of PIP2 in all K163 (Figure 3.3-6A), K175 (Figure 3.3-6B) and two PIP2 (Figure 3.3-

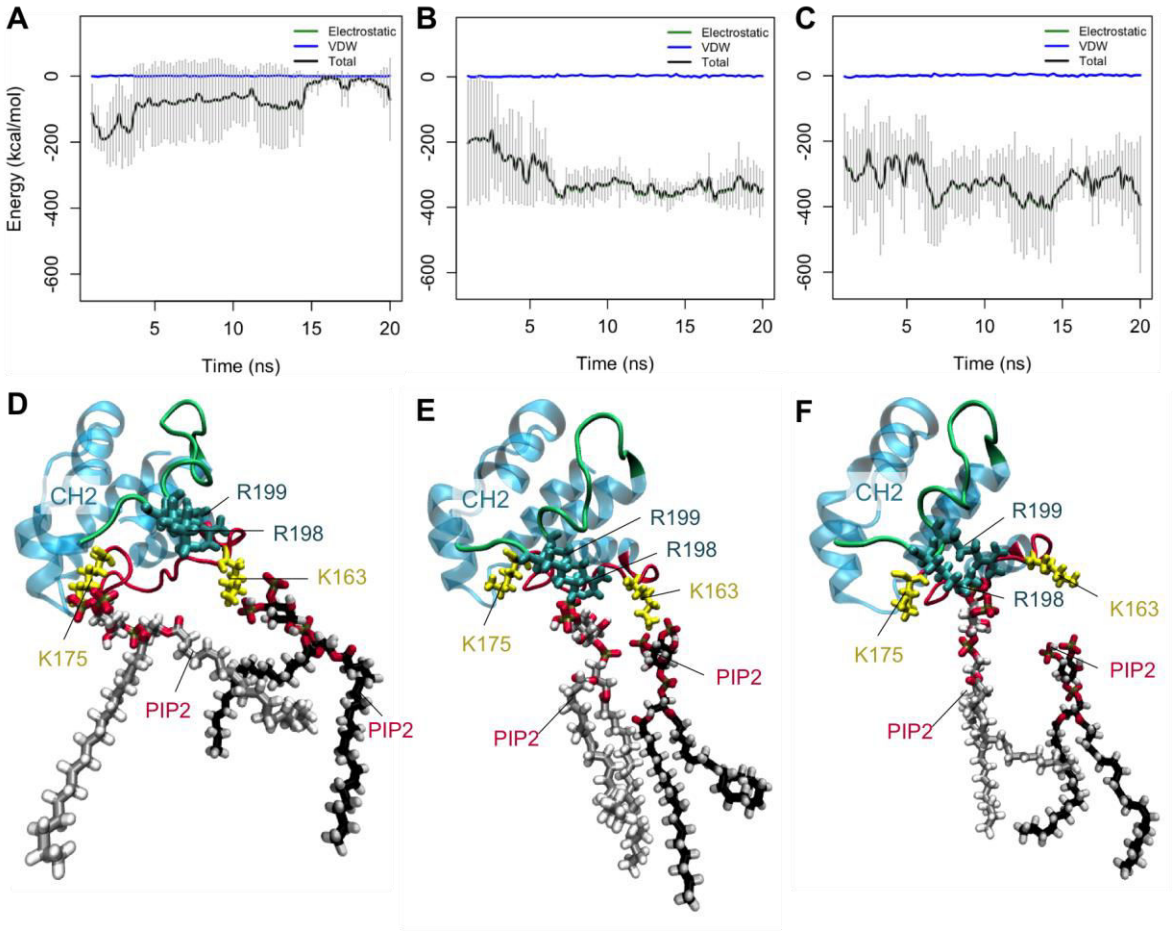

Figure 3.3-4. **Two PIP2 molecules were put next to K175 and K163 residues of the CH2 domain.** A) The interaction of PIP2s with K163 and K175 were weak and unstable throughout these simulations. The backbone of the PIP2 molecules are shown in different colors for clarity. B) Residues R198 and R199 interactions became stronger with the PIP2 molecule engaged with K175 later in the simulations. C) The total interaction energy between α-actinin and PIP2 was stable mainly due to R198 and R199. D) PIP2 molecules were initially engaged with K175 and K163 in the predicted PIP2 binding site, E) but later the PIP2 molecule interacting with K175 moved towards and associated with R198 and R199, while the second PIP2 held onto K163 for a longer time. F) Finally, the second PIP2 also let go of K163 towards the end of simulations. Lipids are not shown for clarity.

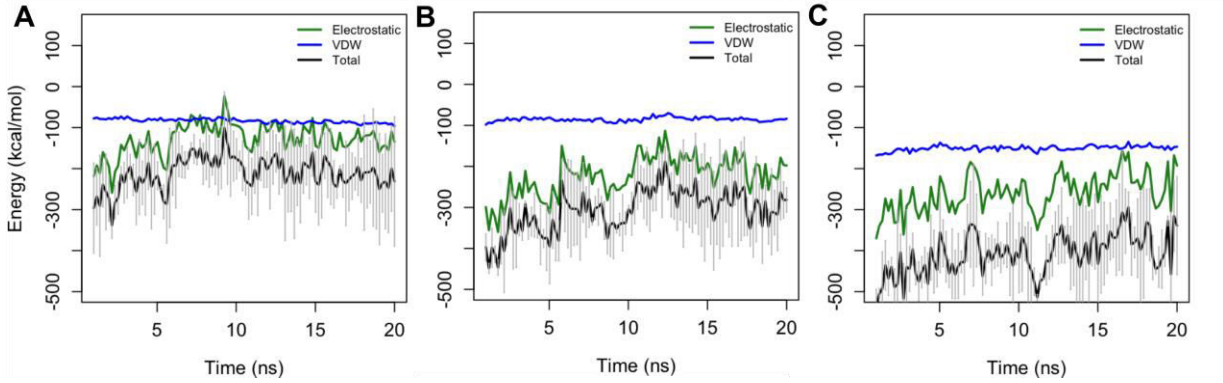

Figure 3.3-5. The interaction between PIP2 and the lipid membrane. A) In the K163 simulations, the electrostatic association of PIP2 with the lipid membrane was broken, while in both B) K175 C) and two PIP2 simulations it was partially maintained.

6C) simulations compared against the control (Figure 3.3-6D). However, this interaction seemed to be more fragile in the K163 simulation and was disrupted for the most part (Figure 3.3-6A). Large error bars in the K175 and K163/K175 simulations indicated that CaM-neck interactionwas not favorable, while their interaction energy reached -200kcal/mol and remained stable for 10 ns in the control simulation (Figure 3.3-6B-C). It should be noted that this interaction was mainly electrostatic.

Looking into the detailed mechanism of regulating the CaM-neck interaction, we observed that a salt bridge was mainly responsible for holding CaM and neck together in the control simulation. This salt bridge was formed farther away from the lipid membrane and between K265 of the neck region and E770 of the CaM domain. This key interaction was weakened or disrupted in the PIP2 simulations since PIP2 binding slightly moved both ABD and CaM domain not allowing these oppositely charged residues to orient correctly for the formation of the salt bridge. One potentially important factor for altering the E770 orientation was the distance of R846 with the lipid membrane. Both R846 and K163 moved towards the lipid membrane via interacting with the PIP2 molecule. As was mentioned, this interaction was disrupted due to the presence of PIP2 that got engaged with both K163 and R846 in the K163 simulations.

Furthermore, the interaction between CaM and ABD was not significantly changed upon PIP2 binding. Although this interaction in the K163 simulations showed a smooth and approximately linear decrease, it did not go beyond that in the control simulations. We also examined CH1 and CH2 interactions with the CaM domain separately but did not observe any specific change upon PIP2 binding suggesting. The main actin-binding site is on CH1 and thus the interaction between CH1 and CH2 partially inhibits actin association. Although our simulations showed that PIP2 did not change the CH1-CH2 interface in 20 ns, it did not necessarily imply that PIP2 would not change this interaction in longer time scales (Figure 3.3-7). Moreover, the angle between PIP2 and CH2 was the most stable in the two PIP2 simulations. This observation, along with the interaction energies, indicated that multiple PIP2 resulted in enhanced binding with the protein compared to a single PIP2. However, the overall angle of the protein with lipids was remained intact. The CH1-CH2 angle plot had the largest error bars in the two PIP2 simulations suggesting that interface might alternate. Lastly the angle between CaM and ABD remained approximately the same.

Protein and lipids

One of the important hypotheses is that PIP2 anchors proteins to the lipid membrane allowing them to locate other binding partners and also modulate them for a certain function. Therefore, it is critical to understand how PIP2 changes protein-lipid interaction. Our results showed that protein-lipid interaction without including the PIP2 molecule's contribution was slightly decreased (Figure 3.3-8A-C), however, the overall interaction energy with PIP2 included as part of the membrane was increased. Specifically, two PIP2 simulations showed a more stable interaction between protein and lipids (Figure 3.3-8C), while this interaction was decreased in both K163 and K175 simulations. In the control simulations, the interaction energy stabilized after 8 ns (Figure 3.3-8D).

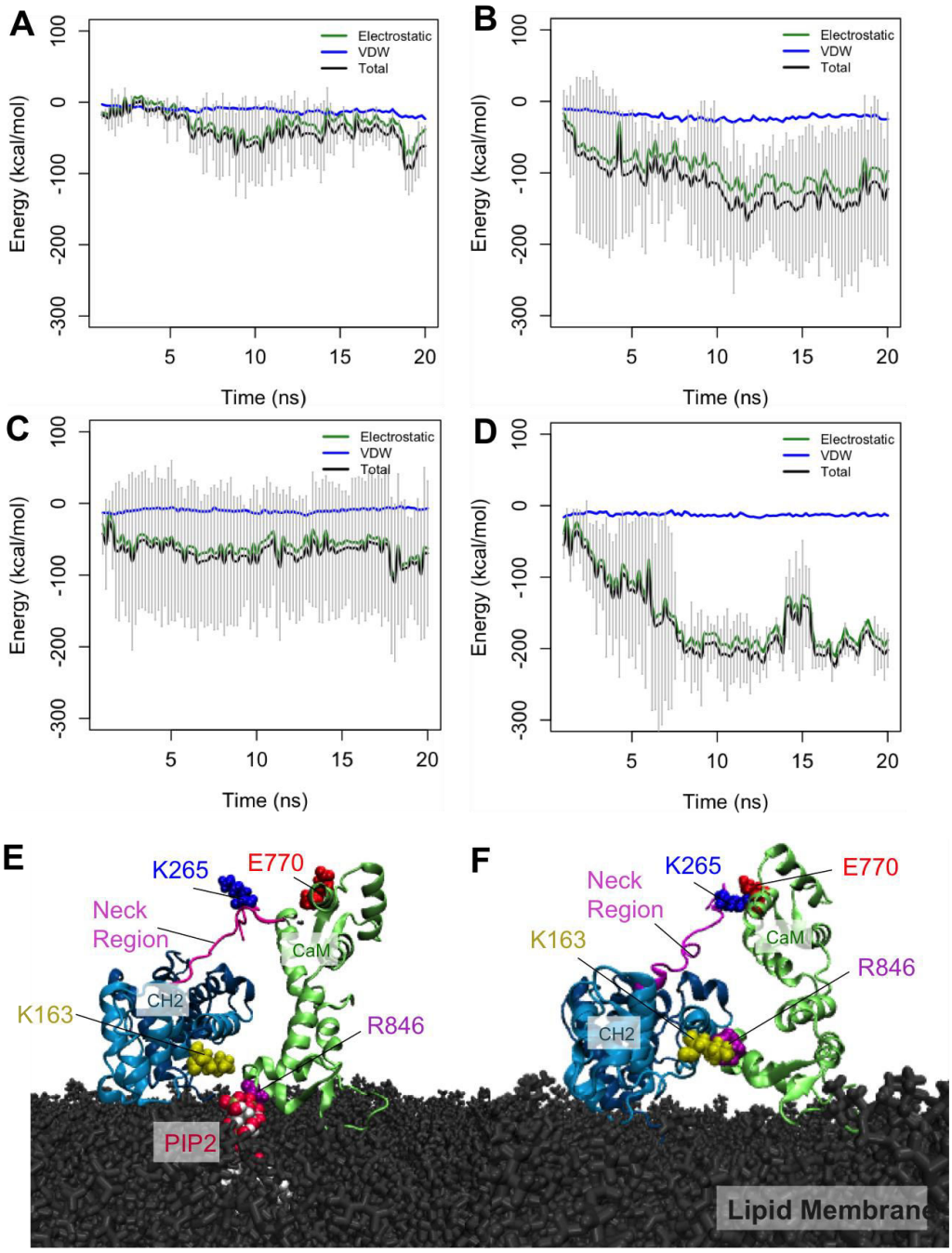

Figure 3.3-6. The interactions between the CaM domain and the neck region connecting CH2 and R1 domains. A) This interaction was the weakest in the K163 simulation compared to B) K175 and C) K163-K175 simulations. D) The strongest interaction between the CaM and neck region occurred in the control simulation. E) Comparing the structure of CaM and neck in the K163 simulation to the control runs showed that PIP2 binding to R846 displaced the CaM domain relative to the neck region disrupting a salt bridge between E770 of the CaM domain and K265 of the neck region lowering their interaction to a great extent. F) This salt bridge was maintained in the control simulations.

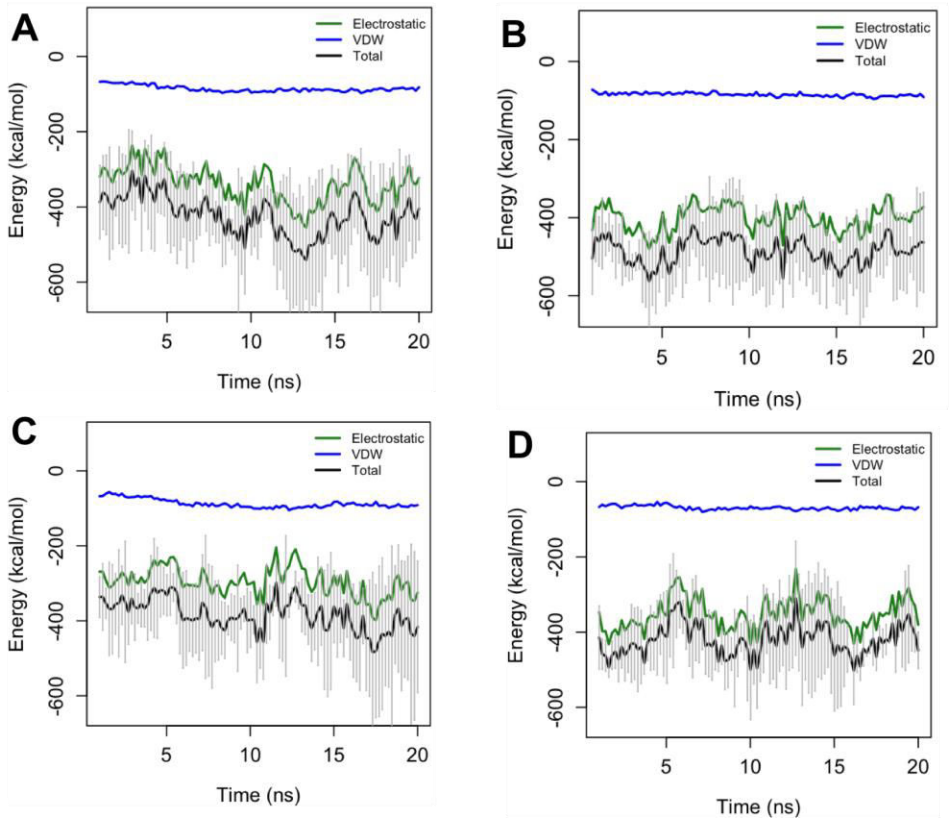

Figure 3.3-7. The average interaction energy between CH1 and CH2. The energy is shown in A) K163, B) K175, C) K163-K175 and D) control simulations.

Furthermore, the distribution of lipids directly interacting with the protein was quite different in the presence and absence of PIP2. The black molecule shown in Figure 3.3-8 is PIP2 and a more continuous distribution of lipids interacting with the lipid membrane was observed in the presence of PIP2 whereas in the absence of PIP2, lipids interacted with the protein in two separate groups each associated with either the CaM or ABD domain. These distinct lipid configurations most likely have different entropic favorability and thus the presence of PIP2 can change the free energy of binding to lipids.

Discussion

Cells sense and respond to mechanical stimuli from the extracellular matrix (ECM) and blood flow. Focal adhesions (FA) are formed at points of contact with the substrate allowing cells to dynamically interact with their environment (Geiger et al. 2009). FAs are composed of several signaling molecules and are regulated via both mechanical and chemical factors. Early focal contacts are weak but they become more mature as actomyosin forces act upon them. FA proteins connect the actin cytoskeleton to the integrin receptors in the cell membrane and are responsible for transferring actomyosin forces to the ECM. Only a few molecules are able to directly connect integrins to the actin cytoskeleton including filamin, α-actinin and talin.

The primary function of α-actinin is to cross-link actin filaments but it also plays a major role in integrin-mediated signal transduction. There are several mechanisms known for regulating α-actinin's function, which may involve both chemical and mechanical factors. For instance, it is well established that α-actinin binds to PIP2 both in muscle and non-muscle cells,

which was proposed to regulate its actin binding activity (Otey & Carpen 2004), but the mechanism of such binding is still elusive.

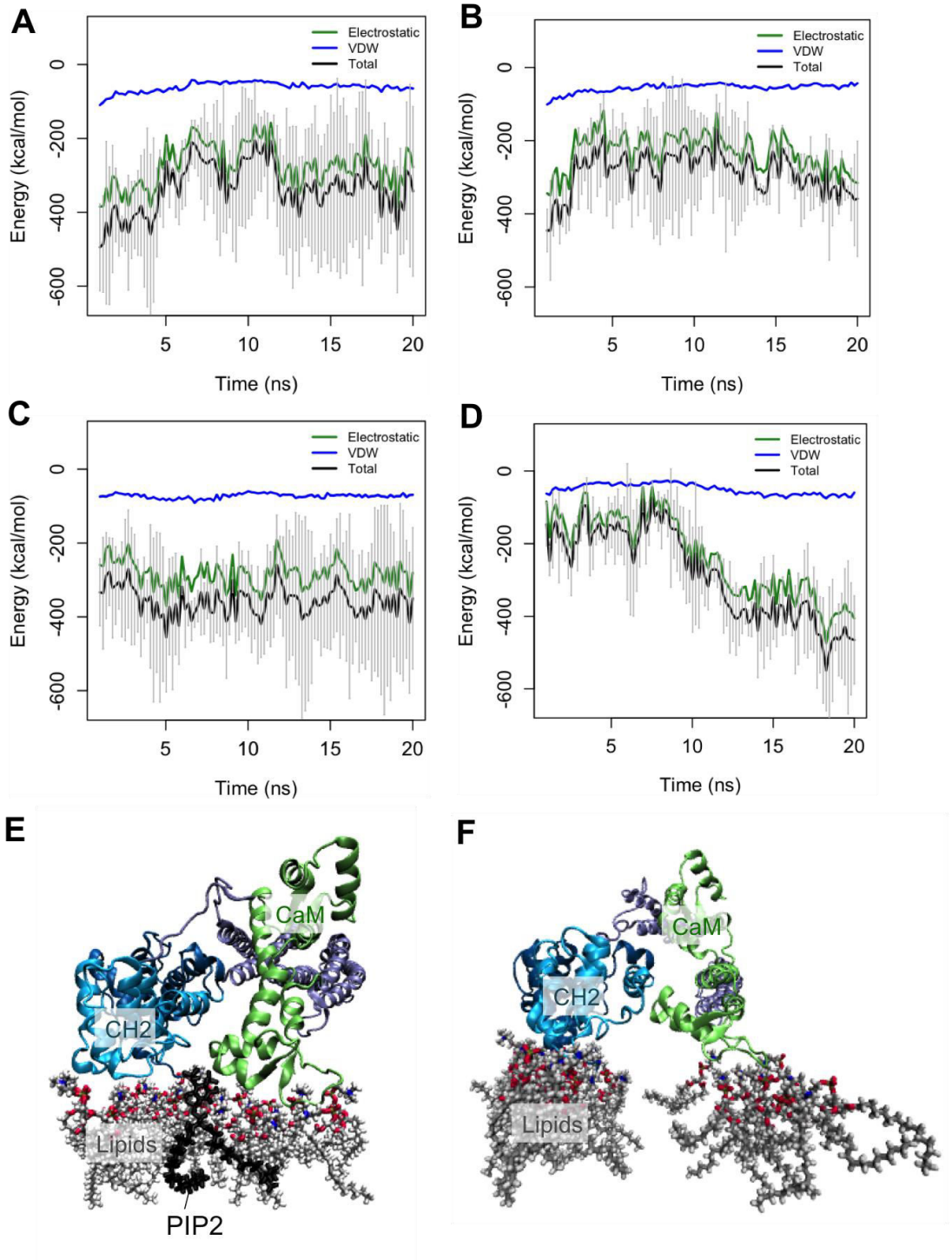

Figure 3.3-8. The lipid interaction with protein is affected by PIP2. The interaction energy between lipids and α-actinin was higher early in A) K163, B) K175 and K163-K175 compared to D) the control simulations. However, the average interaction energy dropped after 8ns in the control simulation. It should be noted that the overall engagement with the lipid membrane is the combination of PIP2 and lipid interaction, thereby, the energy reported in this figure is just a partial engagement with the membrane for parts A-C.

Our simulations showed that PIP2 binding positioned the CaM domain closer to the membrane through interacting with R846. This interaction also reduced the strength of K163 binding, which was the main point of contact in the first half of the simulations even though the binding with the CaM domain was relatively weak. This most likely suggests that the CaM domain is not a primary binding site for PIP2 but rather it regulates its interaction with CH2 in a position-dependent manner. In other words, the CaM domain got engaged only in the K163 simulations. The interaction between PIP2 and the lipid membrane also relied on the residue with which it was bound to. Specifically, PIP2 was partially pulled out of the lipid membrane only in the K163 simulations and not in K175. This was directly related to the position of the α-actinin residues relative to the lipid membrane that controlled the amount of normal forces applied on the PIP2 molecules.

Two PIP2 binding sites have been predicted on the α-actinin molecule. The first one was between helices A and B of the CH2 domain and the second one was at the neighboring loop region, which contained residue R199. Our simulations showed that the second binding site was in fact more favorable. The binding with residue K175 both in single and double PIP2 binding was rapidly transferred to R198/199. This most likely is due to the high concentration of positive charges in that region compared to the original binding site. We observed that the binding with these residues were both strong and stable and resulted in vanishing interactions with K175. However, K175 may be more accessible for the PIP2 molecule compared to R198/R199 and thus might serve as the primary binding residues. Therefore, K175 may position PIP2 close to R198/R199 but the main binding actually occurs with latter. Strong interaction with R198/R199 was observed in both single and double PIP2 simulations may imply that there is no real allosteric effects in forming this specific electrostatic bond. However, K163 interaction was quickly disrupted and the corresponding PIP2 floated freely in the lipid membrane only in the double PIP2 simulations. This probably suggests that a single PIP2 interaction with α-actinin's ABD is more favorable.

Talin engages with β-integrin and eventually dissociates it from α-integrin, which ultimately leads to full integrin activation. A complete dissociation of the subunits is achieved through two subsequent interaction of talin with the cytoplasmic tail of integrin. The first interaction forms with the membrane-distal region (MDist) and the second one is formed with the membrane-proximal region (MP). The second interaction will apply enough force to break the salt bridge between them. α-Actinin binds to the cytoplasmic tail of integrin and prevents talin from binding to this region and thus inhibits integrin activation. Localization of more α-actinins to the lipid membrane results in low- affinity state of integrins for ECM ligands and weakens FAs. PIP2 molecules reside in the lipid membrane and effectively bind to the actin-binding domain of α-actinin. Therefore, high PIP2 density may promote α-actinin binding to integrin by both recruiting them to the cell membrane and by controlling the conformation of the actin-binding domain, which may lead to modified interaction of the CaM domain with the rod domain. Our simulations suggested that PIP2 recruitment stabilized α-actinin's position near the lipid membrane and increases probability of integrin binding, which inhibits talin association, and that is one possible mechanism PIP2 contributes to FA turnover.

CHAPTER 4: Mechanically regulated interaction between α-actinin and vinculin in focal adhesions (Force transduction layer)

Section 4.1 A molecular trajectory of α-actinin activation[1]

α-Actinin is linked to growing focal adhesions via its interaction with vinculin. It also acts as a cross-linker for actin filaments, a process that is putatively modulated by vinculin. The interaction between α-actinin and vinculin is crucial to both α-actinin functionality at focal adhesions and its actin cross-linking activity (Figure 4.1-1). Structurally, α-actinin is an anti-parallel dimer, with each monomer having two calponin-homology (CH) domains at the N-terminus, a central rod domain consisting of four spectrin repeats (R1-R4), and a C-terminal head domain consisting of a calmodulin-homology (CaM) domain (Liu et al. 2004). The two CH domains can exist in either closed conformation (where they are associated) or open conformation (where they are separated) (Figure 4.1-1). The central spectrin repeats are triple helical structures (A-C helices) (Figure 4.1-1B) arranged such that the first and second repeats (R1, R2) of one monomer interact with the third and fourth of the other (R3, R4), forming a stable rod-like structure (Figure 4.1-2) (Liu et al. 2004). Vinculin binding site (αVBS) is located at R4. In the present structure of α-actinin, αVBS is cryptic and needs to be activated and exposed to the solvent prior to vinculin binding (Vogel & Sheetz 2006).

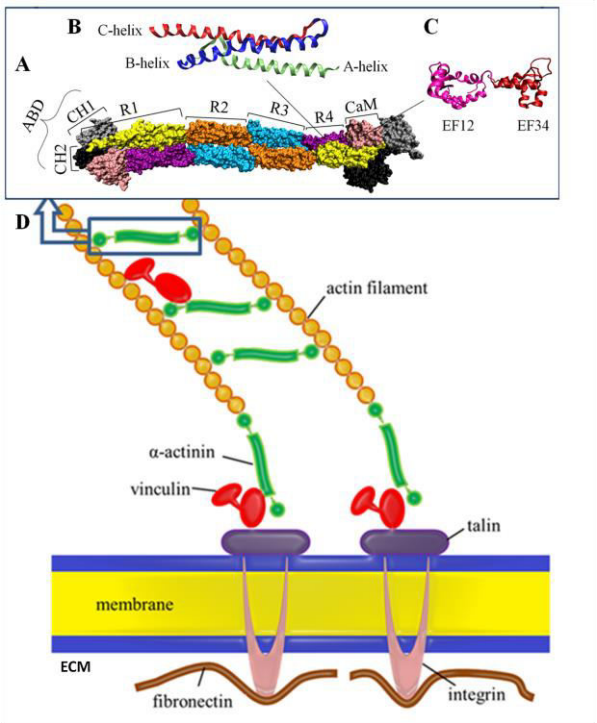

[1] The content of this Chapter has been published in Biophysical Journal, Volume 103, Issue 10, 29 November 2012, Pages 2050–2059 (Shams et al. 2012).

Figure 4.1-1. A cartoon model of a focal adhesion complex depicting the role of vinculin and α-actinin. (*A*) The structural model of α-actinin shown here is constructed by Liu et al. (12). Alpha-Actinin has three main structural domains: the CaM domain, the central rod domain with 4 spectrin repeats, (R1-R4), and two calponin homology domains known as CH1 and CH2. (*B*) The triple helical structure of spectrin repeats (A-C helices) form coiled-coil conformation. (*C*) Four EF hand motifs of the CaM domains (EF12 and EF34). (*D*)The primary role of α-actinin is to cross-link actin filaments, and vinculin is suggested to act as a reinforcing agent. Vinculin, α-actinin, and talin build a physical connection between the cytoskeleton and the extracellular matrix.

The available structure of α-actinin shows that αVBS is cryptic and buried in the rod domain (Figure 4.1-2) (Bois et al. 2005). Previous studies have suggested that αVBS can become activated either by the complete unraveling of the α-actinin structure near αVBS (Winder 1997) or by a specific conformational change in which αVBS swings out of the interface between R1 and R4 (Bois et al. 2005). The αVBS residues are inhibited from swinging out due to hydrophobic contacts with other residues in the rod domain. That site of αVBS, which interacts with the CaM domain, is also inhibited by hydrophobic interactions in both conformations of CH domains but mostly in the closed conformation (Figure 4.1-1). Once activated, αVBS can potentially interact with activated vinculin (Bois et al. 2005).

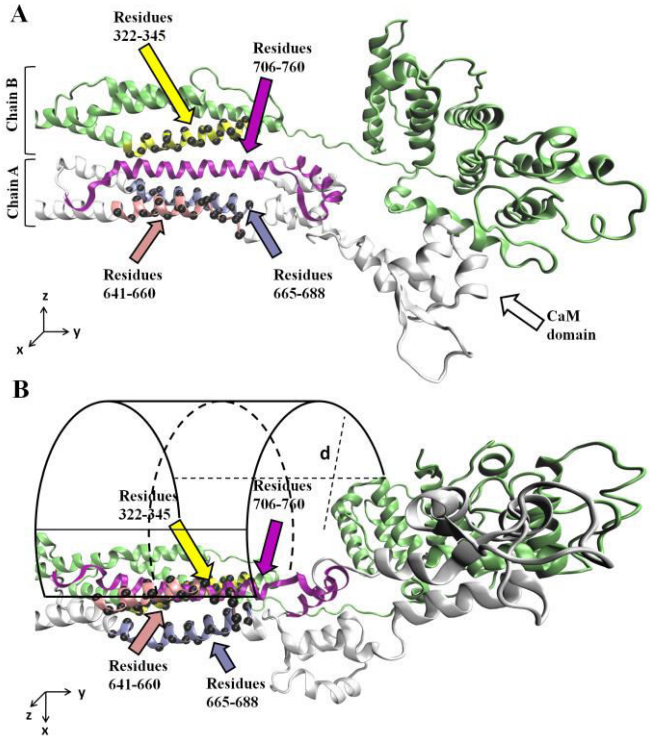

Figure 4.1-2. α-Actinin shown from two different angles. The figure demonstrates αVBS inhibition in the original structure and our pulling mechanism in order to activate it. (*A*) Alpha-actinin is an anti-parallel homodimer consisting of chain A (silver) and chain B (green). αVBS (purple) was pulled out of its inhibited position using a constant velocity MD simulation. Residues 322-345 (yellow) in repeat R1 of chain B, residues 665-688 (ice blue) and residues 641-660 (pink) in repeat R4 of chain A form the reference group (C_αs are shown by black spheres which were restrained during the simulaion). The αVBS is inhibited by the reference group as well as the CaM domain (white). (*B*) The structure shown after -90° rotation along the x-axis with respect to the top figure, emphasizing how αVBS is surrounded by the reference group and consequently inhibited by it. At each window of umbrella sampling, the pulling group containing αVBS is harmonically restrained at distance ***d*** from the reference

group. Since ***d*** is a scalar and does not entitle any direction, the pulling group is free to move on the surface of a hypothetical cylinder (shown in the figure) with radius ***d***.

Aside from its role in focal adhesions, α-actinin is characterized as an actin-filament cross-linker; parallel actin filaments depend on α-actinin for maintaining their spatial arrangement (Hampton et al. 2007; Hemmings et al. 1992). The cytoskeleton continuously sustains mechanical stresses and, as an actin cross-linker, α-actinin is exposed to complex mechanical perturbations. Vinculin has been suggested to act as a reinforcing agent for the interaction between actin and α-actinin (Golji & Mofrad 2010). In this case, α-actinin would serve as a mechanosensor, signaling vinculin to bind to it and reinforce its crosslinking role when exposed to proper stresses. For this to be possible, the activation of αVBS for binding to vinculin would have to be mechanically regulated. Although both experimental (del Rio et al. 2009) and computational evidence (Lee et al. 2007; Vogel & Sheetz 2009) has been proposed to demonstrate the mechanisms by which other mechanosensors such as talin or vinculin are mechanically regulated, no evidence has been given to support α-actinin's mechanosensing behavior. Talin VBS is activated in a stepwise fashion: First, tension in the rod domain causes torsion near the VBS; then, the VBS rotates out of its core (Lee et al. 2007). Vinculin activation also follows a stepwise mechanism. First, surface interaction with a nearby VBS is formed. Second, tension from nearby actin-filaments separates D1 from the rest of vinculin for binding to nearby VBS (Golji et al. 2011). One can speculate that α-actinin activation follows a similar stepwise procedure.

In this study, we investigate three possible scenarios regarding α-actinin activation prior to vinculin binding: 1) the available crystal structure of α-actinin is in an already activated conformation and thus no further conformational change is required, 2) external force is necessary to activate α-actinin, 3) no major force is needed and small biases in the order of thermal energy may easily change the conformation of the molecule. We investigate these possibilities by calculating the free energy profile of the activation process for smooth muscle α-actinin. Towards this task we have generated a trajectory for αVBS activation. Moreover, we discuss physiologically-relevant mechanisms that may lead to αVBS activation.

Materials and Methods

All simulations were performed using the molecular dynamics (MD) package GROMACS (David et al. 2005) and the CHARMM27 force field (Scott et al. 1999).The structure of the entire α-actinin dimer was used for our simulations (PDB ID: 1SJJ) (Liu et al. 2004). A total number of 213,307 water molecules were added to the system. As a result of the extended structure of the α-actinin molecule, a triclinic box with vectors $45\times15\times10$ nm^3 was used that satisfied the minimum image convention criterion in all directions (Figure 4.1-3). The TIP3P water model, for which the CHARMM force field is parameterized, was used in our simulations (Jorgensen et al. 1983). The system contained 54 negative charges that were neutralized by

adding the same number of sodium ions. Two salt added simulations were performed with 50 mM and 150 mM of NaCl, which contained 204 and 612 extra ion pairs, respectively.

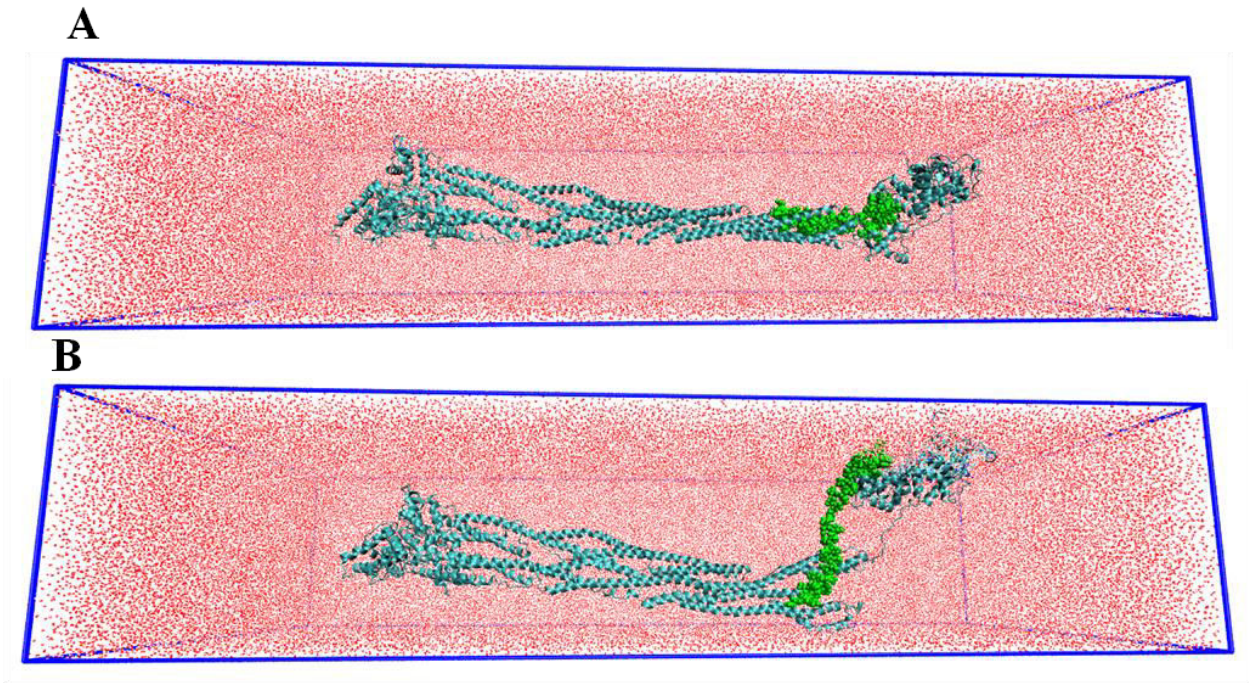

Figure 4.1-3. The confined structure of α-actinin in the water box. This structure shown (A) before and (B) after α-actinin activation. Some of the water molecules are cut out from the front side of the box for the sake of clarity.

A time step of 2 fs was used along with the LINCS algorithm for constraining bonds between hydrogens and heavy atoms (Hess et al. 1997). The electrostatic interactions were calculated using the particle mesh Ewald method (Darden et al. 1993). The structure was initially minimized for 500 steps using the steepest descent algorithm. This was followed by further minimization with the L-BFGS method (Byrd et al. 1995) for 1000 steps to remove any remaining unfavorable contacts. Furthermore, the system was equilibrated in three stages. In the first stage, the equilibration simulation ran for 10 ns in constant volume while all protein atoms were restrained in space using springs with 1000 $\mathrm{kJ\,mol^{-1}nm^{-2}}$ constant. The Nose-Hoover thermostat (Nosé 1984; Hoover 1985) was used to maintain the temperature at 310 K. In the second stage of equilibration, the system underwent 100 ps of molecular dynamics in constant pressure and with the same position restraints as the first step. The pressure was maintained at a reference pressure of 1 bar using the Parrinello-Rahman barostat (Parrinello 1981). The final step of equilibration took 100 ps with the same set of parameters as the second step except that all restraints were removed. This multilevel equilibration reduces high fluctuations in the density of the system.

The umbrella sampling method (Torrie & Valleau 1977) was used to calculate the potential of mean force (PMF). A range of different spring constants were tested (Figure 4.1-4) for the umbrella potential and the value of 3000 $\mathrm{kJ\,mol^{-1}nm^{-2}}$ resulted in smooth, well overlapped histograms. The reaction coordinate was defined as the center of mass distance

between the C_α atoms of residues 712 to 731 of the C-helix of chain A (the pulling group) and residues 641 to 660 along with residues 665 to 688 of chain A and 322 to 345 of chain B (the reference group). The reference step for umbrellas was chosen to be 0.4 Å in order to optimize the overlap of the histograms (Figure 4.1-5). At each umbrella a 1 ns sampling was performed (Figure 4.1-6), and the trajectory was saved every 0.2 ps. The final PMF was calculated using Grossfield's WHAM code (Kumar et al. 1992).

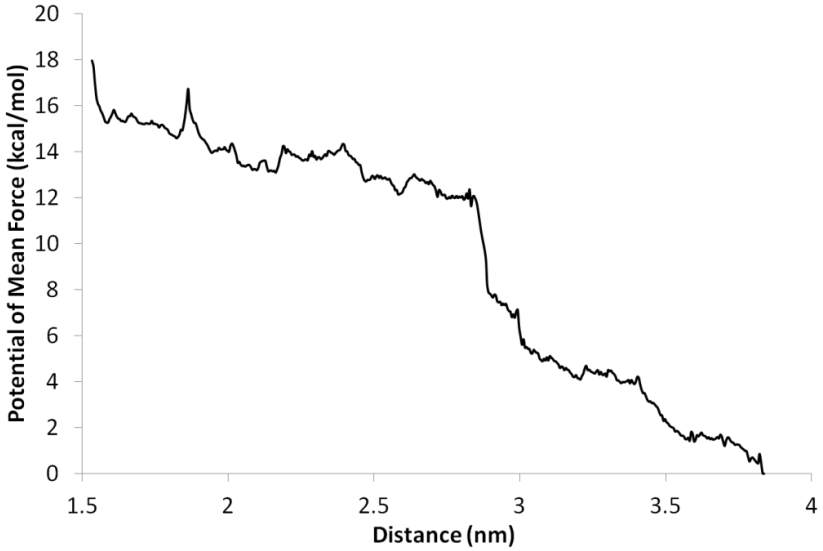

Figure 4.1-4. The potential of mean force calculated with a higher umbrella potential of 4000 kJ/mol nm^2. The downhill behavior of the PMF as well as the point of activation is conserved.

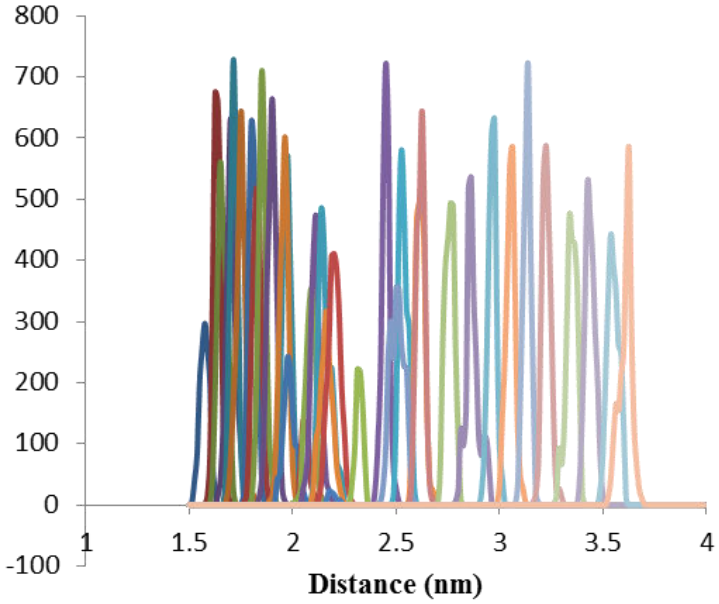

Figure 4.1-5. The histograms generated in the umbrella sampling simulations along the reaction coordinate. They show a good overlap. Thid condition guarantee a good sampling of the system and a smooth potential of mean force.

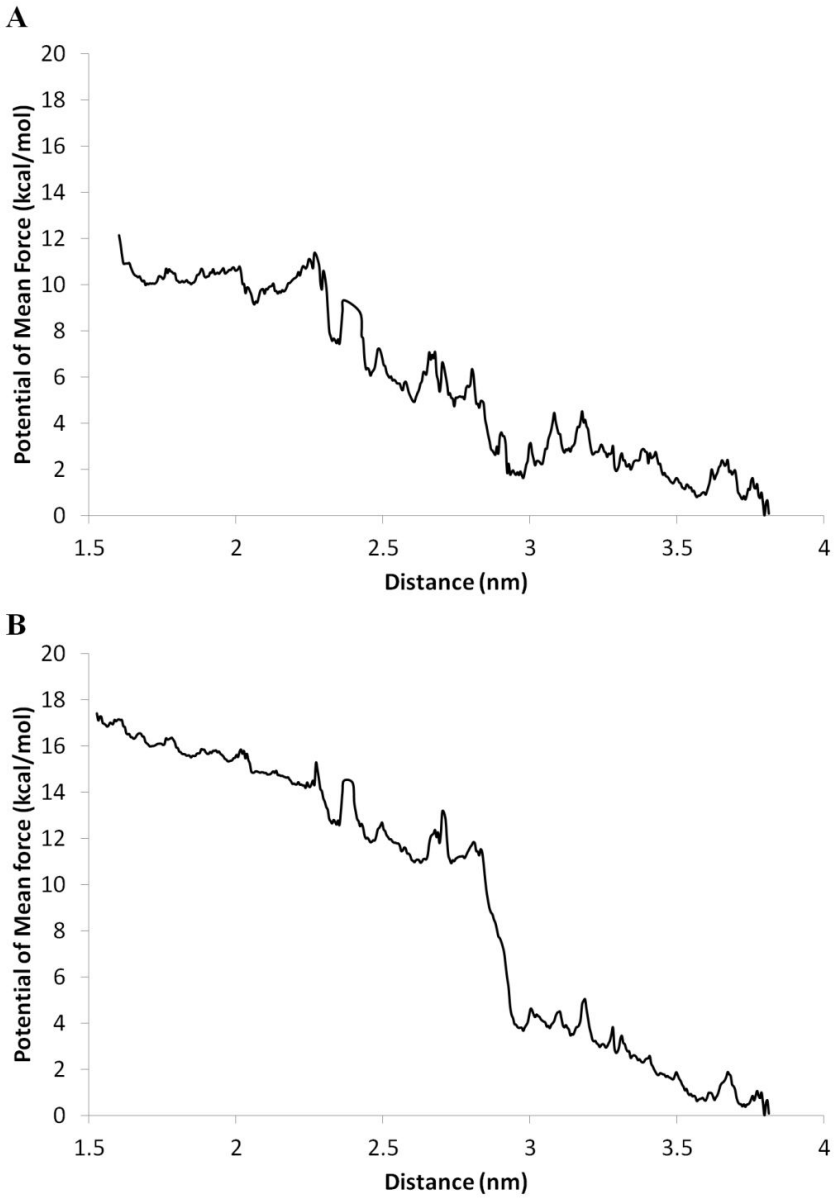

Figure 4.1-6. The potential of mean force calculated using different number of data points. (*A*) 30% of the original data points resulted in a noisy graph. (*B*) Keeping 80% of data points results in a PMF close to the original one showing that the sampling was good enough.

A pulling simulation with constant velocity was performed on the reaction coordinate to observe the activation pathway. Reported results in this study are with 0.005 nm/ps constant velocity. However a lower velocity simulation with 0.0005 nm/ps was performed to confirm the results. The Visual Molecular Dynamics software package (VMD) was used for all post-simulation visualization and analysis (Humphrey et al. 1996). For reviewing general principles of molecular dynamics, please see Chapter 2 of the present dissertation.

Results

It has been suggested that α-actinin activation involves αVBS exposure from the hydrophobic core of the triple helical structure of the R4 repeat in the rod domain (Bois et al. 2005). To evaluate this hypothesis, we generated an activation trajectory using MD simulation, which was then used to calculate the PMF profile of the activation process. For the first part of our study, the trajectory was produced using constant velocity MD simulation for pulling αVBS against its neighboring helices within the rod domain. Moreover, the constant velocity pull was applied to αVBS while three neighboring helices of α-actinin rod domain (reference group) were harmonically restrained. This trajectory was then used to create initial configurations of the system later used for umbrella sampling.

αVBS was initially buried in the rod domain and stabilized by interactions with the neighboring helices. Previous studies revealed that human αVBS is located at the C-helix of R4 (residues 731-760). Sequence alignment of αVBS in smooth muscle chicken isoform, which was used in this study, with human α-actinin revealed a new range of residues for chicken's αVBS (706-739). Kelly et al. observed vinculin binding to the CaM domain of α-actinin, but specific residues were not identified. Therefore, we speculated that the CaM domain serves as an initial anchorage of the vinculin molecule, but full engagement requires α-actinin activation (C-helix exposure). In this study, αVBS was selected as the C-helix of R4 and residues 740-760 of the CaM domain, which is at the surface of the first EF-hand motif (Figure 4.1-1C).

The activation process occurred in three subsequent steps: i) bending of the rod domain due to force transmission from the C-helix to the rod domain via the interactions between the C-helix and its neighboring helices (Figure 3, panels C, D), ii) movement of the CaM domain away from the rod domain pulling the beginning of the C-helix out, iii) complete dissociation of the C-helix from the rod domain, leaving the rod domain to recover the straight structure (Figure 4.1-7, panels E, 3F). An overall twist in the active structure was also evident in the rod domain compared to the inactive structure, suggesting that twisting may also contribute to the activation (Figure 4.1-7).

To quantify the correlation between αVBS activation and the strain experienced by the α-actinin molecule, we related the local changes in the conformation to the more global ones. In the first step of activation, none of the interactions were broken but they worked in concert to transmit the force from αVBS to the rod domain and resulted in bending of the structure. In the second step, the first EF-hand motif was dissociated from the rod domain. Specifically, a hydrogen bond between LYS763 in the CaM domain and THR738 at the end of the C-helix was broken. This interaction was partially responsible for holding αVBS in the inhibited position. In addition, GLN806 in the CaM domain was forced to move away from HIS662 in A-helix of R4 disrupting another hydrogen bond. The C-helix followed the first EF-hand and became partially exposed. The C-helix is initially stabilized by hydrophobic interactions within the rod domain. As the C-helix was being pulled out, these hydrophobic contacts were broken one-by-one from the C- terminus to the N-terminus of the helix in a zipper-like fashion. Interestingly, as each

broke free from its interactions, it was shifted one residue further and formed a new short-lived interaction with the next residue in the chain (Figure 4.1-8). We suggest that formation of these relatively short-lived interactions gives rise to transition states that reduce the energy cost for a more global conformational change. At the last step, salt bridges between αVBS and helices in both the same and the opposite monomers were disturbed. Specifically, GLU712 and ARG715 of αVBS broke free from ARG321 in R1 and GLU690 in R4, respectively.

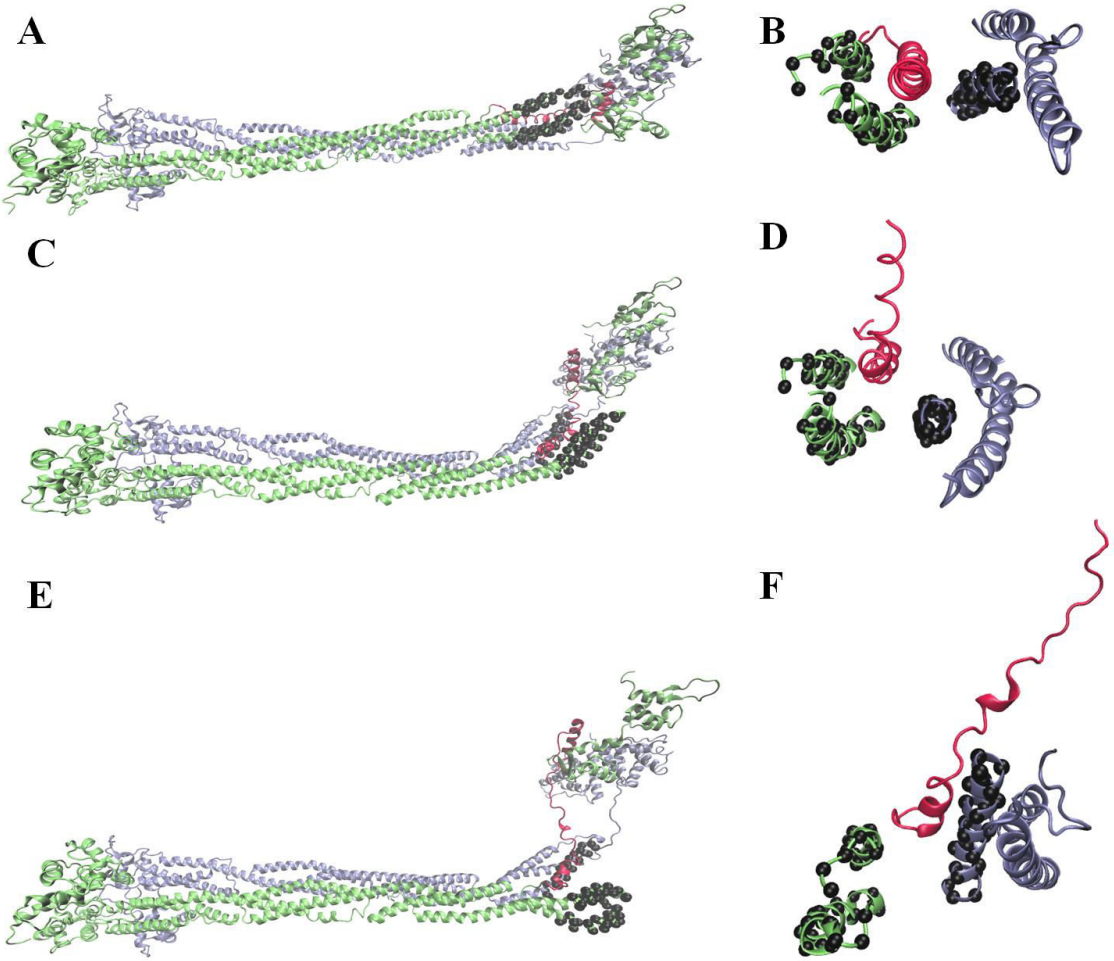

Figure 4.1-7. Conformational changes in the rod domain of α-actinin along the trajectory. C_α atoms of the reference group are marked with black circles. (*A*) The initial frame of the simulation (t=0) shows the inhibited state of αVBS in the rod domain in the straight configuration of the molecule. (*B*) αVBS, colored red, is inhibited by helices in the rod domain. (*C*) In the first stage of activation, the force is transmitted to the rod domain via the hydrophobic interactions of the C-helix with the rest of the rod domain. In this stage, no interactions are disrupted but the molecule undergoes bending. (*D*) Bending of the molecule pushes the αVBS toward the surface of the molecule, as a result of the coupled bending and twisting in the rod domain. (*E*) In the last stage of activation, all the hydrophobic interactions between the C-helix and the rod domain are broken and αVBS is completely exposed to the solvent. (*F*) The twist in the rod domain of the activated structure is obvious compared to panel B. This twist is stabilized by the formation of new interactions between the two monomers in the absence of the C-helix.

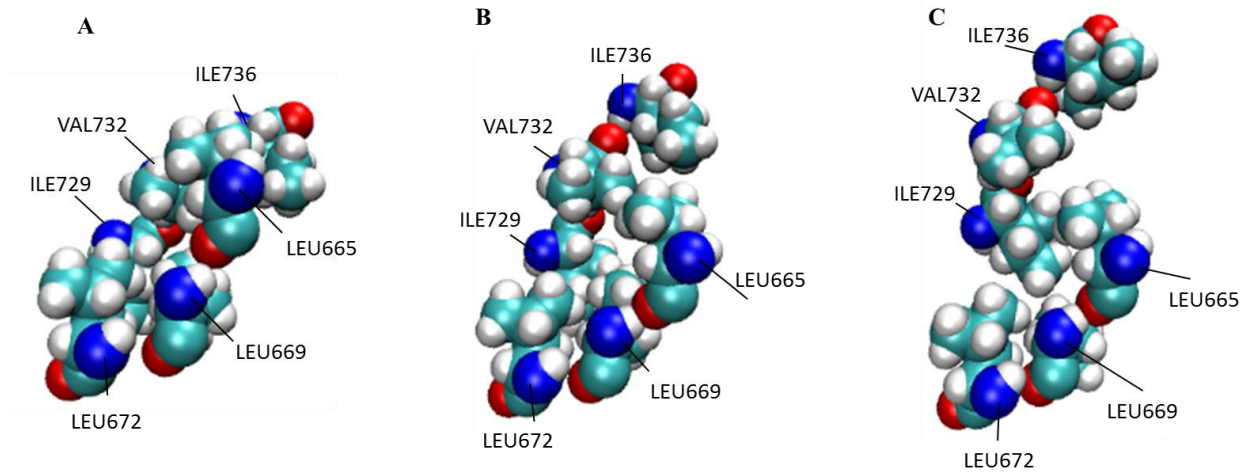

Figure 4.1-8. Hydrophobic packing of αVBS inside the rod domain. (*A*) The residues of C-helix (706-739) interact closely with the A-helix (660-688) in the initial configuration of the system, forming a highly packed hydrophobic region. (*B*) As the force is applied to αVBS, hydrophobic interactions start to break from the end of the C-helix close to the CaM domain. Firstly, as the contact between ILE736 and LEU665 is disrupted, VAL732 shifts one residue further, distorting its interaction with LEU669 and forming a new one with LEU665. The new set of interactions reduces the energy cost for placing the C-helix one residue further along the A-helix. (*C*) Further pulling of the C-helix against the rod domain dissociatesVAL732 from LEU665 and puts ILE729 in contact with LEU665. These short-term interactions distributes a large amount of energy required for a global conformational change among smaller energy packs provided as thermal atomic motions, which is consistent with the diffusive nature of the biological systems.

The solvent accessible surface area (SASA) of αVBS increased at the second stage of activation between 400 to 600ps (Figure 4.1-9A). The SASA value was roughly constant in the last stage of activation, which implied that salt bridges were disrupted in this stage without a significant impact on αVBS inhibition. The number of hydrogen bonds within αVBS and the rod domain continuously decreased over time showing that this type of interaction played an important role in stabilizing αVBS in the rod domain (Figure 4.1-9B).

According to the PMF profile, the system has two stages, separated by a relatively sharp free energy drop of approximately $13k_BT$ (Figure 4.1-13). The first two steps of activation occurred before the energy drop, most likely because of an entropic increase after the C-helix was partially exposed and the CaM domain was freed from the rod domain.

The effect of salinity on the activation trajectory was explored by comparing the neutral system with 50 mM and 150 mM additional salt concentrations added: salinity. The results showed no substantial difference among these simulations with regard to the activation trajectory. The solvent accessible surface area of αVBS for these simulations overlapped, demonstrating that the activation rate is the same for all simulations. Our results suggested that, since αVBS is stabilized via hydrophobic interactions, the activation process is mostly governed by the hydrophobic forces and not electrostatic effects, and thus salinity had negligible effects (Figure 4.1-10). In addition, although a few salt bridges exist at the farther end of the C-helix

with respect to the rod domain in the initial structure, they are buried in the hydrophobic core of the protein and cannot be manipulated by the ions in the system.

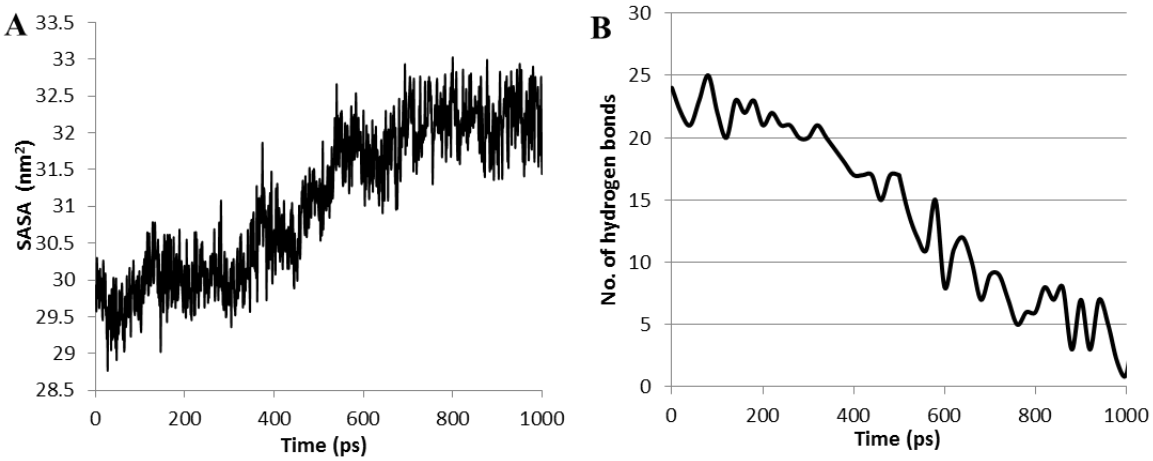

Figure 4.1-9. The solvent accessible surface area (SASA) of αVBS and its hydrogen bonds with the rod domain. (*A*) The SASA of αVBS shows a sharp increase between 400 ps to 600 ps which corresponds to the second stage of the activation process. It demonstrates that αVBS is released after the key hydrophobic interactions are distorted. The last part of the graph is related to the third stage of the activation process in which a few salt bridges are broken. No significant increase in the SASA value is displayed at this stage implying that these salt bridges do not have a major effect on stabilizing αVBS since they are located only at the N-terminus of αVBS. (*B*) The number of hydrogen bonds with αVBS continuously decreases over time demonstrating that hydrogen bonds are important in stabilizing αVBS in the rod domain.

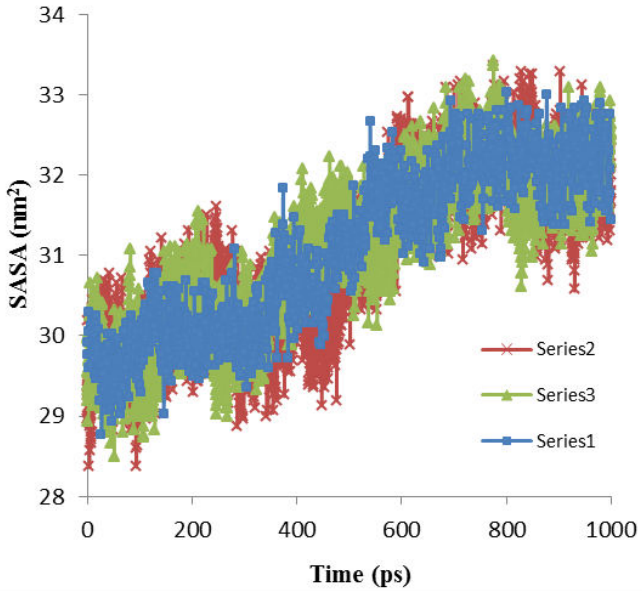

Figure 4.1-10. The effect of salinity on solvent accessible surface area of αVBS. This was measured and compared to the simulation with no salt concentration. In the original simulation, system was only neutralized and no extra salt was included. Addition of 50 mM and 150 mM salt to the system affected neither the trend nor the rate of activation process, most likely because the dominant forces in inhibiting αVBS are hydrophobic and not electrostatic.

To test the reversibility of this activation trajectory, a 1 ns equilibration was carried out on the structure of α-actinin during which all restraints and pulling forces were removed. During this simulation RMSD was equilibrated and αVBS remained in its activated position. During activation several rearrangements occurred within the rod domain, stabilizing the activated structure. Most of the hydrophobic residues dissociated from αVBS formed a new interaction with neighboring helices that compensated for the energy loss due to breakage. The structure also regained its helicity, which was partially disrupted in the process of force application. In addition, the conformational changes throughout the rest of α-actinin, e.g. extension in the connective loop between the ABD and the rod domain, were not reversed. This result indicates that even though an external force (or interaction) on αVBS is needed to accelerate the activation process, the activated structure will most likely be preserved for further interactions with vinculin.

Our fully active structure of αVBS, obtained from the equilibration simulation mentioned above, was compared to the crystal structure of αVBS in complex with vinculin generated by Bois et al. (9). The human αVBS in complex with vinculin head was aligned to chicken's smooth muscle α-actinin in the activated conformation in order to examine the consistency of vinculin head with the full-length α-actinin. As Figure 4.1-11B shows, vinculin head matches the activated α-actinin except for a small overlap with the CaM domain denoted by a circle. This was expected since in the complex, none of the space-filling structures such as CaM and CH domains are present. Therefore, we do not expect to see complete similarity between the structures. The helicity of αVBS is reduced in the activated structure compared to the isolated αVBS increasing the RMSD to 5 Angstroms. However, the overall matching between αVBSs is plausible (Figure 4.1-11).

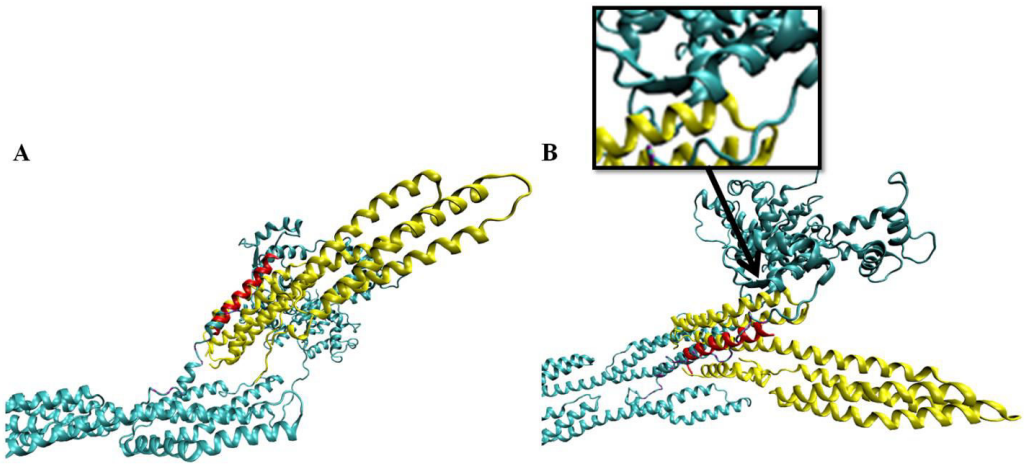

Figure 4.1-11. Activated structure of α-actinin (cyan) aligned to vinculin (yellow) and αVBS (red) complex. (*A*) The side view of the aligned structures depicts the relative position of vinculin head to αVBS. (*B*) The up view of the same configuration as *A* shows a plausible consistency of structures other than a small overlap of vinculin with the actin binding domains of α-actinin marked by the black arrow (this region is magnified in the insert).

The activation trajectory was reproduced using a smaller pulling velocity to measure the pulling rate effects on the activation pathway. Simulation performed with 0.0005 nm/ps pulling rate– versus 0.005 nm/ps used earlier – showed that significantly less force is required for activation with a slower rate of pulling (Figure 4.1-12). However, using a smaller pulling velocity did not notably affect the activation trajectory (Figure 4.1-14) except for the expected observation that the conformational change took more time to present.

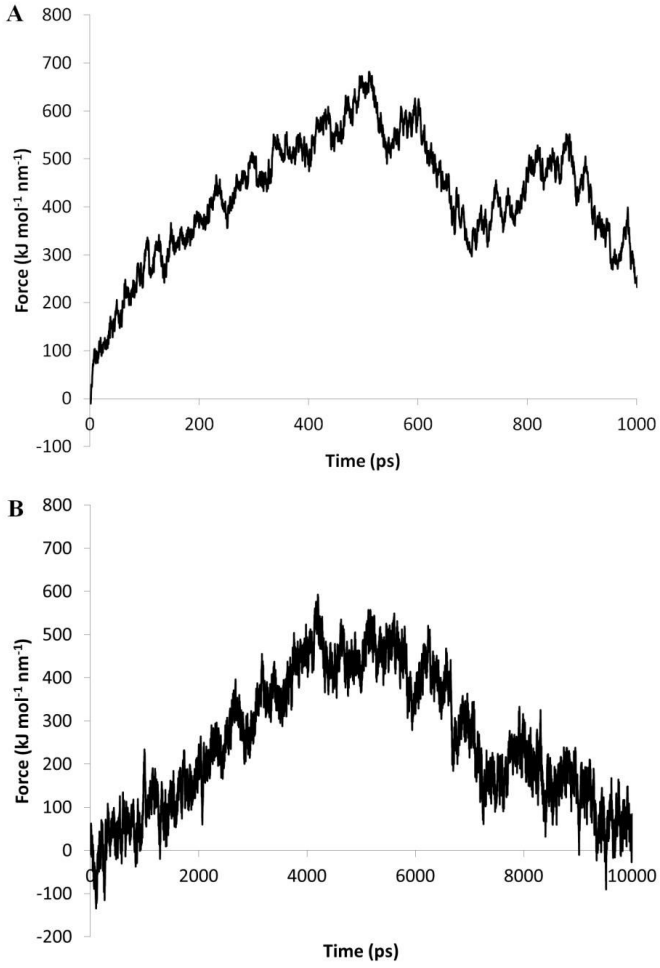

Figure 4.1-12. Force applied to αVBS during activation trajectories generated with different pulling velocities. (*A*) For the pulling velocity of 0.005 nm/ps, the maximum value of force was 650 kJ/(mol nm) that ocurred at 500 ps where the activation process was completed. (*B*) Using a lower pulling velocity of 0.0005 nm/ps, the maximum value of force was 20% less than the original force but the peak was again located at 500 ps.

Discussion

α-Actinin is an essential cytoskeletal protein that plays a primary role in cross-linking actin filaments. Alpha-Actinin's interaction with vinculin plays a part in both reinforcing focal adhesion sites and rearranging actin filaments. It has been suggested that α-actinin activates vinculin by inserting its binding site to the vinculin head and reorganizing helices in that region

(Bois et al. 2005). However, the present atomic structure of α-actinin shows that αVBS is primarily inhibited in the rod domain and thus α-actinin activation should precede vinculin binding, and vinculin activation. In this study, we produced an activation trajectory consistent with the hypothesis proposed by Bois et al., which resulted in the complete exposure of αVBS to the solvent and was in good agreement with the vinculin-αVBS complex resolved by Kelly et al. (Kelly et al. 2006). Our activation trajectory was then used for calculating the potential of mean force (PMF) and measuring the free energy difference between inactive and activated conformations. It should be noted that the smooth muscle α-actinin isoform was used in this study, which are PIP_2-regulated, and not known to directly participate in focal adhesions. However, this model is currently the only complete atomic structure available and thus the best candidate for conducting computational studies on α-actinin activation and elucidating α-actinin's role in focal adhesions. The conformation of ABDs and the CaM domain in the non-muscle isoforms might be different, which can affect the activation pathway to some extent. Based on our results, we speculate that the most important effect would emerge from the degree of CaM association with the rod domain in the non-muscle isoform.

Referring to the PMF profile, the system has two-stages separated by an energy drop of approximately $13K_BT$, i.e. activation releases 8kcal/mol of energy (Figure 4.1-13). The conformational changes related to activation mainly occurred before the energy drop and resulted from breakage of a number of hydrophobic contacts between the C-helix and its neighboring helices within the rod domain that are responsible for the fluctuations observed along the reaction coordinate. Subsequently, a large segment of αVBS was dissociated from the rod domain and became free to float into the solvent which in turn resulted in a relatively large entropic raise of the system. Further αVBS pulling disrupted several salt bridges at the end of the C-helix and αVBS was completely exposed after 1ns of pulling. Aligning the activated αVBS of our simulation to αVBS in complex with vinculin resolved by Bois et al. revealed that the vinculin head fits into the space between αVBS and the rod domain in the full-length structure (Figure 4.1-11A). However, actin binding and CaM domains on α-actinin cause partial steric hindrance for vinculin head and limit its movement (Figure 4.1-11B); therefore, even upon exposure αVBS should make an angle large enough to provide sufficient space for vinculin to be placed close to it and optimize binding.

Simulation of the activated structure in the absence of constraints or forces showed the stability of the activated αVBS structure. The α-actinin molecule reorganized itself to adjust to conformational changes at each stage of activation and reduce the energy cost. For instance, several new interactions were formed within the rod domain to compensate for the missing stabilizing interactions with αVBS after activation (Table 4.1-1). Interestingly other parts of the protein remained stable and intact. No interactions were disrupted in ABD or between CaM and ABD. In fact, ABD followed CaM because of the strong interaction between them. The only other disrupted interaction was between the connective loop from ABD to the rod domain, and

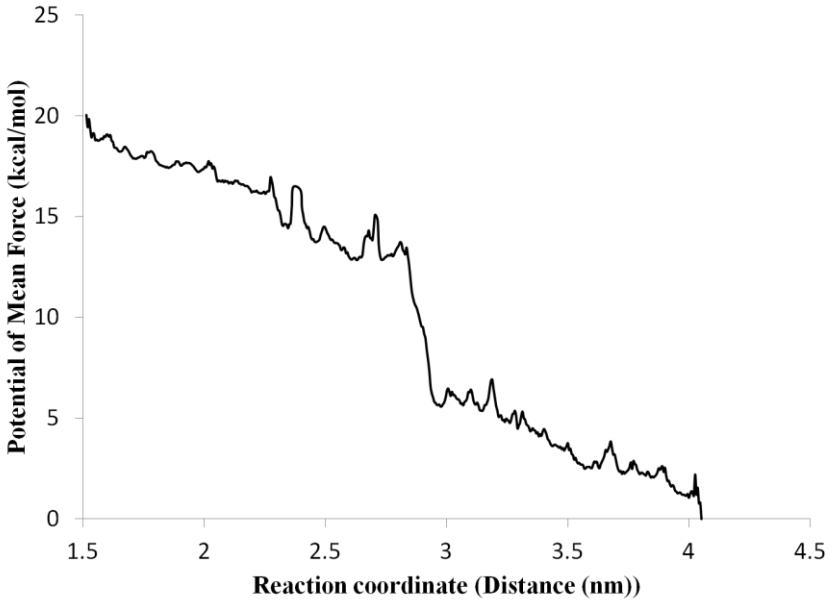

Figure 4.1-13. The potential of mean force (PMF) along the reaction coordinate. The PMF is defined as the distance between the pulling group (consisting of the Cα-s of the residues 712 to 760 of chain A) and the reference group (consisting of the Cα-s of residues 641 to 660 and 665 to 688 of chain A and residues 322 to 345 of chain B). The energy barriers in the left hand side of the PMF profile demonstrate breakage of the hydrophobic interactions and is followed by a $13K_BT$ energy drop resulted in complete exposure of αVBS.

the CaM domain. This loop was mainly hydrophilic and thus stable in solvent. It is worth noting that α-actinin dimerization was maintained during activation, as suggested previously (McGregor et al. 1994).

The simulations used to produce the activation trajectory were carried out with a 0.005 nm/ps pulling velocity, which is substantially faster than the biological range of molecular velocities inside of a living cell. For the umbrella sampling simulations, the structure had been equilibrated at each window and therefore the PMF calculations were independent of the pulling velocity. To evaluate the effect of pulling rate on our activation trajectory, another simulation with 0.0005 nm/ps pulling velocity was performed for 10 ns. However, the force plot of the slow-rate (0.0005nm/ps) activation trajectory showed a 150 kJ/mol nm decrease compared to the original trajectory (Figure 4.1-12). This was most likely because fewer interactions were perturbed at each time and thus the force required to disrupt them was relatively weaker in the high-rate simulation. From a thermodynamic perspective, the system had longer time to reorganize and equilibrate to a new structure at each time point. Aligning two trajectories at similar stages of activation reveals that αVBS follows the same activation pathway in both cases (Figure 4.1-14). Therefore, although our initial pulling velocity was not in the biological range, it resulted in a reasonable activation pathway consistent with slower pulling velocities.

An important conformational change observed while generating the activation trajectory was the bending of the α-actinin rod domain towards the exposed αVBS. The harmonic force applied to pull out αVBS reached 600 kJ $\mathrm{mol}^{-1}\mathrm{nm}^{-1}$ at the end of the first stage of activation causing the rod domain to bend. We previously showed that α-actinin's dominant mode is

bending and bending can be achieved with approximately 100 pN of force in molecular dynamics simulations (Golji et al. 2009), consistent with the results from this study.

Table 4.1-1. Interactions of αVBS with the rod domain before and after activation.

αVBS	Residue in contact with αVBS	Final Interaction*
GLY717	ILE647	ILE679
GLN720	MET651	ILE679
THR724	ILE654	TYR675
MET711	ILE689	ALA640
ILE714	ILE686	ILE647
TRP718	TYR682	TRP646
LEU721	ILE679	ILE647
ILE725	GLU676	ILE654
GLU719	VAL329	TRP369
ALA726	GLN334	LEU283
ARG727	GLU336	VAL362

*Residues in contact with αVBS form new interactions after activation. The final interactions are mostly hydrophobic in nature, which explains the stability of the system after activation.

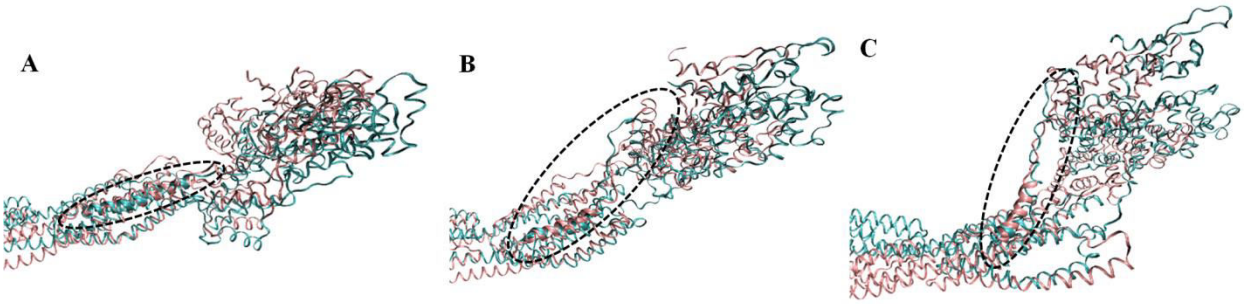

Figure 4.1-14. Snapshots of two trajectories aligned at 10, 50 and 90 percent. The ellipse with dashed line is marking the position of αVBS while the structures are aligned. As it seems αVBS is following a similar activation pathway. Therefore, we expect umbrella sampling calculation to give us the same potential of mean force. Comparison is done between original (pink) and low-velocity (cyan) trajectories in three stages of simulations. (A) Ten percent passed from both trajectories. The αVBS is still in the inactive conformation. (B) Fifty percent passed the trajectories and αVBS is halfway exposed. This point can be considered as a midpoint of activation. (C) The final configuration of the system when the system is in the activated conformation. The extension of αVBS is the same for both trajectories.

It should be emphasized that the activation trajectory reveals a correlation between conformational changes such as bending and/or twisting and αVBS activation, but does not necessarily imply causality. Bending and twisting are both molecular responses to mechanical stimuli and might not be necessary steps towards activation. This implies that external force may induce other activation pathways that do not incorporate these conformational changes.

However, to fully verify whether there exists a causal connection between bending/twisting and the activation phenomenon, future experimental studies are required.

Our results suggest an easily achievable activation state for an isolated α-actinin molecule, i.e. in the unbound state to actin or any other molecule. The trajectory reveals which degrees of freedom are crucial and need to be enhanced or at least remain undisturbed. For instance, Figure 4.1-7 shows that activation initiates from bending the rod domain and terminates by the full dissociation of the C-helix in the R4 spectrin repeat.

Here, we started from the inactive structure of α-actinin but, due to the downhill behavior of the PMF, energy is released upon activation and thus we suggest that no significant work is required for activating the molecule. Therefore, it is possible for α-actinin to bind to vinculin prior to actin binding that may lead to vinculin activation as proposed by Bois et al. Afterwards, vinculin might stay bound or dissociate depending on the direction and level of stress transmitted from actin filaments. In other words, based on our activation trajectory, we hypothesize that the presence of mechanical stimuli may either give rise to or prevent activation. An example of a situation that may inhibit activation involves restricting the movement of the CaM domain farther from the rod domain. The CaM domain directly interacts with the CH domains and thus actin binding may strongly affect its motion. For instance, if two parallel actin filaments cross-linked by α-actinins are under a stress perpendicular to the filament axes, which cause them to move away from one another, α-actinins are stretched and αVBS is probably forced back to the rod domain. This may change the free energy profile of the system, i.e. pulling α-actinin out of the rod domain requires energy that might be provided by other focal adhesion molecules such as zyxin or vinculin itself. A possible activation mechanism of α-actinins in the bound state to actin may be provoked by two sequential steps of stress application: 1) a mechanical strain transmitted from ABDs attached to actin filaments induce global conformational changes such as bending in the rod domain, 2) then vinculin forces the CaM domain to move away from the rod domain resulting in αVBS exposure and stabilization in the new state. The mechanical strain can result from the movement of actin filaments bound to two ends of α-actinin. For instance, if two parallel actin filaments move in the opposite directions parallel to their main axes, then the force may be transmitted to the CaM domain, which leads to pulling the C-helix out of the rod domain. Another scenario involves direct α-actinin binding to integrin suggesting that if the rod domain is held close to the membrane while actins are pushed away by actomyosin contraction, CaM domain is moved away from the rod domain and αVBS becomes exposed. In both of these scenarios, vinculin may play an important role. As actin-ABD linkage is exhausted and trembled upon sustained stress, vinculin may come into play to reinforce the interaction between the two. This is done by first interacting with partially exposed αVBS and further pulling it out then αVBS inserts itself into the vinculin head and reorganizes this area causing a conformational change in the head domain which leads to separation of the tail domain. Furthermore, there are many other possibilities for inducing stress in the α-actinin molecule that may involve binding to other focal adhesion molecules as well as movements of actin filaments. Consequently, the presence of vinculin near αVBS prior and throughout the αVBS activation may greatly

contribute to activation and stabilization of α-actinin in the bound state (Figure 4.1-15). Consequently, α-actinin still acts as a mechanosensor since stress controls the function of the α-actinin molecule but not in the way previously assumed.

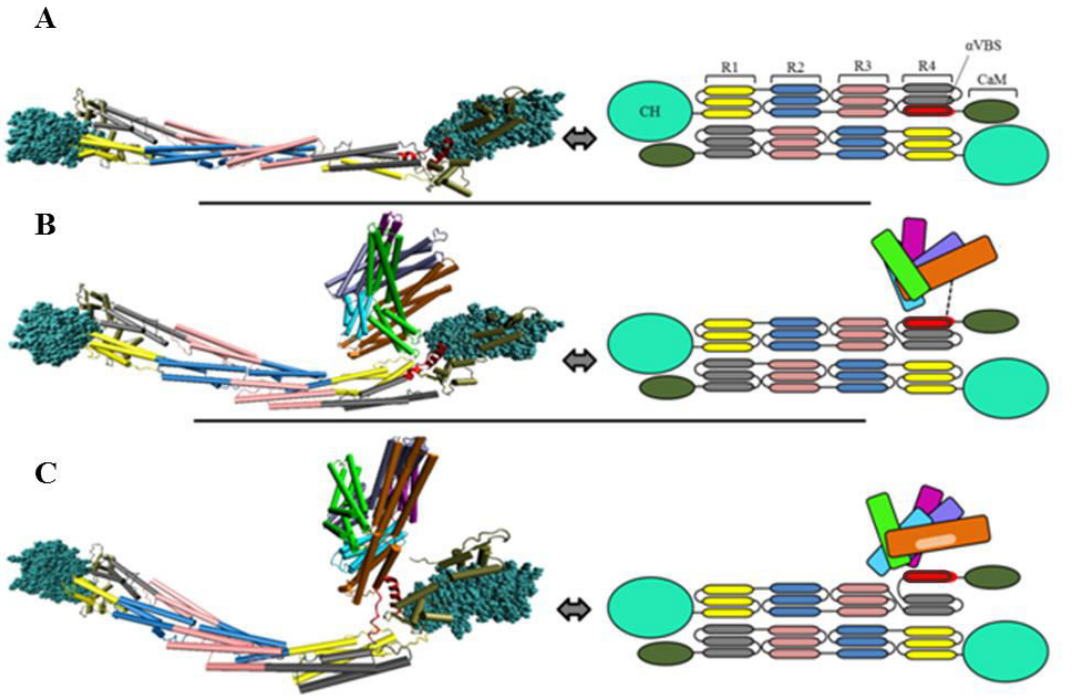

Figure 4.1-15. A model for α-actinin activation and its interaction with vinculin. Molecular structures (12, 47) (right) are made comparable to the cartoon models (left) by using the same color label for each molecular domain. The labels in α-actinin are as follows: CaM domain (cyan), CH domains (dark green), R1 (yellow), R2 (blue), R3 (pink) and R4 (grey). Vinculin domain are labeled as: D1 (orange), D2 (green), D3 (ice blue), D4 (purple) and Vt (light blue). (*A*) The inactive structure of the α-actinin molecule with the αVBS (red) inhibited in the rod domain. (*B*) A twist happens in the rod domain and αVBS becomes partially exposed to solvent, forming a weak interaction with vinculin. (*C*) Interacting with vinculin provides the free energy required for activation. Consequently, αVBS swings out of the R4 spectrin and forms a complex with vinculin.

One may ask: if activation releases energy, then why is the crystal structure in the inactive state? The reason may lie in the preparation and arrangement of α-actinin molecules in the experimental procedure done by Liu et al. (Burridge et al. 1988). α-Actinin molecules form a 2D array that may inhibit activation as a result of the stress that molecules exert on each other in the mesh. Therefore, we cannot conclude that the activation pathway is necessarily unique. It is worth mentioning that the interaction between α-actinin and vinculin was observed in an actin-free environment, which implies at the very least that stress transmitted from actin filaments is not necessary for vinculin binding (Figure 4.1-16A-C) (McGregor et al. 1994). Another possibility is that α-actinin binding would not be sufficient for vinculin activation; although, if vinculin is weakly associated with actin, forces applied from both sides result in activation (Figure 4.1-16D-F). Therefore, in this work we do not necessarily suggest that vinculin becomes activated upon α-actinin binding but no external agent is required for α-actinin association.

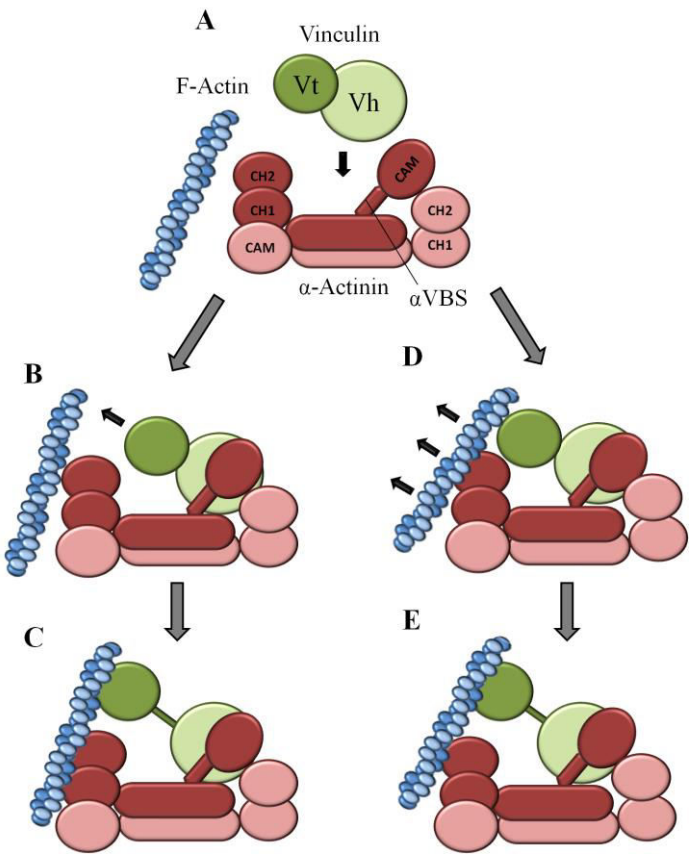

Figure 4.1-16. Two possible mechanisms of vinculin activation upon α-actinin binding are depicted. (*A*) The starting structure of α-actinin is activated as suggested by this study; therefore, vinculin has a high affinity for binding. (*B*) The first activation mechanism suggests that, after associating with α-VBS, vinculin head undergoes conformational changes that results in separation of the tail domain. (*C*) Then, activated Vt forms a strong interaction with actin filaments and reinforces its interaction with α-actinin. (*D*) The second mechanism suggests that vinculin associates with F-actin applying stress to Vt while the head domain is attached to α-actinin. This leads to the head-tail separation shown in (*E*).

The potential of mean force for αVBS activation was calculated using an activation trajectory consistent with Bois et al. (Bois et al. 2005), and some key interactions and conformational changes necessary for activation have been marked. Based on those results, we concluded that α-actinin could become activated using the thermal energy and probably small biasing forces in the order of K_BT applied by binding partners such as vinculin itself. The activation process contributes to α-actinin function within the cell only after the subsequent binding of activated αVBS to vinculin. Do the suggested conformational changes presented here sufficiently allow vinculin to bind αVBS? Does the activated αVBS bind vinculin via a unique binding trajectory? These and similar questions need to be investigated in future studies to fully amplify the impact of αVBS activation.

Section 4.2 α-Actinin binding alters force-induced activation mechanism of vinculin

Cells associate with their microenvironment through integrin-mediated adhesions, which are large protein complexes responsible for signal transduction and play an important role in the sensory machinery (Galbraith et al. 2002; Burridge & Feramisco 1981). However, the mechanism by which adhesion formation and maturation are regulated is poorly understood. Focal adhesions are composed of an integrin signaling layer in which integrin receptors reside on the cellular surface and conduct both inside-out and outside-in signaling (Giancotti 1997). Integrins directly interact with molecules in this layer in order to transmit signals to the force transduction layer and further towards the actin regulatory layer (Case & Waterman 2015). More than 150 proteins are involved in the processes of signal transmission and transduction but only a few are capable of direct binding to players in all different layers of focal adhesions, which make it particularly interesting (Pavalko et al. 1991; Kiema et al. 2006; Wegener et al. 2007). α-Actinin has binding sites for integrin, vinculin and actin that reside in three consecutive layers of focal adhesions. α-Actinin plays an important role in focal adhesion maturation and acts as a mechanosensor undergoing conformational changes upon stress application. Therefore, its affinity for other focal adhesion molecules such as vinculin is regulated by mechanical force, leading to a series of biochemical events important for mechanotransduction. It has been suggested that vinculin reinforces the linkage between α-actinin and the actin cytoskeleton (Kelly et al. 2006) through simultaneous binding to both. Yet, the molecular mechanism of such binding is still illusive.

α-Actinin is an anti-parallel homodimer and each monomer is composed of an actin binding domain at the N-terminal followed by four triple helical spectrin repeats (R1-R4) and a calmodulin-like domain (CaM) at the C-terminal as shown in Figure 1-5 (Liu, Taylor & K. a Taylor 2004). In the α-actinin dimer, monomers are associated through strong hydrophobic interactions within the coiled-coil region of the rod domain (Kelly & Taylor 2005). α-Actinins crosslink both parallel and anti-parallel actin filaments to form polar and bipolar arrays, respectively (Blanchard et al. 1989; Otey & Carpen 2004; Shams et al. 2016; Truong et al. 2015). The vinculin binding site is auto-inhibited in the triple helical structure of the R4 spectrin repeat of the full-length α-actinin structure (PDB ID: 1SJJ) (Liu, Taylor & K. A. Taylor 2004). Vinculin is a focal adhesion protein that links the actin cytoskeleton to several other focal adhesion players such as talin and α-actinin (Bakolitsa et al. 2004). Vinculin structure is composed of a head domain that contains a binding site for α-actinin and a tail domain, which contains the actin binding site (Borgon et al. 2004). We previously applied mechanical forces to the rod domain of α-actinin and unraveled how αVBS is exposed for vinculin binding. In this study, we used full-length structures of both vinculin and activated α-actinin in order to investigate their binding using molecular dynamics simulations, which provides sufficient spatial and temporal resolution for understanding the molecular mechanism of their interplay.

Materials and Method

The full length structure of vinculin was generated in the previous study done by Golji et al. (Golji & Mofrad 2010). The PDB structure contained all domains of vinculin but it lacked the disordered proline-rich region, which was generated using homology modeling. It should be noted that the bound structure of vinculin was minimized and equilibrated for a sufficient prior to using it in the main simulations. The activated structure of α-actinin modeled in our previous study was utilized to form the α-actinin-vinculin complex. Finally, the full-length structures of

vinculin and α-actinin were put next to each other such that the Vinculin head was oriented towards its binding site on α-actinin and helices α1 and α2 were placed next to αVBS.

All simulations will be performed using NAMD (Phillips et al. 2005) and CHARMM27 force field (MacKerell et al. 2001). The system was minimized for 50,000 steps and equilibrated prior to the production runs, which were then used for all reported analyses. The pressure and temperature were kept constant at 1 atom and 310 K values, respectively, using the Langevin methods. The Particle Mesh Ewald (PME) was used to calculate electrostatic interactions. Periodic boundary condition was applied in all three directions and a 2 fs time-step was used in all simulations. The system was solvated using the TIP3P water model and the extra charge of the system was neutralized via adding counter ions to the system. The final ion concentration was set to 15mM, which was consistent with the physiological condition of the cytoplasm. The production run was 50 ns long and repeated three times in order to obtain statistically significant results. Post-processing of trajectories was done using the visual molecular dynamics (VMD) and Bio3D packages in R (Grant et al. 2006). For reviewing general principles of molecular dynamics, please see Chapter 2 of the present dissertation.

Results

Vinculin is a key mechanosensitive player in force transmission across focal adhesion structures. It contains binding sites for many proteins and thus acts as regulatory agent in both focal adhesion maturation and turnover. It interacts with α-actinin, which is primarily an actin cross-linking protein. There is one vinculin binding site on each α-actinin monomer (αVBS), which is within the R4 spectrin repeat and structurally proximal to the actin-binding site. However, this binding site is cryptic in the full-length structure of α-actinin and thus needs to be activated prior to vinculin binding. Therefore, it has been hypothesized that vinculin binding reinforces α-actinin/actin association. However, in the isolated vinculin in the inactive state, the actin-binding site is inhibited via other vinculin domains. It has been shown that the vinculin binding site of talin can activate vinculin when engaged with the D1 domain, which is completely exposed. The αVBS aligns well to the talin VBS but in the reversed orientation. The complex of αVBS and the isolated binding site on α-actinin showed a strong association. However, in the inactive conformation of vinculin, helices α1 and α2 that directly interact with αVBS are in contact and too close to the αVBS insertion. Therefore, αVBS was suggested to first dissociate α1 and α2 and then inserts itself in between them. Furthermore, it was shown that talin VBS results in rearrangement of helices in the vinculin head domain, which is referred to as the helical conversion. The αVBS was suggested to induce the same type of helical conversion in the vinculin head domain. However, the molecular mechanism of vinculin and α-actinin binding is not yet understood.

The interaction between different domains of α-actinin and vinculin

The full length crystal structure of both α-actinin and vinculin were placed next to each other in order to simulate their binding. The α-actinin molecule was in the activated conformation, as found in our previous study (Figure 4.2-1A). αVBS was bound to α1 and α2 helices through hydrophobic interactions (Figure 4.2-1B). However, after 20 ns, the CaM domain strongly engaged with vinculin but only via electrostatic interactions (Figure 4.2-1C). Furthermore, the αVBS was part of the rod domain and thus the interaction with the rest of the rod domain was monitored throughout the simulations.

Not only αVBS from the rod domain of α-actinin interacted with vinculin but also some other parts were involved. Particularly, vinculin did not show any notable interaction with the R1 repeat from the neighboring monomer (Figure 4.2-2A), while it engaged with R4 repeat strongly (Figure 4.2-2B). It should be noted that the αVBS was included in the R4-vinculin interaction energy calculations. Some hydrophobic and polar residues on R4 that contributed to vinculin binding were engaged with αVBS in the inactive conformation of α-actinin. The native structure of R4 (PDB ID: 1SJJ) has a triple helical conformation, while this conformation became partially unfolded upon α-actinin activation and vinculin binding maintained that conformation (Figure 4.2-2E,F). All key interactions with R4 specrin repeat is reported in Figure 4.2-2G. Bold residues were out of the αVBS segment and as shown they formed more than 50% of the total number of residues engaged with vinculin. Furthermore, only hydrophobic residues of αVBS interacted with vinculin, while both polar and hydrophobic residues of other regions in R4 gave rise to strengthening vinculin.

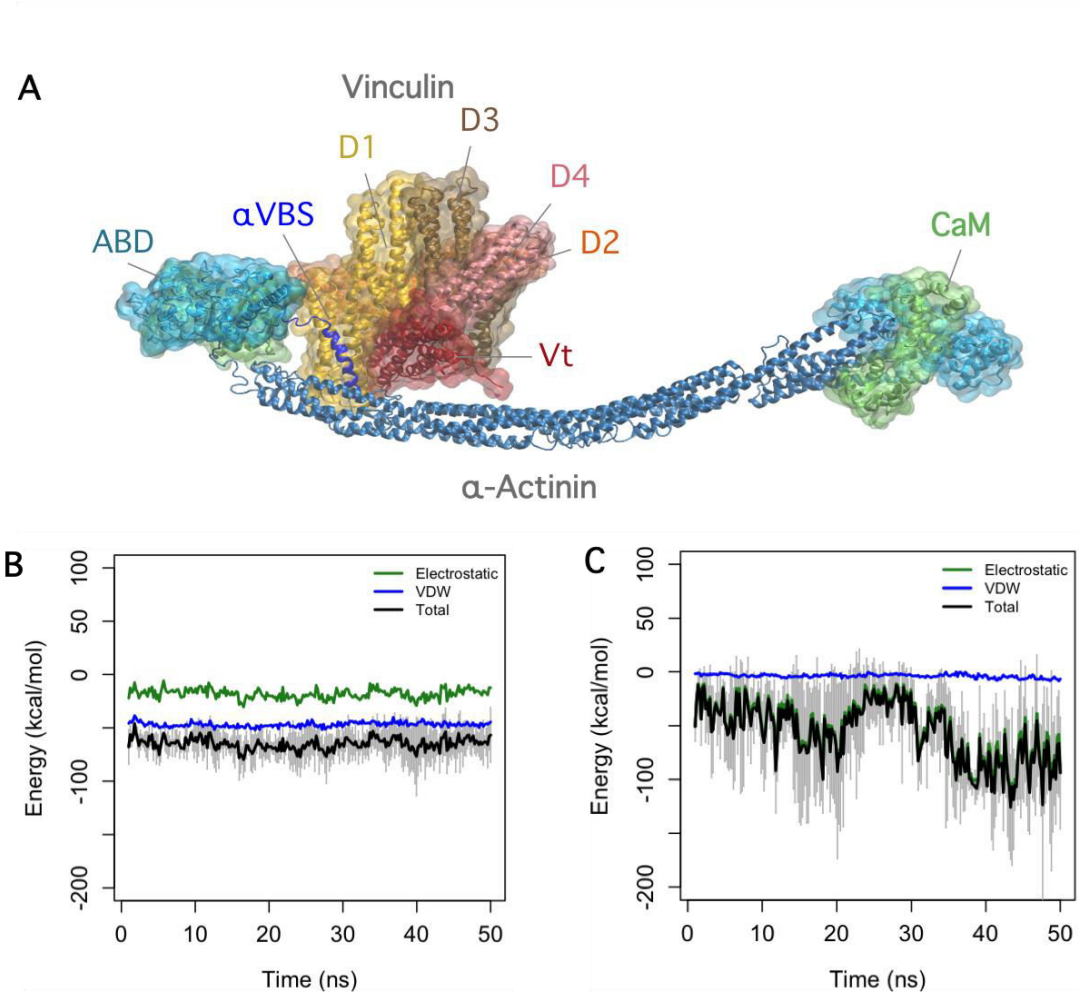

Figure 4.2-1. The interaction between activated α-actinin and vinculin. A) The final configuration of the α-actinin-vinculin complex. The αVBS interacts directly with the D1 domain of vinculin. Important domains of both molecules are labeled. B) The interaction between D1 and αVBS was formed via hydrophobic residues and remained stable throughout the simulations.

The mechanism of αVBS binding

The α1/α2 were associated through three main hydrophobic interactions as shown in Figure 4.2-3A. As αVBS moved closer, it disrupted α1/ α2 interactions and replaced them with new interactions with its own hydrophobic residues (Figure 4.2-3B). In order to quantify and find correlations between binding events, the interaction energy between α1/α2, α1/ αVBS and α2/ αVBS were all calculated. The α1/ α2 helices were rapidly dissociated as αVBS got engaged with α1 and α2 showing a strong correlation between the two. Thereby, our simulations confirmed that αVBS indeed separates α1 and α2 prior to inserting itself in between them. The bound configuration was stable for 50 ns of simulation.

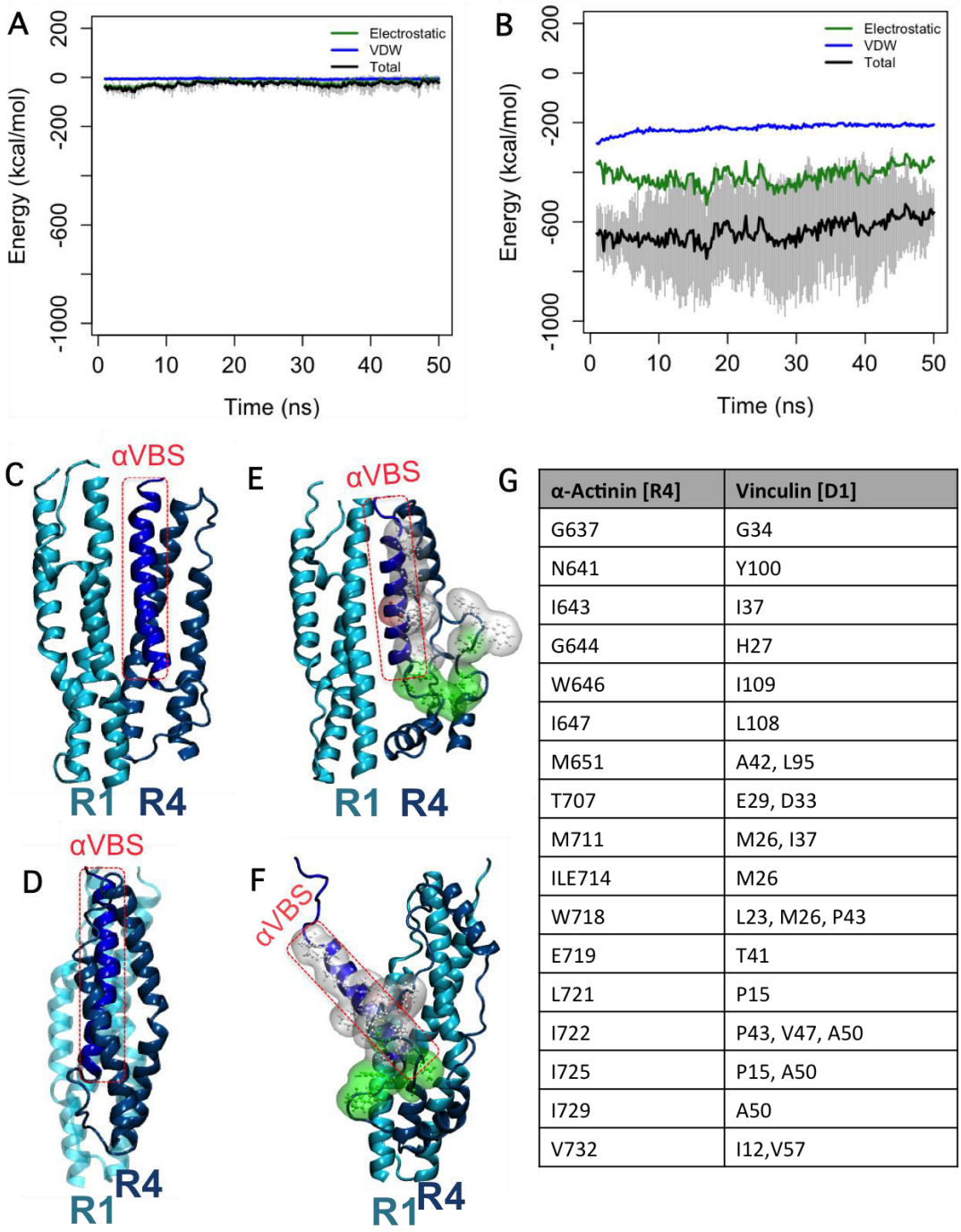

G

α-Actinin [R4]	Vinculin [D1]
G637	G34
N641	Y100
I643	I37
G644	H27
W646	I109
I647	L108
M651	A42, L95
T707	E29, D33
M711	M26, I37
ILE714	M26
W718	L23, M26, P43
E719	T41
L721	P15
I722	P43, V47, A50
I725	P15, A50
I729	A50
V732	I12,V57

Figure 4.2-2. The conformation of R1 and R4 spectrin repeats before and after binding to vinculin. A) The R1 spectrin repeat of the neighboring α-actinin monomer was only weakly associated with vinculin, while B) the R4 domain rod domain of α-actinin, which included the αVBS, firmly associated with vinculin through both hydrophobic and electrostatic interactions. C) The R1 and R4 repeats in the PDB structure (ID: 1SJJ) are nicely folded and the α VBS axis is almost parallel to the axis of the rod domain as also shown in the side view of R4 (D). E,F) The R4 structure was partially unfolded after binding to vinculin while αVBS was exposed. Important residues in vinculin binding are shown in bulky representation. Hydrophobic and polar residues are colored while and green, respectively. G) All key interactions are summarized in the table.

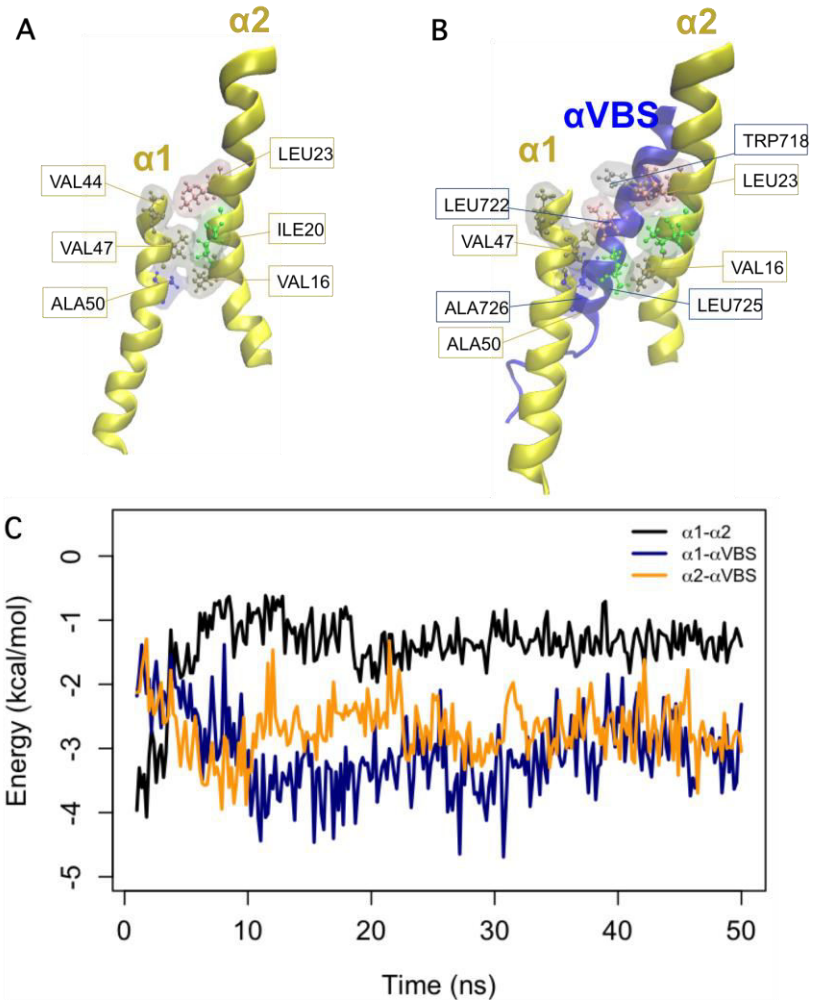

Figure 4.2-3. The main α-actinin binding site resides between helices α1 and α2 on the D1 domain of vinculin. A) Initially, α1 and α2 helices (yellow) were in contact through three main hydrophobic interactions as marked in the figure. B) However, these inter-helical bonds were disrupted by the insertion of αVBS (dark blue) between α1 and α2 helices and new interactions with αVBS were formed. C) The interaction energy between α1- α2 (black) was rapidly weakened by the insertion of αVBS, which replaced previous interactions by new ones with both α1 (blue) and α2 (orange).

Helical conversion after αVBS binding

The arrangement of helices in the initial configuration of the D1 domain is shown in pink in Figure 4.2-4. In the final configuration of the D1 domain (shown in red), the arrangement of helices changed upon αVBS binding such that the final structure seemed relatively twisted. In order to find the change in the relative orientation of helices, we found the angle between the principle axes of all pairs of helices in both initial and final configurations of the system as summarized in Table 1. The coloring of the table is

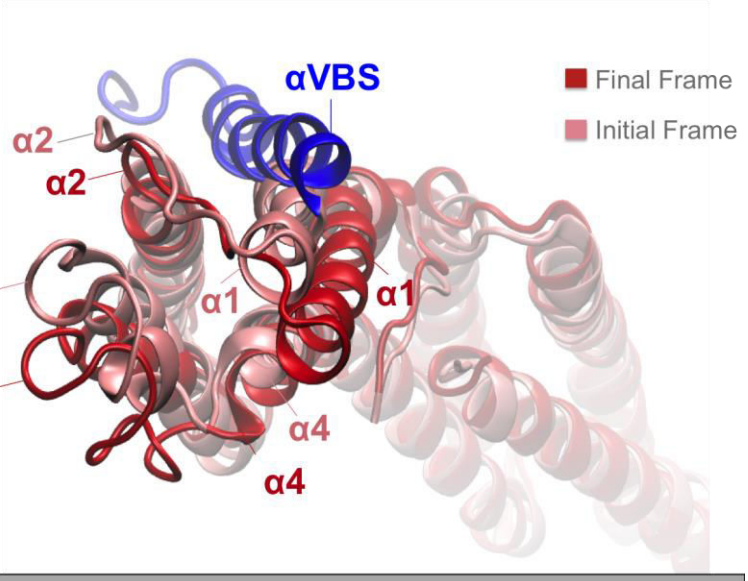

Matrix of angles formed between all pairs of helices in the D1 domain before and after binding to αVBS. The angle of the D1 helices with αVBS is also included.					
	α1	**α2**	**α3**	**α4**	**αVBS**
α1		**149.0±** 1.2	**26.5±** 2.7	**156.7±** 0.4	**151.8±** 2.3
α2	**153.0±** 1.6		**157.5±** 2.6	**24.8±** 1.8	**12.6±** 2.5
α3	**27.8±** 2.4	**159.3±** 5.3		**175.6±** 2.6	**148.9±** 1.3
α4	**156.1±** 2.8	**17.1±** 3.0	**174.6±** 3.3		**32.1±** 1.8
αVBS	**158.9±** 3.1	**19.7±** 12.8	**145.9±** 13.0	**29.2±** 9.6	

Figure 4.2-4. The helical conversion in the vinculin head. A) The initial arrangements of helices (pink) in the D1 domain of vinculin showed a clear rotation after αVBS binding (red). The table shows the angle between helices in both initial and final configurations, which indicates their relative rotation. Angle changes above 3 (degrees) are squared.

consistent with the frames shown in the above structure. Our results showed that the following pairs of helices underwent the most significant angle change: 1) α1-α4, 2) α2- α3 and 3) α2- α4. The αVBS was also included in the calculations in order to find its potential angle change with helices of the D1 domain. Interestingly, the most significant angle change was with α1 and α2 helices.

The effect of α-actinin on the global conformational changes of vinculin

It has been proposed that α-actinin binding can induce significant conformational changes within the vinculin structure such that vinculin can become activated for actin binding. However, it is not yet clear how αVBS binding can affect the interface of Vt with the rest of the vinculin structure. Thereby, we monitored all pairwise interaction energies between vinculin domains, which were found to be mostly electrostatic. No major global conformational changes were observed within the 50 ns of simulation as expected since domain separation occurs in microsecond to millisecond timescale. However, we investigated the stability of key interactions between D1 and Vt domains in the inactive conformation of vinculin. Specifically, A few salt bridges shown as SB1-SB4 in Figure 4.2-5A-B are responsible for holding D1 and Vt domains, two of which were disrupted upon αVBS binding.

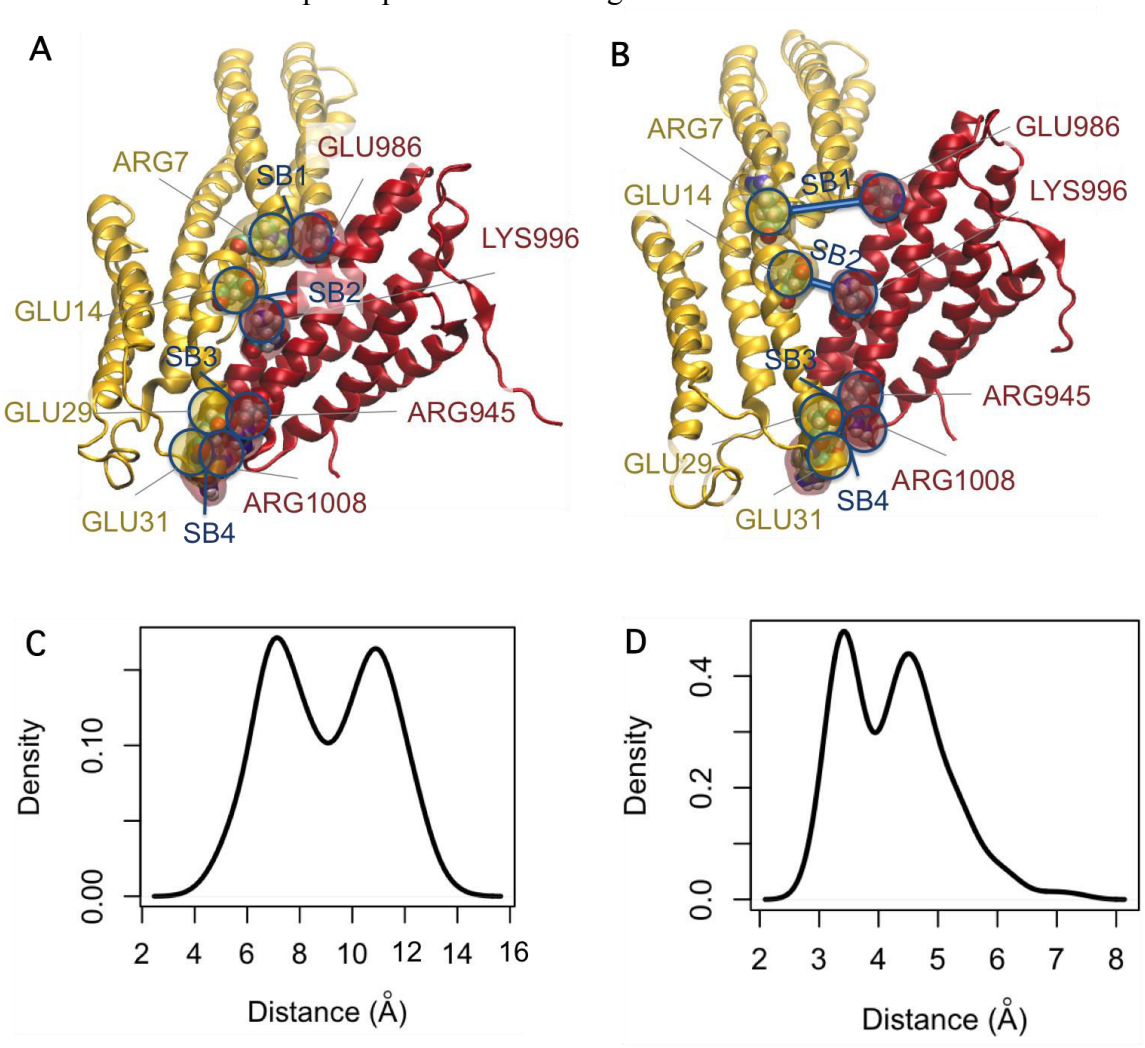

Figure 4.2-5. Important salt bridges holding D1 and Vt domains of vinculin. A) Four salt bridges maintaining the inactive conformation of vinculin are labeled as SB1 to SB4. B) A couple of salt bridges, SB1 and SB2, were broken upon αVBS binding to the D1 domain. C) The density function of the center of mass distances between R7 and E986 (SB1) and also D) E14 and K996 (SB2) manifested two peaks representing two equilibrium distances between these residues. The smaller distance corresponds to the salt bridge.

We monitored the distance between residues involved in the formation of SB1 and SB2 and graphed the density plot of the distance. The density plot is a smoothed and normalized histograms indicating the number of frames in which the system was found in a certain state. In this case, density plots had two peak values showing that two distance values were much more likely for both SB1 and SB2. The smaller peak value corresponded to the presence of salt bridges, while the larger value corresponded to the broken state. It should be noted that the center of mass distance was calculated and thus the distance values do not exactly match those between the charged side chains but the trend would definitely be similar for those.

The normal mode analysis of the vinculin molecule

Vinculin is a mechanosensitive protein and thus conformational changes can occur when an external mechanical perturbation excites its mechanical modes. Therefore, understanding and analyzing its natural modes can provide an important insight into functional regulation of this protein. We conducted the normal mode analysis for both the isolated and α-actinin-bound vinculin and compared them. The first few non-rigid modes, which had the lowest frequency and thus the highest possibility, involved the relative movement of the D4 domain with respect to the rest of the structure such that the angle between D4 and D3 is changed. Full vinculin activation involves separation of D1 from Vt but D4 also plays an important role as its motion can break Vt free from its inhibited conformation. Therefore, any excitation of this mode may result in vinculin activation. Furthermore, we did not observe any modes that directly involved Vt motion from D1 even in the isolated vinculin. This is another evidence that other conformational changes within the vinculin structure are most likely required prior to the actual activation of this molecule.

The shadow around the vinculin structure shows the backbone motion of vinculin in its lowest frequency normal mode (Figure 4.2-6A-B). The RMSF of the atoms quantifies the average fluctuations of each Cα atom along the sequence (Figure 4.2-6C). Domain D2, D3 and Vt experienced minimal motion in the isolated vinculin, while the flexible proline-rich loop region underwent the largest motion as shown in the RSMF plot (Figure 4.2-6C). Both D1 and D4 domains moved relative to all D2, D3 and Vt in the unbound state of vinculin. The D1 (residue 1 to 251) and part of D2 (residues 252 to 300) domains experienced relatively high fluctuations. The D4 domain starting from residue 720 to 837 also showed higher fluctuation than D1 but lower that the loop region.

α-Actinin binding significantly altered the normal modes of vinculin (Figure 4.2-6B). It changed the relative motion of D4 and in the first few modes such that the whole molecule was moving more like a rigid body. Even the motion of the prolin-rich loop region was restricted to a great extend. The reason was a key salt bridges formed between E883 of vinculin and K705 of α-actinin. The D1 domain was engaged with αVBS, its motion was slightly different than the rest of the structure. The RMSF plots showed that the range of fluctuations were much smaller in the presence α-actinin confirming that the D1 domain had a slightly different fluctuations and the flexible loop region had the highest RMSF as expected. Furthermore, vinculin tail is completely trapped between α-actinin's rod domain and vinculin head and thus a forces cannot be directly applied to this domain. However, we observed that binding to α-actinincould changed the intramolecular interactions in vinculin and resulted in the disruption of a couple of salt bridges in the absence of cytoskeletal forces.

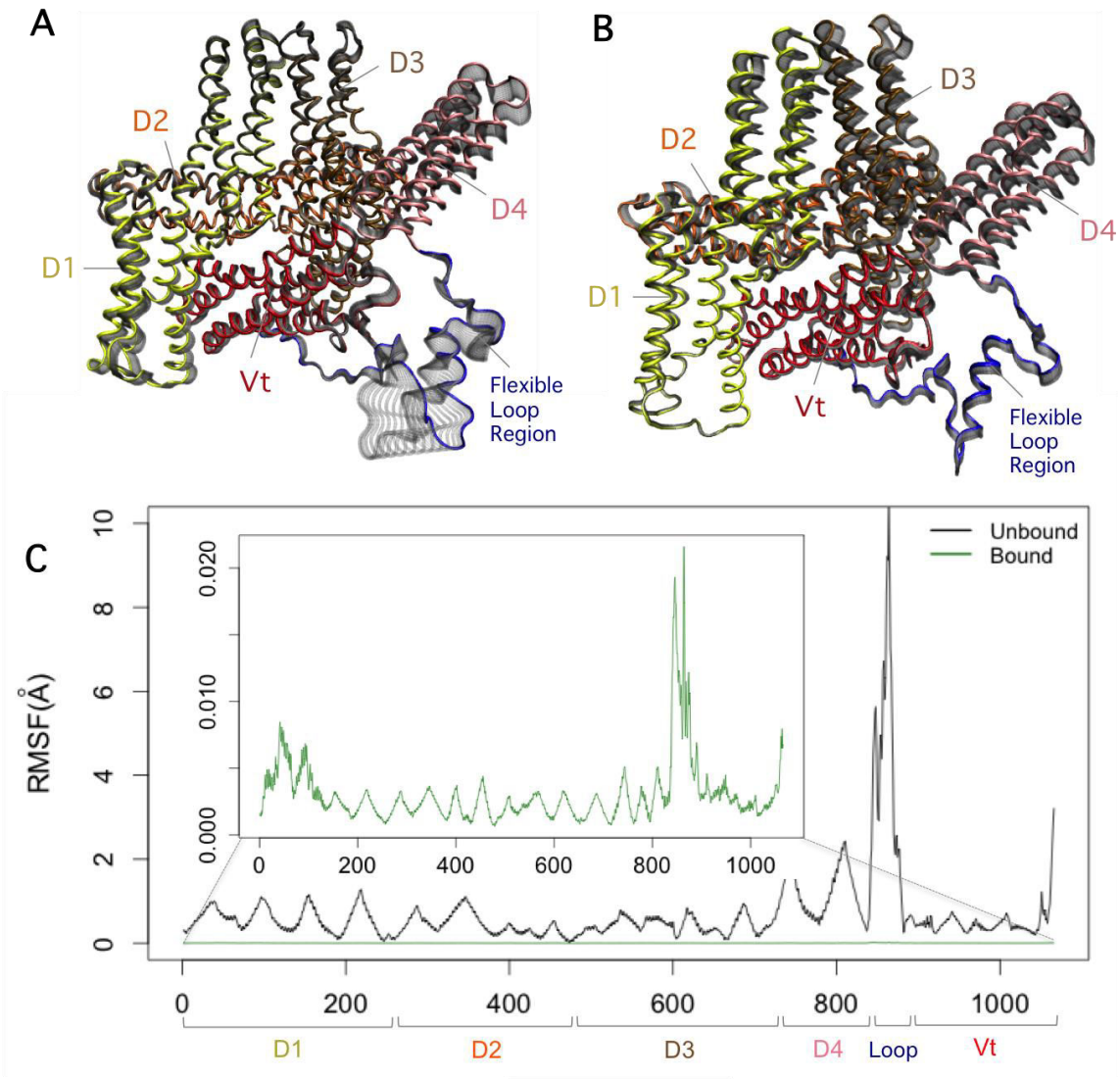

Figure 4.2-6. The normal mode analysis of vinculin before and after binding with α-actinin. A) The first few natural mode of isolated vinculin involved movements of both D4 and D1 relative to the rest of vinculin structure. B) However, in all natural modes of the α-actinin-bound vinculin, the whole structure of vinculin moved more as a rigid body and no relative motion of neither D4 nor D1 were observed. The Shadow around the structures are the backbone in different stages of motion. The RMSF plot of the first natural modes of C) isolated vinculin showed a much higher order of fluctuations compared to D) the α-actinin-bound vinculin.

Discussion

Focal adhesions grow in size as actomyosin contractile forces are transmitted through actin filaments resulting in changes in the stress distribution applied over individual focal adhesion proteins (Rayment et al. 1993). α-Actinin has an interesting spatial and temporal distribution as it binds to various proteins across focal adhesion layers and is also present in both early focal complexes and mature focal adhesions (Otey et al. 1990; Pavalko et al. 1991). As forces are increased, more vinculin molecules are recruited to focal adhesion assemblies and reinforce the coupling between focal adhesion players and the actin cytoskeleton mainly through actin binding (Galbraith et al. 2002). Vinculin is a key regulator of focal adhesions. It enhances

association between actin cytoskeleton and integrin receptors via key focal adhesion proteins, e.g. α-actinin and talin. It is well established that vinculin serves as a mechanosensor since it undergoes conformational changes in response to mechanical stress. It is highly involved in force transmission machinery in the force transduction layer.

Our results showed that vinculin head rapidly formed a strong interaction with αVBS that remained stable throughout the simulation. The mechanism of this binding was consistent with that reported by Bios et al. Specifically, helices α1 and α2 of the vinculin tail first became separated due to the competition of αVBS for the hydrophobic residues on these helices. αVBS then inserted itself in between helices of the D1 domain and forming hydrophobic interactions that replaced their old bond. The final equilibrated structure from our simulations was consistent with the crystal structure of the vinculin head in complex with αVBS (PDB ID: 1YDI). The alignment between primary sequences of αVBS and talin indicated that αVBS bound to the vinculin head in a reversed orientation relative to the bound form of talin VBS. Interestingly, our results showed a similar binding mechanism to vinculin and talin VBS (Izard et al. 2004) in terms of first breaking the α1- α2 interaction followed by a strong binding.

Although αVBS was identified as the primary binding site for vinculin, our results showed that other α-actinin domains could also participate in the interaction between vinculin and α-actinin. Specifically, the CaM domain and its attached spectrin repeat (R4) both associated with vinculin, while R1 spectrin of the neighboring monomer showed no interaction. Interactions with R4 maintained the unfolded structure this repeat in the activated conformation of α-actinin. These interaction are complementary to αVBS interaction and can only form when αVBS gets fully engaged with vinculin The CaM domain associated after about 10 ns of simulation, which indicated that stabilized αVBS binding acted as an anchorage required for the CaM domain binding. Furthermore, the R4 spectrin repeat contained αVBS and inevitably interacted due to its spatial proximity to vinculin. The van der Waals interaction energy was 200 kcal/mol out of which only 100 kcal/mol was attributed to αVBS, the rest are with other hydrophobic residues originally keeping αVBS in its autoinhibited conformation. Relatively unstable electrostatic interactions also formed with the surface of R4 resulting in a total energy of about 600 kcal/mol. It should be emphasized that anchoring vinculin through αVBS was primarily required for complex formation.

One of the important side effects of αVBS binding to vinculin head is helical conversion, i.e. rearrangement of helices in the D1 domain. Our results indeed showed changes in the relative angles of D1 helices after αVBS binding as summarized in Figure 4.2-4. The relative angle of α1 was changed most significantly due to direct interaction with αVBS. Such helical conversion was shown to occur upon talin VBS binding and was proposed to be important for vinculin activation (Nhieu & Izard 2007). We certainly observed rearrangement of helices in the D1 domain of vinculin (see Figure 4.2-4).

Although 50 ns of simulation was not sufficient to capture a global conformational change, our results suggested that α-actinin binding to vinculin head may prime the autoinhibited structure of vinculin for activation. Previously it was shown that vinculin activation does not necessarily involve complete separation of head and tail but rather vinculin undergoes a conformational change in which Vh1 movement relative to Vt is sufficient for exposing actin binding site on Vt. Although we did not observe any major changes in the intra-domain interactions, two key salt bridges were broken upon αVBS binding, likely reducing the stability of the autoinhibited conformation of vinculin as well as the activation forces.

Furthermore, the normal mode analysis suggested that αVBS binding limited average fluctuations of vinculin atoms significantly. Also, the relative motion of domains D1 and D4 was changed to more of a rigid-body type of motion after αVBS binding. Since the relative motion of domains is removed from the natural modes of vinculin upon αVBS binding, breakage of salt bridges in response to αVBS binding may act as an alternative activation mechanism. Moreover, the disordered proline-rich neck region underwent the highest fluctuations as expected.

There are two possible mechanisms by which α-actinin may contribute to vinculin-induced focal adhesion maturation: 1) α-Actinin bound to the β-integrin tail or other focal adhesion proteins undergo cytoskeletal forces, which regulates α-actinin's affinity for vinculin binding. This most likely leads to vinculin recruitment to focal adhesion (Figure 4.2-7A). 2) α-Actinin and vinculin may bind and travel to focal adhesion as a complex as shown in Figure 4.2-7B. As shown previously, α-actinin activation for vinculin binding does not necessarily require an external mechanical stimuli even though applying forces may facilitate this process (Shams et al. 2012).

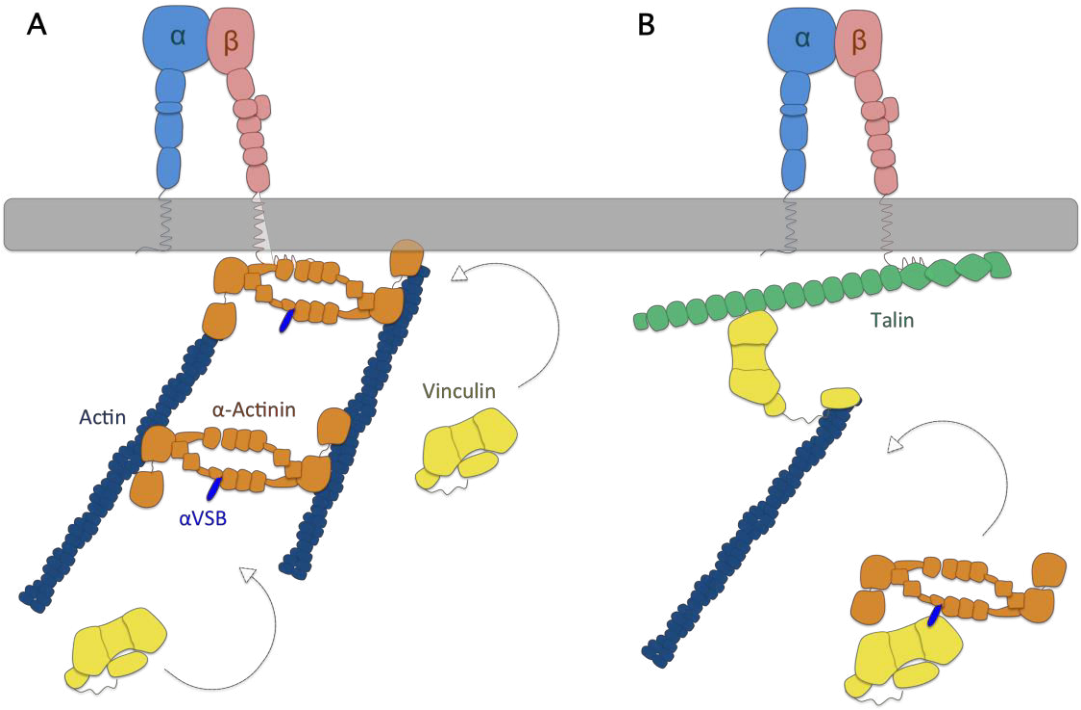

Figure 4.2-7. α-Actinin may bind to vinculin both inside and outside of adhesion complexes. A) α-Actinin bound to focal adhesion proteins such as integrin experiences cytoskeletal forces, which regulates its activity for vinculin binding. This in turn results in vinculin accumulation in focal adhesions. B) α-Actinin and vinculin may bind in the cytoplasm and travel to focal adhesion as a complex.

CHAPTER 5: Regulatory mechanisms of the actin cytoskeleton (The actin regulatory layer of focal adhesions)

Section 5.1 Dynamic regulation of α-actinin's calponin homology domains on F-Actin[1]

The cytoskeleton mediates cell motility and adhesion that are critical for many cellular functions such as differentiation, proliferation and growth (Mofrad & Kamm 2011; Anitei & Hoflack 2012). Cytoskeletal dynamics is central to the force transmission machinery involved in converting mechanical stimuli into biochemical signals via the process of mechanotransduction (Jahed et al. 2014; DeMali et al. 2014). α-Actinin accounts for the highly dynamic behavior of several actin assemblies (Edlund et al. 2001; Kim et al. 2012) and is crucial for cytoskeletal stabilization in both muscle and non-muscle cells (Blanchard et al. 1989). Previous studies have shown that mutations in α-actinin leads to several diseases including muscular dystrophies and cardiomyopathy (Hayashi et al. 2004). Mutation at lysine 255 to glutamate in human α-actinin-4 results in a form of kidney failure, which occurs due to an increased affinity of α-actinin for actin that directly affects the cytoskeletal dynamics (Weins et al. 2007; Galkin et al. 2010).

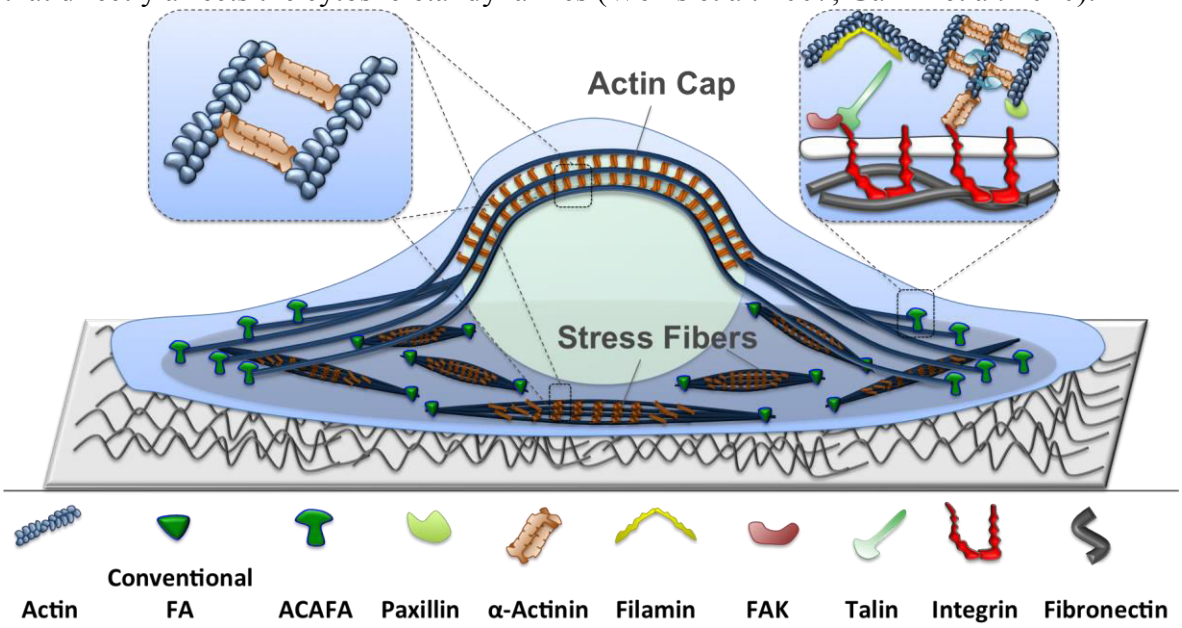

Figure 5.1-1. Cytoskeletal structures are linked to both focal adhesions and cell nucleus. α-Actinins are involved in formation and regulation of various cytoskeletal structures in adherent cells including stress fibers and actin caps. Stress fibers link two conventional focal adhesions and are made up of actin filaments crosslinked by α-actinins (shown in the left insert). The actin cytoskeleton can also be directly linked to focal adhesions through α-actinins (shown in the right insert). Actin caps also have a similar composition as stress fibers but are connected to ACAFA at their ends and are directly associated with the nucleus.

α-Actinin can crosslink both parallel and anti-parallel actin filaments in various cytoskeletal structures and allows emergent actin bundles to exhibit different polarities

[1] The content of this Chapter has been published in Biophysical Journal, Volume 110, Issue 6, 29 March 2016, Pages 1444–1455 (Shams et al. 2016).

(Hampton et al. 2007). For instance, stress fibers are force-bearing actin bundles formed by highly organized α-actinin networks (Hotulainen & Lappalainen 2006). Actin caps are also actin assemblies that directly connect the cell-substrate adhesions to the nucleus and are extended along the polarization axis of the cell as shown in Figure 5.1-1 (Kim et al. 2012; Chambliss et al. 2013). It has also been observed that α-actinin could link two points on a single actin filament, suggesting that the α-actinin function is tightly associated with its interesting angular and linear elastic properties (Hampton et al. 2007).

α-Actinin is a highly mechanosensitive molecule and has many important binding partners among focal adhesion players (Shams, Golji & Mohammad R. K. Mofrad 2012; Bois et al. 2005; Roca-Cusachs et al. 2013a; Hampton et al. 2007; Edlund et al. 2001; Hotulainen & Lappalainen 2006). For instance, vinculin has a crucial role in force transmission and is recruited to the high stress regions in focal adhesion (Carisey et al. 2013; Lee et al. 2008; Carisey & Ballestrem 2011; Holle et al. 2013). Its simultaneous interaction with actin and α-actinin reinforces the α-actinin-actin complex and possibly affect the local stiffness of the cytoskeleton (Bois et al. 2005). Vinculin's binding site on α-actinin (αVBS) is within the fourth spectrin repeat (R4) and is likely to be mechanically regulated (Shams, Golji & Mohammad R K Mofrad 2012). α-Actinin can also directly link the actin cytoskeleton to the integrin receptors through its rod domain and contribute to both formation and maturation of focal adhesions (Roca-Cusachs et al. 2013b; Otey et al. 1993; Tadokoro et al. 2011).

The CH domains are likely to be mechanically regulated and can either take a closed or an open conformation. It has been shown that the open conformation, in which the CH domains are dissociated, has a higher affinity for actin as shown in Figure 5.1-2C (Galkin et al. 2010; Borrego-Diaz et al. 2006). The CH1 domain contains the main actin binding sites that are mostly located on the protein surface except for ABS1, which is buried within the CH1-CH2 interface and only becomes accessible in the open conformation (Borrego-Diaz et al. 2006), thereby mutations that destabilize the interface, e.g. K255E may increase the actin binding affinity. It has also been shown that the CH1-CH2 fragment has a higher affinity for actin compared to the isolated CH1 suggesting a regulatory role for CH2 (Way 1992). However, the dynamic behavior of α-actinin during actin binding and the effect of ABD conformation on that are still elusive.

In this section, we study and characterize the binding between actin and two distinct ABD conformations of the full-length α-actinin using molecular dynamics (MD) simulations. We also investigate the effect of the K237E mutation in chicken α-actinin, which corresponds to the K255E mutation in human, on the actin binding strength by exploring interactions of the mutant α-actinin during actin association and comparing the free energy profile of the mutant against the wild type. Our results are consistent with recent experimental studies and provide new insight on the molecular details that can further be employed to design modern therapeutics for impaired cellular functions associated with the cytoskeletal structure and dynamics.

Materials and Methods

All simulations were performed using the NAMD molecular dynamics package (Phillips et al. 2005) and CHARMM27 force field (MacKerell, et al. 1998). The structure of the full-length α-actinin (Protein Data Bank (PDB) ID: 1SJJ) was used (Liu et al. 2004) to model interactions with three actin monomers (PDB ID: 3LUE) as shown in Figure 5.1-2A (Galkin et al. 2010). In the initial configuration of all binding simulations, the CH domains of the full-length α-actinin were positioned near two of the actin monomers isolated from the rest of the F-actin structure such that the ABD orientation relative to actin was similar to that in the structure

of the actin-ABD complex (3LUE). α-Actinin was then moved away from actin until a distance of 10 Å between the closest atoms of actin and those of α-actinin was reached. Constraints on the proteins were imposed during equilibration simulations allowing water layers to form between them.

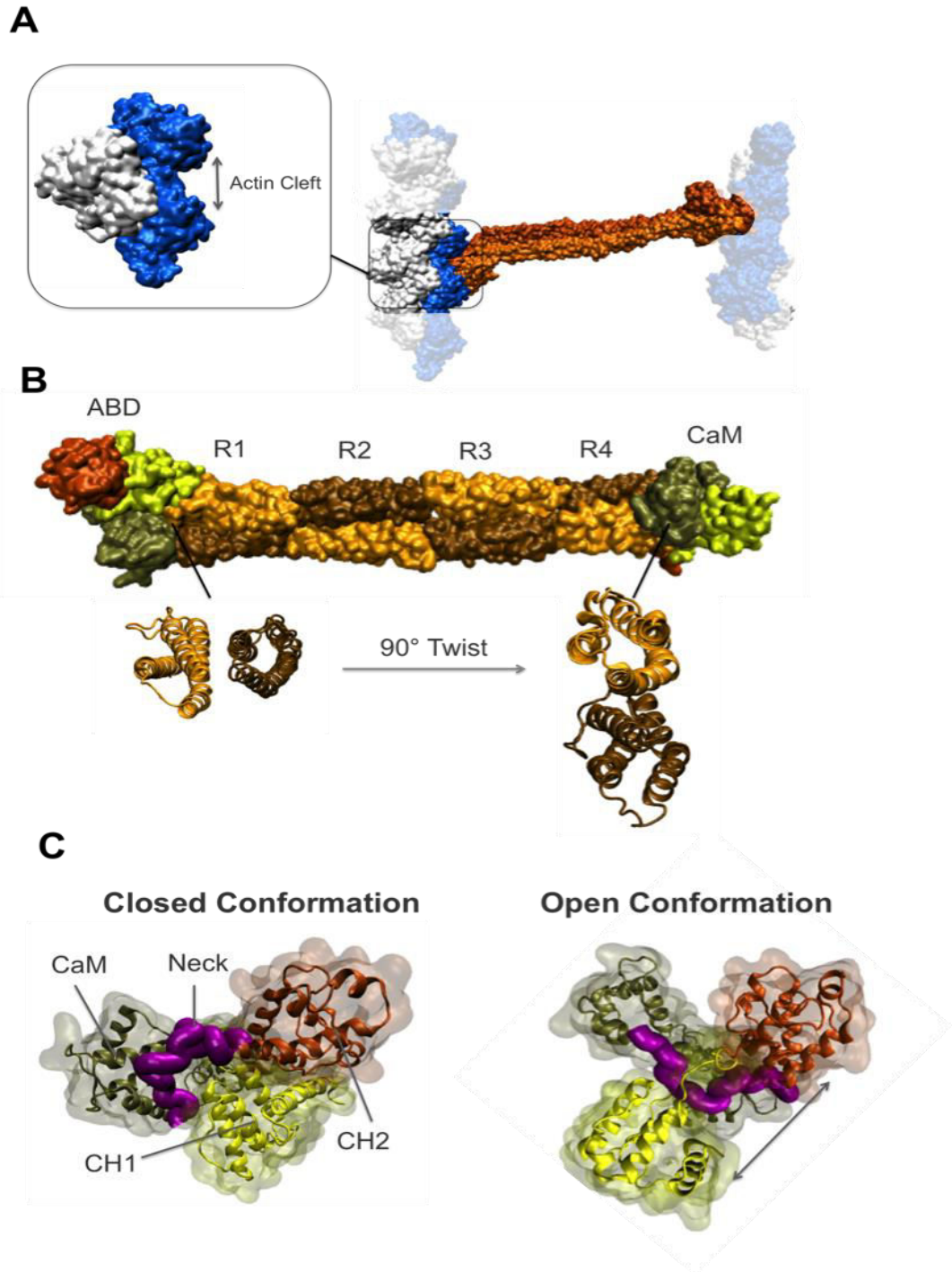

Figure 5.1-2. The α-actinin structure. Important domains of the full-length α-actinin structure (PDB ID: 1SJJ). A) The α-actinin (*orange*) molecule can crosslink two actin filaments each made up of two strands shown in *white* and *blue*. The F-actin model used in our simulations consisted of three actin monomers that represents the simplest form

of filamentous actin. Only two out of the three actin monomers can form a direct contact with α-actinin, which are referred to as the proximal actin monomers throughout the paper. A cleft is formed between the proximal actin monomers provided a space for α-actinin binding. B) The actin binding domain of α-actinin is located at the N-terminus of each monomer consisting of two calponin homology domains, CH1 (*yellow*) and CH2 (*dark orange*), followed by four spectrin repeats forming the rod domain (*sequentially colored in light orange and ochre*) and the CaM domain at the C-terminal end (*tan*). A 90° twist of the rod domain is indicated by the cross-sectional views of the two ends. C) The ABD domain takes two distinct conformations referred to as the closed (left) and open (right) conformations. In the closed conformation, CH1 (*yellow*) and CH2 (*orange*) are in contact and the neck region (*purple*) is positioned out of the CH1-CH2 interface, while in the open conformation CH domains are separated and the neck region sits in between them. The CaM domain (*tan*) also inserts itself between CH1 and CH2 in the open conformation.

Due to the elongated structure of α-actinin, a triclinic box was used with the box vectors of 41.2x18.2x15.8 nm^3, which satisfied the minimum image convention in all directions. A consistent version of the TIP3P water model with the CHARMM27 force field was used to solvate the simulation cell (Jorgensen et al. 1983). The charge of the system was neutralized and the final ion concentration of the simulation cell was set to 150 mM of KCl in order to mimic the physiological condition inside the cytoplasm. The total number of atoms including protein, water and ions reached 1,411,817.

The SHAKE algorithm was used to manage the bonds between hydrogens and heavy atoms. Electrostatic interactions were modeled using the particle mesh Ewald (PME) method and switching functions were applied to non-bonded interactions within the cut-off distance. All systems were initially minimized for 100,000 steps in order to remove all bad contacts and equilibrated for 1 ns using the NPT ensemble after which energy, pressure and the root mean square deviation (RMSD) of all simulations were monitored. The temperature was maintained at 310 using the Langevin dynamics and the pressure was kept at 1 bar with the Langevin piston. Periodic boundary conditions were applied in all three directions and a time-step of 2 fs was used. All production simulations ran for 60 ns using the NPT ensemble.

The umbrella sampling method (Torrie & Valleau 1977) was used to calculate the potential of mean force (PMF) for both wild type (WT) and mutated α-actinins. A range of different spring constants for the umbrella potential was examined in order to generate a series of smooth histograms with acceptable overlaps. The reaction coordinate was defined as the center of mass (COM) distance between the C_α atoms of CH1 (residue 26 to 146) and CH2 (residue 147 to 250) domains. In order to produce the initial configuration of each umbrella window, a steered molecule dynamics simulation was performed in which the CH domains were pulled against each other with a constant rate of 0.005 nm/ps until the open conformation was reached. The step size along the reaction coordinate was set to 1 Å, which resulted in an optimized overlap between histograms. The total sampling time for each umbrella window was 1 ns as the CH1-CH2 distance was restrained using a spring constant of 3000 kJ $Å^{-2}$ mol^{-2}. It should be noted that for some umbrella windows a stiffer spring constant (3500-4500 kJ $Å^{-2}$ mol^{-2}) was necessary to avoid off-center displacement of the histograms. The trajectory was saved every 0.2 ps to gather sufficient sampling data. The final PMF and histograms were obtained using the "g_wham" analysis tool in GROMACS.

The visual molecular dynamics software package (VMD) was used for visualizing and post-processing the results (Humphrey et al. 1996). Also, residue K237 was mutated to glutamate using the VMD plug-in (Humphrey et al. 1996). The mutated α-actinin structure was carefully minimized and equilibrated prior to putting it in complex with actin in order to allow structural adjustments and remove bad contacts around the mutation site. The normal mode analysis and

root mean square fluctuations were calculated using the Bio3D package in R (Grant et al. 2006). This work used resources of Extreme Science and Engineering Discovery Environment (XSEDE) (Towns et al. 2014). For reviewing general principles of molecular dynamics, please see Chapter 2 of the present dissertation.

Results

Cell motility is highly dependent on the dynamic nature of the actin cytoskeleton at both cellular and molecular levels. Networks of actin filaments crosslinked by α-actinin form both 2D and 3D cytoskeletal structures with various sizes and shapes. It has been shown that the dynamics of actin assemblies are determined by the time scale of crosslinking (Ehrlicher et al. 2015; Tojkander et al. 2012). Furthermore, it has been shown that the ABD conformation of α-actinin directly impacts actin association, thus mutations at the CH1-CH2 interface may interfere with the actin binding affinity of α-actinin. The K255E mutation in human α-actinin-4 is associated with a type of kidney disease and as shown by the fluorescence microscopy, this mutation triples the affinity of α-actinin for F-actin and increases the average contractile stress by generating larger forces on the substrate. This mutation maps onto K237E in chicken α-actinin used in our simulations (Figure 5.1-3). We investigated the underlying mechanism of α-actinin binding to F-actin and the effect of K237E mutation on both the ABD conformation and the strength of actin binding using all-atomic molecular dynamics simulations. Our results showed that the open conformation of ABD associated to actin with a higher strength and predicted a potential role for the CaM domain in regulating actin binding. Furthermore, our simulations indicated that the K237E mutation in chicken α-actinin decreased the level of forces required for opening the CH domains.

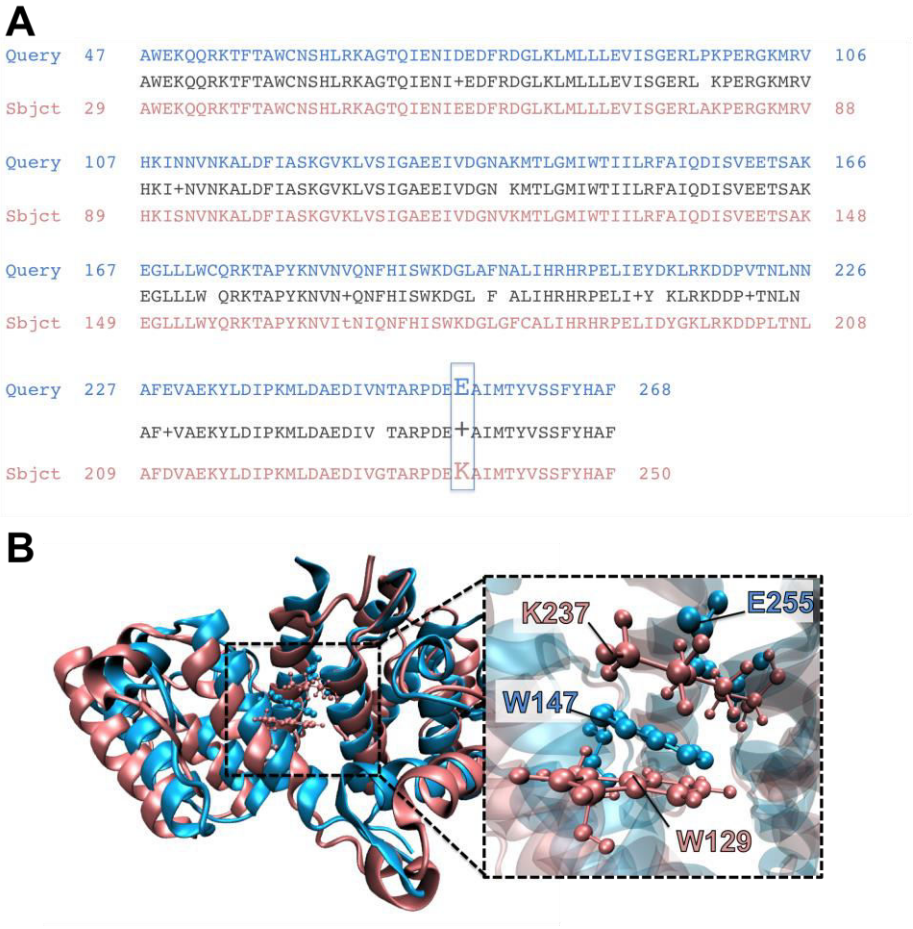

Figure 5.1-3. Sequence and structural alignments between human and chicken α-actinins. The location of K255E mutation on human's α-actinin (*blue,* PDB ID: 2R0O) was compared to chicken's α-actinin (*pink,* PDB ID:

1SJJ). A) are compared. The sequence alignment between the chicken and human α-actinins shows that residue 47 of human's α-actinin maps onto residue 29 of chicken's α-actinin and therefore residue 255 of human's α-actinin aligns with residue 237 of chicken's. B) Structural alignment also shows that the position of K237 in the chicken ABD overlaps with residue E255 in the human α-actinin interacting closely with a nearby tryptophan W147, which corresponds to W129 in the chicken α-actinin.

In the crystal structure of the smooth muscle α-actinin (PDB ID: 1SJJ), the ABD domain of each α-actinin monomer holds a different conformation (Figure 5.1-2). We explored the binding between each of the ABD conformations with an actin trimer, however only two actin monomers were proximal to the ABD and the third one integrated them together (Figure 5.1-2A). Also, in the initial configurations of all simulations, the distance between the surface atoms of F-actin and α-actinin was at least 10 Å, while binding sites faced each other in order to reduce the diffusion time. It should be noted that the actin trimer, also referred to as the trimer nucleus, is a core from which actin polymerization initiates and thus can be considered as the simplest form of the filamentous actin. Moreover, initial trials showed that the actin trimer was likely to drift away before it could form a complex with α-actinin. Therefore, constraints were applied to the center of masses of actin monomers in order to shorten the time of dynamic complex formation, The high diffusivity of the actin trimer is not physiologically realistic, since actin monomers are usually confined within larger filaments. Therefore, we put soft harmonic restraints on C_α of three residues namely G13, G74 and G156 of each actin monomer in order to inhibit large translational and rotational motions throughout the simulations. Using the full-length α-actinin instead of the isolated ABD allowed us to study correlations between the structure and dynamics of different α-actinin domains upon actin binding. It should be noted that the actin trimer was placed only at one end of the α-actinin molecule in each simulation. In order to avoid confusion and repetitive terminology, we labeled our simulations and ABDs as summarized in Table 5.1-1.

Table 5.1-1. Labels used to refer to simulations and ABD conformations

Definition	Label
Simulations in which the Open ABD of the Wild type α-actinin was placed near actin	OW
Simulations in which the Closed ABD of the Wild type α-actinin was placed near actin	CW
Simulations in which the Open ABD of the Mutant α-actinin was placed near actin	OM
Simulations in which the Closed ABD of the Mutant α-actinin was placed near actin	CM
The open conformation of ABD	oABD
The closed conformation of ABD	cABD

The effect of ABD conformation on the strength of actin binding and the cleft size

In the OW simulations (see Table 5.1-1), the CH1 domain formed a strong interaction (the average energy: -500±100kcal/mol) with actin after 30 ns that remained stable for the following 30 ns (Figure 5.1-4A). On the contrary, CH1 formed a much weaker interaction with

actin in the CW simulations (Table 5.1-1) with the average interaction energy of -68.8±37.7 kcal/mol (Figure 5.1-4B). Moreover, CH1 in the actin-associated open conformation of ABD (oABD) became engaged with both proximal actin monomers and formed three salt bridges with each as shown in Figure 5.1-4C, while part of the CH1 binding site in the closed conformation of ABD (cABD) was inhibited by CH2 and could only interact with a single actin monomer. Although the initial orientation of

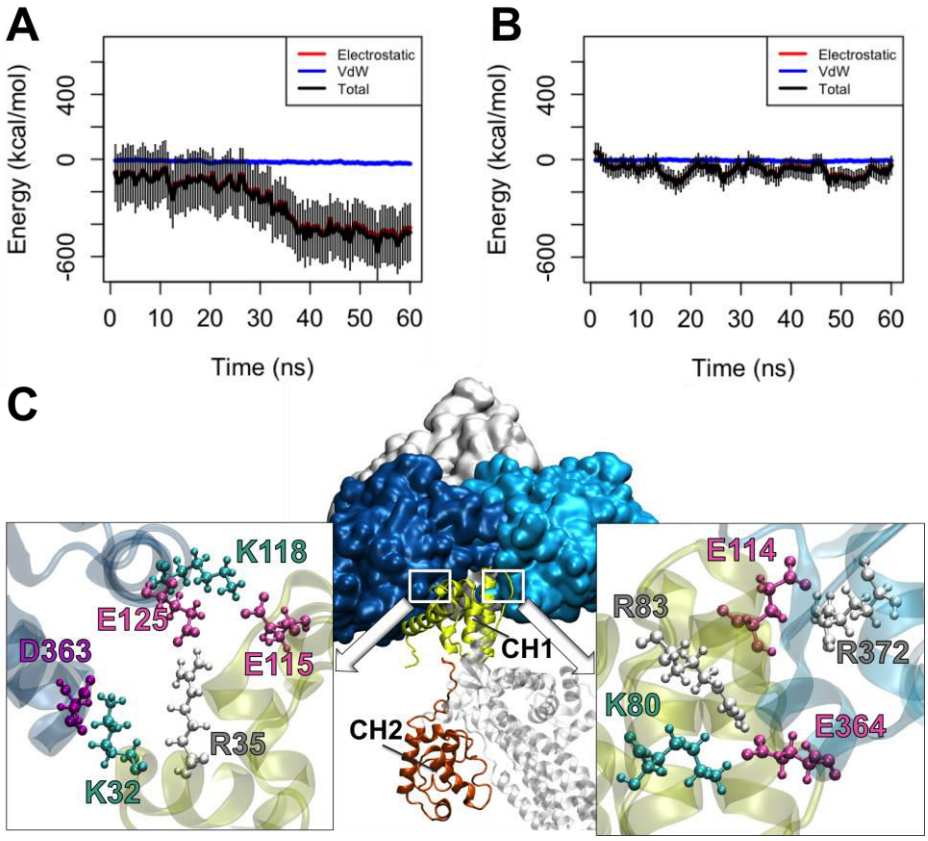

Figure 5.1-4. The interaction between different ABD conformations and actin. A) The CH1 domain of the oABD associated with actin after 30 ns with the final interaction energy of 550 kcal/mol averaged over three trials in the OW simulations. The interaction was stable for the last 20 ns of all trials. B) On the contrary, the CH1 domain of the cABD did not strongly associate with actin within the 60 ns of simulation. C) The interfaces between CH1 (*yellow*) of the oABD and two proximal actin monomers (*blue*) in the OW simulations are shown after 60 ns. Residues involved in all three salt bridges formed between CH1 and each actin monomer are highlighted (colors: arginine (*white*), lysine (*turquoise*), glutamic acid (*pink*) and aspartic acid (*purple*).

CH1 relative to actin was adjusted based on the cryo-EM structure, the CH1-actin interface was formed during the simulation and was not taken from the docked results reported by Galkin et al.

The solvent accessible surface area (SASA) of the cABD decreased for the first 20 ns after which the average SASA did not notably change. This implied that the contact area of the cABD with actin remained intact during that time (Figure 5.1-6). However, the detailed analysis of the binding trajectory revealed that the contact area of the cABD with actin dynamically changed in the last 35 ns and most interactions were transient.

The actin cleft between the two proximal actin monomers served as the binding pocket for the ABD (Figure 5.1-5A). The size of the cleft was notably decreased by the oABD binding,

while it only slightly increased upon the cABD association (Figure 5.1-5B-C). Comparing the density plots of the cleft size after the cABD and oABD binding showed a clear shift in the peak value of the cleft size indicating the sensitivity of the cleft to the ABD conformation (Figure 5.1-5D-E).

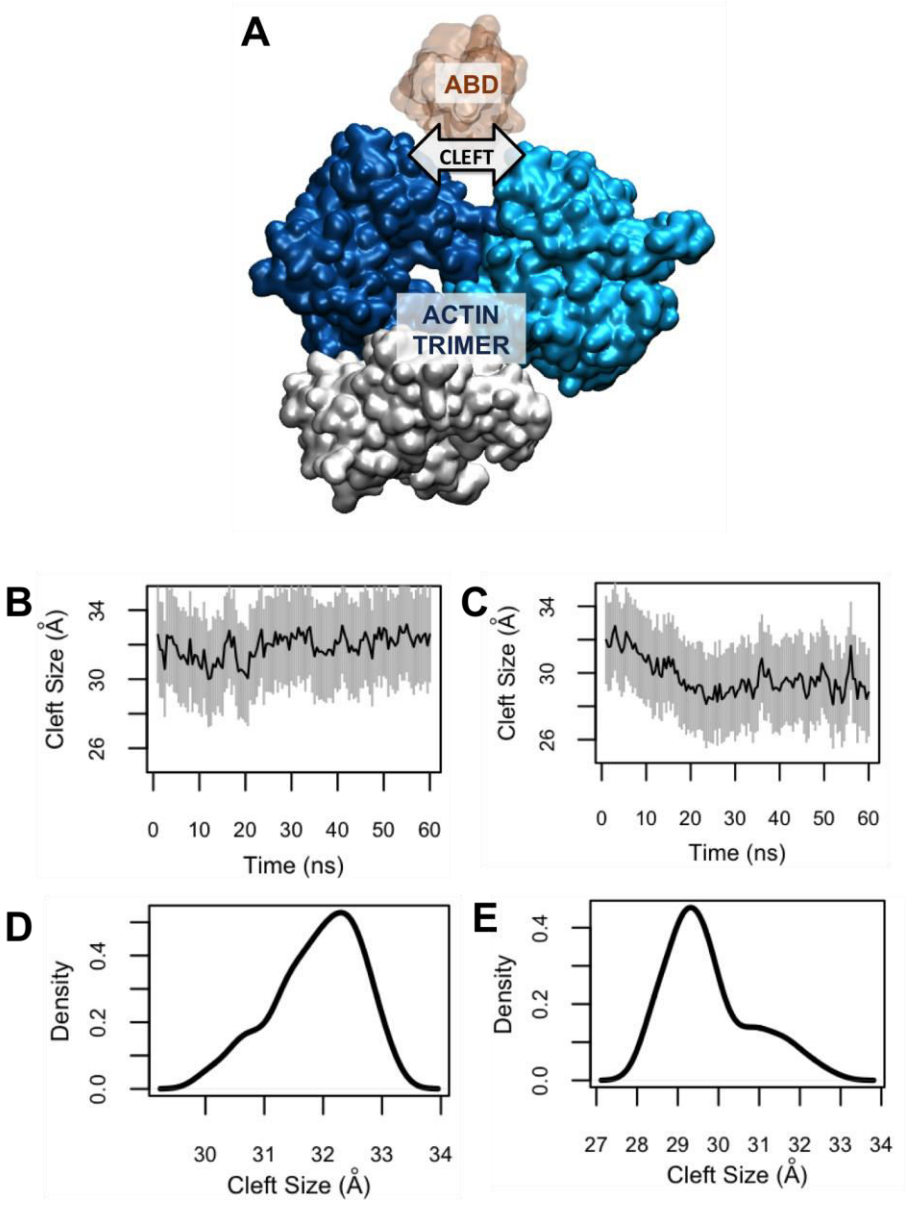

Figure 5.1-5. The size of the actin cleft was affected by CH1 only after binding to the open conformation of ABD. A) The structure of the actin trimer (*blue* and *white*) is shown in the presence of the ABD (*orange*). B) The actin cleft size remained fairly constant upon binding to the closed conformation of ABD (cABD), C) whereas it notably decreased after associating with the oABD. (D, E) The cleft size density plots are shown for a clear comparison. The peak value of the cleft after the oABD binding was 29 Å, while it was 32.5 Å for that after cABD binding.

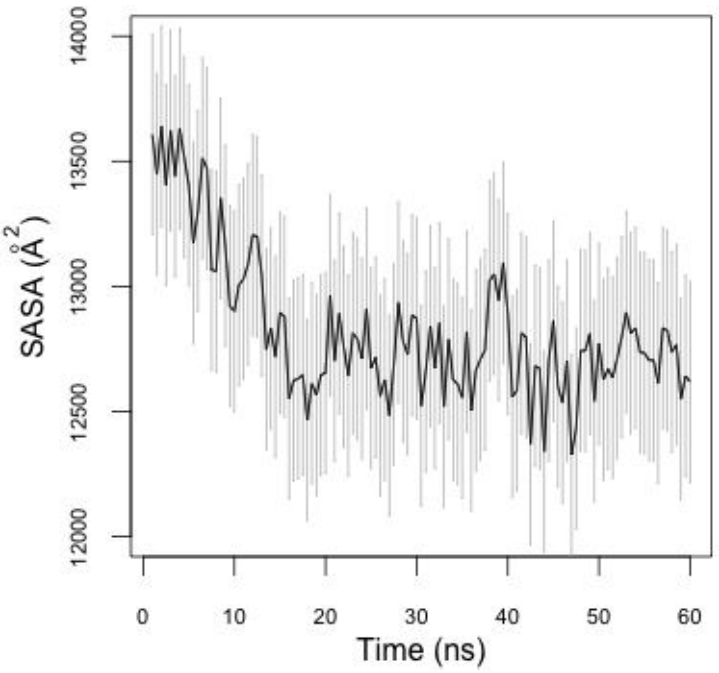

Figure 5.1-6. The average solvent accessible surface area (SASA) of CH2 in in the CW simulations. SASA decreased in the first 20ns but remained constant afterwards.

The ABD orientation relative to actin

The F-actin axis corresponds to the principal axis of the two proximal actin monomers in the actin trimer, therefore the relative orientation of the ABD along F-actin was easily quantified (Figure 5.1-7A). The oABD orientation in the OW simulations (Table 5.1-1) did not change drastically (Figure 5.1-7B), while the cABD rotated about 30° relative to its initial orientation with respect to actin in the CW simulations (see Table 5.1-1 and Figure 5.1-7C). Importantly, the initial and final orientations of cABD and oABD were different from one another as shown by the position of peaks in the density plots shown in Figures 5D and 5E.

We also examined three other initial orientations of the oABD relative to actin in order to study other potentially favorable orientations for actin binding. The oABD was isolated from the rest of the structure and rotated around an axis orthogonal to F-actin for 90°, 180°, and 270° with respect to the original orientation used in all other binding simulations (Figure 5.1-8A-B). The oABD was equilibrated in complex with the actin trimer in four different simulations and energies were calculated and summarized after 5 ns as shown in Figure 5.1-8C. The results showed that the 180° rotation of the oABD resulted in a very favorable binding to actin in a short time. Furthermore, the 270°- rotated oABD also formed a strong interaction suggesting that various binding modes may occur between actin and α-actinin.

The role of the CaM domain in regulating actin binding

Since the CaM domain closely interacts with the ABD, it can directly influence both the orientation and distance of the ABD from actin. The CaM domain next to the closed ABC (cABD) was initially associated with the flexible neck region linking the cABD to the rod domain in the CW simulations (see Table 5.1-1) but was disassociated (Figure 5.1-9A) as CH2 started to interact with actin around 15 ns (Figure 5.1-9B). Specifically, an important interaction

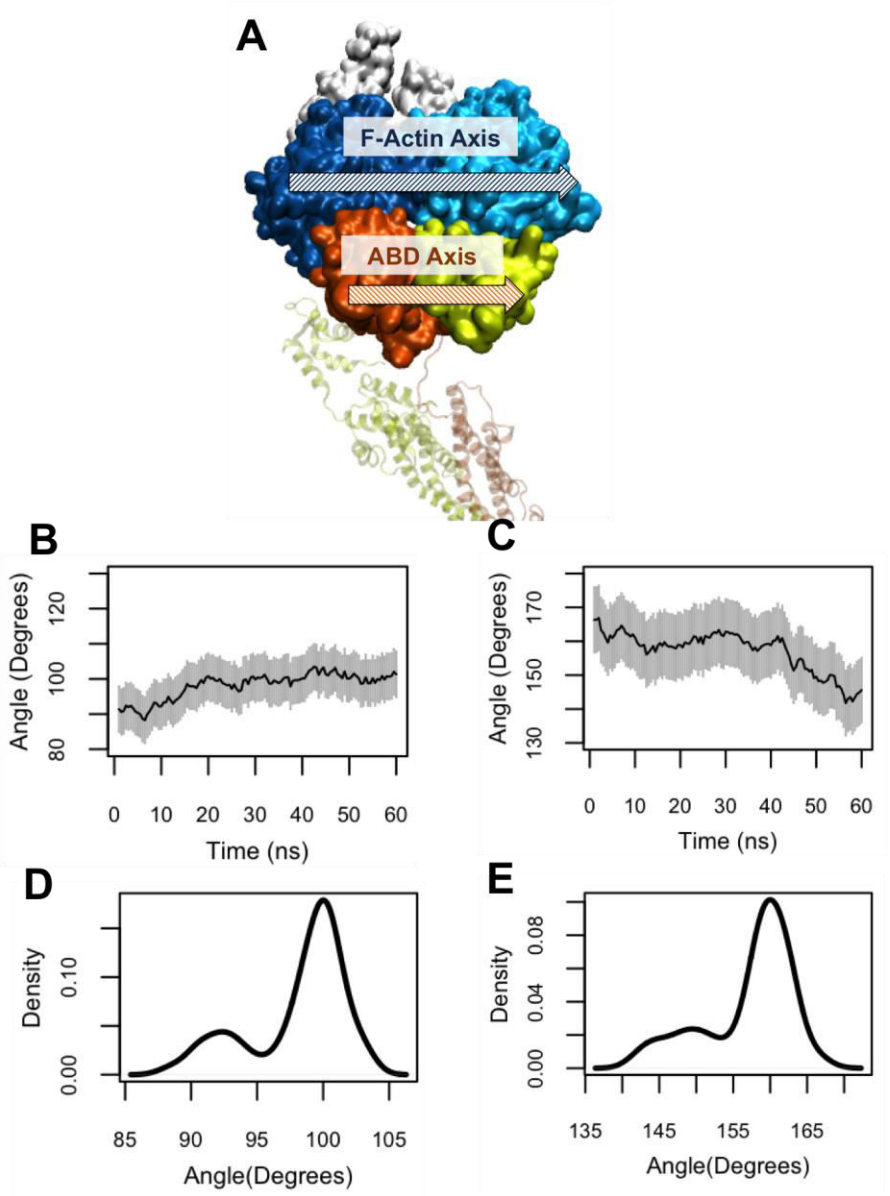

Figure 5.1-7. The angle between ABD and F-actin axes. A) The principal axes of F-actin (*Blue*) and the ABD domain (*orange* and *yellow*). (B, C) The angle between the principle axes of cABD and oABD relative to actin in the CW and OW simulations, respectively, showed a clear difference. B) This angle did not change significantly after the oABD binding and ranged between 90° to 100°, whereas C) it changed from 170° to 145° after the cABD binding. (E, F) Density plots show the peak value differences between the oABD (90°) and cABD (160°). Note that plots are presented in the same scale but different ranges.

between K265 in the neck region and D760 in the CaM domain was broken upon actin binding. In all simulations, the end-to-end distance of the neck region decreased pulling the cABD towards the rod domain. The EF1-hand motif engaged with the CH1 domain of the neighboring monomer after dissociating from the neck region.

A salt bridge between R157 and D851 linked the CaM domain and the cABD in two out of three CW trials but its disruption in the third CW simulation released the CaM domain and resulted in

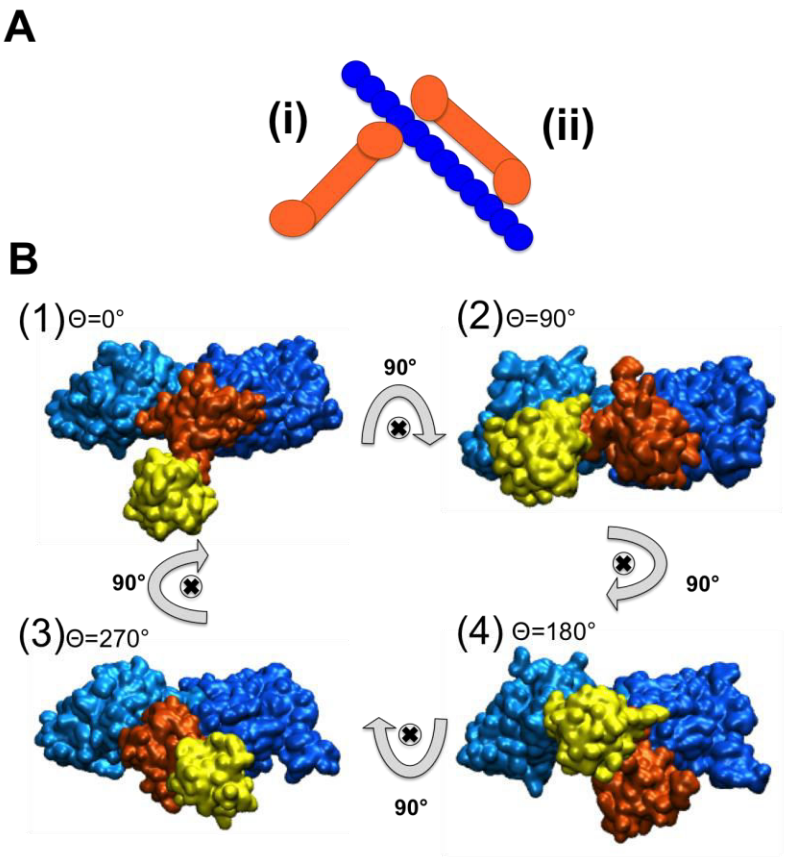

C

	vdW	Electrostatic	Non-bonded
0	-3.13461	-16.0191	**-19.1537308**
90	-3.9473	14.59553	10.64823462
180	-10.739	-126.446	**-137.185023**
270	-9.89444	-90.7407	**-104.083758**

Figure 5.1-8. Different orientations of the oABD relative to actin were examined. A) α-Actinin can either (i) cross-link two actin filament or (ii) bind to a single one and thus more than one initial configuration might be favorable. B) The oABD was isolated from the rest of the α-actinin structure from which four different orientations were produced by rotating the oABD around an axis perpendicular to the F-actin axis (shown by ⊗). C) Comparing the binding energies of all oABD orientations to actin showed that the 180° rotated oABD formed the strongest binding in a shorter time (5 ns) compared to the original orientation (0°) used in all 60 ns binding simulations. Also, the 270° rotated oABD also formed a strong interaction after 5 ns.

a more effective binding between CH2 and actin (Figure 5.1-9C-D). Only in this trial CH2 engaged with both proximal actin monomers and the interaction with the second monomer followed the disruption of the salt bridge. In two other trials, CH1 loosely associated with the second actin monomer blocking it from binding to CH2. Furthermore, the CaM domain itself associated with actin only in the presence of the salt bridge

Torsion angle and allosteric effects

The torsional motion was illustrated by calculating the angle between the ABDs of the two ends of α-actinin in both CW and OW simulations (Figure 5.1-10A). The maximum change in the angle relative to the first frame of the CW simulations was 20° (Figure 5.1-10B), which was two times higher than that of the OW simulations (Figure 5.1-10C). This difference probably suggests that actin binding at one end can be transmitted as a mechanical signal to the other end by triggering the torsional mode of the molecule. Both plots in Figures 7B and 7C indicate a single cycle of a periodic motion but the peaks occurred at different time points of the OW and CW simulations (Figures 7B-C).

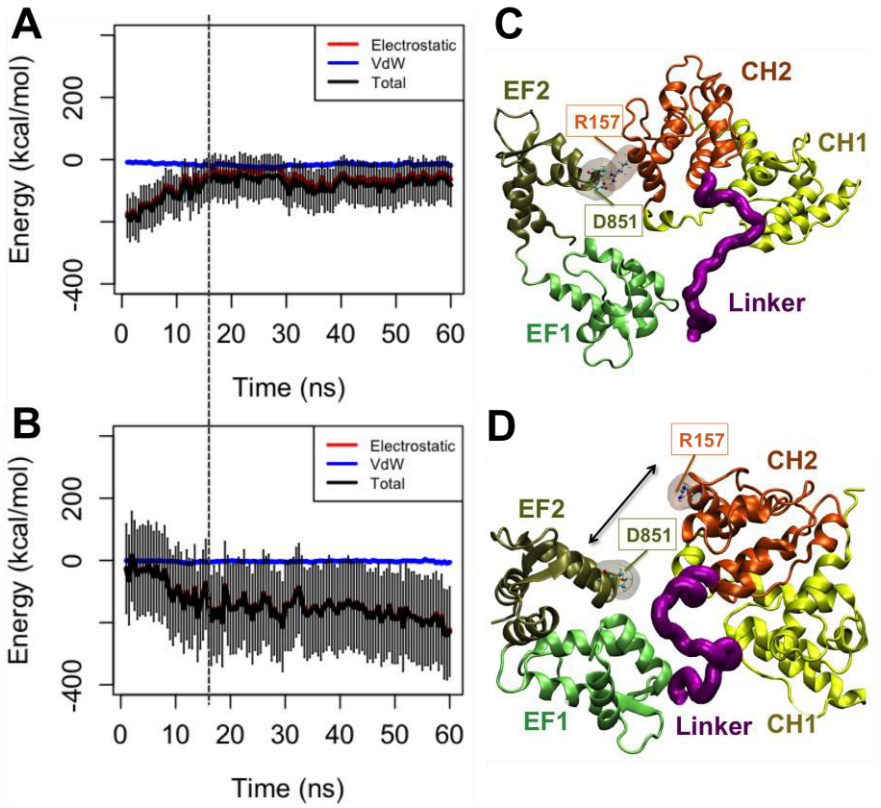

Figure 5.1-9. The CaM domain was released from the neck region as CH2 associated with actin in the CW simulations. A) The interaction energy between CaM and the neck region was reduced around 18 ns (indicated by the dashed line) as B) the CH2 domain got engaged with actin. In one of the three CW trials, a salt bridge between D851 in CaM and R157 in CH2 was released allowing CH2 to form a more effective interaction with actin.

The root mean square fluctuations (RMSF) were calculated for both α-actinin monomers in the CW and OW simulations (Figure 5.1-12). The rod domain consistently showed the lowest fluctuations in all simulations. The cABD of the actin-bound monomer and the CaM domain of the neighboring monomer seemed to be correlated in the CW simulations (dashed boxes in Figures 8A-B). The CH1 domain of the actin-bound oABD (dashed box in Figure 5.1-12C) showed lower fluctuations compared to that of the other monomer with the closed ABD (dashed box in Figure 5.1-12D).

The role of the K237E mutation and the potential of mean force

A mutant model of α-actinin was generated from the wild type (PDB ID: 1SJJ) and aligned with the initial configuration of α-actinin in both CW and OW simulations in order to investigate the effect of the K237E mutation on actin binding. The mutant model was minimized and equilibrated in isolation prior to using it in the actin binding simulations to allow for possible structural adjustments. Our results showed that the CH1 domain of the mutant α-actinin in OM simulations associated with actin with an average interaction energy of -188.9±74.2 kcal/mol that was slightly lower than that in the OW simulations (-284.6±155.6 kcal/mol). Furthermore, our

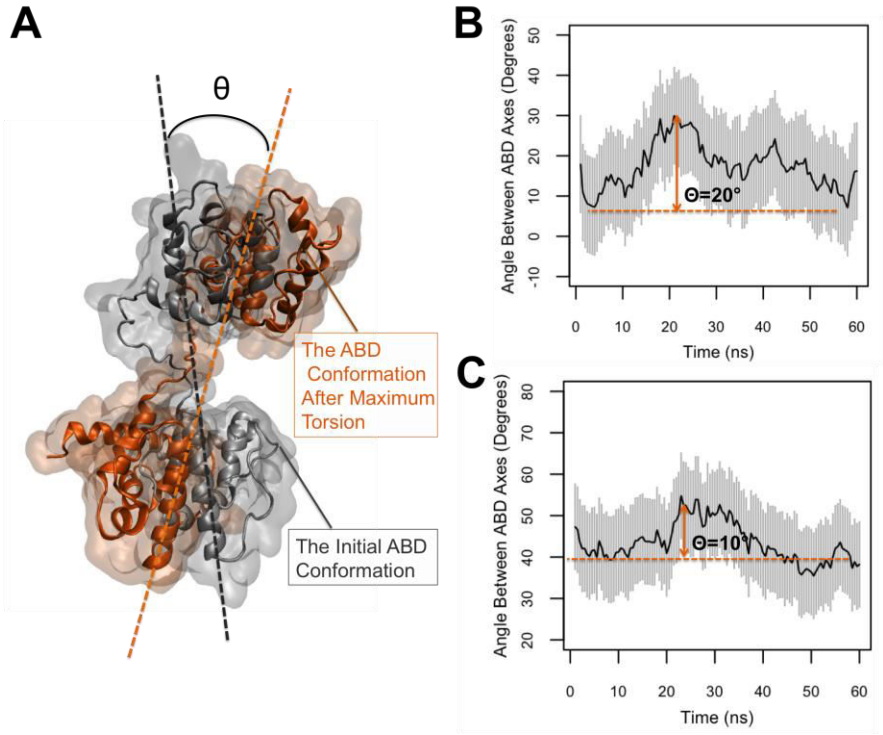

Figure 5.1-10. The twist of the α-actinin molecule. A) The symbol θ represents the maximum change in the angle between the ABD axes relative to the initial frame (maximum torsion). B) In the CW simulations, the value of θ averaged across three trials was 20° that was two times larger than that in C) the OW simulations.

results indicated that the binding between the mutant α-actinin and actin was less abrupt and gradually strengthened over the course of 60 ns, while that binding with the wild type α-actinin formed within the first 20 ns and remained stable for the following 20 ns (Figure 5.1-11).

Our results suggested that the interface of the CH domains did not significantly change upon the mutation. We also examined all interactions of K237 at the interface that could potentially be altered after the mutation. It was previously suggested that W147 in the human CH1, which maps to W129 in the chicken CH1 (Figure 5.1-3), forms a hinge-like connection with K255 in the human CH2 (K237 in the chicken CH2) maintaining the closed conformation (Weins et al. 2007). Our simulations also showed that the most significant interaction of K237 was with W129 (-6.1±2.3 kcal/mol) that was lowered after the mutation (-2.7±1.7 kcal/mol). Other nearby residues were W30, Q34, T37 and F38 but none of them showed a significant interaction. However, only Q34 formed a notable interaction with E237 in the mutant, which was not very stable (-7.3±6.3 kcal/mol). Furthermore, the interaction energy between CH2 of the mutant oABD and R1 of the same monomer was lowered to -66.8±26.2 kcal/mol from -173.7±34

kcal/mol in the wild type. Also, the distance between CH1 and CH2 was slightly smaller in the mutant than that of the wild type, which may allow for more spontaneous regulatory interactions.

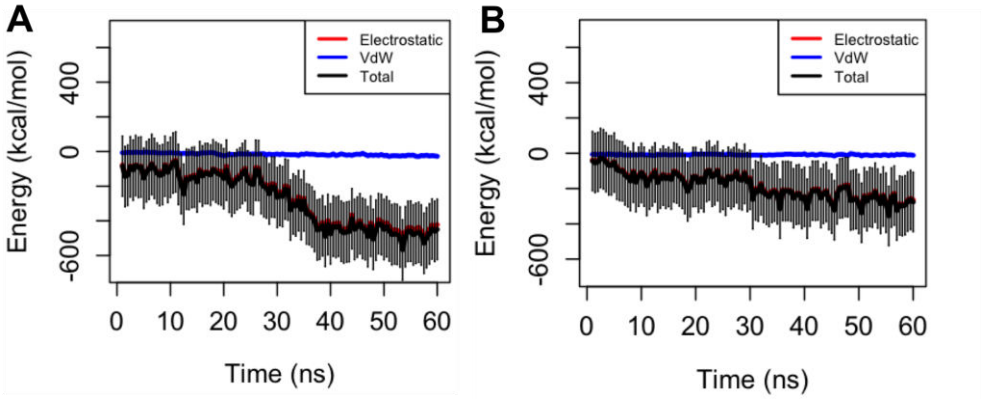

Figure 5.1-11. The interaction between CH1 and actin. The energy of A) the wild type α-actinin dropped more abruptly compared to B) the mutant α-actinin.

In order to estimate the free energy cost of changing the ABD conformation from closed to open, we used the steered molecular dynamics simulations to separate the CH domains of the cABD and produce an artificial open conformation. The closed-to-open trajectory was then used to extract initial configurations of the umbrella windows from which the potential of mean force (PMF) was calculated. Since the structure of individual CH domains are independent of whether hey are paired or not, the distance between them seemed to be a reasonable reaction coordinate for the PMF calculation.

The PMF profile of both wild type (black) and mutant (green) α-actinins are shown in Figure 5.1-13 in which the horizontal axis is the separation distance between the centers of masses of the CH domains. Although, the energy landscape is quite rough, the minimum corresponding to the closed conformation (~2.7 nm) was clearly similar between the wild type and mutant. The PMF profiles followed each other closely up to 3 nm but deviated from that point on and a new minimum was formed for the mutant at the open state.

Discussion

α-Actinin is a major cytoskeletal component involved in crosslinking actin filaments in stress fibers and linking them to focal adhesions as well as forming actin caps between the nucleus and adhesion sites. Therefore, any dysfunction of this protein can lead to serious pathogenic conditions mostly caused by the changes in its actin binding affinity. Although, it was shown that the ABD conformation is a deterministic factor in regulating the α-actinin function, current studies including the available crystal structures of ABD do not provide much information on the ABD dynamics neither in isolation nor during associating with actin. Certain point mutations in the ABD domain have been linked to human diseases (Galkin et al. 2010), however, possible regulatory mechanisms targeted by those mutations are not yet fully understood. In the present study, we investigated a mutation at residue K255 in the ABD of human α-actinin that results in late-onset form of kidney failure. To our knowledge, this is the first computational study on characterizing the effect of the K255E mutation in humans, which maps to the K237E mutation in chicken,on the binding between the full-length α-actinin and F-

actin compared against the wild type. Our simulations showed that the K237E mutation in chicken α-actinin reduced the
forces required for opening the CH domains. Moreover, our results indicated a clear favorability of the open conformation of ABD for actin binding and also predicted a role for the CaM domain in regulating actin association.

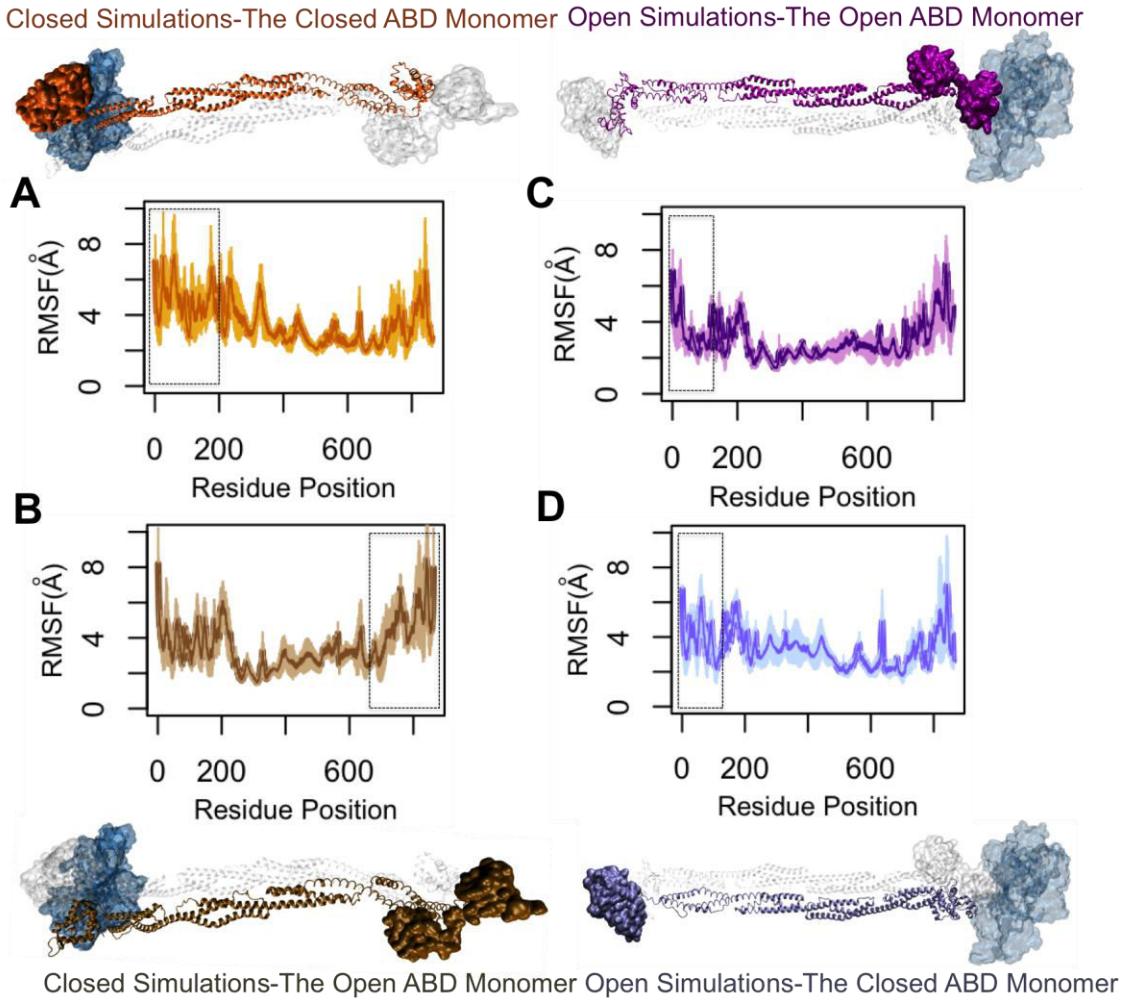

Figure 5.1-12. The root mean square fluctuations (RMSF) of α-actinin monomers both in bound and unbound states to actin. The rod domain had the lowest level of fluctuations in both CW and OW simulations. A) The cABD domain (residues 25-250) in the CW simulations (the *orange* α-actinin monomer) underwent a slightly lower fluctuations compared to B) the open ABD that was far relative to actin (the *tan* α-actinin monomer). However, the CaM domain near actin (the C-terminal of the monomer with open ABD) showed a similar level of fluctuations to the cABD of its neighboring monomer in the CW simulations (dashed boxes). C) In the OW simulations, the RMSF of the CH1 domain of the oABD was lowered upon actin binding (the *purple* α-actinin monomer) and was clearly different from that of the CH2 domain in the same monomer, while the closed ABD that was far from actin did not show any clear difference between RMSFs of CH1 and CH2 (the *iceblue* α-actinin monomer). All plots are averaged over three trials.

Hampton et al. suggested that α-actinin had to be a flexible crosslinker as opposed to a rigid molecular component in order to allow the observed mechanical properties of cytoskeletal structures (Hampton et al. 2007). Therefore, it is important to understand how structural features

of α-actinin influences its molecular rigidity as well as its binding to actin in both health and disease.

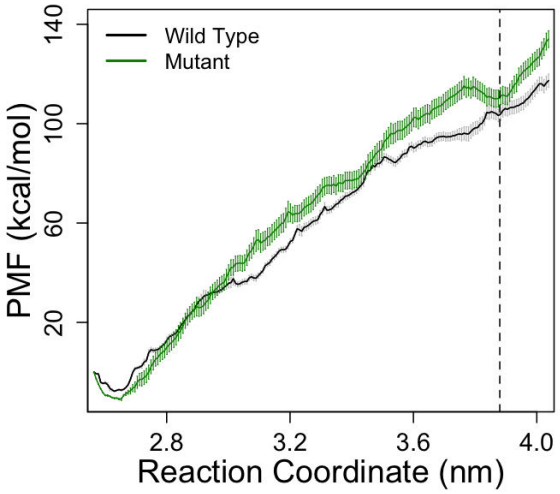

Figure 5.1-13. The potential of mean force of wild type and mutant α-actinin. Comparing the PMF profiles of the wild type (*black*) and mutant (*green*) α-actinins shows that a new minimum (at 3.9 nm) was created upon the K237E mutation. The CH1-CH2 distance was taken as the reaction coordinate for the umbrella sampling calculations. Profiles are fairly similar up to 3 nm but deviate after that. The slope of the mutant PMF is slightly higher but reaches a short plateau around 3.3 nm. The error bars were calculated using the bootstrap analysis.

Furthermore, it was shown that α-actinin can also link two points on a single actin filament (Hampton et al. 2007), thus the orientation of α-actinin relative to actin may alter based on it binding status.

There are various hypotheses on the mechanism of binding between different ABD conformations to actin. In this study, we explored the binding mechanisms of both ABD conformations to actin using molecular dynamics simulations. However, it should be noted that as comparably high-resolution structural data that can uniquely resolve the atomic positions of our proteins is not available, both α-actinin and actin structures were extensively minimized and equilibrated until the system energy became stable. Furthermore, as molecular dynamics simulations take atomic scale interactions into account, it can be used to predict protein-protein binding interfaces using reliable force fields such as CHARMM27 (Zhao et al. 2014; Piana et al. 2011). Protein structures will presumably reach an equilibrium state after a sufficiently long simulation time even if the simulations start off a low-resolution structure. It should be noted that atomic-level predictions have a lower confidence due to the resolution of the initial structures, however both coarse and fine analyses can provide insight into the dynamics of the system and can further be validated in future experimental studies.

Since the CH1 domain containing the main actin binding sites is in contact with CH2 in the closed conformation, it has been suggested that the open conformation of ABD should have a higher affinity for actin due to a lower steric hindrance imposed by CH2 (Galkin et al. 2010). Our simulations confirmed that the open conformation was indeed more favorable for actin binding as CH1 of the oABD formed 6 stable salt bridges with both proximal actin monomers, while the interaction between CH1 of the cABD and actin was much weaker. Furthermore, we observed that the actin cleft was narrowed down upon binding to the oABD possibly generating

a higher a local stress. This suggests that the accumulation of cross-linkers may decrease the average length and affect the stress distribution along actin filaments.

Moreover, the final configuration of the CH1-actin complex in the OW simulations was similarly oriented compared to the structure of the CH1-decorated F-actin (PDB ID: 3LUE). Our results suggested that CH2 prevents CH1 from effective binding to actin by the following mechanisms: 1) Blocking part of the actin binding site on CH1, i.e. residues K32 and R35, which are exposed in oABD (Galkin et al. 2010), and 2) interacting with one of the actin monomers across the cleft and inhibiting it from engaging with CH1.

Borrego-Diaz et al. (Borrego-Diaz et al. 2006) proposed a mechanism for actin binding by which CH2 of the cABD first associates with actin filaments releasing CH1 for further interactions with actin. We also observed that CH2 in the CW simulations interacted relatively strongly with actin prior to CH1 but we did not capture full dissociation of CH1-CH2 in 60 ns most likely because either the time-scale of such conformational change is longer or axial stress along actin is also necessary (Borrego-Diaz et al. 2006).

Because the CaM domain is the close proximity and most often interacting with the cABD, it has an important regulatory role in the actin binding activity of α-actinin but the molecular mechanism is not yet fully understood. In the muscle isoform (α-actinin 2,3), phosphatidylinositol 4,5-biphosphate (PIP2) regulates the ABD function by disrupting the hydrophobic interaction between the CaM domain and the neck region (Sjöblom et al. 2008), while in the non-muscle α-actinin isoforms 1 and 4, the CaM domain regulates the actin binding activity of the neighboring ABD via calcium binding (Burridge & Feramisco 1981). A similar function has also been observed for some other members of the specrin family (Travé et al. 1995).

We did not include the calcium ions within the EF-hand motifs in our simulations but still observed some correlations between the actin binding activity of ABD and interactions of the CaM domain (Tang et al. 2001). Specifically, the CaM domain associated with both CH2 and actin placing the cABD next to just one actin monomer in two trials of the CW simulations, while dissociated CaM allowed CH2 to engage simultaneously with both proximal actin monomers pushing CH1 away from actin in the third trial. It should be noted that this was the only result not consistent among all trials. Interaction of CH2 with two actin monomers may prevent effective transmission of forces to the cABD since most likely CH1 and CH2 need to be pulled against one another via axial tension along F-actin for complete opening of the cABD. Therefore, we suggest that the CaM domain is likely to be involved in regulating the ABD conformation by controlling the transmission of mechanical forces to the cABD. Furthermore, we observed that the association of the CaM domain to the same actin monomer as CH2 resulted in stronger anchorage to actin and thus may play a role in the early stages of the binding between the cABD and actin. However, in the OW simulations the relative positions of the CaM domain and the neck region with respect to the actin-bound oABD remained intact implying that no further conformational changes was required for regulating the actin binding activity of the oABD. Again it should be noted that the dynamics of α-actinin binding to actin can also be highly influenced by Ca^{2+} and PIP2 and other regulatory factors.

We observed several distinct motions of α-actinin in the OW and CW simulations upon actin binding. Specifically, deviation of the cABD axis from its original orientation after actin binding was larger than that of the oABD in all trials (Figure 5.1-4). This suggests that the ABD can reorient even in its bound state to actin in a conformation-dependent manner and is not confined to its initial alignment. Furthermore, we investigated the binding between different

oABD orientations and actin for a shorter timescale in order to gain insight into the effect of the initial ABD angle on the strength of its actin binding. We observed that the 180°-rotated oABD that was the reversed orientation relative to the initial configuration of oABD used in all OW simulations (also referred to as the 0° rotation) and the 270°-rotated oABD formed the most favorable interactions in 5 ns (Figure 5.1-8). Since α-actinin can crosslink both parallel and anti-parallel actin filaments that easily rearrange and move in all possible directions, dynamic adaptation to the new arrangements is most likely a critical characteristic of α-actinin as an actin crosslinker also suggested by our simulations.

Interestingly, in all OW simulations the rod domain was curved in the opposite direction of that in the CW simulations (Figure 5.1-14). This suggests that the bending mode of the α-actinin molecule can be triggered during actin binding but the phase of such motion may be dependent on the ABD conformation. Also, twisting is one of top molecular modes of α-actinin that may be signified by the angle between the principle axes of ABDs at the two ends of the molecule. Our results showed that the oABD binding to actin caused a larger twist in the molecule compared to that of the cABD. This may imply that strong actin binding anchors the molecule at one end but still allows for large changes in the ABD orientation at the other end, i.e. α-actinin does not act like a rigid body after binding to actin. Furthermore, since α-actinin monomers are tied together via strong hydrophobic interactions within the coiled-coil structure of the rod domain, it is conceivable to expect some allosteric communication between the two ends of the molecule. We suggest that a mechanical signal is transferred upon actin binding between the two end of the molecule via triggering the natural modes of the rod domain, i.e. twisting (Figure 5.1-10 and Supplementary Movie S1) and bending (Figure 5.1-14 and Supplementary movie S2).

We further studied the effect of the K237E mutation on both the ABD conformation and actin binding. No appreciable conformational changes were observed in the cABD domain upon the mutation per se, however, the average interaction energy of the CH1-CH2 interface over time was changed from -428.50 ± 58.99 in the wild type compared against that -319.67 ± 80.10 in the mutant (Figure 5.1-15). This may imply that the mutation alone is not sufficient to initiate the closed-to-open conformational change, at least not in the nanosecond time-scale, and mechanical tension may either be necessary to expedite or complete this process. We also observed that the interactions between the mutant α-actinin and actin formed more gradually compared to the wild type (Figure 5.1-15). This may suggest that the mutation created more transition states between the bound and unbound states with actin resulting in a smoother binding. Specifically, the probability of actin association may increase upon the mutation since introducing a higher number of transition states tends to expedite both physical and chemical reactions.

It has been shown that the CH1-CH2 fragment has a higher affinity than the isolated CH1 for actin suggesting an important regulatory role for CH2, however it is not yet clear how mutations in CH2 can influence the binding between CH1 and actin (Way 1992). We suggest that this could be due to the following: CH2 anchors the ABD to actin placing CH1 in the right orientation and contributes to regulating the size of the actin cleft, while CH1 alone is small and globular in shape and would probably have to rely on diffusion for adjusting to a favorable orientation relative to actin.

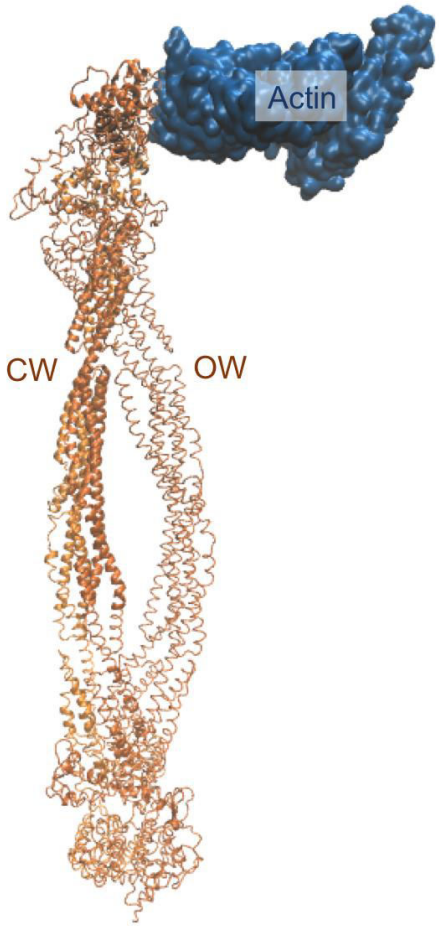

Figure 5.1-14. The curvature of the α-actinin rod domain. The curvature of the rod domain was different between the CW and OW simulations putting the ABD of the other end in slightly different positions.

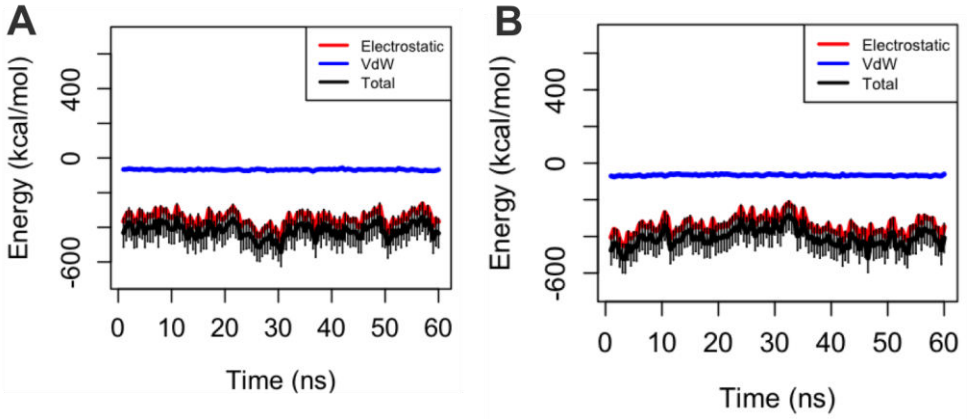

Figure 5.1-15. **The CH1-CH2 binding energy.** The energy was averaged over three trials in both A) the CW and CM (*right*) simulations. The K237E mutation decreased the binding energy in the first 30ns of the CM simulations but did not cause complete dissociation of the CH domains.

Our simulations showed that CH2 of the mutant α-actinin was released from the R1 spectrin repeat in the rod domain in all trials and thus experienced lower hindrance for spatial movements towards CH1, which may be important for regulating its orientation and binding. We would like to further emphasize that our results provide an insight into the dynamics of the system in the nanosecond time-scale and thus different average behaviors may be expected in longer times, e.g. microseconds and milliseconds.

The constant-rate pulling simulations indicated that the force required to separate CH1 and CH2 was markedly lower for the mutant compared to that for the wild type (Figure 5.1-16). Specifically, a notable difference in the pulling forces was observed as the CH1-CH2 interface was being disrupted, while before and after that time force curves followed each other closely (Figure 5.1-16). Since there was no negatively charged residues in the vicinity of K237, we did not expect any direct influence of the charge on the CH1-CH2 interface. However, the pulling trajectories showed that the K237/E237 residue moved very close to D27 during opening and causing a strong attraction/repulsion between glutamate and aspartate. Furthermore, the pulling simulations showed that an interaction between residue 237 and R134 on the CH1-CH2 linker region occurred around the same time as the trend of the pulling forces between the CH domains of the mutant deviated from that of the wild type (Figure 5.1-16). The bond between CH2 and the linker region reduces the likelihood of structural reformation to the closed conformation. This is another potential reason why the K237E mutation stabilizes the open conformation as suggested by the minimum in the PMF plot (Figure 5.1-13). This indicates that the mutation does not directly induce a conformational change in the ABD. However, as the CH1-CH2 interface is altered in response to mechanical stimuli or other physical cues, the interaction pattern may change upon the mutation.

Moreover, the PMF profile of α-actinin was calculated using the umbrella sampling method and the errors bars were estimated by the bootstrap analysis in order to quantify the free energy cost of the closed-to-open conformational change in the ABD for both wild type and mutant α-actinins. The free energy difference between the closed and open conformations of the CH domains were -112.6±2.6 kcal/mol and -119.8±4.9 kcal/mol for the wild type and mutant, respectively. One obvious difference between the two PMF profiles is the appearance of a local minimum where the open conformation was reached for the mutant. This may suggest that the open conformation of the mutant is relatively more stable compared to the wild type as the system gets trapped within a local minimum. It should be noted that actin monomers were not included in the umbrella sampling simulations, since they would introduce many extra degrees of freedom to the system making it increasingly more difficult to carry out the free energy calculation with a reasonable accuracy. However, the direction of tension and the presence of F-actin may affect the PMF profile especially the first potion where CH1 and CH2 are still in contact. Our results suggested that the open conformation of the mutant α-actinin is more stable (Figure 5.1-13) and also requires lower forces (Figure 5.1-16).

In summary, we proposed a molecular mechanism for the binding between α-actinin and actin based on a consensus among all our simulation trials as follows: 1) The α-actinin molecule diffuses towards the actin filament most likely with ABDs in the closed conformation and adjusts its orientation (Figure 5.1-17A). 2) The binding between CH2 and one actin monomer occurs first, which may be regulated by the CaM domain (Figure 5.1-17B, the CaM domain is not shown for clarity), and is followed by the CH1 interaction with the other monomer across the actin cleft. 3) Axial tension along the actin filament broadens the cleft causing the distance between CH1 and CH2 to change as they are bound to two different actin monomers. A

transition state is reached where the CH1-CH2 interface is altered by the mechanical stimuli and D27 is pulled towards the interface. In the wild type, D27 will face K237 creating a strong attraction that may prevent further opening of the ABD unless it is overcome by the axial tension along F-actin (Figure 5.1-17C). However, the negative charge of D27 faces E237 in the mutant creating a repulsive force that may expedite and reduce the amount of forces required for further ABD opening (Figure 5.1-17D). 4) As the CH2 domain is completely dissociated, CH1 moves further into the actin cleft and replaces CH2 due to its high affinity for actin (Figure 5.1-17E).

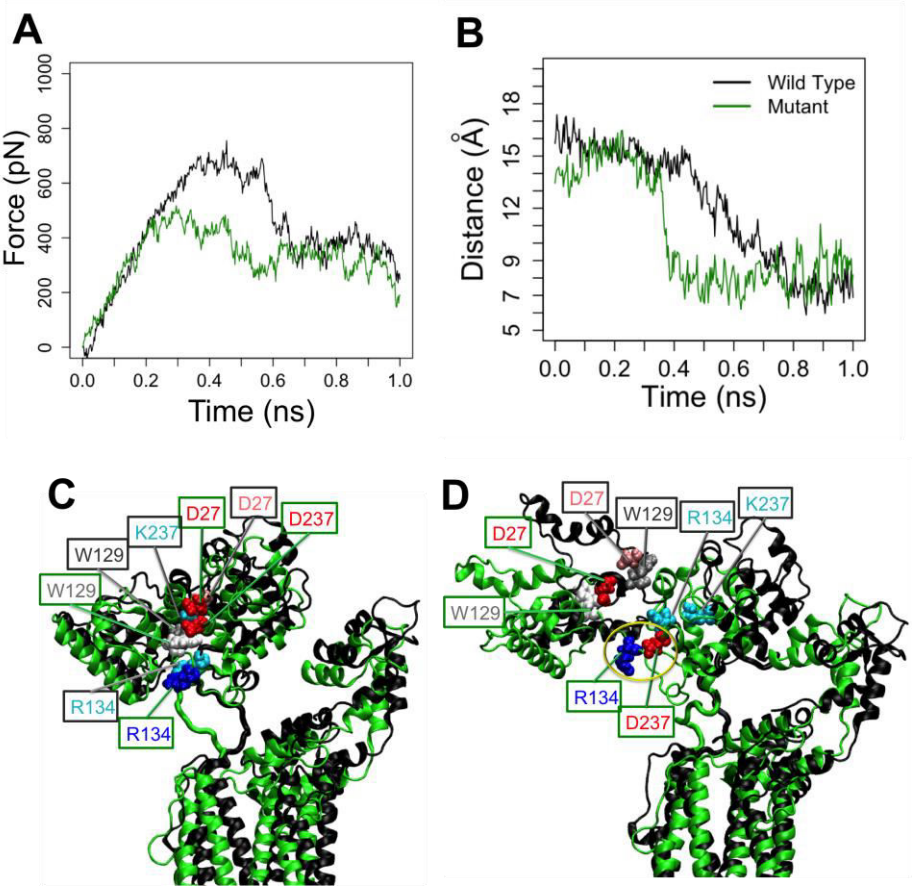

Figure 5.1-16. Mechanical forces required to separate CH domains in both wild type and mutant α-actinins. A) Forces used to separate the CH domains with a constant rate of 0.005 ps/nm for the wild type (black) and mutant (green) α-actinin. Clearly the mutant required lower forces for separating the CH domains. B) The distance between residues 237 and R134 in the neck region sharply changed in the mutant simultaneous with the deviation in the pulling forces (A). C) The initial configuration of the wild type (black) and mutant (green) before pulling. All important residues are marked. D) After pulling, D237 and R134 formed an interaction that held CH2 close to the CH1-CH2 linker region that most likely prevented the reformation of the closed conformation.

Conclusion

The conformation and dynamics of the ABD domain of α-actinin play an important regulatory role in actin binding and here we proposed a mechanism for that. Our simulations predicted that the K237E mutation in the chicken α-actinin, which corresponds to K255E mutation in human associated with a type of kidney failure, change the free energy landscape and most likely stabilize the open conformation of the ABD. Furthermore, the flexibility of the ABD orientation relative to actin suggests that α-actinin can crosslink F-actins with different angles

leading to formation of various actin assemblies. Also, actin association at one end of the α-actinin molecule may be transmitted as a mechanical signal via the natural modes of the rod domain. Our simulations shed light on understanding controversies about the effect of the ABD conformation and mutations in that domain on the actin binding activity of α-actinin. Therefore, the insight from our simulations can be used to develop novel techniques and therapeutics to interfere with the α-actinin function and the kidney disease associated with the K255E mutation in humans.

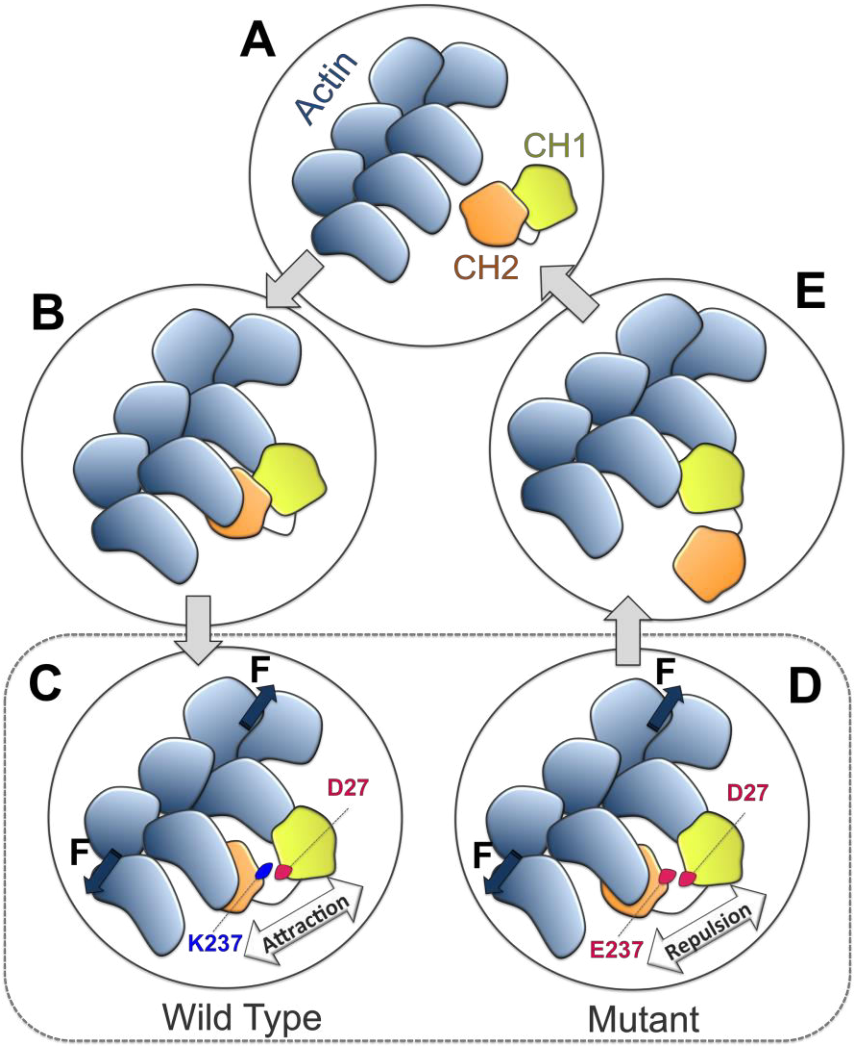

Figure 5.1-17. The proposed mechanism of the ABD binding to actin. A) The cABD diffuses towards the actin filament B) allowing CH2 to engage with an actin monomer along F-actin that is followed by a weak interaction of CH1 with a neighboring actin monomer. C) Axial tension along F-actin broadens the actin cleft and partially opens the cABD. Residue D27 on CH1 moves towards the interface with CH2 resulting in either a strong attraction towards K237 in the wild type or a repulsion against E237 in the mutant and thus further opening of the ABD would require different amount of forces depending on the type of residue 237. D) As CH1 and CH2 are completely separated by axial tension and the steric hindrance imposed by CH2 is removed, CH1 moves further into the actin cleft and replaces CH2 on the other monomer. Therefore, the open conformation can be maintained in the bound state to actin.

Supporting material Two movies are available at http://www.biophysj.org/biophysj/supplemental/S0006-3495(16)00212-5.

Section 5.2 Reorganization of Actin through Interaction with Single-Wall Carbon Nanotube[1]

CNTs can be synthesized as single- or multiple-layer tubular structures with a wide range of different properties. Single wall carbon nanotubes (SWCNTs) are preferred for biomedical applications for reasons such as their high length to diameter aspect ratio, high axial stiffness, inactivity in chemical reactions and negligible fluctuations at body temperature. While several studies have examined the thermal, chemical and mechanical properties of CNTs,(Dresselhaus et al. 2004; Odom & Huang 1998; Treacy, M.M.J., Ebbesen, T.W., Gibson 1996; Lorin X. Benedict 1996) for biological applications, where the introduction of external agents can disrupt natural functionalities of cells and thus organs, the specific effects of CNT on the system behavior must be further explored. Moreover, in some cases the strength of CNT interaction might be of interest. For example, site specific drug deliveries require modifications of CNTs by attaching other molecules and/or ions that increase binding affinities for target molecules.(Zhang et al. 2011) Such processes, usually referred to as functionalization, necessitate a detailed understanding of CNT interactions with both target and newly attached molecules.

Many biological functions of the cell depend highly on filamentous actin (F-actin). For example, cell migration requires continuous reorganization of actin filaments, a dynamic process that is directly influenced by G-actin interaction. Other important cellular processes directly related to F-actin distribution are cell proliferation, differentiation and growth.(Mofrad & Kamm 2006) Any external agent with even a slight affinity for F-actin may affect the inter-monomer interaction and thereby influence the force generation machinery within cells that in turn may affect cell adhesion.(Yaron et al. 2011)

Recently, we observed changes in F-actin structures inside the cell upon the uptake of SWCNTs.(Holt et al. 2010; Brian D. Holt et al. 2012; Yaron et al. 2011) In these previous works, SWCNTs were dispersed using Pluronic F127 (PF127), which is a biocompatible polymer. Our work revealed that the cytoskeletal structure, force generation and proliferation of SWCNT-treated fibroblasts is modified.(Brian D. Holt et al. 2012) Actin filaments were shorter and redistributed in the SWCNT-treated cells compared to the control assay. In the same study, the main SWCNT binding sites on actin were investigated. Herein, we present a detailed study on SWCNT interaction with F-actin using both computational and experimental techniques. Specifically, all-atom molecular dynamics simulations were used to characterize the SWCNT-actin interaction, while near-infrared (NIR) fluorescence and Raman spectroscopies confirmed direct interactions between actin and SWCNT (without PF127 polymer) *ex vivo*. In our model, we explored the SWCNT interaction with actin trimer that is an intermediate state before polymerization and contains the primary filamentous interactions.(Tuszynski et al. 2003) In this study, we investigated the effect of SWCNT on the monomer-monomer interaction, which may potentially influence actin reorganization in the cytoskeleton.

Materials and Methods

Docking

Hex interactive docking software was used to generate the initial configurations of the SWCNT-actin complex.(Macindoe et al. 2010) Geometric compatibility was taken into account

[1] The content of this Chapter has been published in ACS nano in 2013, Volume 8, Issue 1, Pages 188 to 197 (Shams et al. 2014).

in obtaining the optimized bound structures. The top ten docking structures were classified into two different classes, from each of which one representative was selected (Figure 5.2-1).

Molecular dynamics simulations

All molecular dynamics simulations were carried out using NAMD 2.9 molecular dynamics software package(Phillips et al. 2005) and CHARMM27 force field.(MacKerell et al. 2001) Periodic boundary conditions were applied in all three directions. The entire system was then minimized for 5000 steps, which was followed by a 1 ns equilibration in constant pressure. The equilibrated structure was then used for studying the binding interaction between SWCNT and actin in a 40 ns-simulation, which ran with 1 fs time-step. Particle mesh Ewald (PME) was applied to model the electrostatic interactions, and the SWITCH algorithm, with cut-off distance of 1.2 nm, was used for calculating van der Waals (VDW) forces. The NPT ensemble was used for the production run to sample our system where pressure and temperature remained constant at 1 bar and 310 K using Langevin's piston and the Nose-Hoover thermostat,(Nosé 1984) respectively. All system preparation, visualization and post-processing analyses were performed using Visual Molecular Dynamics (VMD) software.(Humphrey et al. 1996)

The structure of actin trimer positioned in the filamentous arrangement was obtained from the Protein Data Bank (PDB: 3LUE). This structure was minimized and equilibrated in a water box prior to final simulations in order to remove all bad contacts. SWCNT geometry was generated with both (n,m) indices set to 5. The length and diameter of SWCNT were chosen to be 11 nm and 0.67 nm, respectively. Three sets of distinct initial configurations found from docking calculations where SWCNT structure was placed approximate to the equilibrate actin groove region where the closest atoms were more than 0.7 nm away. The explicit water molecules were included to solvate the SWCNT-actin complex (water model: TIP3P). In addition to neutralizing the system, 0.15 mM of KCl ions were added to the simulation box in order to resemble ionic concentrations in cell. The number of atoms for the SWCNT-actin configurations was approximately 300,000. For reviewing general principles of molecular dynamics, please see Chapter 2 of the present dissertation.

Experimental methods

Preparation of G-actin: G-actin was prepared using the Actin Filament Biochem Kit (Cytoskeleton, Inc.; Denver, CO, USA) according to manufacturer's recommendations. Briefly, muscle actin (250 µg) was resuspended at 4° C to 0.4 mg/mL in "General Actin Buffer" plus 0.2 mM ATP. The mixture was left on ice for 3.5 h to completely disassemble small oligomers; then it was centrifuged at 4° C at 14,000×*g* for 15 min. The supernatant was immediately aspirated, diluted in ultrapure water at 4° C to a final volume of 2 mL (for SWCNT dispersion) and immediately added to SWCNTs for dispersion as described below.

Preparation of F-actin: F-actin oligomers were prepared using the Actin Filament Biochem Kit (Cytoskeleton, Inc.; Denver, CO, USA) according to manufacturer's recommendations. Briefly, muscle actin (250 µg) was resuspended to 1.25 mg/mL in "General Actin Buffer" plus 0.2 mM ATP. The mixture was left on ice for 50 min to disassemble filaments that formed during freeze/thaw. Concentrated "Actin Polymerization Buffer" was added at 1:10 v/v, and the mixture was incubated for 45 min at room temperature. These conditions yield filaments ~0.2 to 3 □m long. The filaments were diluted in ultrapure water to a final volume of 2 mL (for SWCNT dispersion) and immediately added to SWCNTs for dispersion as described below.

SWCNT Dispersion: CoMoCAT® single wall carbon nanotubes (SWCNTs) highly enriched (> ~40%) in (6,5) chirality with an aggregate, average diameter of ~0.78 nm and a median SWCNT length of ~1.5 μm (SWeNT® SG65; SouthWest NanoTechnologies, Inc.; Norman, OK, USA) were dispersed using G-actin or F-actin oligomers at 1:10 w/w. Actin mixtures were added to SWCNT powder, and the final sample dilution was 1.3×10^{-3} wt.% SWCNTs for sonication. Samples were probe-tip sonicated in a 3 mL glass vial for 2 h at 6 W; then they were centrifuged at 21,000×*g* for 7 min. Supernatents were aspirated and characterized *via* optical methods as described below.

SWCNT s–Actin Dispersion Characterization:

UV–vis–NIR absorbance spectroscopy: Samples were subjected to ultraviolet–visible–near-infrared (UV–vis–NIR) absorbance spectroscopy (Varian Cary 5000 UV–vis–NIR spectrophotometer). A known absorbance coefficient of 2.6 (abs mL)/(mg mm) at 930 nm(Fagan et al. 2008) was used to calculate final SWCNT concentration. The peaks of absorbance arise from the chirality-specific van Hove singularities of the density of states and qualitatively indicate dispersion quality.

Raman spectroscopy: Raman spectroscopy (inVia confocal Raman microscope with a 785 nm laser; Renishaw, Inc.) confirmed the presence of SWCNTs: strong G-band at ~1591 cm^{-1} indicating an sp^2 hybridized structure and radial breathing modes (RBMs) at ~150–300 cm^{-1} indicating tube structures with ~1 nm diameters.(Dresselhaus et al. 2005) The presence of individual SWCNTs was confirmed by the presence of RBMs < 250 cm^{-1}, and a generally pristine SWCNT structure (*i.e.*, minimal defects) was confirmed by a small disorder-band (D-band at ~1300 cm^{-1}): G-band.(Dresselhaus et al. 2005)

NIR fluorescence spectroscopy: SWCNT dispersion quality was further analyzed by NIR fluorescence spectroscopy (Nanolog Spectrofluorometer with a liquid-nitrogen-cooled Symphony InGaAs–1700 detector; Horiba Jobin Yvon). The samples were diluted to < 0.1 abs cm^{-1} in the NIR and were interrogated with excitation and emission slit widths of 10 nm and an integration time per excitation wavelength of 120 s. The excitation grating was blazed at 500 nm (1200 groves/mm), and the emission grating was blazed at 1200 nm (150 grooves/mm). Fluorescence heatmaps represent corrected fluorescence intensity normalized by corrected excitation intensity. Nanosizer software was used to identify and mathematically fit each chirality's excitation/emission maxima using a Voigt 2D model.

Results

The purpose of this study is to explore the molecular level interactions between actin and SWCNT in order to shed light on the alterations of cell shape and morphology observed in the experimental studies done by Holt et al.(Brian D. Holt et al. 2012; Holt et al. 2010; Yaron et al. 2011) Here, we investigate SWCNT-actin association using both all-atom molecular dynamics (MD) simulations and NIR spectroscopy. For the computational portion of our purpose, we used (5,5)-SWCNT, which has a diameter within the experimental range and a size appropriate for modeling. Three actin monomers arranged in the filamentous order (trimer nucleus) in complex with SWCNT was monitored throughout the simulation. To highlight the effect of SWCNT on the conformation of F-actin and the dynamics of their internal interaction more rigorously, a separate control MD simulation was conducted containing the actin trimer only and was later compared to the SWCNT-actin binding simulations. The control simulation ran for the same time interval and with the same equilibrated structure of the actin trimer as that in the SWCNT binding simulation.[2] In the initial configuration of the trimer all three monomers were in close contact, two being in the axial direction of the actin filament (referred to as proximal monomers 1 and 2 or 'P_1' and 'P_2' throughout the text). The third monomer is referred to as the distal monomer or 'D' (Figure 5.2-1).

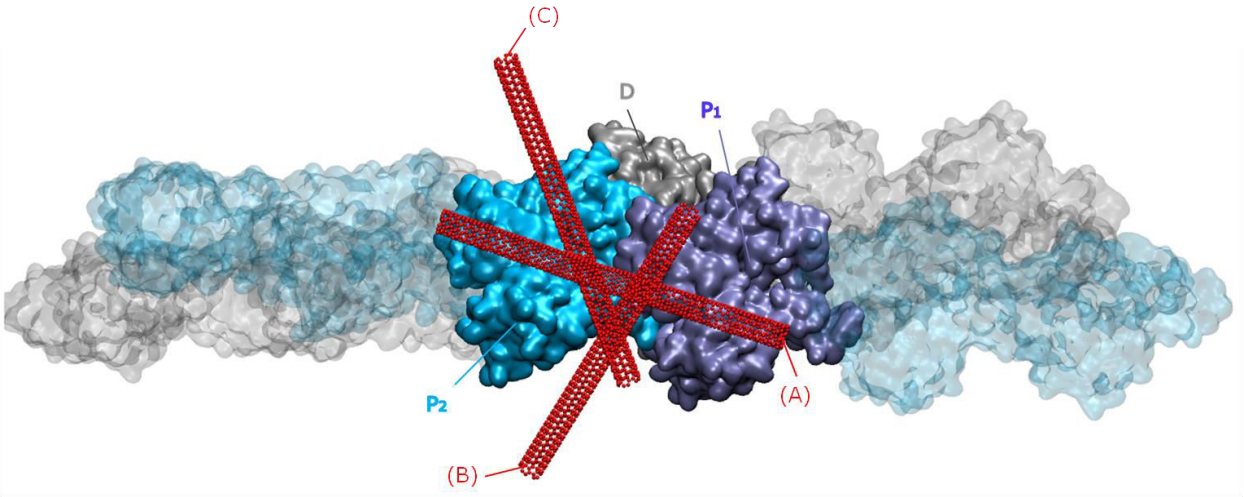

Figure 5.2-1. Three distinct initial configurations of SWCNT relative to actin. Orientation (A) of SWCNT was previously found to be favorable(Brian D. Holt et al. 2012) for actin binding. Orientations (B) and (C) were generated using docking of SWCNT on the actin trimer in the filamentous order (bold along the actin polymer shown in transparent representation). The two actin monomers proximal to SWCNT are labeled P_1 and P_2, while the third monomer in the neighboring strand that is more distal is labeled D.

Molecular dynamics simulations. Distinct orientations of SWCNT relative to actin were generated in order to account for a broad range of binding possibilities between the two inside the cell (Figure 5.2-1). First, we used Hex docking server (Macindoe et al. 2010) to find the top 10 candidates according to geometry matching. After categorizing similar docked structures, we found two distinct complexes out of which the one with highest geometrical compatibility was selected as a representative for further MD studies. Although results from all three initial

[2] Most of the results are presented in the presence and absence of SWCNT in the same plot and thus referred to as W-CNT and W/O-CNT, respectively, in order to avoid repetition of terms.

configurations showed consistency in some aspects, each suggest interesting case-specific interactions that are reported separately in the results section.

In the initial configuration of binding mode A, the SWCNT axis was aligned along the actin filament and positioned proximal to the groove formed between the two actin strands. Previously we found this region to effectively bind to SWCNT.(Brian D. Holt et al. 2012) The minimum distance between the nearest carbon atom of the SWCNT structure to actin residues was adjusted to be approximately 0.7 nm. That was within the range of both electrostatic and van der Waals (VDW) forces; however, it allowed water layers to form at the interface in the initial setting prior to any stable binding. It was observed that after less than 3 ns, the SWCNT/actin binding was established. The binding location of SWCNT tends to remain close to the actin groove and further stabilize its position during the simulation confirming our previous results.(Brian D. Holt et al. 2012)

Interaction energies —sum of van der Waals and electrostatic terms— were monitored for all three binding modes. The interaction energy of mode A continued to stabilize in the first 10 ns, and it dropped to -140 kcal/mol (Figure 5.2-2A). The average energy of binding mode A (-134.23 kcal/mol) was higher than mode B (-92.11 kcal/mol) that itself is larger, by approximately the same amount, than mode C energy (-45.93 kcal/mol), implying the stronger SWCNT-actin interaction in mode A (Figure 2B and 2C). The energies follow the similar trend as the docking analysis.

The solvent accessible surface area (SASA) of SWCNT reached a stable value of 0.5 nm^2 within the first 3 ns (Figure 5.2-3). For binding mode B, although the interaction energy was relatively stable, SASA increased in time within the last 20 ns. The SASA plot for mode C fluctuated sharply after 18 ns, showing unstable surface association with actin, which is consistent with the interaction energy. Therefore, SASA alone is not indicative of stable binding per se, and it should be interpreted along with energies. All SASA and energy graphs were averaged over three trials for each binding mode.

Among all the actin residues on the surface involved in SWCNT interactions, 50% were hydrophobic, which is relatively high on an overall hydrophilic surface, including ALA143, VAL29 and TYR336 on P_1, and ALA275, ILE327 and PRO329 on P_2, which were energetically most favorable. SWCNT atoms were assumed to be neutral, thereby, electrostatic interactions were automatically eliminated.

Our results showed that residues capable of forming multiple VDW interactions are crucial for SWCNT association. For instance, residues with aromatic side chains, such as tyrosine, made a number of interactions with carbon rings on the SWCNT surface, which is very similar in appearance to the $\pi..\pi$ bond; however, it should be noted that quantum mechanical effects such as overlap in atomic orbitals are not accounted for in MD simulations. In addition, residues with extended side chains, such as lysine and aspartic acid, also associated strongly to the surface of SWCNT composing a sequence of interactions. Therefore, all polar, charged and nonpolar residues contributed to SWCNT binding.

In all trials, we observed two interesting types of SWCNT motions relative to the actin surface: 1) sliding or translocation along the SWCNT axis and 2) rotational motion around the axis of SWCNT. However, each trial showed some unique characteristics that are worth mentioning individually. Figure 5.2-8A shows a long sliding motion for the first trial starting from 5 ns to the end of the 40 ns simulation. However, during the sliding period, there are short intervals, for example between 10 to 15 ns, at which SWCNT is approximately stationary relative to actin. Moreover, the SWCNT sliding motion changed direction at three instances: 18

ns, 20 ns and 23 ns. One significant rotational motion for the same trial occurred in the first 2.5 ns (Figure 5.2-8B). There are two sudden changes in the rotational angle around 10 ns and 24 ns. Also, the average angle changed from 80º to 60º at 19 ns. In the second trial, the sliding motion changed direction several times, mainly at 5 ns, 25 ns and 35 ns, while SWCNT was sliding mostly in one direction in the first trial (Figure 5.2-8C). However, SWCNT was rotating mostly in one direction throughout the second trial (Figure 5.2-8D). The trend of the rotational motion in the third trial is similar to the second one (Figure 5.2-8F). The sliding motion in the third trial was less significant than the other two (Figure 5.2-8E).

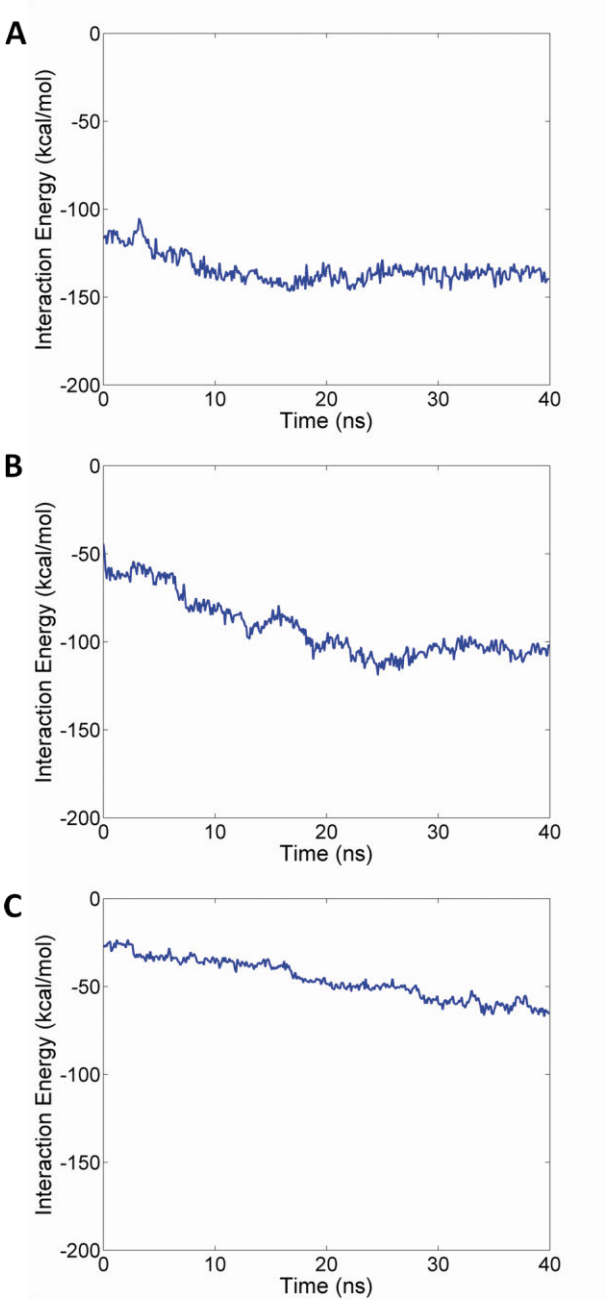

Figure 5.2-2. Interaction energy between SWCNT and actin. (A) mode A, (B) mode B, and (C) mode C. All modes show an increase in interaction energy, and the highest and lowest interaction energies were observed in

modes A and C, respectively. Mode C was also scored lower than mode B based on docking results. A higher engagement of SWCNT with actin is seen in mode A while the interfacial areas are smaller in all other modes.

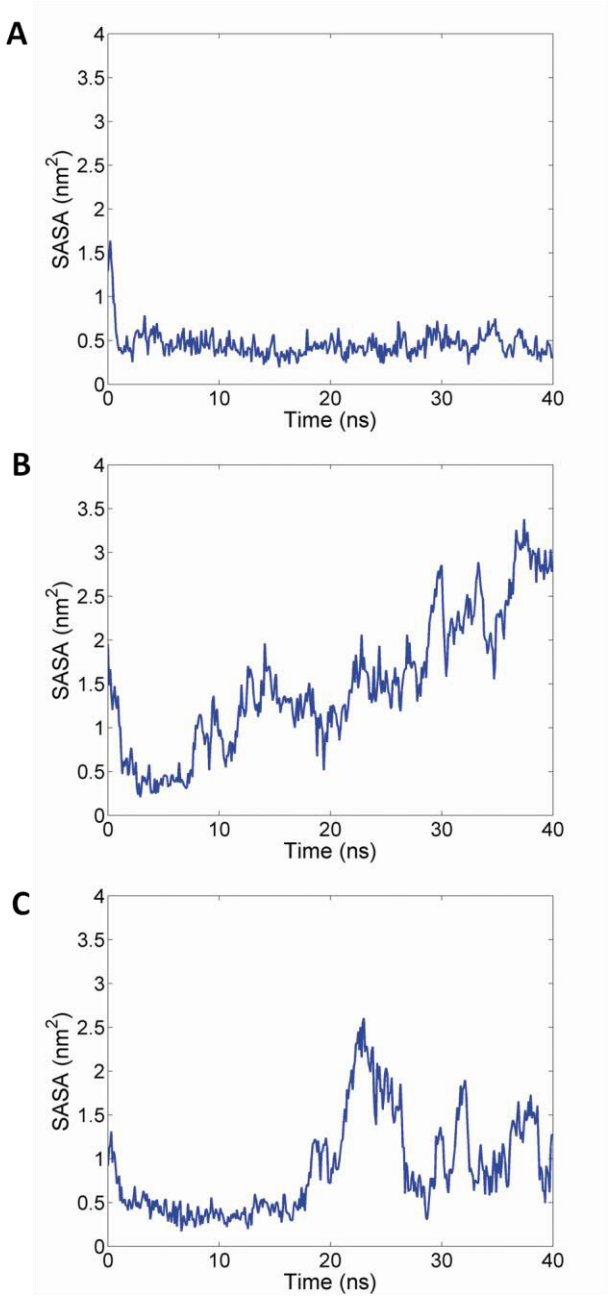

Figure 5.2-3. Average solvent accessible surface area (SASA) for SWCNT in three binding modes for (A) mode A, (B) mode B, and (C) mode C. SWCNT in mode A showed the lowest and most stable SASA which is in agreement with its strong stable interaction with actin. The exposed surface of SWCNT decreased to 0.5 nm2 in less than 2.5 ns indicating a stable interaction with actin throughout the simulation. In contrast to mode A, mode B steadily gains SASA or in other words loses its contact with actin.

One trial of both modes B and C (Figures S1A, S1E, S2A and S2C) showed a long directional motion of SWCNT along its axis (~3 nm), while no significant sliding occurred in the other two trials of these modes. However, the rotational motion was notably increased in modes B and C, which is likely to be due to reduced association of SWCNT to actin compared to A.

All carbon atoms, except those at the edges of SWCNT, identically form equi-energy interactions with a certain type of atom. Therefore, although actin residues in the SWCNT/actin interface remained fixed, SWCNT slid along the actin surface, while simultaneously rotating around its own axis. The energy of interaction between P_1 and P_2 shows more stability compared to the control simulation. Despite the relative motion of SWCNT and actin, SASA did not change after the first 8 ns implying that rotation and sliding did not involve any local dissociation of residues (Figure 5.2-3).

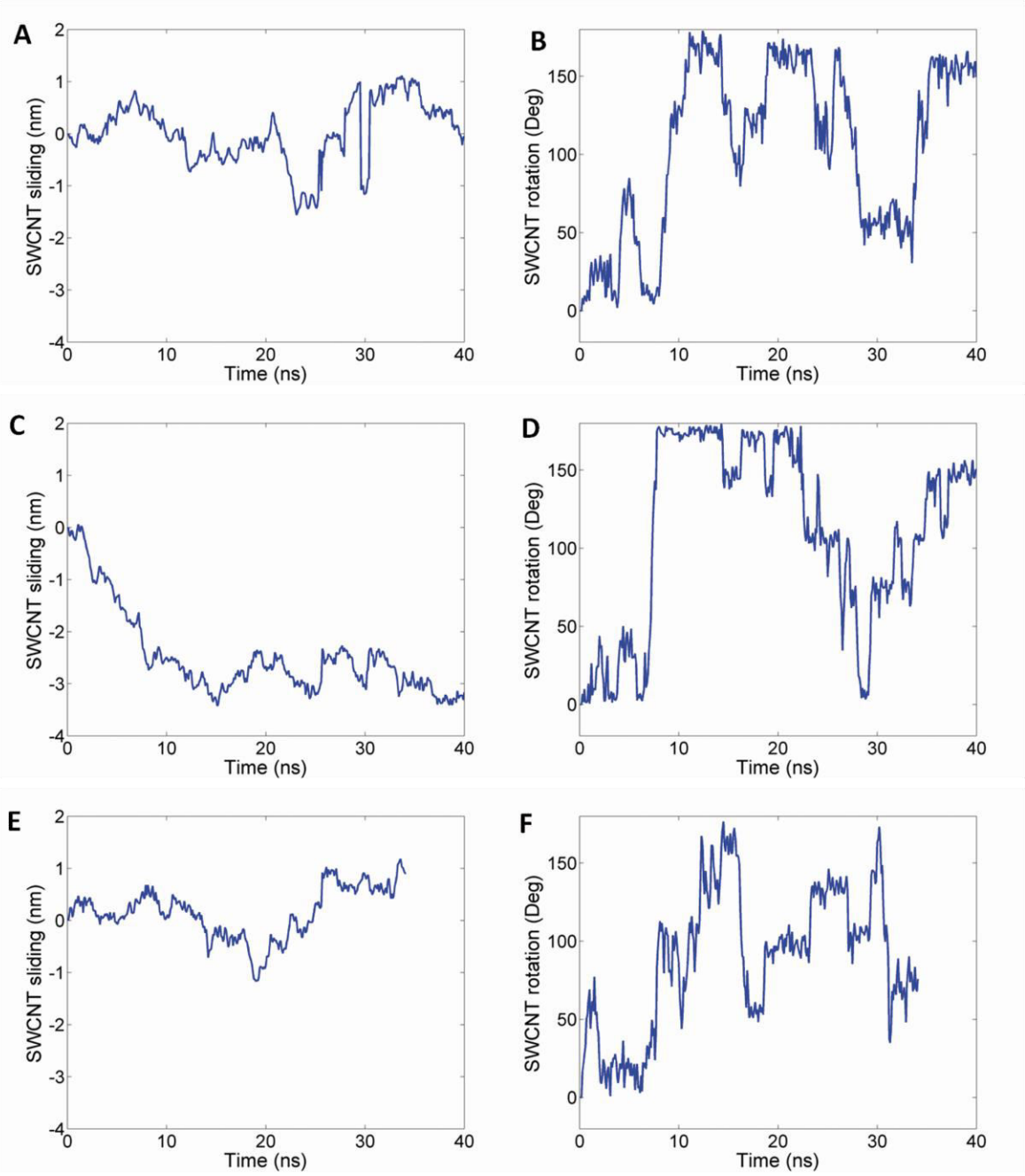

Figure 5.2-4. SWCNT sliding and rotation for mode B. (A) Sliding in trial 1, (B) rotation in trial 1, (C) sliding in trial 2, (D) rotation in trial 2, (E) sliding in trial 3, and (F) rotation in trial 3.

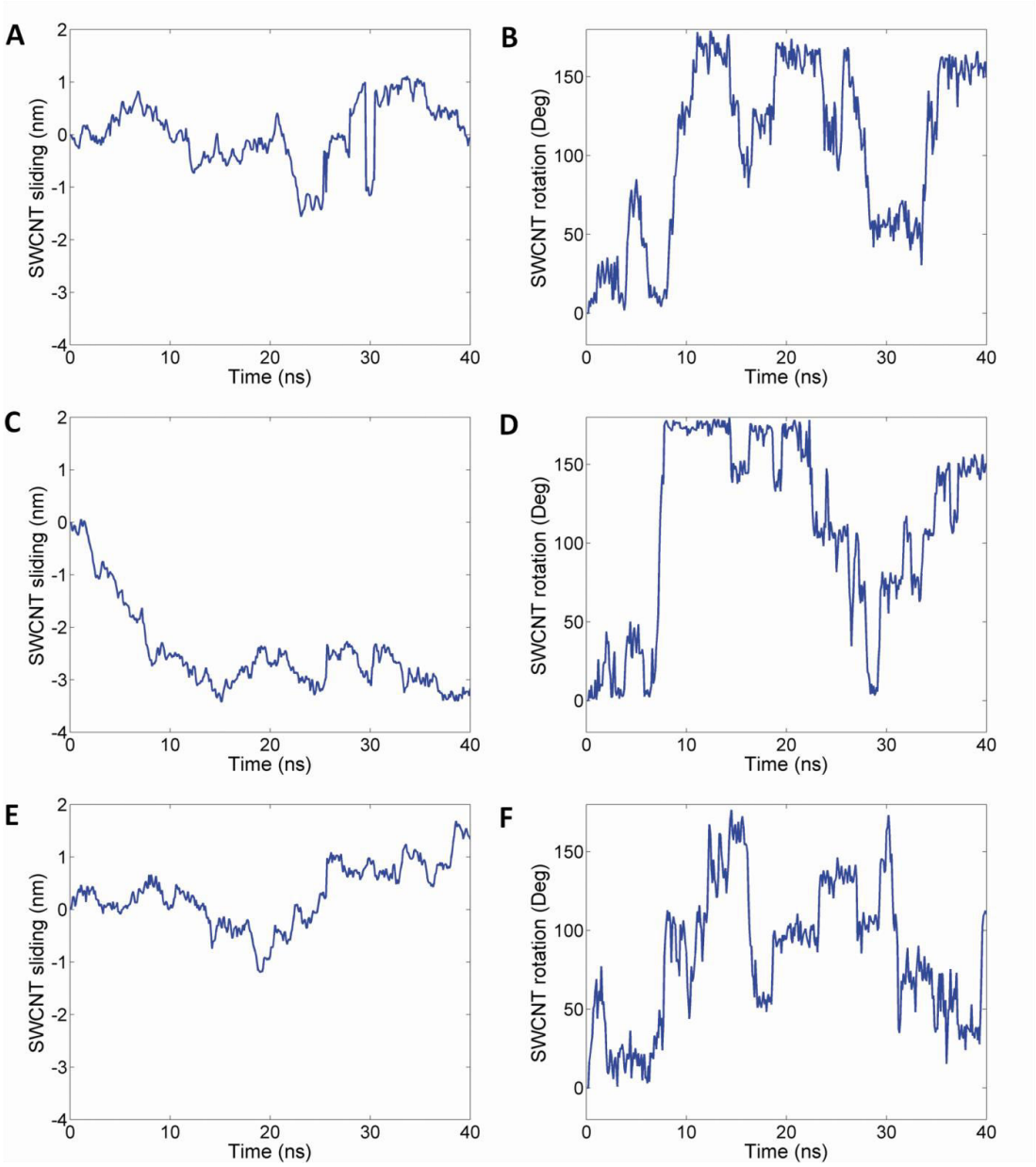

Figure 5.2-5. SWCNT sliding and rotation for mode C. (A) Sliding in trial 1, (B) rotation in trial 1, (C) sliding in trial 2, (D) rotation in trial 2, (E) sliding in trial 3, and (F) rotation in trial 3.

Figure 5.2-9 shows the pairwise interactions within the actin trimer for all binding modes. In the control simulation, the interaction energies of P_1-P_2 and P_2-D slightly increased throughout the simulation, while the distal monomer interaction with P_1 was negligible at all times. The slight repulsion within the actin trimer is most likely an artifact of not having the rest of the actin filament in the model (Figure 5.2-9A). Interestingly, the presence of SWCNT stabilized P_1-P_2 and P_2-D interaction regardless of the binding mode (Figure 5.2-9B-C). However, P_1-D interaction was enhanced upon SWCNT binding in mode C (Figure 5.2-9D).

Both hydrogen bonding and hydrophobic interactions contributed to stabilizing the interface, e.g. ALA727 and GLU194 of P_1 were in contact with ILE368 and ASN110 of D. The

fluctuations in radius of gyration (Rg) of none of actin monomers within the trimer in any of the binding modes showed significant variations upon SWCNT binding implying that the overall conformation of F-actin was maintained (Figure 5.2-6). The root mean square fluctuation of SWCNT was maximized in the middle and both ends, which is in agreement with the previous studies (Figure 5.2-7).

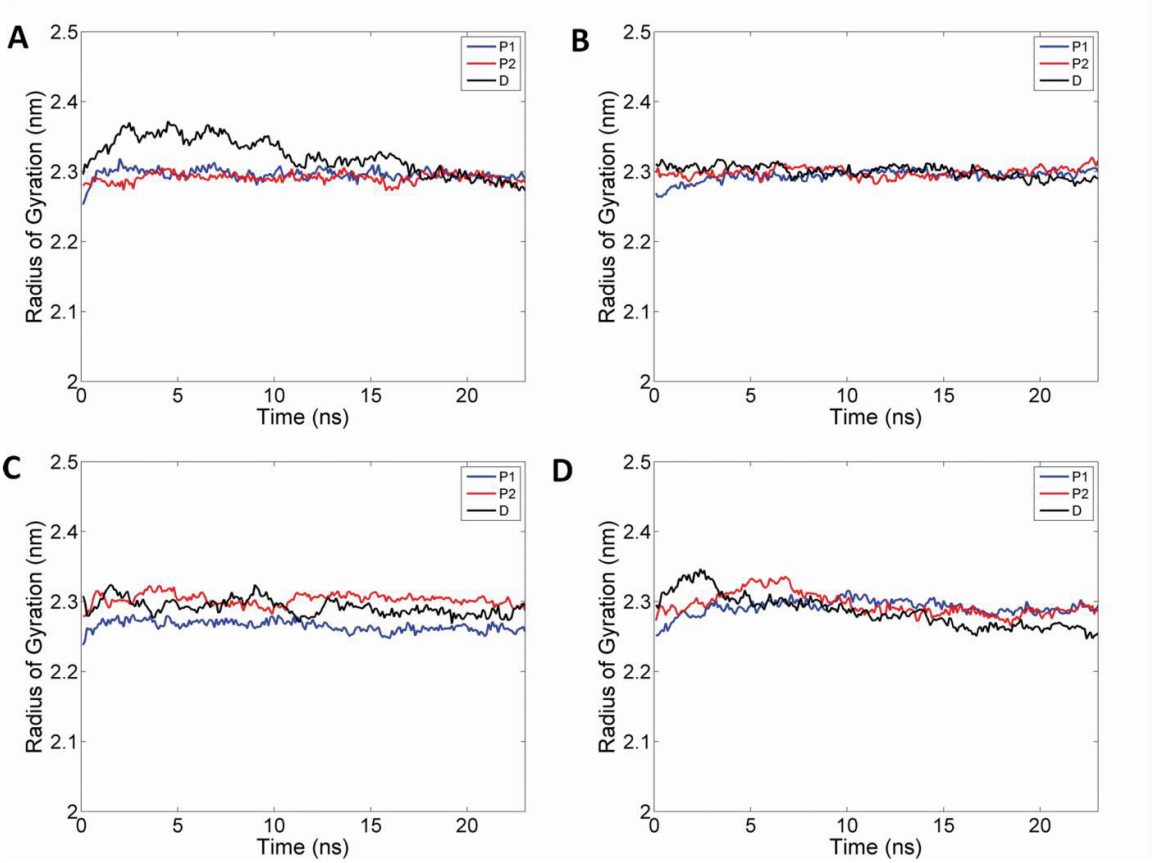

Figure 5.2-6. Radius of gyration of actin monomers averaged over three trials. (A) Control simulation, (B) mode A, (C) mode B, and (D) mode C. The obtained values showed stable behavior in all cases.

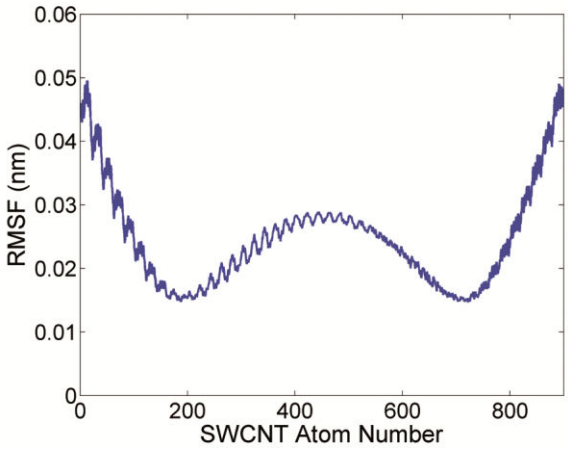

Figure 5.2-7. Root mean square fluctuations of the SWCNT structure. Atoms in the middle region of CWCNT undergo higher range of motion compared to two ends of the structure.

SWCNTs–Actin Dispersions. Since our modeling results demonstrated that there is an energetically favorable interaction directly between SWCNTs and F-actin, we experimentally examined the capability of G-actin monomers and polymerized F-actin oligomers to form stable suspensions of individually dispersed nanotubes (see Methods). Note, when nanotubes are added to water, VDW interactions cause them to aggregate and bundle. However, adhering surfactants and macromolecules allow SWCNTs to be individually dispersed, a widely used approach to create stable nanotube suspensions. The individualization of nanotubes and the stability of the resultant suspensions qualitatively suggest the interaction strength between the macromolecules and nanotubes. We characterized the SWCNT dispersions by F-actin and G-actin with complementary techniques to determine yield (by UV–vis–NIR absorbance spectroscopy), SWCNT defects (by Raman spectroscopy) and dispersion quality (by NIR fluorescence spectroscopy).

UV–vis–NIR absorbance spectroscopy of dispersed SWCNTs showed numerous peaks (Figure 5.2-10A), which indicate that the nanotubes are dispersed in water by both F-actin and G-actin.(O'Connell et al. 2002) The yield from G- and F-actin (Figure 5.2-10B), determined using a known absorbance coefficient at 930 nm,(Holt et al. 2011; Brian D Holt, McCorry, et al. 2012; Brian D Holt, Dahl, et al. 2012; Fagan et al. 2008; Holt et al. 2010) is similar not only to the yield from other protein dispersions(Holt et al. 2011; Brian D Holt, McCorry, et al. 2012) but also is similar to the yield of deoxycholate- (DOC) dispersed SWCNTs: a surfactant that has shown excellent dispersion capability of SWCNTs.(Wenseleers et al. 2004)

We used Raman spectroscopy to further verify the yield and to quantify the quality of the SWCNTs after the dispersion process (Figure 5.2-10C). The intensity of the disorder-band (at ~1300 cm^{-1}), which represents the number of defects in the SWCNT sp^2 structure, was ~10% compared to the intensity of the G-band (~1590 cm^{-1}), which represents the total amount of nanotubes in the suspension.(Dresselhaus et al. 2005) Therefore, we do not think that the dispersion process with F-actin and G-actin introduced defects into the nanotubes.

NIR fluorescence spectroscopy is particularly sensitive to the dispersion quality (*i.e.*, whether nanotubes are individually dispersed or in small bundles).(Bachilo et al. 2002; O'Connell et al. 2002) NIR fluorescence heatmaps demonstrate that both F-actin (Figure 5.2-10D) and G-actin (Figure 5.2-10E) were able to individually disperse SWCNTs. However, their fluorescence intensities (insets of Figure 5.2-10D, E) are only ~5% of the fluorescence intensity obtained for DOC dispersed SWCNTs (insets of Figure 5.2-10F) and ~20% of the fluorescence intensities obtained for other protein dispersed SWCNTs.(Brian D Holt, McCorry, et al. 2012) We suspect that while actin structures can interact with SWCNTs, as demonstrated by our modeling results and as observed experimentally both in cells and *ex vivo*,(Holt et al. 2010; Brian D. Holt et al. 2012) actin likely also generates small bundles of SWCNTs. As a result, actin can provide a high yield of nanotube dispersion (at a similar yield to SWCNTs–DOC) due to small bundles which allow SWCNTs to remain dispersed but are non-fluorescing, resulting in relatively weak fluorescence intensity.

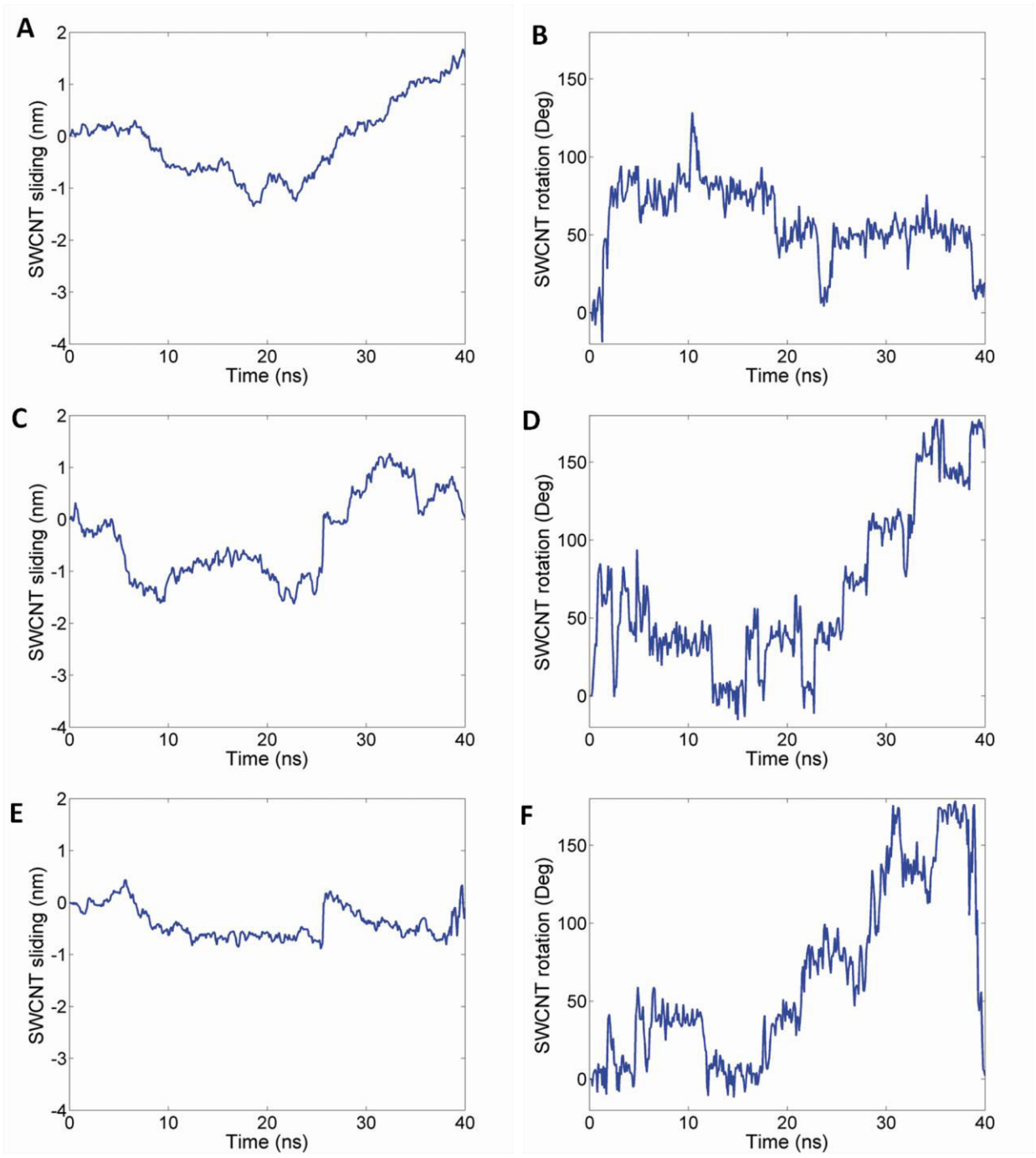

Figure 5.2-8. SWCNT sliding and rotation for mode A. (A) Sliding in trial 1, (B) rotation in trial 1, (C) sliding in trial 2, (D) rotation in trial 2, (E) sliding in trial 3, and (F) rotation in trial 3. SWCNT shows different kinematic behavior in each trial, which can be attributed to the highly dynamic nature of its interaction with actin. While in trial 1 SWCNT continues to travel in a certain direction starting from the middle of simulation time, in other trials it returns to its original position. On the other hand, SWCNT rotation is lowest in trial 1 in comparison to the other trials. Rotation shows stepwise changes while sliding motion is smoother. Sliding and rotational motions do not appear to be coupled.

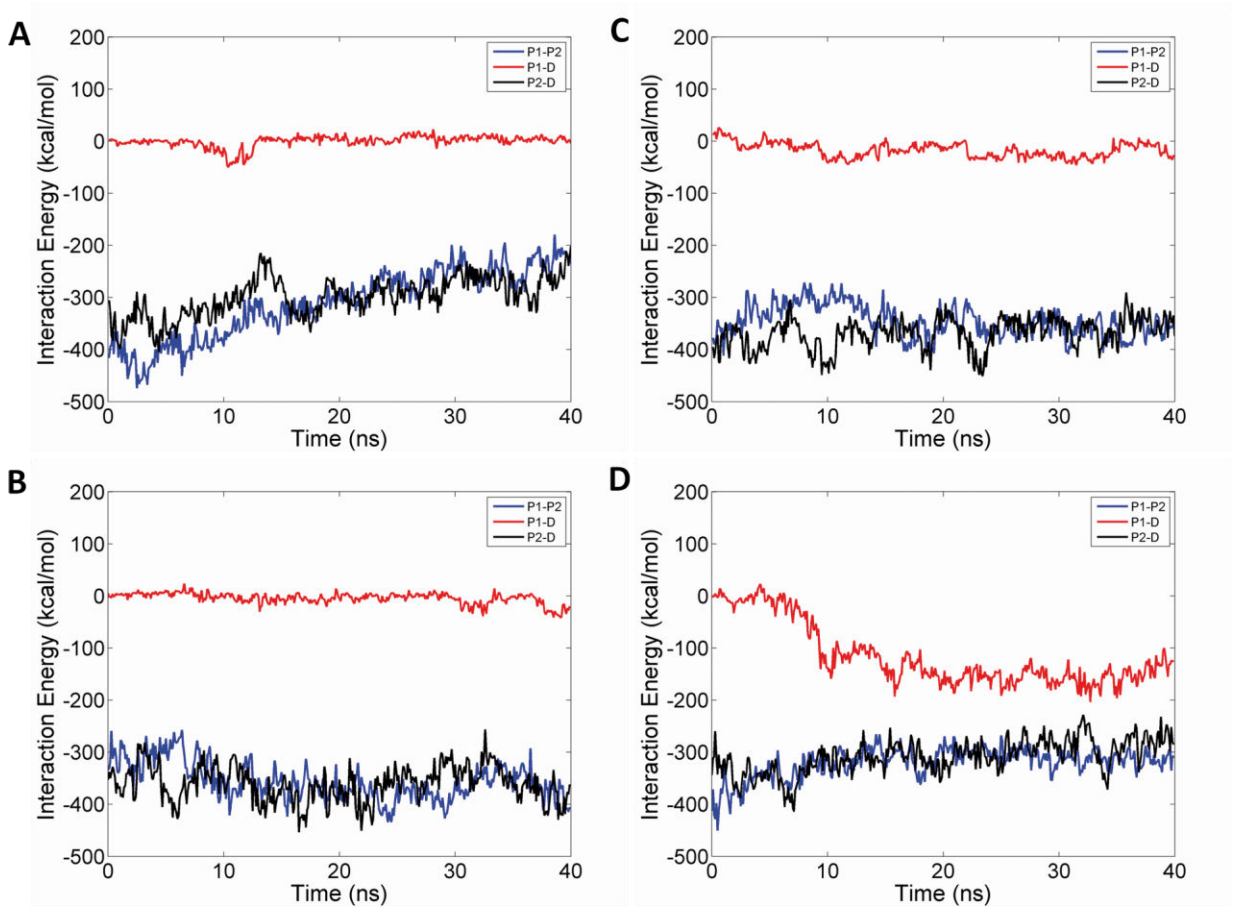

Figure 5.2-9. The average pairwise interactions within the trimer. (A) The interaction energies of all possible pairs of actin monomers (see the legend) in the absence of SWCNT. The P1-P2 and P2-D energies are increasing in time although they are relatively stable compared to P1-D interaction, which is negligible. (B) The P1-P2 and P2-D interaction energies are stabilized upon SWCNT association. However, the third monomer interaction remained the same. All pairwise energies are averaged over three trials.

Discussion

It has recently been observed that the cytoskeletal structure of cell is highly influenced by SWCNT insertion at concentration levels more than 30 µg/mL using confocal microscopy.(Brian D. Holt et al. 2012; Holt et al. 2010) In treated cells, actin filaments are observed at the apical surface and are shortened and branched, and stress fiber formation is disturbed. Interestingly, imaging F-actin (with fluorescently-labeled phalloidin) versus G-actin (with fluorescently-labeled DNase) shows stronger interaction of SWCNTs with F-actin, despite the entropic advantages of the monomeric G-actin. Furthermore, the traction forces on the substrate are reduced in SWCNT-treated cells. However, these previous studies used a surfactant polymer (PF127) to disperse SWCNTs in water. In cells, it is unclear if the PF127 is lost due to numerous membrane interactions and/or displacement by proteins. Here, we investigate the direct interaction between actin and SWCNT (without PF127) using both all-atom MD and NIR fluorescence spectroscopy in order to investigate the correlation between the observations mentioned above and the SWCNT-actin interaction with high precision. The experimental

evidence that actin can directly disperse SWCNTs in water justifies our initial simulation conditions that the SWCNT and actin filament can stably and directly interact.

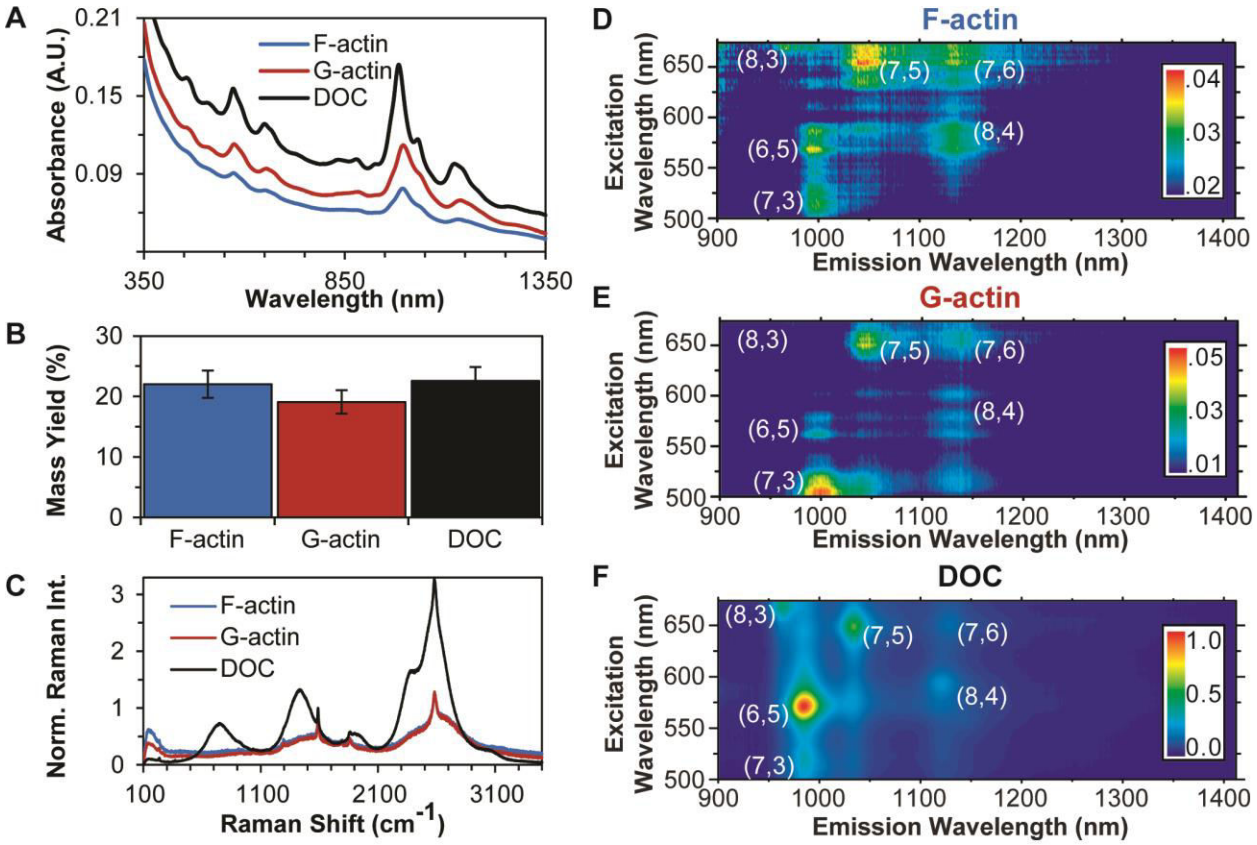

Figure 5.2-10. SWCNTs–actin dispersions characterization. (A) UV-vis-NIR absorbance spectroscopy of SWCNTs–actin dispersions. The peaks arise from the van Hove singularities of the density of states and qualitatively indicate dispersion quality. (B) Using a known absorbance coefficient at 930 nm(Fagan et al. 2008) and known initial masses and final volumes, the proportion of SWCNTs remaining in the supernatant after centrifugation was determined and indicated relatively efficient dispersion of SWCNTs, especially for proteins.(Brian D Holt, McCorry, et al. 2012) (C) Raman spectroscopy confirmed the presence of SWCNTs (G-band at ~1591 cm-1 and radial breathing modes (150–300 cm-1)).(Dresselhaus et al. 2005) For comparison, the data is normalized to each sample's G-band. Note that the large, board peak at ~2200 – 2900 cm-1 primarily arises from real space SWCNT fluorescence at ~950 – 1016 nm that is unfiltered in our system. (D–F) NIR fluorescence spectroscopy heat maps of SWCNT fluorescence. Chiralities are indicated on the heat maps for visual aid. The color scale bar inset indicates the dynamic range of the intensity range scaling (normalized to DOC).

We observed a stable binding interaction forming between SWCNT and actin, particularly in mode A and somewhat in mode B. Interfacial residues of actin in contact with SWCNT are mostly hydrophobic since SWCNT was treated as an electrically neutral and nonpolar molecule. Although the density of hydrophobic residues is not high on the actin surface, we observed that 50% of all interactions in mode A, which showed the largest interface of actin with SWCNT, were hydrophobic demonstrating that SWCNT preferred a local hydrophobic region as its binding site. Moreover, we observed that all residues with planar and

extended side chains were able to form multiple VDW contacts with carbon atoms of SWCNT. As a result, all polar, charged and nonpolar residues can contribute to stabilizing SWCNT binding.

An interesting phenomenon observed in the simulation was the 'surface rubbing' of SWCNT on actin in two independent directions: 1) sliding along and 2) rotating about its own axis (see Figure 5.2-8). Although we quantified the average behavior of all binding modes, the unique characteristics of sliding and rotational motions in each mode, such as directionality and duration were also independently studied. The results from these studies indicated that the dynamics of sliding and rotational motion was mainly due to thermal fluctuation of residues on actin surface. Interestingly, the rotational motion showed a stepwise behavior; however, the frequency could not be specified since it is most likely associated with the thermal motion of actin residues, which is random in nature. Conversely, sliding motion was continuous and in some cases even directional. We could not find any specific strong coupling between sliding and rotation; however, there were instances in which weak correlations were observed. In these observations, rotation and sliding occurred subsequently where rotation preceded sliding (Figure 5.2-8). One possible reason for 'surface rubbing' could be the hydrophobic forces pushing SWCNT atoms towards the actin surface and thus hydrophobicity of the region around the bound interface may determine the direction of motion. From our results we infer that statistically, actin atom is likely to associate with all SWCNT carbons with equal interaction energy; thus, the entropic forces promote maximizing sampling of the phase space. Therefore, the combined sliding and rotational motions could be interpreted as the spatial sampling of the SWCNT surface. Potential controllability of the sliding motion may have interesting applications such as cytoskeletal remodeling and drug release.

Therefore, both entropic and hydrophobic forces are responsible for actin redistribution inside the cell; however, our results showed that actin-SWCNT interaction is also energetically favorable. Moreover, direct dispersion of SWCNTs by F-actin observed by NIR fluorescence spectroscopy was in agreement with the MD simulations. Since actin filaments tend to associate with SWCNT, the intra-monomer interaction may be modified in longer time-scales that may in turn affect the intrinsic properties of actin filaments such as mechanical stability. We also observed a reduced NIR fluorescence of actin-dispersed SWCNTs compared with the yield by UV–vis–NIR absorbance and Raman spectroscopy. This suggests that SWCNTs are dispersed as small bundles, perhaps suggesting the energetically-favorable state of nanotubes with small bundles of actin filaments. Sliding motion of SWCNT may contribute to changing the dynamics of cytoskeletal redistribution and bundling capability of F-actin as well as force bearing properties such as persistence length and bending stiffness. In addition, SWCNTs change the affinity of F-actins for each other.

The pairwise interaction between proximal actin monomers (P_1-P_2) upon SWCNT association is enhanced since the attraction of actin toward SWCNT cancels out the slight repulsion between the monomers (Figure 5.2-2A). Interestingly, P_1-D interaction was notably increased from negligible values to -150 kcal/mol in mode C. Therefore, inter-monomer interactions are affected upon SWCNT binding. One interesting observation was the detachment of the D monomer in one of the mode C trials due to the twist of SWCNT normal to its own axis (Figure 5.2-11).

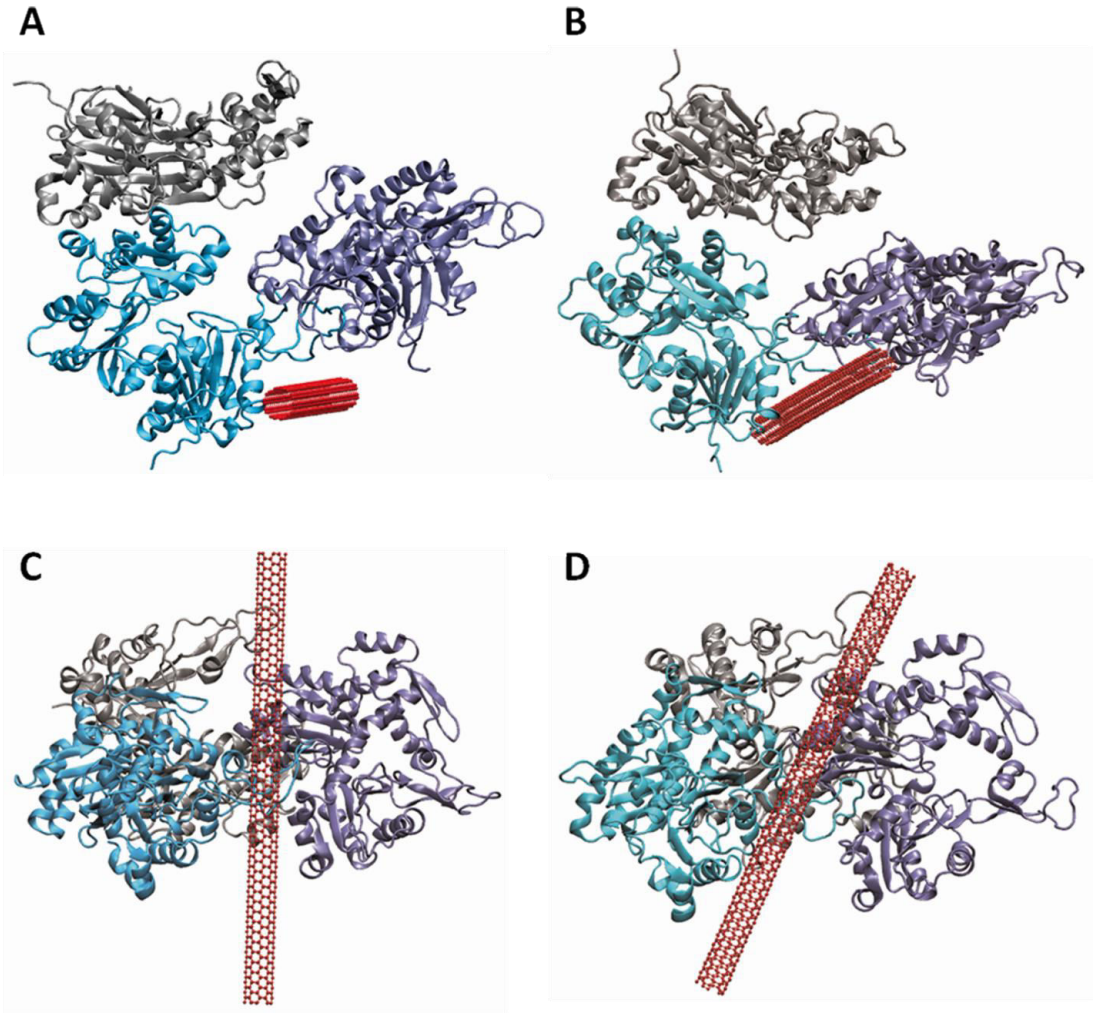

Figure 5.2-11. Dissociation of P2 and D. (A) Initial condition (view 1), (B) final position (view 1), (C) Initial condition (view 2), and (D) final position (view 2). In one of the binding mode C trials, monomers P2 and D began to dissociate; however, other trials did not show a similar behavior. This observed detachment can hypothetically be attributed to the large rotation of SWCNT followed by conformational changes in P2.

Actin bundling requires cross-linking of actin filaments via certain molecules such as α-actinin and filamin.(Kesner et al. 2010; Chen et al. 2009; Shams et al. 2012) The association of actin filaments with SWCNT may hinder actin interaction with α-actinin since its binding site overlaps with mode B, which is located between P_1 and P_2.

Interaction of a single G-actin with SWCNT is energetically less favorable than two actin monomers together. Therefore, it is expected that filament formation precedes SWCNT association. This is indeed consistent with experimental observations of the distribution of fluorescently tagged G-actin and F-actin in normal and SWCNT-treated cells.(Brian D. Holt et al. 2012) It can be concluded that SWCNT affinity is a collective effect of actin monomers in the filamentous arrangement.

The RMSF plot of SWCNT shows that fluctuations of carbon atoms in SWCNT were higher in the mid-point and both ends, showing that the most stationary contact area was observed at approximately one quarter of length from both edges (see Figure 5.2-7). The RMSF

plot of SWCNT remains unchanged upon actin binding independent of the binding mode indicating that local fluctuations of the SWCNT atoms are not affected by the global motions on actin such as sliding and rotation.

It is noteworthy that the SWCNTs attached to cytoskeletal actins are subject to acto-myosin force generation machinery; especially those closer to the cell edge experience forces in the order of piconewtons. Therefore, it is expected that force transmission machinery would be affected upon SWCNT association prohibiting natural protrusions.

In summary, our results revealed the dynamics of direct actin-SWCNT interaction in three distinct binding modes. Inter-monomer interactions of actin are dependent on the SWCNT binding mode and may be increased or decreased in strength. Therefore, cytoskeletal reorganization is mainly due to the modified pairwise interactions in actin upon SWCNT uptake.

Summary

Cellular mechanotransduction, the process by which cells sense mechanical signals and convert them to biochemical signals, is critical to many biological functions including cell migration and stem cell differentiation. One of the most widely studied pathways of cellular mechanotransduction is the integrin-mediated focal adhesions that directly link the cytoskeleton to the extracellular matrix (ECM). Focal adhesions are dynamic molecular complexes that can sense and transmit mechanical forces from the membrane to the cytoskeleton. Cytoskeletal structures such as stress fibers and actin caps are connected to conventional and actin-cap-associated-focal-adhesions (ACAFA), respectively, from which forces are transmitted. However, the mechanism by which the focal adhesions molecules are orchestrated has remained illusive. One hypothesis is the existence of molecular mechanosensors, molecules whose structure and function are regulated by mechanical cues from both extra- and intracellular factors.

Integrin-mediated signaling is crucial for cell-substrate adhesion formation and may be triggered from both intra- and extra-cellular interactions. Talin engages with the β-integrin tail and allosterically induces conformational changes in the extracellular domain of the integrin heterodimer. Although, talin binding was shown to be sufficient for integrin activation, other cytoplasmic proteins can directly interfere with the talin-integrin interaction and alternate signaling. Specifically, α-actinin plays versatile roles in regulating $\alpha_{IIb}\beta_3$ versus $\alpha_5\beta_1$ integrin. It has been shown that α-actinin competes with talin in activating the $\alpha_{IIb}\beta_3$ integrin, while it cooperates with talin for activating $\alpha_5\beta_1$. Here, we compared and contrasted the molecular mechanism of $\alpha_{IIb}\beta_3$ versus $\alpha_5\beta_1$ integrin activation in the presence and absence of α-actinin. Our results showed that cytoplasmic proteins, talin and α-actinin, induce composition-dependent conformational changes in the transmembrane domain of specific integrins that in turn alters their natural response to mechanical signals.

Filamin plays a key role in cellular biomechanics as an actin cross-linker and as a versatile focal adhesion binding partner. It binds directly to integrins, a family of mechanosensitive transmembrane receptors that mediate attachment to several extracellular ligands such as fibronectin, collagen, and laminin. Filamin binds β-integrin at its cytoplasmic tail, competing with talin, a major integrin activator that plays a chief role in cell adhesion. Herein, we develop molecular dynamics models to study the mechanism of early binding of $\alpha_{IIb}\beta_3$ integrin with filamin A (FLNa). Our models predict three important electrostatic interactions and one stabilizing hydrophobic interaction that mediate binding between filamin and integrin. In its native conformation, filamin's integrin binding site is auto-inhibited. Our models help shed light on the role of integrin binding on regulating filamin activation. Finally, the effect of talin on the filamin-integrin interaction is explored and possible scenarios of the interplay among these molecules are examined.

The mechanisms by which living cells respond to mechanical stimuli are not yet fully understood. It has been suggested that mechanosensing proteins play an important role in mechanotransduction since their binding affinities are directly affected by the external stress. α-Actinin is an actin cross-linker and may also act as a mechanosensor in adhesion sites. Its interaction with vinculin is suggested to be mechanically regulated. An activation trajectory was generated in which α-actinin's vinculin-binding site moves out of the rod domain, leading to approximately an 8 kcal/mol free energy release. The activation trajectory reveals several local and global conformational changes along the activation pathway accompanied by the breakage of a number of key interactions stabilizing the inhibited structure. These results may shed light on the role of α-actinin in mechanotransduction and focal adhesion formation.

α-Actinin is an essential actin crosslinker involved in cytoskeletal organization and dynamics. The molecular conformation of α-actinin's actin-binding domain (ABD) regulates its association with actin and thus mutations in this domain can lead to severe pathogenic conditions. A point mutation at lysine 255 in human α-actinin-4 to glutamate increases the binding affinity resulting in stiffer cytoskeletal structures. The role of different ABD conformations and the effect of K255E mutation on ABD conformations remain elusive. To evaluate the impact of K255E mutation on ABD binding to actin we use all-atom molecular dynamics and free energy calculation methods and study the molecular mechanism of actin association in both wild type α-actinin and in the K225E mutant. Our models illustrate that the strength of actin association is indeed sensitive to the ABD conformation, predict the effect of K255E mutation – based on simulations with the K237E mutant chicken α-actinin – and evaluate mechanism of α-actinin binding to actin. Furthermore, our simulations showed that the CaM domain binding to the linker region was important for regulating the distance between actin and ABD. Our results provide valuable insights into the molecular details of this critical cellular phenomenon and further contribute to an understanding of cytoskeletal dynamics in health and disease.

Single wall carbon nanotubes (SWCNTs) have been widely used for biological applications in recent years, and thus it is critical to understand how these inert nanomaterials influence cell behavior. Recently, it has been observed that cellular phenotypes such as proliferation, force generation and growth change upon SWCNT treatment, and SWCNTs directly affect the organization and redistribution of the actin cytoskeleton. However, the interactions between SWCNTs and actin at the molecular level or how this interaction changes actin structure remain largely unknown. Here, we investigated direct interaction of actin with SWCNT using all-atom molecular dynamics simulations and NIR spectroscopy of actin-dispersed SWCNTs. Actin can stably bind to the SWCNT surfaces via hydrophobic interactions but still allows nanotubes to slide and rotate on the actin surface. Our results establish several nanoscale conformational changes for the actin-SWCNT complexes, and we suggest these changes likely induce reorganization of actin filaments observed at larger scales.

In summary, these studies provide detailed structural insights into the molecular mechanisms of mechanical signal transmission across the three focal adhesion layers so called integrin signaling, force transduction and actin regulatory. Such understanding is required for engineering new proteins and developing novel therapeutics important for adhesion-related diseases.

Future directions

The insight and protocols generated in this work may be expanded and used for investigating the relation between the structure and function of other mechanosensitive proteins. Furthermore, a mechanistic approach for tracking forces within the structure of proteins inspired by the analyses provided in this work would be highly beneficial to the field of mechanobiology. Each focal adhesion complex includes different types of integrin receptors connected to a unique composition of proteins. Studying individual integrin heterodimers and their associated proteins give rise to a modular approach for understanding force transmission mechanisms from the ECM to the cytoskeleton. Such an approach will provide a great insight into the specific role of individual proteins in integrin signaling and potential redundancies in their function, which has still remained illusive.

Reference

Anitei, M. & Hoflack, B., 2012. Bridging membrane and cytoskeleton dynamics in the secretory and endocytic pathways. *Nature cell biology*, 14(1), pp.11–9. Available at: http://dx.doi.org/10.1038/ncb2409 [Accessed August 21, 2015].

Anthis, N.J. et al., 2009. The structure of an integrin/talin complex reveals the basis of inside-out signal transduction. *The EMBO journal*, 28(22), pp.3623–32. Available at: http://www.pubmedcentral.nih.gov/articlerender.fcgi?artid=2782098&tool=pmcentrez&rendertype=abstract [Accessed May 13, 2015].

Bachilo, S.M. et al., 2002. Structure-assigned optical spectra of single-walled carbon nanotubes. *Science (New York, N.Y.)*, 298(5602), pp.2361–6.

Baker, D. & Sali, A., 2001. Protein structure prediction and structural genomics. *Science (New York, N.Y.)*, 294(5540), pp.93–6. Available at: http://science.sciencemag.org/content/294/5540/93.abstract [Accessed February 28, 2016].

Bakolitsa, C. et al., 2004. Structural basis for vinculin activation at sites of cell adhesion. *Nature*, 430(6999), pp.583–6. Available at: http://www.ncbi.nlm.nih.gov/pubmed/15195105 [Accessed February 13, 2016].

Balaban, N.Q. et al., 2001. Force and focal adhesion assembly: a close relationship studied using elastic micropatterned substrates. *Nature cell biology*, 3(5), pp.466–72. Available at: http://dx.doi.org/10.1038/35074532 [Accessed September 11, 2015].

Bianco, A., Kostarelos, K., et al., 2005. Biomedical applications of functionalised carbon nanotubes. *Chemical communications (Cambridge, England)*, (5), pp.571–7. Available at: http://www.ncbi.nlm.nih.gov/pubmed/15672140 [Accessed November 6, 2012].

Bianco, A., Hoebeke, J., et al., 2005. Cationic carbon nanotubes bind to CpG oligodeoxynucleotides and enhance their immunostimulatory properties. *Journal of the American Chemical Society*, 127(1), pp.58–9. Available at: http://www.ncbi.nlm.nih.gov/pubmed/15631447.

Biasini, M. et al., 2014. SWISS-MODEL: modelling protein tertiary and quaternary structure using evolutionary information. *Nucleic acids research*, 42(Web Server issue), pp.W252–8. Available at: http://nar.oxfordjournals.org/content/42/W1/W252 [Accessed July 10, 2014].

Blanchard, A., Ohanian, V. & Critchley, D., 1989. The structure and function of alpha-actinin. *Journal of muscle research and cell motility*, 10(4), pp.280–9. Available at: http://www.ncbi.nlm.nih.gov/pubmed/2671039 [Accessed July 2, 2014].

Bois, P.R.J. et al., 2005. Structural dynamics of alpha-actinin-vinculin interactions. *Molecular and cellular biology*, 25(14), pp.6112–22. Available at: http://www.pubmedcentral.nih.gov/articlerender.fcgi?artid=1168820&tool=pmcentrez&rendertype=abstract [Accessed July 2, 2014].

Bois, P.R.J. et al., 2006. The vinculin binding sites of talin and α-actinin are sufficient to activate vinculin. *Journal of Biological Chemistry*, 281(11), pp.7228–7236.

Borgon, R. a et al., 2004. Crystal structure of human vinculin. *Structure (London, England : 1993)*, 12(7), pp.1189–97. Available at: http://www.ncbi.nlm.nih.gov/pubmed/15242595 [Accessed March 22, 2013].

Borrego-Diaz, E. et al., 2006. Crystal structure of the actin-binding domain of alpha-

actinin 1: evaluating two competing actin-binding models. *Journal of structural biology*, 155(2), pp.230–8. Available at: http://www.ncbi.nlm.nih.gov/pubmed/16698282 [Accessed June 14, 2014].
Bukoreshtliev, N. V., Haase, K. & Pelling, A.E., 2013. Mechanical cues in cellular signalling and communication. *Cell and Tissue Research*, 352(1), pp.77–94.
Burridge, K. et al., 1988. Focal adhesions: transmembrane junctions between the extracellular matrix and the cytoskeleton. *Annual review of cell biology*, 4, pp.487–525. Available at: http://www.annualreviews.org/doi/abs/10.1146/annurev.cb.04.110188.002415 [Accessed February 13, 2016].
Burridge, K. & Feramisco, J.R., 1981. Non-muscle α-actinins are calcium-sensitive actin-binding proteins. *Nature*, 294(5841), pp.565–567. Available at: http://dx.doi.org/10.1038/294565a0 [Accessed July 2, 2014].
Buschmann, I. et al., 2010. Pulsatile shear and Gja5 modulate arterial identity and remodeling events during flow-driven arteriogenesis. *Development (Cambridge, England)*, 137(13), pp.2187–96. Available at: http://www.ncbi.nlm.nih.gov/pubmed/20530546 [Accessed May 9, 2016].
Byrd, R.H. et al., 1995. A Limited Memory Algorithm for Bound Constrained Optimization. *SIAM Journal on Scientific Computing*, 16(5), pp.1190–1208. Available at: http://epubs.siam.org/doi/abs/10.1137/0916069 [Accessed February 3, 2015].
Calderwood, D.A. et al., 2001. Increased filamin binding to beta-integrin cytoplasmic domains inhibits cell migration. *Nature cell biology*, 3(12), pp.1060–8. Available at: http://dx.doi.org/10.1038/ncb1201-1060 [Accessed May 13, 2015].
Calderwood, D.A., Campbell, I.D. & Critchley, D.R., 2013. Talins and kindlins: partners in integrin-mediated adhesion. *Nature reviews. Molecular cell biology*, 14(8), pp.503–17. Available at: http://dx.doi.org/10.1038/nrm3624 [Accessed March 30, 2015].
Campbell, I.D. & Humphries, M.J., 2011. Integrin structure, activation, and interactions. *Cold Spring Harbor perspectives in biology*, 3(3). Available at: http://www.pubmedcentral.nih.gov/articlerender.fcgi?artid=3039929&tool=pmcentrez&rendertype=abstract [Accessed August 24, 2015].
Carisey, A. et al., 2013a. Vinculin regulates the recruitment and release of core focal adhesion proteins in a force-dependent manner. *Current biology : CB*, 23(4), pp.271–81. Available at: http://www.ncbi.nlm.nih.gov/pubmed/23375895 [Accessed March 1, 2013].
Carisey, A. et al., 2013b. Vinculin regulates the recruitment and release of core focal adhesion proteins in a force-dependent manner. *Current biology : CB*, 23(4), pp.271–81. Available at: http://www.sciencedirect.com/science/article/pii/S0960982213000122 [Accessed July 17, 2014].
Carisey, A. & Ballestrem, C., 2011. Vinculin, an adapter protein in control of cell adhesion signalling. *European journal of cell biology*, 90(2-3), pp.157–63. Available at: http://www.sciencedirect.com/science/article/pii/S0171933510001214 [Accessed July 17, 2014].
Case, L.B. et al., 2015. Molecular mechanism of vinculin activation and nanoscale spatial

organization in focal adhesions. *Nature Cell Biology*, 17(7), pp.880–892. Available at: http://www.nature.com/doifinder/10.1038/ncb3180.

Case, L.B. & Waterman, C.M., 2015. Integration of actin dynamics and cell adhesion by a three-dimensional, mechanosensitive molecular clutch. *Nature cell biology*, 17(8), pp.955–963. Available at: http://dx.doi.org/10.1038/ncb3191.

Chambliss, A.B. et al., 2013. The LINC-anchored actin cap connects the extracellular milieu to the nucleus for ultrafast mechanotransduction. *Scientific reports*, 3, pp.1087–1093. Available at: http://www.pubmedcentral.nih.gov/articlerender.fcgi?artid=3548190&tool=pmcentrez&rendertype=abstract [Accessed May 28, 2014].

Chen, H. et al., 2013. Mechanical perturbation of filamin A immunoglobulin repeats 20-21 reveals potential non-equilibrium mechanochemical partner binding function. *Scientific reports*, 3, p.1642. Available at: http://www.pubmedcentral.nih.gov/articlerender.fcgi?artid=3622079&tool=pmcentrez&rendertype=abstract [Accessed May 13, 2015].

Chen, H., Choudhury, D.M. & Craig, S.W., 2006. Coincidence of actin filaments and talin is required to activate vinculin. *The Journal of biological chemistry*, 281(52), pp.40389–98. Available at: http://www.ncbi.nlm.nih.gov/pubmed/17074767 [Accessed February 13, 2016].

Chen, H.S., Kolahi, K.S. & Mofrad, M.R.K., 2009a. Phosphorylation facilitates the integrin binding of filamin under force. *Biophysical journal*, 97(12), pp.3095–104. Available at: http://www.pubmedcentral.nih.gov/articlerender.fcgi?artid=2793350&tool=pmcentrez&rendertype=abstract [Accessed February 25, 2013].

Chen, H.S., Kolahi, K.S. & Mofrad, M.R.K., 2009b. Phosphorylation facilitates the integrin binding of filamin under force. *Biophysical journal*, 97(12), pp.3095–104. Available at: http://www.sciencedirect.com/science/article/pii/S0006349509015148 [Accessed May 13, 2015].

Cherukuri, P. et al., 2004. Near-infrared fluorescence microscopy of single-walled carbon nanotubes in phagocytic cells. *Journal of the American Chemical Society*, 126(48), pp.15638–9. Available at: http://www.ncbi.nlm.nih.gov/pubmed/15571374.

Choi, C.K. et al., 2008. Actin and alpha-actinin orchestrate the assembly and maturation of nascent adhesions in a myosin II motor-independent manner. *Nature cell biology*, 10(9), pp.1039–50. Available at: http://www.pubmedcentral.nih.gov/articlerender.fcgi?artid=2827253&tool=pmcentrez&rendertype=abstract [Accessed March 30, 2016].

Ciobanasu, C., Faivre, B. & Le Clainche, C., 2014. Reconstituting actomyosin-dependent mechanosensitive protein complexes in vitro. *Nature Protocols*, 10(1), pp.75–89.

Coutinho, A. et al., 2007. Conformational changes in human integrin alphaIIbbeta3 after platelet activation, monitored by FRET. *Biophysical chemistry*, 130(1-2), pp.76–87. Available at: http://www.ncbi.nlm.nih.gov/pubmed/17714854 [Accessed July 16, 2014].

Critchley, D.R. & Gingras, A.R., 2008. Talin at a glance. *Journal of cell science*, 121(Pt 9), pp.1345–7. Available at: http://jcs.biologists.org/content/121/9/1345 [Accessed January 30, 2016].

Darden, T., York, D. & Pedersen, L., 1993. Particle mesh Ewald: An N·log(N) method

for Ewald sums in large systems. *The Journal of Chemical Physics*, 98(12), p.10089. Available at: http://scitation.aip.org/content/aip/journal/jcp/98/12/10.1063/1.464397 [Accessed July 9, 2014].
David, V.D.S. et al., 2005. GROMACS: Fast, flexible, and free. *Journal of computational chemistry*, 26(16), pp.1701–1718.
Day, C.A. et al., 2012. Analysis of protein and lipid dynamics using confocal fluorescence recovery after photobleaching (FRAP). *Current protocols in cytometry / editorial board, J. Paul Robinson, managing editor ... [et al.]*, Chapter 2, p.Unit2.19. Available at: http://www.pubmedcentral.nih.gov/articlerender.fcgi?artid=3538152&tool=pmcentrez&rendertype=abstract [Accessed March 31, 2016].
Debiec, K.T., Gronenborn, A.M. & Chong, L.T., 2014. Evaluating the strength of salt bridges: a comparison of current biomolecular force fields. *The journal of physical chemistry. B*, 118(24), pp.6561–9. Available at: http://www.pubmedcentral.nih.gov/articlerender.fcgi?artid=4064690&tool=pmcentrez&rendertype=abstract [Accessed May 13, 2015].
DeMali, K.A., Sun, X. & Bui, G.A., 2014. Force transmission at cell-cell and cell-matrix adhesions. *Biochemistry*, 53(49), pp.7706–17. Available at: http://dx.doi.org/10.1021/bi501181p [Accessed March 16, 2015].
Djinović-Carugo, K. et al., 1999. Structure of the alpha-actinin rod: molecular basis for cross-linking of actin filaments. *Cell*, 98(4), pp.537–46. Available at: http://www.ncbi.nlm.nih.gov/pubmed/10481917 [Accessed March 30, 2016].
Dresselhaus, B.M.S., Dresselhaus, G. & Charlier, J.C., 2004. Electronic , thermal and mechanical properties of carbon nanotubes. , pp.2065–2098.
Dresselhaus, M.S. et al., 2005. Raman spectroscopy of carbon nanotubes. *Physics Reports*, 409(2), pp.47–99.
Edlund, M., Lotano, M. a & Otey, C. a, 2001. Dynamics of alpha-actinin in focal adhesions and stress fibers visualized with alpha-actinin-green fluorescent protein. *Cell motility and the cytoskeleton*, 48(3), pp.190–200. Available at: http://www.ncbi.nlm.nih.gov/pubmed/11223950.
Ehrlicher, A.J. et al., 2015. Alpha-actinin binding kinetics modulate cellular dynamics and force generation. *Proceedings of the National Academy of Sciences of the United States of America*, 112(21), pp.6619–24. Available at: http://www.pnas.org/content/112/21/6619.short [Accessed September 7, 2015].
Fagan, J. a. et al., 2008. Length Fractionation of Carbon Nanotubes Using Centrifugation. *Advanced Materials*, 20(9), pp.1609–1613.
Feng, Y. & Walsh, C.A., 2004. The many faces of filamin: a versatile molecular scaffold for cell motility and signalling. *Nature cell biology*, 6(11), pp.1034–8. Available at: http://www.ncbi.nlm.nih.gov/pubmed/15516996 [Accessed May 13, 2015].
Fraley, T.S. et al., 2003. Phosphoinositide binding inhibits alpha-actinin bundling activity. *The Journal of biological chemistry*, 278(26), pp.24039–45. Available at: http://www.ncbi.nlm.nih.gov/pubmed/12716899 [Accessed July 2, 2014].
Fukami, K. et al., 1994. alpha-Actinin and vinculin are PIP2-binding proteins involved in signaling by tyrosine kinase. *The Journal of biological chemistry*, 269(2), pp.1518–22. Available at: http://www.ncbi.nlm.nih.gov/pubmed/8288618.
Galbraith, C.G., Yamada, K.M. & Sheetz, M.P., 2002. The relationship between force

and focal complex development. *The Journal of cell biology*, 159(4), pp.695–705. Available at: http://www.pubmedcentral.nih.gov/articlerender.fcgi?artid=2173098&tool=pmcentrez&rendertype=abstract [Accessed May 26, 2014].

Galkin, V.E., Orlova, A., Salmazo, A., Djinovic-carugo, K., et al., 2010. Opening of tandem calponin homology domains regulates their affinity for F-actin. *Nature Publishing Group*, 17(5), pp.614–616. Available at: http://dx.doi.org/10.1038/nsmb.1789.

Galkin, V.E., Orlova, A., Salmazo, A., Djinovic-Carugo, K., et al., 2010. Opening of tandem calponin homology domains regulates their affinity for F-actin. *Nature structural & molecular biology*, 17(5), pp.614–6. Available at: http://www.pubmedcentral.nih.gov/articlerender.fcgi?artid=2921939&tool=pmcentrez&rendertype=abstract [Accessed May 27, 2014].

García-Alvarez, B. et al., 2003. Structural Determinants of Integrin Recognition by Talin. *Molecular Cell*, 11(1), pp.49–58. Available at: http://www.sciencedirect.com/science/article/pii/S1097276502008237 [Accessed May 13, 2015].

Gardel, M.L. et al., 2008. Traction stress in focal adhesions correlates biphasically with actin retrograde flow speed. *The Journal of Cell Biology*, 183(6), pp.999–1005. Available at: http://www.ncbi.nlm.nih.gov/pubmed/19075110.

Geiger, B., Spatz, J.P. & Bershadsky, A.D., 2009. Environmental sensing through focal adhesions. *Nature reviews. Molecular cell biology*, 10(1), pp.21–33. Available at: http://dx.doi.org/10.1038/nrm2593 [Accessed March 17, 2015].

Giancotti, F.G., 1997. Integrin signaling: specificity and control of cell survival and cell cycle progression. *Current Opinion in Cell Biology*, 9(5), pp.691–700. Available at: http://www.sciencedirect.com/science/article/pii/S0955067497801238 [Accessed March 30, 2016].

Golji, J., Collins, R. & Mofrad, M.R.K., 2009. Molecular mechanics of the alpha-actinin rod domain: bending, torsional, and extensional behavior. *PLoS computational biology*, 5(5), pp.e1000389–e1000406. Available at: http://www.pubmedcentral.nih.gov/articlerender.fcgi?artid=2676514&tool=pmcentrez&rendertype=abstract [Accessed November 2, 2012].

Golji, J., Lam, J. & Mofrad, M.R.K., 2011. Vinculin activation is necessary for complete talin binding. *Biophysical journal*, 100(2), pp.332–40. Available at: http://www.sciencedirect.com/science/article/pii/S0006349510014220 [Accessed June 22, 2015].

Golji, J. & Mofrad, M.R.K., 2010. A molecular dynamics investigation of vinculin activation. *Biophysical journal*, 99(4), pp.1073–81. Available at: http://www.pubmedcentral.nih.gov/articlerender.fcgi?artid=2920635&tool=pmcentrez&rendertype=abstract [Accessed June 22, 2015].

Golji, J. & Mofrad, M.R.K., 2013. The interaction of vinculin with actin. *PLoS computational biology*, 9(4), p.e1002995. Available at: http://journals.plos.org/ploscompbiol/article?id=10.1371/journal.pcbi.1002995 [Accessed August 22, 2015].

Golji, J. & Mofrad, M.R.K., 2014. The talin dimer structure orientation is mechanically regulated. *Biophysical journal*, 107(8), pp.1802–9. Available at:

http://www.sciencedirect.com/science/article/pii/S0006349514009503 [Accessed June 22, 2015].
Goult, B.T. et al., 2013. RIAM and vinculin binding to talin are mutually exclusive and regulate adhesion assembly and turnover. *The Journal of biological chemistry*, 288(12), pp.8238–49. Available at: http://www.pubmedcentral.nih.gov/articlerender.fcgi?artid=3605642&tool=pmcentrez&rendertype=abstract [Accessed May 13, 2015].
Grant, B.J. et al., 2006. Bio3d: an R package for the comparative analysis of protein structures. *Bioinformatics (Oxford, England)*, 22(21), pp.2695–6. Available at: http://www.ncbi.nlm.nih.gov/pubmed/16940322 [Accessed August 14, 2015].
Guex, N. & Peitsch, M.C., 1997. SWISS-MODEL and the Swiss-PdbViewer: an environment for comparative protein modeling. *Electrophoresis*, 18(15), pp.2714–23. Available at: http://www.ncbi.nlm.nih.gov/pubmed/9504803 [Accessed July 23, 2014].
Hampton, C.M., Taylor, D.W. & Taylor, K. a, 2007. Novel structures for alpha-actinin:F-actin interactions and their implications for actin-membrane attachment and tension sensing in the cytoskeleton. *Journal of molecular biology*, 368(1), pp.92–104. Available at: http://www.pubmedcentral.nih.gov/articlerender.fcgi?artid=1919418&tool=pmcentrez&rendertype=abstract [Accessed January 4, 2013].
Harburger, D.S. & Calderwood, D.A., 2009. Integrin signalling at a glance. *Journal of cell science*, 122(Pt 2), pp.159–63. Available at: http://jcs.biologists.org/content/122/2/159.short [Accessed July 2, 2014].
Harrison, B.S. & Atala, A., 2007. Carbon nanotube applications for tissue engineering. *Biomaterials*, 28(2), pp.344–53.
Hayashi, T. et al., 2004. Tcap gene mutations in hypertrophic cardiomyopathy and dilated cardiomyopathy. *Journal of the American College of Cardiology*, 44(11), pp.2192–201. Available at: http://www.ncbi.nlm.nih.gov/pubmed/15582318 [Accessed July 2, 2014].
Haydari, Z. & Mofrad, M.R.K., Role of talin1/kindlin3 interaction in integrin clustering. *Biophysical journal*.
Heller, D. a. et al., 2005. Single-Walled Carbon Nanotube Spectroscopy in Live Cells: Towards Long-Term Labels and Optical Sensors. *Advanced Materials*, 17(23), pp.2793–2799. Available at: http://doi.wiley.com/10.1002/adma.200500477 [Accessed November 1, 2012].
Hemmings, L., Kuhlman, P.A. & Critchley, D.R., 1992. Analysis of the actin-binding domain of alpha-actinin by mutagenesis and demonstration that dystrophin contains a functionally homologous domain. *The Journal of cell biology*, 116(6), pp.1369–80. Available at: http://www.pubmedcentral.nih.gov/articlerender.fcgi?artid=2289384&tool=pmcentrez&rendertype=abstract [Accessed February 13, 2016].
Hess, B. et al., 1997. LINCS: A linear constraint solver for molecular simulations. *Journal of Computational Chemistry*, 18(12), pp.1463–1472. Available at: http://doi.wiley.com/10.1002/%28SICI%291096-987X%28199709%2918%3A12%3C1463%3A%3AAID-JCC4%3E3.0.CO%3B2-H [Accessed May 29, 2014].

Holle, A.W. et al., 2013. In situ mechanotransduction via vinculin regulates stem cell differentiation. *Stem cells (Dayton, Ohio)*, 31(11), pp.2467–77. Available at: http://www.pubmedcentral.nih.gov/articlerender.fcgi?artid=3833960&tool=pmcentrez&rendertype=abstract [Accessed April 16, 2015].

Holt, B.D. et al., 2012. Altered Cell Mechanics from the Inside: Dispersed Single Wall Carbon Nanotubes Integrate with and Restructure Actin. *Journal of Functional Biomaterials*, 3(2), pp.398–417.

Holt, B.D. et al., 2010. Carbon nanotubes reorganize actin structures in cells and ex vivo. *ACS nano*, 4(8), pp.4872–8.

Holt, B.D., Dahl, K.N., et al., 2012. Cells Take up and Recover from Nanotubes with Two Distinct Rates. , (4), pp.3481–3490.

Holt, B.D., McCorry, M.C., et al., 2012. Not all protein-mediated single-wall carbon nanotube dispersions are equally bioactive. *Nanoscale*, 4(23), pp.7425–34.

Holt, B.D., Dahl, K.N. & Islam, M.F., 2011. Quantification of uptake and localization of bovine serum albumin-stabilized single-wall carbon nanotubes in different human cell types. *Small (Weinheim an der Bergstrasse, Germany)*, 7(16), pp.2348–55.

Hoover, W., 1985. Canonical dynamics: Equilibrium phase-space distributions. *Physical Review A*, 31(3), pp.1695–1697. Available at: http://link.aps.org/doi/10.1103/PhysRevA.31.1695 [Accessed June 3, 2014].

Hotulainen, P. & Lappalainen, P., 2006. Stress fibers are generated by two distinct actin assembly mechanisms in motile cells. *The Journal of cell biology*, 173(3), pp.383–94. Available at: http://jcb.rupress.org/content/173/3/383.short [Accessed May 27, 2014].

Huang, Y., Zhang, W. & Gunst, S.J., 2011. Activation of vinculin induced by cholinergic stimulation regulates contraction of tracheal smooth muscle tissue. *The Journal of biological chemistry*, 286(5), pp.3630–44. Available at: http://www.pubmedcentral.nih.gov/articlerender.fcgi?artid=3030367&tool=pmcentrez&rendertype=abstract [Accessed February 13, 2016].

Humphrey, J.D., Dufresne, E.R. & Schwartz, M.A., 2014. Mechanotransduction and extracellular matrix homeostasis. *Nature Reviews Molecular Cell Biology*, 15(12), pp.802–812. Available at: http://dx.doi.org/10.1038/nrm3896.

Humphrey, W., Dalke, A. & Schulten, K., 1996. VMD-visual molecular dynamics. *J. Mol. Graphics*, 14, pp.33–38.

Humphrey, W., Dalke, A. & Schulten, K., 1996. VMD: visual molecular dynamics. *Journal of molecular graphics*, 14(1), pp.33–8, 27–8. Available at: http://www.ncbi.nlm.nih.gov/pubmed/8744570 [Accessed May 24, 2014].

Iskratsch, T., Wolfenson, H. & Sheetz, M.P., 2014. Appreciating force and shape — the rise of mechanotransduction in cell biology. *Nature Publishing Group*, 15(12), pp.825–833. Available at: http://dx.doi.org/10.1038/nrm3903\n10.1038/nrm3903.

Ithychanda, S.S. et al., 2009. Identification and characterization of multiple similar ligand-binding repeats in filamin: implication on filamin-mediated receptor clustering and cross-talk. *The Journal of biological chemistry*, 284(50), pp.35113–21. Available at: http://www.pubmedcentral.nih.gov/articlerender.fcgi?artid=2787372&tool=pmcentrez&rendertype=abstract [Accessed May 13, 2015].

Iwamoto, D. V & Calderwood, D.A., 2015. Regulation of integrin-mediated adhesions.

Current Opinion in Cell Biology, 36(Figure 2), pp.41–47. Available at: http://linkinghub.elsevier.com/retrieve/pii/S0955067415000757.
Izard, T. et al., 2004. Vinculin activation by talin through helical bundle conversion. *Nature*, 427(6970), pp.171–5. Available at: http://dx.doi.org/10.1038/nature02281 [Accessed February 13, 2016].
Jahed, Z. et al., 2014. Mechanotransduction pathways linking the extracellular matrix to the nucleus. *International review of cell and molecular biology*, 310, pp.171–220. Available at: http://www.ncbi.nlm.nih.gov/pubmed/24725427 [Accessed June 22, 2015].
Jiang, G. et al., 2003. Two-piconewton slip bond between fibronectin and the cytoskeleton depends on talin. *Nature*, 424(6946), pp.334–7. Available at: http://www.ncbi.nlm.nih.gov/pubmed/12867986 [Accessed March 31, 2016].
Jorgensen, W.L. et al., 1983. Comparison of simple potential functions for simulating liquid water. *The Journal of Chemical Physics*, 79(2), pp.926–935. Available at: http://scitation.aip.org/content/aip/journal/jcp/79/2/10.1063/1.445869 [Accessed May 26, 2014].
Kahana, E. & Gratzer, W.B., 1991. Properties of the spectrin-like structural element of smooth-muscle alpha-actinin. *Cell motility and the cytoskeleton*, 20(3), pp.242–8. Available at: http://www.ncbi.nlm.nih.gov/pubmed/1773450.
Kalli, A.C., Campbell, I.D. & Sansom, M.S.P., 2011. Multiscale simulations suggest a mechanism for integrin inside-out activation. *Proceedings of the National Academy of Sciences of the United States of America*, 108(29), pp.11890–5. Available at: http://www.pubmedcentral.nih.gov/articlerender.fcgi?artid=3141943&tool=pmcentrez&rendertype=abstract [Accessed May 13, 2015].
Kam, N.W.S. & Dai, H., 2005. Carbon nanotubes as intracellular protein transporters: generality and biological functionality. *Journal of the American Chemical Society*, 127(16), pp.6021–6. Available at: http://www.ncbi.nlm.nih.gov/pubmed/15839702.
Kam, N.W.S., Liu, Z. & Dai, H., 2006. Carbon nanotubes as intracellular transporters for proteins and DNA: an investigation of the uptake mechanism and pathway. *Angewandte Chemie (International ed. in English)*, 45(4), pp.577–81. Available at: http://www.ncbi.nlm.nih.gov/pubmed/16345107 [Accessed November 8, 2012].
Kanchanawong, P. et al., 2010. Nanoscale architecture of integrin-based cell adhesions. *Nature*, 468(7323), pp.580–4. Available at: http://dx.doi.org/10.1038/nature09621 [Accessed May 7, 2016].
Katta, S., Krieg, M. & Goodman, M.B., 2015. Feeling Force: Physical and Physiological Principles Enabling Sensory Mechanotransduction. *Annual Review of Cell and Developmental Biology*, 31(1), pp.347–371. Available at: http://www.annualreviews.org/doi/10.1146/annurev-cellbio-100913-013426.
Kelley, L.A. et al., 2015. The Phyre2 web portal for protein modeling, prediction and analysis. *Nature protocols*, 10(6), pp.845–858. Available at: http://dx.doi.org/10.1038/nprot.2015.053 [Accessed May 8, 2015].
Kelly, D.F. et al., 2006. Structure of the alpha-actinin-vinculin head domain complex determined by cryo-electron microscopy. *Journal of molecular biology*, 357(2), pp.562–73. Available at: http://www.ncbi.nlm.nih.gov/pubmed/16430917 [Accessed November 9, 2012].
Kelly, D.F. & Taylor, K.A., 2005. Identification of the beta1-integrin binding site on

alpha-actinin by cryoelectron microscopy. *Journal of structural biology*, 149(3), pp.290–302. Available at: http://www.ncbi.nlm.nih.gov/pubmed/15721583 [Accessed April 1, 2016].

Kesner, B. a et al., 2010. Isoform divergence of the filamin family of proteins. *Molecular biology and evolution*, 27(2), pp.283–95. Available at: http://www.ncbi.nlm.nih.gov/pubmed/19805437 [Accessed January 20, 2013].

Kiema, T. et al., 2006. The molecular basis of filamin binding to integrins and competition with talin. *Molecular cell*, 21(3), pp.337–47. Available at: http://www.sciencedirect.com/science/article/pii/S1097276506000311 [Accessed May 8, 2015].

Kim, D.-H. et al., 2012. Actin cap associated focal adhesions and their distinct role in cellular mechanosensing. *Scientific reports*, 2, pp.555–517. Available at: http://www.pubmedcentral.nih.gov/articlerender.fcgi?artid=3412326&tool=pmcentrez&rendertype=abstract [Accessed June 2, 2014].

Kim, H., Nakamura, F., Lee, W., Shifrin, Y., et al., 2010. Filamin A is required for vimentin-mediated cell adhesion and spreading. *American journal of physiology. Cell physiology*, 298(2), pp.C221–36. Available at: http://www.pubmedcentral.nih.gov/articlerender.fcgi?artid=4380480&tool=pmcentrez&rendertype=abstract [Accessed May 13, 2015].

Kim, H., Nakamura, F., Lee, W., Hong, C., et al., 2010. Regulation of cell adhesion to collagen via beta1 integrins is dependent on interactions of filamin A with vimentin and protein kinase C epsilon. *Experimental cell research*, 316(11), pp.1829–44. Available at: http://www.ncbi.nlm.nih.gov/pubmed/20171211 [Accessed May 13, 2015].

Kim, M., Carman, C. V & Springer, T.A., 2003. Bidirectional transmembrane signaling by cytoplasmic domain separation in integrins. *Science (New York, N.Y.)*, 301(5640), pp.1720–5. Available at: http://www.sciencemag.org/content/301/5640/1720.abstract [Accessed July 20, 2014].

Kong, F. et al., 2009. Demonstration of catch bonds between an integrin and its ligand. *The Journal of cell biology*, 185(7), pp.1275–84. Available at: http://www.pubmedcentral.nih.gov/articlerender.fcgi?artid=2712956&tool=pmcentrez&rendertype=abstract [Accessed March 31, 2016].

Kostarelos, K. et al., 2007. Cellular uptake of functionalized carbon nanotubes is independent of functional group and cell type. *Nature nanotechnology*, 2(2), pp.108–13.

Kumar, S. et al., 1992. THE weighted histogram analysis method for free-energy calculations on biomolecules. I. The method. *Journal of Computational Chemistry*, 13(8), pp.1011–1021. Available at: http://doi.wiley.com/10.1002/jcc.540130812 [Accessed June 3, 2014].

Kuo, J.-C. et al., 2011. Analysis of the myosin-II-responsive focal adhesion proteome reveals a role for β-Pix in negative regulation of focal adhesion maturation. *Nature cell biology*, 13(4), pp.383–93. Available at: http://www.pubmedcentral.nih.gov/articlerender.fcgi?artid=3279191&tool=pmcentrez&rendertype=abstract [Accessed March 30, 2016].

Lacerda, L. et al., 2007a. Cell-penetrating CNTs for. , 2(6), pp.38–43.

Lacerda, L. et al., 2007b. Cell-penetrating CNTs for delivery of therapeutics. , 2(6), pp.38–43.

Lad, Y. et al., 2007. Structure of three tandem filamin domains reveals auto-inhibition of ligand binding. *The EMBO journal*, 26(17), pp.3993–4004. Available at: http://www.pubmedcentral.nih.gov/articlerender.fcgi?artid=1948075&tool=pmcentrez&rendertype=abstract [Accessed May 13, 2015].

Lau, T.-L. et al., 2009. The structure of the integrin alphaIIbbeta3 transmembrane complex explains integrin transmembrane signalling. *The EMBO journal*, 28(9), pp.1351–61. Available at: http://www.pubmedcentral.nih.gov/articlerender.fcgi?artid=2683045&tool=pmcentrez&rendertype=abstract [Accessed July 23, 2014].

Lawson, C. et al., 2012. FAK promotes recruitment of talin to nascent adhesions to control cell motility. *The Journal of cell biology*, 196(2), pp.223–32. Available at: http://www.pubmedcentral.nih.gov/articlerender.fcgi?artid=3265949&tool=pmcentrez&rendertype=abstract [Accessed November 3, 2014].

Lee, S.E. et al., 2008. Molecular dynamics study of talin-vinculin binding. *Biophysical journal*, 95(4), pp.2027–36. Available at: http://www.sciencedirect.com/science/article/pii/S0006349508701607 [Accessed June 22, 2015].

Lee, S.E., Kamm, R.D. & Mofrad, M.R.K., 2007. Force-induced activation of talin and its possible role in focal adhesion mechanotransduction. *Journal of biomechanics*, 40(9), pp.2096–106. Available at: http://www.ncbi.nlm.nih.gov/pubmed/17544431 [Accessed June 22, 2015].

Lele, T.P. et al., 2008. Investigating complexity of protein-protein interactions in focal adhesions. *Biochemical and biophysical research communications*, 369(3), pp.929–34. Available at: http://www.pubmedcentral.nih.gov/articlerender.fcgi?artid=2730744&tool=pmcentrez&rendertype=abstract [Accessed March 30, 2016].

Lindahl, E. et al., 2006. NOMAD-Ref: visualization, deformation and refinement of macromolecular structures based on all-atom normal mode analysis. *Nucleic acids research*, 34(Web Server issue), pp.W52–6. Available at: http://www.pubmedcentral.nih.gov/articlerender.fcgi?artid=1538881&tool=pmcentrez&rendertype=abstract [Accessed March 4, 2016].

Liu, J. et al., 2015. Structural mechanism of integrin inactivation by filamin. *Nature structural & molecular biology*, 22(5), pp.383–389. Available at: http://www.nature.com/nsmb/journal/v22/n5/full/nsmb.2999.html?WT.ec_id=NSMB-201505 [Accessed April 21, 2015].

Liu, J., Taylor, D.W. & Taylor, K. a, 2004. A 3-D reconstruction of smooth muscle alpha-actinin by CryoEm reveals two different conformations at the actin-binding region. *Journal of molecular biology*, 338(1), pp.115–25. Available at: http://www.ncbi.nlm.nih.gov/pubmed/15050827 [Accessed July 2, 2014].

Liu, J., Taylor, D.W. & Taylor, K.A., 2004. A 3-D reconstruction of smooth muscle alpha-actinin by CryoEm reveals two different conformations at the actin-binding region. *Journal of molecular biology*, 338(1), pp.115–25. Available at: http://www.sciencedirect.com/science/article/pii/S0022283604001858 [Accessed July 23, 2014].

Lorin X. Benedict, S.G.L. and M.L.C., 1996. HEAT CAPACITY OF CARBON NANOTUBES. *Solid State Communications*, 100(3), pp.177–180.

Lu, Q. et al., 2004. RNA Polymer Translocation with Single-Walled Carbon Nanotubes. *Nano Letters*, 4(12), pp.2473–2477. Available at: http://pubs.acs.org/doi/abs/10.1021/nl048326j.

Lv, C. et al., 2014. Single-molecule force spectroscopy reveals force-enhanced binding of calcium ions by gelsolin. *Nature Communications*, 5, pp.1–9. Available at: http://www.nature.com/doifinder/10.1038/ncomms5623.

Macindoe, G. et al., 2010. HexServer: an FFT-based protein docking server powered by graphics processors. *Nucleic acids research*, 38(Web Server issue), pp.W445–9.

MacKerell, A.D. et al., 1998. All-Atom Empirical Potential for Molecular Modeling and Dynamics Studies of Proteins †. *The Journal of Physical Chemistry B*, 102(18), pp.3586–3616. Available at: http://dx.doi.org/10.1021/jp973084f [Accessed May 29, 2014].

MacKerell, a D., Banavali, N. & Foloppe, N., 2001. Development and current status of the CHARMM force field for nucleic acids. *Biopolymers*, 56(4), pp.257–65.

McGregor, A. et al., 1994. Identification of the vinculin-binding site in the cytoskeletal protein alpha-actinin. *The Biochemical journal*, 301 (Pt 1, pp.225–33. Available at: http://www.pubmedcentral.nih.gov/articlerender.fcgi?artid=1137166&tool=pmcentrez&rendertype=abstract [Accessed February 13, 2016].

Mehrbod, M., Trisno, S. & Mofrad, M.R.K., 2013. On the activation of integrin αIIbβ3: outside-in and inside-out pathways. *Biophysical journal*, 105(6), pp.1304–15. Available at: http://www.ncbi.nlm.nih.gov/pubmed/24047981.

Minton, K., 2014. Mechanotransduction: A stiff response. *Nature Reviews Molecular Cell Biology*, 15(8), p.500.

Mofrad, M.R.K., 2009. Rheology of the Cytoskeleton. *Annual Review of Fluid Mechanics*, 41(1), pp.433–453. Available at: http://www.annualreviews.org/doi/abs/10.1146/annurev.fluid.010908.165236 [Accessed February 13, 2016].

Mofrad, M.R.K. & Kamm, R.D., 2011. *Cytoskeletal Mechanics Models and Measurements in Cell Mechanics*, New York, New York, USA: Cambridge University Press.

Mofrad, M.R.K. & Kamm, R.D., 2006. *Cytoskeletal Mechanics: Models and Measurements in Cell Mechanics*,

Moser, M. et al., 2009. The tail of integrins, talin, and kindlins. *Science (New York, N.Y.)*, 324(5929), pp.895–9. Available at: http://www.sciencemag.org/content/324/5929/895.abstract [Accessed June 2, 2015].

Nhieu, G.T. Van & Izard, T., 2007. Vinculin binding in its closed conformation by a helix addition mechanism. *The EMBO journal*, 26(21), pp.4588–4596.

Nosé, S., 1984. A unified formulation of the constant temperature molecular dynamics methods. *The Journal of Chemical Physics*, 81(1), p.511. Available at: http://scitation.aip.org/content/aip/journal/jcp/81/1/10.1063/1.447334 [Accessed May 27, 2014].

Nurden, P. et al., 2011. Thrombocytopenia resulting from mutations in filamin A can be expressed as an isolated syndrome. *Blood*, 118(22), pp.5928–37. Available at: http://www.ncbi.nlm.nih.gov/pubmed/21960593 [Accessed May 13, 2015].

O'Connell, M.J. et al., 2002. Band gap fluorescence from individual single-walled carbon nanotubes. *Science (New York, N.Y.)*, 297(5581), pp.593–6.
Oakes, P.W. et al., 2012. Tension is required but not sufficient for focal adhesion maturation without a stress fiber template. *The Journal of cell biology*, 196(3), pp.363–74. Available at: http://www.pubmedcentral.nih.gov/articlerender.fcgi?artid=3275371&tool=pmcentrez&rendertype=abstract [Accessed March 7, 2016].
Odom, T.W. & Huang, J., 1998. Atomic structure and electronic properties of single-walled carbon nanotubes. , 391(January), pp.1997–1999.
Otey, C. a et al., 1993. Mapping of the alpha-actinin binding site within the beta 1 integrin cytoplasmic domain. *The Journal of biological chemistry*, 268(28), pp.21193–7. Available at: http://www.ncbi.nlm.nih.gov/pubmed/7691808.
Otey, C.A. & Carpen, O., 2004. Alpha-actinin revisited: a fresh look at an old player. *Cell motility and the cytoskeleton*, 58(2), pp.104–11. Available at: http://www.ncbi.nlm.nih.gov/pubmed/15083532 [Accessed October 9, 2015].
Otey, C.A., Pavalko, F.M. & Burridge, K., 1990. An interaction between alpha-actinin and the beta 1 integrin subunit in vitro. *The Journal of cell biology*, 111(2), pp.721–9. Available at: http://www.pubmedcentral.nih.gov/articlerender.fcgi?artid=2116186&tool=pmcentrez&rendertype=abstract [Accessed April 1, 2016].
Pantarotto, D., Singh, R., et al., 2004. Functionalized carbon nanotubes for plasmid DNA gene delivery. *Angewandte Chemie (International ed. in English)*, 43(39), pp.5242–6.
Pantarotto, D., Briand, J.-P., et al., 2004. Translocation of bioactive peptides across cell membranes by carbon nanotubes. *Chemical communications (Cambridge, England)*, (1), pp.16–7. Available at: http://www.ncbi.nlm.nih.gov/pubmed/14737310.
Parrinello, M., 1981. Polymorphic transitions in single crystals: A new molecular dynamics method. *Journal of Applied Physics*, 52(12), p.7182. Available at: http://scitation.aip.org/content/aip/journal/jap/52/12/10.1063/1.328693 [Accessed May 26, 2014].
Pavalko, F.M. et al., 1991. Alpha-actinin: a direct link between actin and integrins. *Biochemical Society transactions*, 19(4), pp.1065–9. Available at: http://www.ncbi.nlm.nih.gov/pubmed/1794463 [Accessed April 1, 2016].
Pentikäinen, U. & Ylänne, J., 2009. The regulation mechanism for the auto-inhibition of binding of human filamin A to integrin. *Journal of molecular biology*, 393(3), pp.644–57. Available at: http://www.ncbi.nlm.nih.gov/pubmed/19699211 [Accessed March 19, 2013].
Petrich, B.G. et al., 2007. Talin is required for integrin-mediated platelet function in hemostasis and thrombosis. *The Journal of experimental medicine*, 204(13), pp.3103–11. Available at: http://jem.rupress.org/content/204/13/3103.short [Accessed July 23, 2014].
Phillips, J.C. et al., 2005. Scalable molecular dynamics with NAMD. *Journal of computational chemistry*, 26(16), pp.1781–802. Available at: http://www.pubmedcentral.nih.gov/articlerender.fcgi?artid=2486339&tool=pmcentrez&rendertype=abstract [Accessed May 21, 2013].
Piana, S., Lindorff-Larsen, K. & Shaw, D.E., 2011. How robust are protein folding

simulations with respect to force field parameterization? *Biophysical journal*, 100(9), pp.L47–9. Available at: http://www.sciencedirect.com/science/article/pii/S0006349511004097 [Accessed December 11, 2014].

Plotnikov, S.V. et al., 2012. Force Fluctuations within Focal Adhesions Mediate ECM-Rigidity Sensing to Guide Directed Cell Migration. *Cell*, 151(7), pp.1513–1527. Available at: http://www.pubmedcentral.nih.gov/articlerender.fcgi?artid=3821979&tool=pmcentrez&rendertype=abstract [Accessed October 7, 2015].

Pollard, T.D. & Cooper, J.A., 2009. Actin, a central player in cell shape and movement. *Science (New York, N.Y.)*, 326(5957), pp.1208–12. Available at: http://www.pubmedcentral.nih.gov/articlerender.fcgi?artid=3677050&tool=pmcentrez&rendertype=abstract [Accessed July 11, 2014].

Popowicz, G.M. et al., 2006. Filamins: promiscuous organizers of the cytoskeleton. *Trends in biochemical sciences*, 31(7), pp.411–9. Available at: http://www.ncbi.nlm.nih.gov/pubmed/16781869 [Accessed May 13, 2015].

Provasi, D. et al., 2014. Talin-driven inside-out activation mechanism of platelet αIIbβ3 integrin probed by multimicrosecond, all-atom molecular dynamics simulations. *Proteins*, 82(12), pp.3231–40. Available at: http://www.ncbi.nlm.nih.gov/pubmed/24677266 [Accessed May 13, 2015].

Pudas, R. et al., 2005. Structural basis for vertebrate filamin dimerization. *Structure (London, England : 1993)*, 13(1), pp.111–9. Available at: http://www.ncbi.nlm.nih.gov/pubmed/15642266 [Accessed May 13, 2015].

Rayment, I. et al., 1993. Structure of the actin-myosin complex and its implications for muscle contraction. *Science (New York, N.Y.)*, 261(5117), pp.58–65. Available at: http://www.ncbi.nlm.nih.gov/pubmed/8316858 [Accessed April 1, 2016].

Ridley, A.J. et al., 2003. Cell migration: integrating signals from front to back. *Science (New York, N.Y.)*, 302(5651), pp.1704–9. Available at: http://www.ncbi.nlm.nih.gov/pubmed/14657486 [Accessed July 10, 2014].

del Rio, A. et al., 2009. Stretching single talin rod molecules activates vinculin binding. *Science (New York, N.Y.)*, 323(5914), pp.638–41. Available at: http://www.ncbi.nlm.nih.gov/pubmed/19179532 [Accessed February 13, 2016].

Ritchie, D.W., 2008. Recent progress and future directions in protein-protein docking. *Current protein & peptide science*, 9(1), pp.1–15. Available at: http://www.ncbi.nlm.nih.gov/pubmed/18336319 [Accessed March 31, 2016].

Roca-Cusachs, P. et al., 2013a. Integrin-dependent force transmission to the extracellular matrix by α-actinin triggers adhesion maturation. *Proceedings of the National Academy of Sciences of the United States of America*, 110(15), pp.E1361–70. Available at: http://www.pubmedcentral.nih.gov/articlerender.fcgi?artid=3625291&tool=pmcentrez&rendertype=abstract [Accessed July 9, 2014].

Roca-Cusachs, P. et al., 2013b. Integrin-dependent force transmission to the extracellular matrix by α-actinin triggers adhesion maturation. *Proceedings of the National Academy of Sciences of the United States of America*, 110(15), pp.E1361–70. Available at: http://www.pnas.org/content/110/15/E1361.long [Accessed May 28, 2014].

Rognoni, L. et al., 2012. Dynamic force sensing of filamin revealed in single-molecule experiments. *Proceedings of the National Academy of Sciences of the United States of America*, 109(48), pp.19679–84. Available at: http://www.pnas.org/content/109/48/19679.short [Accessed May 13, 2015].

Sakisaka, T. et al., 1997. Phosphatidylinositol 4,5-bisphosphate phosphatase regulates the rearrangement of actin filaments. *Mol Cell Biol*, 17(7), pp.3841–3849. Available at: http://www.ncbi.nlm.nih.gov/pubmed/9199318\nhttp://mcb.asm.org/content/17/7/3841.full.pdf.

Sampson, L.J., Leyland, M.L. & Dart, C., 2003. Direct interaction between the actin-binding protein filamin-A and the inwardly rectifying potassium channel, Kir2.1. *The Journal of biological chemistry*, 278(43), pp.41988–97. Available at: http://www.ncbi.nlm.nih.gov/pubmed/12923176 [Accessed May 13, 2015].

Schneidman-Duhovny, D. et al., 2005. PatchDock and SymmDock: servers for rigid and symmetric docking. *Nucleic acids research*, 33(Web Server issue), pp.W363–7. Available at: http://www.pubmedcentral.nih.gov/articlerender.fcgi?artid=1160241&tool=pmcentrez&rendertype=abstract [Accessed January 19, 2016].

Schwartz, M.A., 2010. Integrins and extracellular matrix in mechanotransduction. *Cold Spring Harbor perspectives in biology*, 2(12), p.a005066. Available at: http://www.pubmedcentral.nih.gov/articlerender.fcgi?artid=2982167&tool=pmcentrez&rendertype=abstract [Accessed August 18, 2015].

Scott, W.R.P. et al., 1999. The GROMOS Biomolecular Simulation Program Package. *The Journal of Physical Chemistry A*, 103(19), pp.3596–3607. Available at: http://dx.doi.org/10.1021/jp984217f [Accessed November 2, 2015].

Shams, H. et al., 2014. Actin reorganization through dynamic interactions with single-wall carbon nanotubes. *ACS nano*, 8(1), pp.188–97. Available at: http://dx.doi.org/10.1021/nn402865e [Accessed October 29, 2015].

Shams, H. et al., 2016. Dynamic Regulation of α-Actinin's Calponin Homology Domains on F-Actin. *Biophysical Journal*, 110(6), pp.1444–1455. Available at: http://www.sciencedirect.com/science/article/pii/S0006349516002125 [Accessed March 30, 2016].

Shams, H., Golji, J. & Mofrad, M.R.K., 2012. A molecular trajectory of α-actinin activation. *Biophysical journal*, 103(10), pp.2050–9. Available at: http://www.pubmedcentral.nih.gov/articlerender.fcgi?artid=3512038&tool=pmcentrez&rendertype=abstract [Accessed July 2, 2014].

Shams, H., Golji, J. & Mofrad, M.R.K., 2012. Molecular Trajectory of Alpha-Actinin Activation. *Biophysical journal*, 103(10), pp.2050–2059.

Shi Kam, N.W. et al., 2004. Nanotube molecular transporters: internalization of carbon nanotube-protein conjugates into Mammalian cells. *Journal of the American Chemical Society*, 126(22), pp.6850–1. Available at: http://www.ncbi.nlm.nih.gov/pubmed/15908924.

Singh, R. et al., 2005. Binding and condensation of plasmid DNA onto functionalized carbon nanotubes: toward the construction of nanotube-based gene delivery vectors. *Journal of the American Chemical Society*, 127(12), pp.4388–96.

Sjöblom, B., Salmazo, A. & Djinović-Carugo, K., 2008. Alpha-actinin structure and regulation. *Cellular and molecular life sciences : CMLS*, 65(17), pp.2688–701.

Available at: http://www.ncbi.nlm.nih.gov/pubmed/18488141 [Accessed June 12, 2015].
Smart, S.K. et al., 2006. The biocompatibility of carbon nanotubes. *Carbon*, 44(6), pp.1034–1047.
Stossel, T.P. et al., 2001. Filamins as integrators of cell mechanics and signalling. *Nature reviews. Molecular cell biology*, 2(2), pp.138–45. Available at: http://dx.doi.org/10.1038/35052082 [Accessed May 13, 2015].
Tadokoro, S. et al., 2011a. A potential role for α-actinin in inside-out αIIbβ3 signaling. *Blood*, 117(1), pp.250–8. Available at: http://www.ncbi.nlm.nih.gov/pubmed/20940419 [Accessed January 2, 2013].
Tadokoro, S. et al., 2011b. A potential role for α-actinin in inside-out αIIbβ3 signaling. *Blood*, 117(1), pp.250–8. Available at: http://www.ncbi.nlm.nih.gov/pubmed/20940419 [Accessed July 15, 2014].
Tadokoro, S. et al., 2003. Talin binding to integrin beta tails: a final common step in integrin activation. *Science (New York, N.Y.)*, 302(5642), pp.103–6. Available at: http://www.sciencemag.org/content/302/5642/103.short [Accessed July 22, 2014].
Tang, J., Taylor, D.W. & Taylor, K.A., 2001. The three-dimensional structure of alpha-actinin obtained by cryoelectron microscopy suggests a model for Ca(2+)-dependent actin binding. *Journal of molecular biology*, 310(4), pp.845–58. Available at: http://www.ncbi.nlm.nih.gov/pubmed/11453692 [Accessed July 27, 2015].
Tojkander, S., Gateva, G. & Lappalainen, P., 2012. Actin stress fibers--assembly, dynamics and biological roles. *Journal of cell science*, 125(Pt 8), pp.1855–64. Available at: http://jcs.biologists.org/content/125/8/1855.short [Accessed September 29, 2015].
Torrie, G.M. & Valleau, J.P., 1977. Nonphysical sampling distributions in Monte Carlo free-energy estimation: Umbrella sampling. *Journal of Computational Physics*, 23(2), pp.187–199. Available at: http://www.sciencedirect.com/science/article/pii/0021999177901218 [Accessed June 3, 2014].
Towns, J. et al., 2014. XSEDE: Accelerating Scientific Discovery. *Computing in Science and Engineering*, 16(5), pp.62–74.
Travé, G. et al., 1995. Molecular mechanism of the calcium-induced conformational change in the spectrin EF-hands. *The EMBO journal*, 14(20), pp.4922–31. Available at: http://www.pubmedcentral.nih.gov/articlerender.fcgi?artid=394594&tool=pmcentrez&rendertype=abstract [Accessed August 19, 2015].
Treacy, M.M.J., Ebbesen, T.W., Gibson, J.M., 1996. Exceptionally high young's modulus observed for individual carbon nanotubes. *Nature*, 381, pp.678–680.
Truong, T., Shams, H. & Mofrad, M.R.K., 2015. Mechanisms of integrin and filamin binding and their interplay with talin during early focal adhesion formation. *Integr. Biol.* Available at: http://pubs.rsc.org/en/content/articlehtml/2015/ib/c5ib00133a [Accessed July 14, 2015].
Tuszynski, J.A., Brown, J.A. & Sept, D., 2003. Models of the Collective Behavior of Proteins in Cells : Tubulin , Actin and Motor Proteins. *J. Biol. Phys.*, 29, pp.401–428.
Vinogradova, O. et al., 2002. A Structural Mechanism of Integrin αIIbβ3 "Inside-Out"

Activation as Regulated by Its Cytoplasmic Face. *Cell*, 110(5), pp.587–597. Available at: http://www.sciencedirect.com/science/article/pii/S0092867402009066 [Accessed May 13, 2015].
Vogel, V., 2006. MECHANOTRANSDUCTION INVOLVING MULTIMODULAR PROTEINS: Converting Force into Biochemical Signals. *Annual Review of Biophysics and Biomolecular Structure*, 35(1), pp.459–488. Available at: http://www.annualreviews.org/doi/abs/10.1146/annurev.biophys.35.040405.102013.
Vogel, V. & Sheetz, M., 2006. Local force and geometry sensing regulate cell functions. *Nature reviews. Molecular cell biology*, 7(4), pp.265–75. Available at: http://www.ncbi.nlm.nih.gov/pubmed/16607289 [Accessed July 10, 2014].
Vogel, V. & Sheetz, M.P., 2009. Cell fate regulation by coupling mechanical cycles to biochemical signaling pathways. *Current opinion in cell biology*, 21(1), pp.38–46. Available at: http://www.sciencedirect.com/science/article/pii/S0955067409000040 [Accessed February 11, 2016].
Way, M., 1992. Evidence for functional homology in the F-actin binding domains of gelsolin and alpha-actinin: implications for the requirements of severing and capping. *The Journal of Cell Biology*, 119(4), pp.835–842. Available at: http://jcb.rupress.org/content/119/4/835.abstract?sid=ed1bfc29-7071-49f8-a4d2-5c9274fa8c4c [Accessed August 19, 2015].
Wegener, K.L. et al., 2007. Structural basis of integrin activation by talin. *Cell*, 128(1), pp.171–82. Available at: http://www.ncbi.nlm.nih.gov/pubmed/17218263 [Accessed May 8, 2015].
Weins, A. et al., 2007. Disease-associated mutant alpha-actinin-4 reveals a mechanism for regulating its F-actin-binding affinity. *Proceedings of the National Academy of Sciences of the United States of America*, 104(41), pp.16080–5. Available at: http://www.pubmedcentral.nih.gov/articlerender.fcgi?artid=2042165&tool=pmcentrez&rendertype=abstract.
Wenseleers, W. et al., 2004. Efficient Isolation and Solubilization of Pristine Single-Walled Nanotubes in Bile Salt Micelles. *Advanced Functional Materials*, 14(11), pp.1105–1112.
von Wichert, G. et al., 2003. Force-dependent integrin-cytoskeleton linkage formation requires downregulation of focal complex dynamics by Shp2. *The EMBO journal*, 22(19), pp.5023–35. Available at: http://www.pubmedcentral.nih.gov/articlerender.fcgi?artid=204475&tool=pmcentrez&rendertype=abstract [Accessed March 30, 2016].
Winder, S.J., 1997. The membrane-cytoskeleton interface: the role of dystrophin and utrophin. *Journal of muscle research and cell motility*, 18(6), pp.617–29. Available at: http://www.ncbi.nlm.nih.gov/pubmed/9429156 [Accessed February 13, 2016].
Yang, W. et al., 2007. Carbon nanotubes for biological and biomedical applications. *Nanotechnology*, 18(41), p.412001. Available at: http://stacks.iop.org/0957-4484/18/i=41/a=412001?key=crossref.aeb11a066db59e3a3288108524722634 [Accessed October 29, 2012].
Yao, M., Qiu, W., et al., 2014. Force-dependent conformational switch of α-catenin controls vinculin binding. *Nature Communications*, 5. Available at: http://www.nature.com/doifinder/10.1038/ncomms5525.
Yao, M., Goult, B.T., et al., 2014. Mechanical activation of vinculin binding to talin locks

talin in an unfolded conformation. *Scientific Reports*, 4. Available at: http://www.nature.com/doifinder/10.1038/srep04610.

Yaron, P.N. et al., 2011. Single wall carbon nanotubes enter cells by endocytosis and not membrane penetration. *Journal of nanobiotechnology*, 9(1), p.45.

Ye, F., Lagarrigue, F. & Ginsberg, M.H., 2014. SnapShot: Talin and the Modular Nature of the Integrin Adhesome. *Cell*, 156(6), pp.1340–1340.e1. Available at: http://www.ncbi.nlm.nih.gov/pubmed/24630731 [Accessed April 15, 2015].

Ye, F., Snider, A.K. & Ginsberg, M.H., 2014. Talin and kindlin: the one-two punch in integrin activation. *Frontiers of medicine*, 8(1), pp.6–16. Available at: http://www.ncbi.nlm.nih.gov/pubmed/24477625 [Accessed May 13, 2015].

Zaidel-Bar, R. et al., 2003. Early molecular events in the assembly of matrix adhesions at the leading edge of migrating cells. *Journal of cell science*, 116(Pt 22), pp.4605–13. Available at: http://www.ncbi.nlm.nih.gov/pubmed/14576354 [Accessed May 24, 2013].

Zhang, W. & Gunst, S.J., 2006. Dynamic association between alpha-actinin and beta-integrin regulates contraction of canine tracheal smooth muscle. *The Journal of physiology*, 572(Pt 3), pp.659–76. Available at: http://www.pubmedcentral.nih.gov/articlerender.fcgi?artid=1780001&tool=pmcentrez&rendertype=abstract [Accessed March 30, 2016].

Zhang, W., Zhang, Z. & Zhang, Y., 2011. The application of carbon nanotubes in target drug delivery systems for cancer therapies. *Nanoscale research letters*, 6(1), p.555. Available at: http://www.pubmedcentral.nih.gov/articlerender.fcgi?artid=3210734&tool=pmcentrez&rendertype=abstract [Accessed November 14, 2012].

Zhao, C.L. et al., 2014. The interaction of CRM1 and the nuclear pore protein Tpr. *PloS one*, 9(4), pp.e93709–e93721. Available at: http://journals.plos.org/plosone/article?id=10.1371/journal.pone.0093709 [Accessed November 25, 2015].

Ziegler, W.H., Liddington, R.C. & Critchley, D.R., 2006. The structure and regulation of vinculin. *Trends in cell biology*, 16(9), pp.453–60. Available at: http://www.ncbi.nlm.nih.gov/pubmed/16893648 [Accessed January 27, 2016].